Metallophores as Tools for Antibiotic Drug Development and the Study of Bacterial Metal Homeostasis

By

Minhua Cao

A dissertation submitted in partial fulfillment of the requirements for the degree of

Doctor of Philosophy

(Chemistry)

At the

UNIVERSITY OF WISCONSIN-MADISON

2025

Date of final oral examination: 05/06/2025

Members of the Final Oral Committee:
Eszter Boros, Associate Professor, Chemistry
Monica Neugebauer, Assistant Professor, Biochemistry
Thomas C. Brunold, Professor, Chemistry
Helen E. Blackwell, Professor, Chemistry

Metallophores as Tools for Antibiotic Drug Development and the Study of Bacterial Metal Homeostasis

By

Minhua Cao

Under the supervision of Associate Professor Eszter Boros

At the University of Wisconsin-Madison

Abstract of the Dissertation

Antibiotic resistance poses a critical global health threat, contributing to an estimated 4.95 million deaths in 2019 alone. The efficacy of conventional antibiotics is increasingly compromised by the emergence of resistant strains, limiting treatment options. To circumvent these resistance mechanisms, alternative strategies are being explored, including the use of siderophores, microbe secondary metabolite, to hijack bacterial iron import pathways for cytotoxic payload delivery inspired by natural antibiotics. This approach has gained significant traction, exemplified by the FDA approval of Cefiderocol, a siderophore antibiotic, and extensive efforts to develop other siderophore-based antibiotics. However, our knowledge of the uptake and stability of these compounds remains incomplete.

To advance our understanding of siderophore uptake and stability, we developed and applied radiolabeled and photoaffinity-labeled small molecule tools. First, we developed a dual radiolabeling strategy using ^{67}Ga and ^{124}I to track both in vitro and in vivo behavior. This revealed that Ga siderophore conjugates are internalized as metal complexes via siderophore-mediated

uptake. In vivo studies, utilizing a murine infection model, demonstrated probe degradation primarily through metal cargo decomplexation, though Ga-D6-I exhibited significant uptake in infected tissue (Chapter 2). Second, based on the Fe-D1/FoxA co-crystal structure, we designed and optimized photoaffinity probes to understand their reactivity and validate their ability to target siderophore transmembrane transporters. These probes successfully labeled isolated FoxA protein (Chapter 3). Third, when applied to live bacterial cells, these probes facilitated the visualization and identification of siderophore-binding proteins, suggesting a potential role for OmpF in the uptake of these compounds (Chapter 4). Overall, this research provides valuable insights into the stability and uptake mechanisms of Ga-siderophore conjugates, offering new tools and strategies for future studies on siderophore-antibiotic acquisition and pharmacokinetics.

Acknowledgements

To all who have walked alongside me on this path, offering guidance, encouragement, and even gentle challenges: know that your presence has been instrumental in shaping not only my understanding of science but also the very person I have become. My deepest gratitude for the mark you have each left on my journey.

To the inspiring individuals who shaped my education, their passion and dedication to teaching making a profound difference. To my teachers, who transformed chemistry into a source of wonder. Your phrase, 'All the physical world is made of atoms, and all interactions happen within those empty spaces,' remains with me. Thank you for demystifying higher education and demonstrating its accessible to anyone driven by curiosity, questions, and dedication.

To Eszter, I am grateful for your guidance, advice, and for encouraging us to aim higher. Your belief in my abilities, which often surpassed my own, and your encouragement to step outside my comfort zone have significantly shaped me as a scientist. Having you as a role model has been truly transformational. Witnessing your journey has profoundly shifted my perspective. It has opened up possibilities I hadn't fully imagined before.

To my group, both past and present members, thank you for your support, which has made this journey both possible and enjoyable. To Apurva, though our time together was brief, I appreciate the opportunity to have learned from you. Your dedication and effort have been truly inspirational. To Darek and Jennifer, thank you for sharing this entire journey with me. It has been a joy to witness your growth into the scientists you are today. Your effort and dedication inspired me to persevere. Axia, your support during challenging times was invaluable, and you made the

bacterial assay work enjoyable. It was a pleasure to share this journey with you and to witness your growth into a brilliant and strong scientist. Thank you for being so unapologetically you; I truly appreciate your directness and straightforwardness. I learned a great deal from you. Andrey, thank you for your advice and help; it was great working with you on the infection imaging project. Owen, knowing I partially influenced your decision to join the group, I hope you have fun during your journey. Emma, thank you for taking over the siderophore project. While it is not an easy one, I hope you come to appreciate and learn with each challenge. You are a very capable person, and I know you will do well; I look forward to seeing your future work. Morgan, Georgia, Zhuoran, and Edith, thank you for your company and enthusiasm; you brighten the workplace and bring new energy to the group. I know you will do incredible things. To Marie, thank you for taking over this project at such an advanced stage. I truly appreciate your enthusiasm and help; thanks to you, its completion is now within reach. While it presents challenges, I have confidence in your ability to succeed, and I wish you the very best of luck.

My appreciation extends to our collaborators, Henning Tidow and Inokentijs Josts (Kesha), for their invaluable contributions. To Gregory (Greg) Sabat from the mass spectrometry core, whose expertise was essential to this work. To Justin Acheson and Justin Dang, thank you for generously sharing your knowledge and easing my transition into chemical biology. And to all the wonderful individuals who offered guidance and support along the way, including my committee, thank you.

To my friends Junia and Stephanie, you are all extraordinary individuals. Your friendship has enriched my life and made the difficult moments more bearable. Thank you for your unwavering support and for the countless meaningful conversations. Wenyan and Heitor, thank

you so much for your help, friendship, and down-to-earth advice. You made the transition to the USA easier and helped me not miss Brazil so intensely. Thank you for always being there when I needed you.

To Aaron, your love and support made this achievement possible. It simply wouldn't have happened without you. You believed in me when I doubted myself. Thank you for being there every step of the way, through the late nights. I am incredibly fortunate to have you in my life.

And to Mom and Dad, thank you for believing in the transformative power of education, a belief you instilled in me even when it seemed beyond your reach. You left behind your home, your entire world, and dedicated yourselves to providing us with a better future. I owe everything to your love and dedication.

Table of Contents

List of Main Text Figures

Chapter 1

Chapter 2

Chapter 4

Chapter 5

List of Main Text Tables

Chapter 1

Chapter 2

Glossary

DFO	Deferoxamine
THF	Tetrahydrofuran
HOAc	Acetic acid
TFA	Trifluoroacetic acid
KOH	Potassium hydroxide
DMF	Dimethylformamide
DCM	Dichloromethane
DIPEA	Diisopropylethylamine
PyBop	Benzotriazol-1-yloxytripyrrolidinophosphonium hexafluorophosphate
HBTU	Hexafluorophosphate Benzotriazole Tetramethyl Uronium
TBTA	Tris((1-benzyl-4-triazolyl)methyl)amine
Tren-Cam	4-((2-(bis(2-(2,3-dihydroxybenzamido)ethyl)amino)ethyl)carbamoyl)-2,3-dihydroxybenzoic acid
RT	Room temperature
O/N	Over night
HPLC	High performance liquid chromatography
LC-MS	Liquid chromatography–mass spectrometry
UV	Ultraviolet
EDTA	Ethylenediaminetetraacetic acid
LB	Luria-Bertani
OD	Optical density

HEPES	2-[4-(2-hydroxyethyl)piperazin-1-yl]ethanesulfonic acid
WT	Wild type
CPM	Counts per minute
DEA	Diethylamine
DMSO	Dimethyl sulfoxide
MIC	Minimum inhibitory concentration
MHB	Mueller-Hinton broth
LB	Lysogeny broth/ Luria–Bertani medium
Iodo-gen	1,3,4,6-tetrachloro-3α,6α-diphenyl-glycoluril
eV	Electronvolt
HRMS	High resolution mass spectrometry
SDS	Sodium dodecyl sulfate
SDS-PAGE	Sodium dodecyl sulfate polyacrylamide gel electrophoresis
TRIS	Tris(hydroxymethyl)aminomethane
TBS	Tris-buffered saline
PBS	Phosphate buffered saline
BSA	Bovine serum albumin
BME	Beta-mercaptoethanol
OG	n-Octyl-Beta-D-Glucopyranoside

Chapter 1: Introduction

1.1 Antibiotic resistance: an increasing threat to healthcare

The discovery antimicrobial drugs marked a turning point in the fight against infectious diseases. Prior to the antibiotic era, bacterial infections, particularly bacteremia, accounted for approximately 15% of all human deaths.[8] The clinical implementation of sulfonamide antibiotics resulted in a reduction of mortality rates to approximately 2%, and proved the efficacy of these therapeutic interventions.[9] Traditional antibiotics work through two primary mechanisms: bactericidal action, characterized by direct bacterial killing (e.g., β-lactams, aminoglycosides, fluoroquinolones), and bacteriostatic action, characterized by inhibition of bacterial proliferation (e.g., tetracyclines, sulfonamides, oxazolidinones) (Figure 1.1).[10] These agents target essential bacterial processes, including cell wall biosynthesis, protein synthesis, nucleic acid replication, metabolic pathways, and membrane integrity.[11] However, following their discovery and initial success, decades of widespread antibiotic exposure, misuse, and overuse worldwide has exerted substantial selective pressure on bacterial populations,

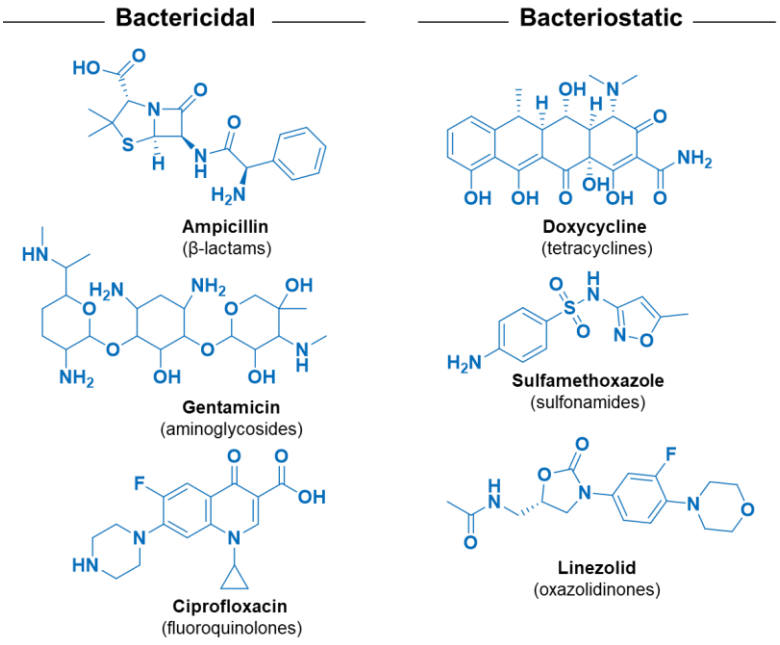

Figure 1. 1: Examples of bactericidal and bacteriostatic clinically approved antibiotic

accelerating the evolution and proliferation of drug-resistant pathogens. These drug-resistant pathogens diminish the therapeutic efficacy of antimicrobial agents and threaten to reverse the gains achieved during the antibiotic era.[9]

The decrease of therapeutic potency is attributed to the molecular strategies employed by bacteria, which are broadly categorized as intrinsic or acquired resistance. Intrinsic resistance leverages existing genetic material for survival, while acquired resistance arises from the introduction of novel genetic material. At the molecular level, these mechanisms include: a reduction of drug influx via downregulation of porin proteins; active efflux of antibiotics through enhanced efflux pump activity; diminished antibiotic binding affinity due to target modification; circumvention of inhibited targets through alternative metabolic pathways; target protection by preventing the antibiotic from interacting with target protein; and enzymatic inactivation of antibiotics (Figure 1.2).[7,12] Additionally, acquired resistance can be disseminated through horizontal gene transfer and lead to rapid propagation of resistance mechanisms across bacterial populations. Collectively, these strategies enable pathogenic organisms to evade the antibiotic

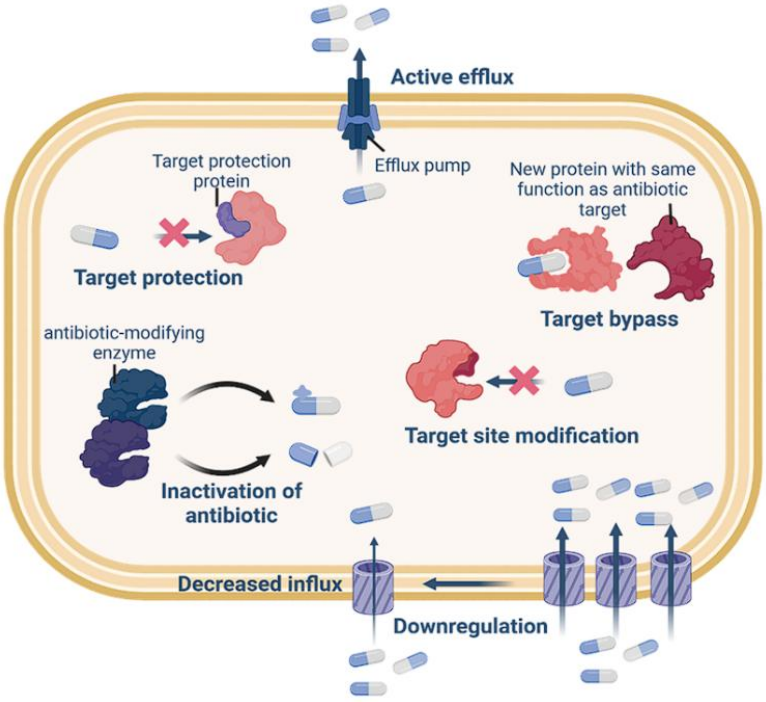

Figure 1. 2 Schematic overview of molecular mechanism of antibiotic resistance. [3,7]

mechanisms of action and as a result, the majority of clinically used antibiotics have produced at least one antibiotic-resistant strain.[13]

The proliferation of antibiotic-resistant bacteria has led to a global crisis. The World Health Organization (WHO) classifies the alarming rise of antimicrobial resistance (AMR) as one of the most pressing global public health threats with an estimated 4.95 million global deaths attributable to AMR. [14] Within the United States, the Centers for Disease Control and Prevention (CDC) estimates that AMR results in 2.8 million infections and 35,900 deaths annually within hospital settings. [2,15]

Pathogens that are especially resistant to antibiotics pose an additional threat to public health infrastructure, because people are most likely to encounter them in a healthcare environment. The increasing prevalence of extended-spectrum beta-lactamase (ESBL)-producing organisms, now a dominant cause of healthcare-associated infections in the United States, and the global dissemination of drug-resistant ESKAPE pathogens (*Enterococcus faecium*, *Staphylococcus aureus*, *Klebsiella pneumoniae*, *Acinetobacter baumannii*, *Pseudomonas aeruginosa*, and *Enterobacte*r species) are major causal agents of hospital-acquired infections .[16] Therefore, the development of novel antibiotic classes capable of circumventing current resistant mechanisms is crucial to mitigate the escalating threat of drug-resistant pathogens.

1.2 The role of siderophores in iron acquisition

Iron acquisition is vital for bacterial survival and pathogenicity because it is a crucial nutrient involved in various biological processes, such as enzyme activity and DNA synthesis. [17] However, iron bioavailability is limited. Under aerobic conditions, iron primarily exists in its Fe^{3+}

oxidation state. At neutral pH, free aqueous Fe^{3+} exhibits extremely low solubility (on the order of 10^{-18} M) due to the formation of hydroxide species, rendering it insufficient to support microbial growth (~10^{-6} M). [18,19] The availability of ferrous iron is further diminished and tightly regulated in aerobic environments due to instability and Fenton chemistry. In the presence of hydrogen peroxide, a byproduct of aerobic respiration, Fe^{2+} can form highly reactive and damaging hydroxyl radicals (OH•).[20] To mitigate toxicity within biological organisms, iron proteins tightly regulate iron homeostasis, to maintain concentrations of free Fe^{3+} at approximately 10^{-24} M.[19]

As a result of iron scarcity, pathogenic bacteria have evolved complex mechanisms to acquire iron. One strategy involves the direct appropriation of iron from host proteins to scavenge and sequester iron from the host via outer membrane receptors that recognize transferrin and lactoferrin. This strategy for iron extraction is mediated by anchored proteins like TbpA/TbpB.[4] Additionally, under iron-limited conditions, bacteria can also utilize heme stored in host proteins, such as ferritin, and hemoglobin. This heme acquisition method involves exotoxin secretion of hemolysins and proteases

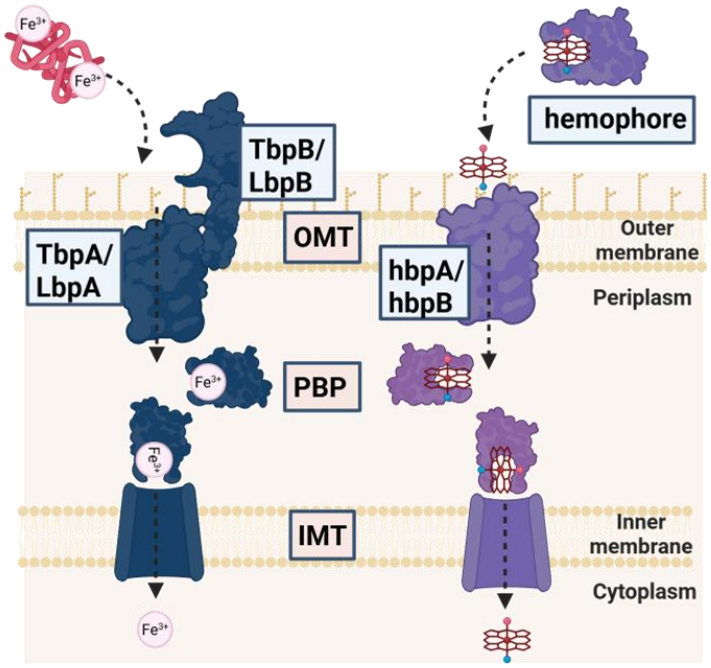

Figure 1. 3: Some of the iron acquisition strategy employed by pathogenic bacteria: (Dark blue) Fe^{3+} acquisition from transferrin and lactoferrin where anchored proteins such as TbpA/TbpB extracts Fe^{3+}. (Purple) Acquisition of heme from host proteins. Both acquisition systems require an outer membrane protein (OMT), a periplasm binding protein (PBP), and an inner membrane transporter (IMT) permease.[4]

to lyse host cells and release heme, which is then uptake by heme transporters such as HpuA/HpuB (Figure 1.3). [4,21]

Beyond these strategies for iron acquisition, microorganisms also employ secretion of siderophores. These low-molecular-weight, secondary metabolites (500-1500 Da) are characterized by their exceptionally high iron-binding affinity, with formation constants (K_f) exceeding 10^{30}.[22] This enables efficient iron scavenging and sequestration from diverse environments. *E. coli* produces enterobactin (Ent), a siderophore that exemplifies this strategy, exhibiting an extraordinary iron stability constant of approximately $[Fe(Ent)]^{3-}$ 10^{49} , representing one of the most potent iron chelators identified to date.[23] Siderophores form soluble Fe^{3+} complexes, which are actively transported into the cell via TonB-dependent transporters (TBDTs),

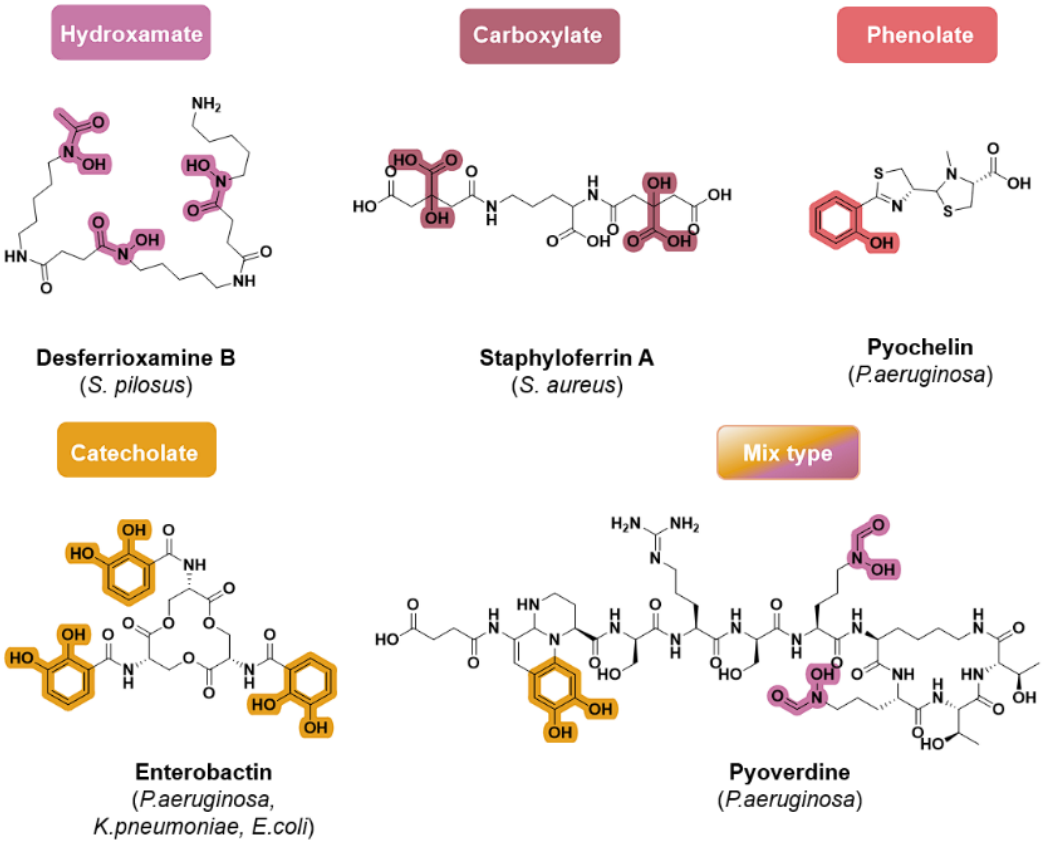

Figure 1. 4: Examples of siderophores containing the four different iron-binding moieties and the bacteria strains that produce them.

with high specificity and selectivity for iron-siderophore complex uptake.[24] This active iron uptake system represents the most prevalent microbial strategies for nutrient acquisition: nearly all known bacterial species produce siderophores. [25]

Siderophores are classified by their iron-binding moieties: catecholates, hydroxamates, phenolates, carboxylates, and mixed types, which incorporate combinations of these functional groups (Figure 1.4). These ligand combinations rely on a limited set of iron-binding donors, but the scaffolds are typically unique to individual species.[26] Studies in *E. coli* have revealed that each siderophore class may be associated with distinct acquisition systems, each involving a unique set of siderophore-mediated proteins.[27,28]

In Gram-negative bacteria, the iron-siderophore acquisition system involves the uptake of iron-siderophore complexes by outer membrane transporter (OMT) that are TBDT dependent. These receptors exhibit structural specificity and selectivity toward classes of metal-bound siderophores. Within the periplasm, the iron-siderophore complex is then shuttled by a periplasmic binding protein (PBP) to the inner membrane transporter (IMT). Finally, the metal ion is released within the cytoplasm, often through reduction of the metal or degradation of the siderophore, for example, as observed with $[Fe(Ent)]^{3-}$ in *E. coli* (Figure 4b). [29,30] Variations in this system exist across bacterial species. In *P. aeruginosa* with the siderophore pyoverdine, iron release occurs in the periplasm via reduction by the FpvG inner-membrane reductase, followed by the transport of Fe^{2+} into the cytoplasm.[31] In contrast, Gram-positive employs siderophore-binding proteins (SBPs) that undergo conformational changes upon binding, thereby activating a permease and facilitating membrane crossing (Figure 4a). [32]

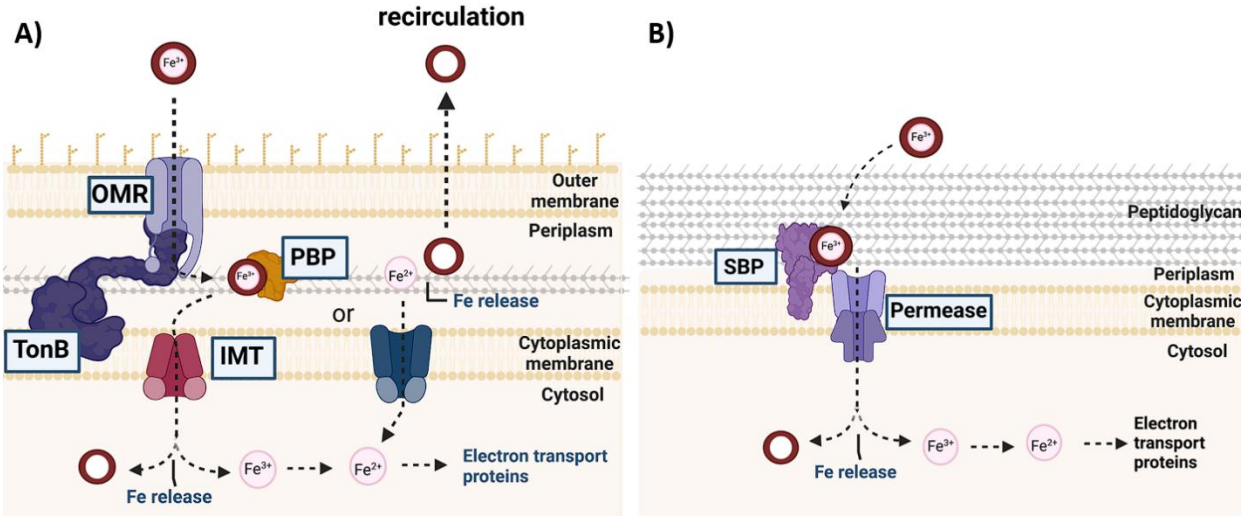

Figure 1. 5: A) Gram-negative siderophore import. Top to bottom, uptake of ion-siderophore complex by outer OMR which it is assisted by TonB protein. In the periplasm, the iron-siderophore complex is shuttle to the inner membrane by PBP protein uptake by the IMT or iron is released in the periplasm where the iron is uptake into the cytosol and the apo-siderophore is recirculated . In the cytosol, $Fe3^{+}$ is reduced to $Fe2^{+}$ and goes to electron transport proteins [1,2,5].B) Gram-positive siderophore import. Top to bottom, ion-siderophore complex binds a SBP that activates a permease leading to membrane crossing. In the cytosol, $Fe3^{+}$ is reduced to $Fe2^{+}$ and goes to electron transport proteins. [6]

Within the host environment, the efficacy of bacterial iron acquisition directly correlates to virulence.[33] To ensure successful infection, pathogenic bacteria strategically deploy siderophores to scavenge and sequester iron from host transport proteins.[34,35] Experimental evidence demonstrates that bacterial strains capable of robust siderophore synthesis and selective siderophore recognition exhibit a marked increase in virulence, particularly during the critical stages of colonization and infection.[26,33,36] However, this strategy is countered by the host's defense mechanisms secretion of lipocalin 2 (Lcn2). This iron-siderophore complex binding protein recognizes $[Fe(Ent)]^{3-}$ to intercept bacterial iron acquisition.[37] The selective pressure imposed by host defenses is driving the evolution of siderophores. For example, salmochelin, a C-glucosylated enterobactin variant, in *Salmonella,* pathogenic *E. coli* , and certain *Klebsiella* strains, evades Lcn2

recognition.[34,38] The siderophore acquisition system is central not only to bacterial survival, but also to the success of infection, as it directly impacts the bacteria's ability to grow and establish disease within the host.

1.3 Sideromycins: natural siderophore antibiotics

The scarcity of bioavailable iron resulted in bacteria strains capable of acquiring xenosiderophores, siderophores synthesized by microorganisms that co-exist in their habitats. This iron piracy serves to minimize biosynthetic energy expenditure in nutrient-depleted environments. [26] This opportunistic behavior has, in turn, driven the evolution of sideromycins, natural siderophore antibiotics (Figure 1.6). Sideromycins are composed of a siderophore covalently linked to a cytotoxic payload and effectively exploit bacterial siderophore uptake systems for targeted intracellular delivery in strains competing for limited resources and nutrients. [39]

Among the most well-studied sideromycins are albomycin and salmycin (Figure 1.6), which act as broad-spectrum antibiotics exhibiting potent antimicrobial activity. Albomycin, produced by *Streptomyces sp.*, effective against gram-negative bacteria, disrupts protein synthesis by inhibiting seryl-tRNA synthetase (SerRS) through the intracellular delivery of its thioheptose nucleoside.[26,40-42] The uptake mechanism of albomycin in *E. coli* internalizes using the same outer membrane transporter (OMT) as ferrichrome, FhuA. Subsequently, the periplasmic binding protein FhuD facilitates its transfer to the inner membrane ABC transporter, FhuBC, culminating in cytoplasmic delivery.[43,44] Within the cytoplasm, the peptidase PepN hydrolyzes the amide bond, releasing the thioheptose nucleoside to exercise its antimicrobial action. Fe^{3+} is then reduced to Fe^{2+}, which dissociates from the siderophore for electronic processes. In albomycin-producing

organisms, the albomycin biosynthetic gene cluster (BGC) encodes *AbmK*, a SerRS conferring immunity the endogenously produced sideromycin by making homologous target protein resistant to thioheptose nucleoside.[45] In addition, the albomycin still functions as an iron carrier beside its antibacterial properties, albeit with a reduced efficiency compared to ferrichrome. [44]

On the other hand, salmycin, produced by *Streptomyces violaceus*, is a broad-spectrum antibiotic active against gram-positive bacteria, presumed to inhibit protein synthesis. Like albomycin, salmycin enters bacterial cells via the hydroxamate transport system. There is experimental evidence indicating that for salmycin, iron reduction triggers intramolecular cyclization, which results in the antibiotic payload release.[46] In summary, the evolutionary pressures of iron scarcity have driven the development of sophisticated bacterial mechanisms, including xenosiderophore acquisition and sideromycin production, highlighting the intricate

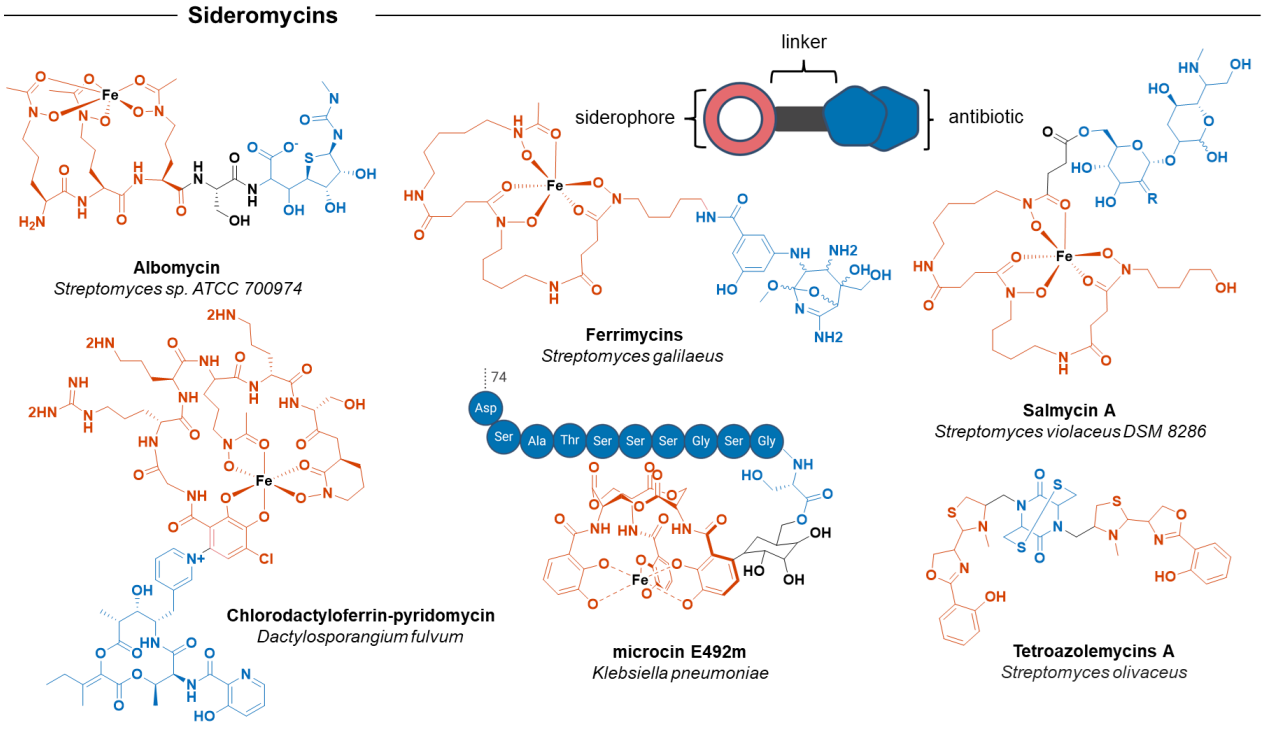

Figure 1. 6: Reported natural sideromycins. Red= siderophore, black=linker, blue= antibiotic.

interplay between nutrient competition and antimicrobial defense and presenting an opportunity for medicinal inorganic chemistry to investigate structure-activity relationships and strategies to perturb iron homeostasis as means to access new antibacterial mechanisms.

1.4 Synthetic sideromycins and trojan horse conjugates.

Given the growing challenge of antibiotic resistance, the bacterial reliance on siderophore-mediated iron acquisition, utilizing receptors absent in mammals, offers a promising therapeutic avenue for targeted drug delivery. [47] Many groups, including ours, are focused on the development of synthetic sideromycins, or "Trojan Horse" antibacterials, to repurpose clinically approved therapeutics. [48,49] This approach circumvents common resistance mechanisms, such as increased efflux pumps and decreased drug permeability, by leveraging bacteria's own active transport systems and acute nutritional need for iron.[11]

The success of this strategy is demonstrated by the 2019 FDA and 2020 EMA (European Medicines Agency) approvals of Cefiderocol for the treatment of gram-negative bacterial (GNB) infections in adults (Figure 1.5).[50,51] Cefiderocol, a catechol-substituted cephalosporin, effectively inhibits bacterial cell wall synthesis, demonstrating potent activity against clinically relevant pathogens such as *K. pneumoniae, E. coli, P. aeruginosa, and A. baumannii*. Its sideromycin-mimetic action allows it to overcome carbapenem resistance in GNB infections by utilizing bacterial iron-siderophore transporters (CirA, Fiu, PiuA) to bypass resistance mechanisms like altered porin permeability and increased efflux.[50]

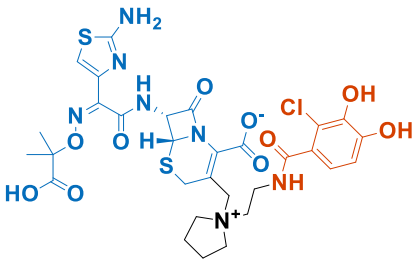

Figure 1. 7: Cefiderocol (Fetroja®) , catechol-substituted cephalosporin siderophore antibiotic. Red= siderophore, black=linker, blue= antibiotic.

Building upon the proven efficacy of siderophore-based antibiotics, the development of these therapeutics encompasses both semi-synthetic and synthetic methodologies. Semi-synthetic strategies leverage native siderophores as structural templates, which are subsequently modified to yield conjugates exhibiting close structural homology to native sideromycins. Conversely, the synthetic route involves the design and construction of synthetically more accessible siderophore mimetics with iron-chelating functionalities to facilitate intracellular delivery.[26] Both methodologies incorporate variable linkers, cleavable and non-cleavable, and carry therapeutic payloads consisting of either drug molecules or pro-drugs.[52]

Recent progress in the development of semi-synthetic and synthetic siderophore-antibiotic conjugates reveals that various drug payloads can be effectively delivered to periplasmic and cytoplasmic targets, resulting in promising antimicrobial efficacy. For example, Bronstrup et al. developed conjugates with cleavable linkers designed for cytoplasmic antibiotic delivery. Their lead compound, a deferoxamine-based conjugate featuring a quinone trimethyl lock, with para-nitrobenzyl-based, linked to ciprofloxacin (conjugate 17), exhibited a MIC of ≤ 1 μM against *E. coli* strains.[52] Similarly, Mong et al. explored structural variations in salmycin analogues to enhance efficacy against methicillin-susceptible *S. aureus* (MSSA). Their Deferri-Glc-Hept N Sal analogue 7' exhibited an MIC of 0.12 μM against MSSA clinical isolates.[53]

Table 1. 1: Reported minimum inhibitory concentration (MIC) values (μM) in iron-deficient media for siderophore conjugates.

Compound	*E. coli*	*MSSA#1*	*PA01*	Ref
17	≤ 1	-	-	[52]
5C	-	-	1.07	[56]
Ciprofloxacin	0.24	-	0.38	[52][56]
Deferri-Glc-Hept N Sal anologue 7	-	0.25	-	[53]
Salmycin	-	1	-	[53]
ASO 12	0.8	-	-	[55]
PNA*	UD	-	-	[55]
D-Ent-ox-Pt(IV)	UD	-	-	[54]
Pt(IV)	UD			[54]
MLEB-22043	0.17	-	0.085	[57]
Aztreonam	0.27	-	9.19	[57]

UD = undetermined; * PNA= ASO 12 without siderophore

Additionally, Nolan et al. repurposed anticancer platinum(IV) prodrugs for antimicrobial applications, leveraging enterobactin pathways. Their conjugate, D-Ent-ox-Pt(IV), exhibited modest growth inhibition, at 7.5 μM reduced the culture turbidity by 50% in *E. coli* (Figure 1.6, Table 1.1).[54]

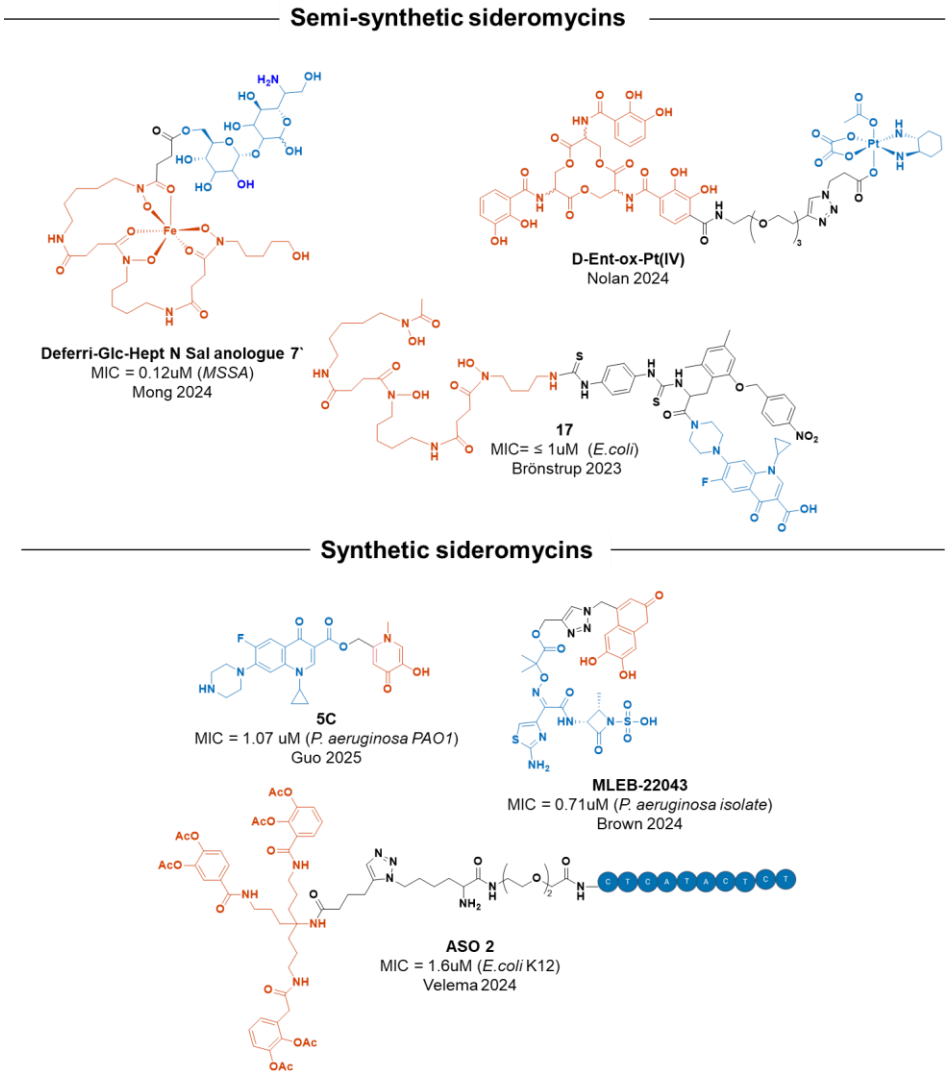

Figure 1. 8: Examples of recent semi-synthetic and synthetic sideromycins (siderophore-antibiotic conjugates) and their minimum inhibitory concentrations (MICs).

Alongside these advancements, the development of fully synthetic siderophore antibiotics has also yielded promising results. Velema et al. designed a catechol-based siderophore, mimicking enterobactin, conjugated to antisense oligonucleotides (ASOs) targeting the acpP gene.

ASO 12 conjugate demonstrated an MIC of 0.8 μM against *E. coli* strains.[55] Addressing the challenge of biofilm formation, Guo et al. developed phenolated siderophore-like molecules, specifically hydroxypyridin-4(1H)-ones, with cleavable ester linkers conjugated to ciprofloxacin. Conjugate 5C exhibited a minimum inhibitory concentration of 1.07 μM and a 61.7% reduction in biofilm formation against *P. aeruginosa*.[56] Finally, to accelerate the discovery of novel siderophore antibiotics, Brown et al. established a high-throughput screening methodology targeting catechol-based siderophores analogous to Cefiderocol. Their lead compound, MLEB-22043, comprised a coumarin-based catechol clicked to a monobactam antibiotic, with an MIC of 0.7 μM against clinical isolates of *P. aeruginosa* (Figure 1.8, Table 1.1*)*.[57]

1.5 Inhibitory activity of xenometal and xeno-metallophores

While siderophores exhibit a high affinity for Fe^{3+}, these natural iron chelators also have the capacity to coordinate other non-bioavailable trivalent metal ions, including Ga^{3+} (0.76 Å), Sc^{3+} (0.87 Å), and In^{3+} (0.93 Å), which share comparable ionic radii and coordination chemistry with high-spin Fe^{3+} (0.78 Å).[47,58,59] Due to their structural and chemical resemblance to iron(III), these xenometals (non-endogenous metals) can be effectively complexed by siderophores and subsequently transported into cells via iron-mediated uptake pathways.[60] The disruption of bacterial iron homeostasis by Ga^{3+}, Sc^{3+}, and In^{3+}, has shown promise in antimicrobial drug development. While these ions exhibit structural homology to iron(III), their inability to undergo redox chemistry under physiological conditions prevents them from fulfilling iron's biological roles, thereby exerting antimicrobial effects.[61]

Gallium (Ga) salts and complexes have been extensively studied for their antineoplastic activity. Given the increased iron demand of cancer cells, Ga acts as an iron mimic, facilitating its

transfer and uptake. Gallium nitrate has progressed to phase II clinical trials for bladder cancer and non-Hodgkin's lymphoma.[62] Beyond anti-cancer properties, Ga-salts have emerged as particularly promising antimicrobial agents. Prior investigations, including those conducted by our research group, have demonstrated the capacity of gallium salts and complexes to inhibit bacterial growth.[63,64] For instance, Ga-nitrate has been shown to exhibit antimicrobial efficacy against *Acinetobacter baumannii* both in vitro and in vivo.[65] Furthermore, a Ga-citrate formulation is currently undergoing Phase II clinical trials for the treatment of *P. aeruginosa* pulmonary infections in cystic fibrosis patients. [66] Deferoxamine-gallium (Ga-DFO) has been shown to exert inhibitory growth activity against *P. aeruginosa* and to effectively impede biofilm formation as well as Ga-DfoB-loracarbef sideromycin against *M. luteus*. [67]

Table 1. 2: Reported minimum inhibitory concentration (MIC) values (μM) in iron-deficient media for xenometal siderophore.

Compound	*E.coli*	*S. aureus*	*PA01*	Ref
In-DFO	75	300	150	-
Ga-DFO	UD	UD	UD	-
Fe-D1	7.5	30	-	[76]
Ga-D1	1.9	0.9	-	[76]
D1	3.8	3.8	-	
Ciprofloxacin	0.9	0.9	0.9	[76]
$[Sc(Ent)]^{3-}$	300	300	-	[70]
In-5j*	>605.2	-	18.9	[71]
Ga-5a*	2.6	-	21.2	[71]
Gentamicin	1	-	2.1	[71]
#Bi + cefiderocol	1	-	0.06	[72]
#Ga + cefiderocol	1	-	0.06	[72]
Cefiderocol	1	-	4	[72]

UD = undetermined; * 1:1 stoichiometry; # 50μM of the metal

Other iron-mimicking metals, scandium and indium, have shown been evaluated in *K. pneumoniae* and *E.coli*, with $[Sc(Ent)]^{3-}$ demonstrating particularly promising antimicrobial activity.[68-70] Furthermore, Ramström et al. have reported that gallium and indium nor-pyochelin analogues display antimicrobial activity against *P. aeruginosa*. Both gallium(III) (5a-Ga MIC 21.2 μM) and indium(III) (5j-In MIC 18.9 μM) complexes are capable of inhibiting bacterial growth in multidrug-resistant *P. aeruginosa* clinical isolates.[71] Beyond these metals, Sun et al. have shown

that bismuth(III) competes with iron(III) for Cefiderocol binding. These results indicate an increased bismuth uptake, decreased iron uptake in bacterial cells, and the formation of a 1:1 Bi(III)-Cefiderocol complex in vitro. Importantly, the co-administration of Bi(III) or Ga(III) drugs significantly enhances the efficacy of Cefiderocol against *P. aeruginosa* and *Burkholderia cepacia*, leading to a 64-fold reduction in the minimum inhibitory concentration (Table 1.2).[72]

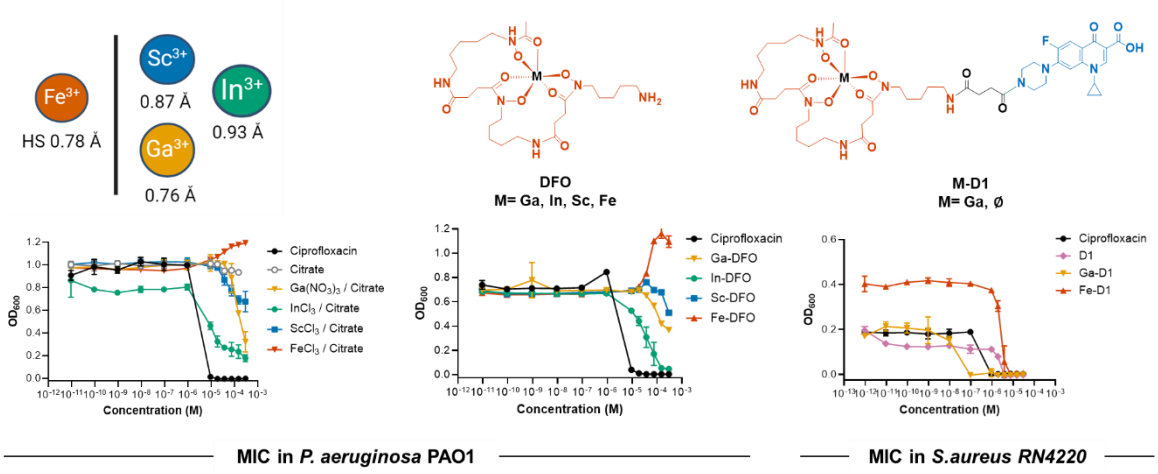

Figure 1. 9: Minimum inhibitory concentration of (MIC): Of the Fe, Sc, In, and Ga metal salts and Ga, In, Sc, and Fe-DFO in *P. aeruginosa*; and Fe,Ga and apo-D1 in S. *aureus*. (work done by Joelle El Hamouche and Dr. Axia Marlin).

Building upon established findings, our group has shown that Ga, Sc, and In metal salts possess inherent growth inhibitory properties against *P. aeruginosa* PAO1, with a clear trend of potency: In > Ga > Sc. Deferoxamine (DFO) complexation increases the antimicrobial efficacy of xenometals, with In-DFO exhibiting the highest potency, followed by Ga-DFO and Sc-DFO, albeit results reported by others,[73] could not reproduce the high potency values reported. This demonstrates that utilizing the synergistic effect of siderophore-xenometal complexes alongside antibiotics holds promise for potent antimicrobial therapies. This was demonstrated by Ga-D1, our first-generation siderophore-antibiotic conjugate, which shows a substantial increase in

antimicrobial activity compared to the metal-free, apo-siderophore conjugate and the ferric analogue (Figure 1.9).[74]

1.5 Outline of Dissertation

Xenometallomycins are a new class of antibiotic drug molecules with great potential and yet unknown mechanisms of action. A better understanding of the uptake and mechanism of action of these compounds will inform the rational structural design of next-generation xenometallomycins. This dissertation details the development of novel molecular tools and methodologies designed to elucidate the stability and uptake mechanisms of xenometallophores and xenometallophore-siderophore antibiotic conjugates. The long-term aim is to translate a deeper understanding of these stability and uptake mechanisms into the rational design and synthesis of effective siderophore-based antibiotics, capable of hijacking bacterial iron transport systems for therapeutic application. These efforts include (a) the development of a dual radiolabeling strategy utilizing ^{67}Ga and ^{124}I to investigate the in vivo and in vitro stability of xenometallophores (Chapter 2); (b) The design, synthesis, and validation of multimodal chemical tagging strategies for deferoxamine-based siderophore photoaffinity probes, incorporating a diazirine photoactive moiety, aimed to evaluate reactivity and labeling preferences in single amino acid residues and siderophore protein; and (c) the application of these deferoxamine-diazirine probes in live cells for protein target labeling, visualization, and identification.

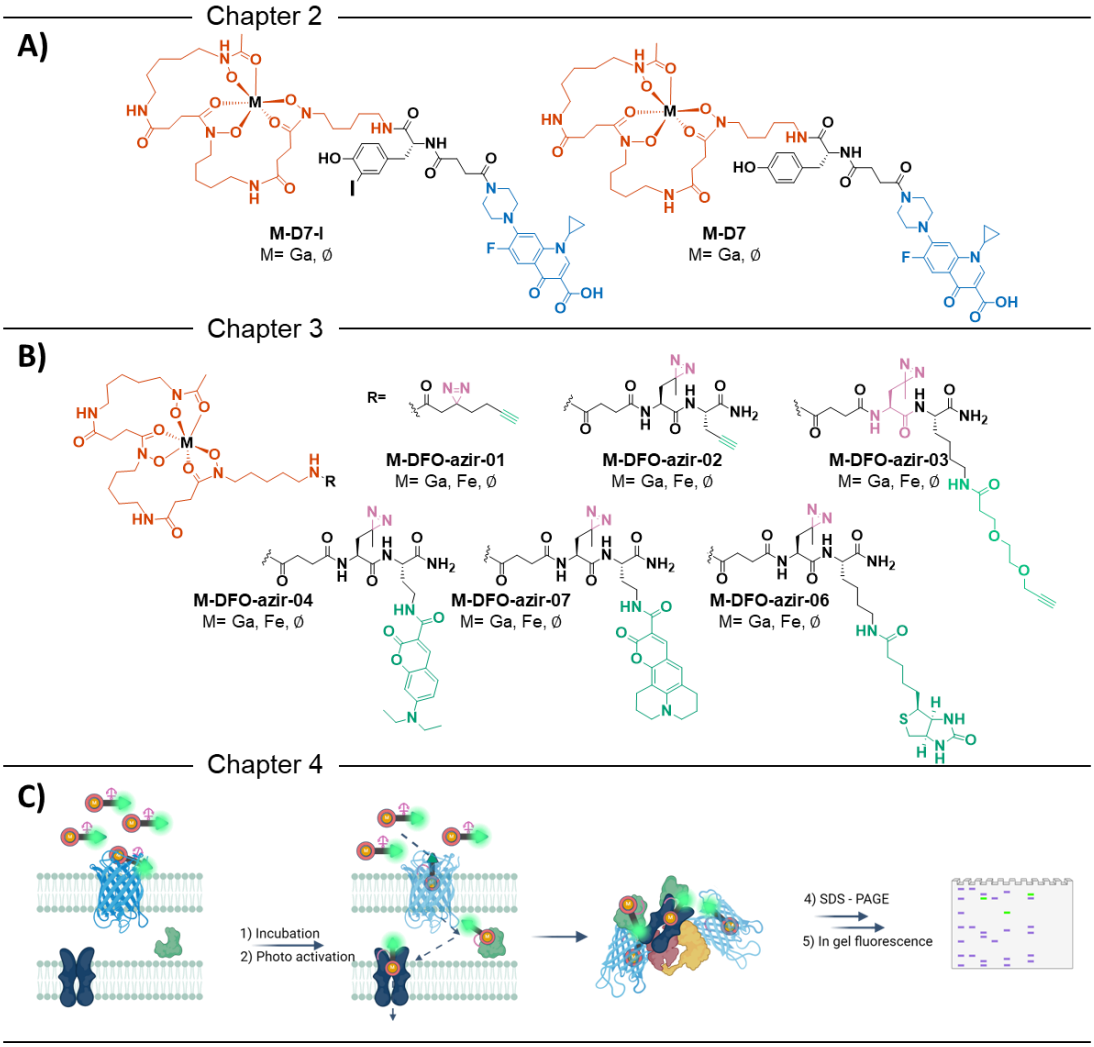

Figure 1.10: Summary of each chapter: A) Deferoxamine base siderophore carrying ciprofloxacin antibiotic for multi radiolabeling tag. B) Deferoxamine base siderophore photoaffinity probes containing diazirine photo active moiety, and alkyne or direct conjugation of optical probe and biotin. C) Live bacterial cell labeling with deferoxamine photoaffinity probes scheme.

Chapter 2: Multi-Isotope Tagging Strategy to track the siderophore-conjugate uptake.

The work described within this chapter (excluding Section 2.2.1) is published as:

Pandey, A.; **Cao, M**.; Boros, E. Tracking Uptake and Metabolism of Xenometallomycins Using a Multi-Isotope Tagging Strategy. *ACS Infectious Diseases*. **2022**, 8 (4), 878-888. DOI: 10.1021/acsinfecdis.2c00005.

2.1 Summary of this work:

"All synthesis, characterization, and experiments with M-**D6** and M-**D6**-I were performed by Apurva Pandey. All synthesis, characterization, and experiments with M-**D7** and M-**D7**-I were performed by Minhua Cao. The manuscript was written by Apurva Pandey, with Minhua Cao contributing results and discussion, and edited by Eszter Boros.

2.2 Introduction

2.2.1 Introduction to prior methods of evaluation siderophore conjugate uptake

The efficacy of xenometal siderophore-antibiotic conjugates relies on their ability to mimic native siderophores, by exploiting the bacterial iron-siderophore uptake pathways to enter bacteria cells.[34,75] In addition to the efficacy of uptake, many other factors contribute to in vivo efficacy of a xenometal siderophore-antibiotic conjugate: (1) metal complex stability in vivo and in vitro, (2) compound uptake and distribution, (3) cytotoxic payload selection, and (4) antibiotic mechanism of action.[26] Furthermore, we have no well-established understanding of the importance of metal release or payload detachment from the siderophore for enhanced antimicrobial activity.[76]

Consequently, a comprehensive understanding of the bacterial siderophore-mediated uptake mechanism is indispensable for drug evaluation, validation, and optimization.[77] Several methodologies are currently employed to elucidate and quantify this uptake process: A) Iron-Dependent Antibacterial Activity Assays: These assays assess the antimicrobial activity of conjugates under iron-sufficient and iron-limited conditions, simulating the iron-restricted

environment of the host.[46] B) Genetic Mutant Studies: This approach involves the generation and analysis of bacterial mutants that exhibit either targeted gene knock-outs or evolve resistance to the compound of interest. These mutants provide insights into the uptake and mechanism of action the conjugate.[57] C) Competition Assays: These experiments examine the influence of native siderophores on the activity of the conjugate. A reduction in conjugate activity in the presence of native siderophores indicates a shared uptake pathway.[78] D) Growth Recovery Assays: This method evaluates the ability of siderophore conjugates to restore growth in bacterial strains lacking native siderophore biosynthesis. Successful growth recovery suggests that the conjugate can utilize the same siderophore-mediated uptake pathways and provides a reliable source of mobile iron.[79] E) Fluorescence Labeling: This technique employs the conjugation of a fluorophore to the siderophore moiety, enabling the visualization and quantification of compound uptake, accumulation, and intracellular localization.[80] F) Radiolabeling: This method utilizes radiolabeled siderophores conjugates to track uptake and distribution in vitro and in vivo. This can be accomplished through the formation of inert complexes with radioisotopes such as $^{58/59}$Fe,[81,82] ^{51}Cr, ^{89}Zr,[83] or $^{67/68}$Ga,[83,84] or through covalent labeling with isotopes such as ^{14}C or ^{3}H.[85] These techniques allow for precise quantification of compound uptake and distribution, often with minimal structural perturbation (Figure 2.1).

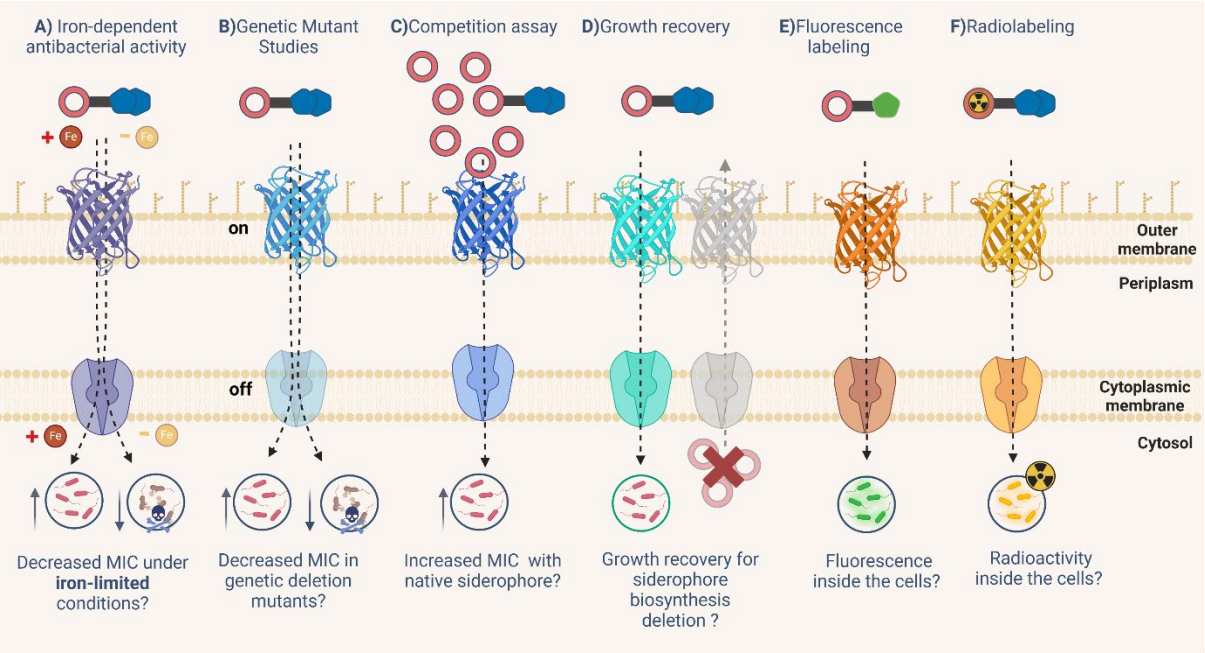

Figure 2. 1: Methods to investigate siderophore conjugate uptake in bacteria.

2.2.2 Introduction to our work

This work focused on xenometallomycins, or Trojan horse conjugates that incorporate a non-endogenous metal ion for co-delivery and a means to enhance the antibiotic's potency.[86,87] Previously, we have synthesized and tested siderophore antibiotic conjugates Ga-**D1**, Ga-**D2** and Ga-**D5** (Figure 1), inspired by the structure of natural product antibiotics salmycin and albomycin respectively.[78,86-90] Our constructs were comprised of 3 components: the siderophore, a linker and an antibiotic. Due to the peptide nature of these constructs, sequence modification is especially easily accessible. We showed that the co-delivery of Ga(III) as the redox inactive mimic of Fe(III) produces enhanced potency when compared with the *apo*-(metal free) or Fe-bound siderophore conjugate. Our first-generation lead construct Ga-**D2** (Figure 2.2) demonstrated good, broad spectrum potency in *Escherichia coli* (*E. coli*), *Staphylococcus aureus* (*S. aureus*), *P. aeruginosa* and *Klebsiella Pneumoniae* (*K. pneumoniae*) with a minimum inhibitory concentration for 90%

inhibition of growth (MIC_{90}) of 0.2, 1.9, 3.8 μM and 12.5 μM.[87] We subsequently demonstrated that the xenometallomycin concept was applicable in vivo, with the second-generation compound Ga-**D5** (Galbofloxacin, Figure 2.2). Galbofloxacin not only selectively accumulated in a *S. aureus* soft tissue infection in mice, but also effectively treated infection at molar doses where the parent drug ciprofloxacin was not effective.[86] Even though synthetic siderophore-antibiotic conjugates have been extensively explored, compound efficacy remains difficult to predict. Furthermore, the exact mechanism of antiproliferative activity of Ga(III) siderophore complexes is not well established and requires further elucidation.

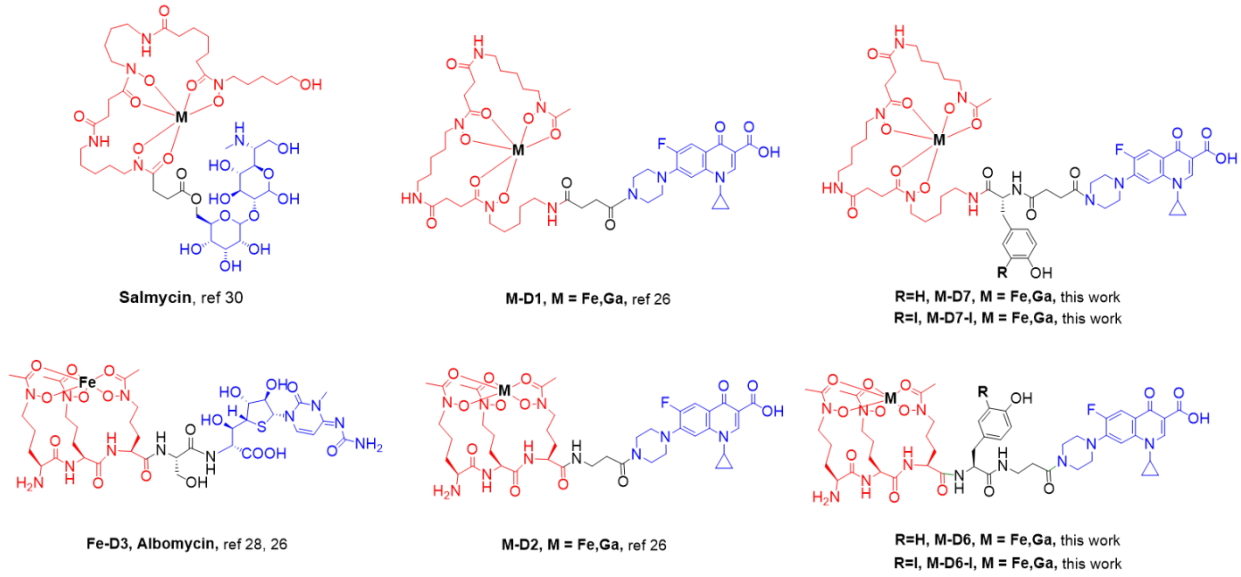

Figure 2.2: Chemical structures of (top panel) structurally related deferoxamine siderophore-antibiotic conjugates synthesized and investigated previously, as well as the subject of studies in this work: **D1**, **D7**, salmycin. (Bottom panel) Chemical structures of structurally related linear desferrichrome siderophore-antibiotic conjugates have been synthesized and investigated previously, as well as the subject of studies in this work: **D2**, **D6**, albomycin (Fe-**D3**), a "Trojan horse" conjugate produced by Streptomyces. Black: Metal ion, red: siderophore, black: linker, blue: antibiotic.

Current methods to elucidate the transport mechanisms of these constructs involve modulation of expression levels of transport proteins, followed by bacterial growth assessment in the presence of siderophores or siderophore-antibiotic conjugates.[91-94] These methods, however cannot provide information on the efficiency of transport of individual components, the metabolic stability of constructs or their potential for in vivo applications. More specific and quantitative readouts are needed for characterizing siderophore-mediated iron transport in vitro and in vivo.

The use of radioactive isotopes is very convenient in this regard. The feasibility of this approach was originally demonstrated by Raymond and coworkers using radioactive ^{14}C tag incorporation into siderophores during (bio)synthesis.[35] Later, Decristoforo and coworkers labeled siderophores with ^{68}Ga and ^{89}Zr demonstrating accumulation of the ^{68}Ga-labeled compound in *P. aeruginosa* and *S. aureus* infected muscles.[83,95-97] However, labeling for the assessment of the pharmacokinetic properties and metabolic stability of synthetic siderophore antibiotic constructs has remained underutilized. Here, we employ a multi-isotope tagging approach to elucidate the uptake, metabolism, and in vivo distribution of siderophore-conjugates using short-lived, biomedical isotopes. This approach enables us to monitor the stability of the siderophore complex and the integrity of the siderophore-antibiotic conjugate in concert. The proposed radioactive labeled siderophore conjugates incorporate the following components (Figure 2.3) : 1) Radiotracer **M** is incorporated by direct coordination of a radiometal tracer to siderophore. We employed $^{67}Ga(III)$ ($t_{1/2}$ = 3.3 d, as a non-redox active Fe mimic) to study metabolism bifunctional siderophores linear desferrichrome and deferoxamine, utilized by *S. aureus*, *S. pneumoniae*, and *E. coli* will be synthesized and functionalized using conventional organic chemistry techniques. 2) In order to install a covalent tag on the siderophore-conjugate, we incorporate linker sequences

with a tyrosine residue. The tyrosine residue enables incorporation of the other radiotracer **X** via radioiodination with ^{124}I ($t_{1/2}$ = 4.2 d) for PET imaging. 3) To mimic the previously studied structures, we appended the antibacterial drug (ciprofloxacin) as the model drug conjugate.

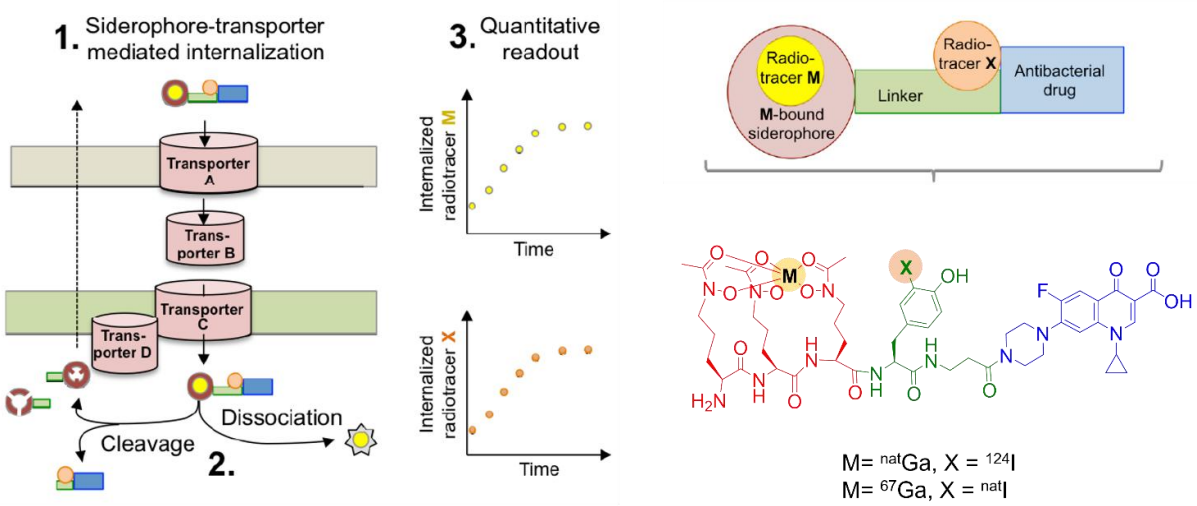

Figure 2. 3: (Left) Proposed internalization pathway for the siderophore antibiotic construct, cytoplasmic metabolism, and direct quantification of isotope internalization in a Gram-negative bacterium. (Right) Siderophore-antibiotic conjugate implementing the dual.

Previously, we had already demonstrated that ^{67}Ga is suitable to study the biodistribution and pharmacokinetics of our first generation siderophore antibiotic conjugates ^{67}Ga-**D1,** ^{67}Ga-**D2** and Galbofloxacin (Figure 2.2).[86,87] The goal of this work was to probe the viability of ^{124}I as a complementary, covalent linker tag. The isotope ^{124}I is extensively utilized for the design and synthesis of positron emission tomography (PET) radiotracers. Its convenient 4.2 d half-life and high β energy ($E_{\beta+(max)}$ = 819 KeV) allows for time intensive radiosynthesis protocols and PET imaging studies.[98] Moreover, labeling chemistry for ^{124}I is well established, and a wide variety of compounds have been labeled for molecular imaging purposes with PET: *m*-Iodobenzylguanidine (MIBG) is used in diagnosis (labeled with ^{123}I or ^{124}I) and therapy (labeled with ^{131}I) of neuroblastoma and pheochromocytoma.[99,100] [^{124}I]Iodo-azomycin-galactopyranoside ([^{124}I]IAZG)

has been studied as a hypoxia imaging agent [101-104] and ^{124}I-labeled uracil derivative Iodine-124-1-(2-deoxy-2-fluoro-1-D-arabinofuranosyl)-5-iodouracil (FIAU) has been reported as a PET radiotracer for non-invasive imaging of musculoskeletal bacterial infection.[105]

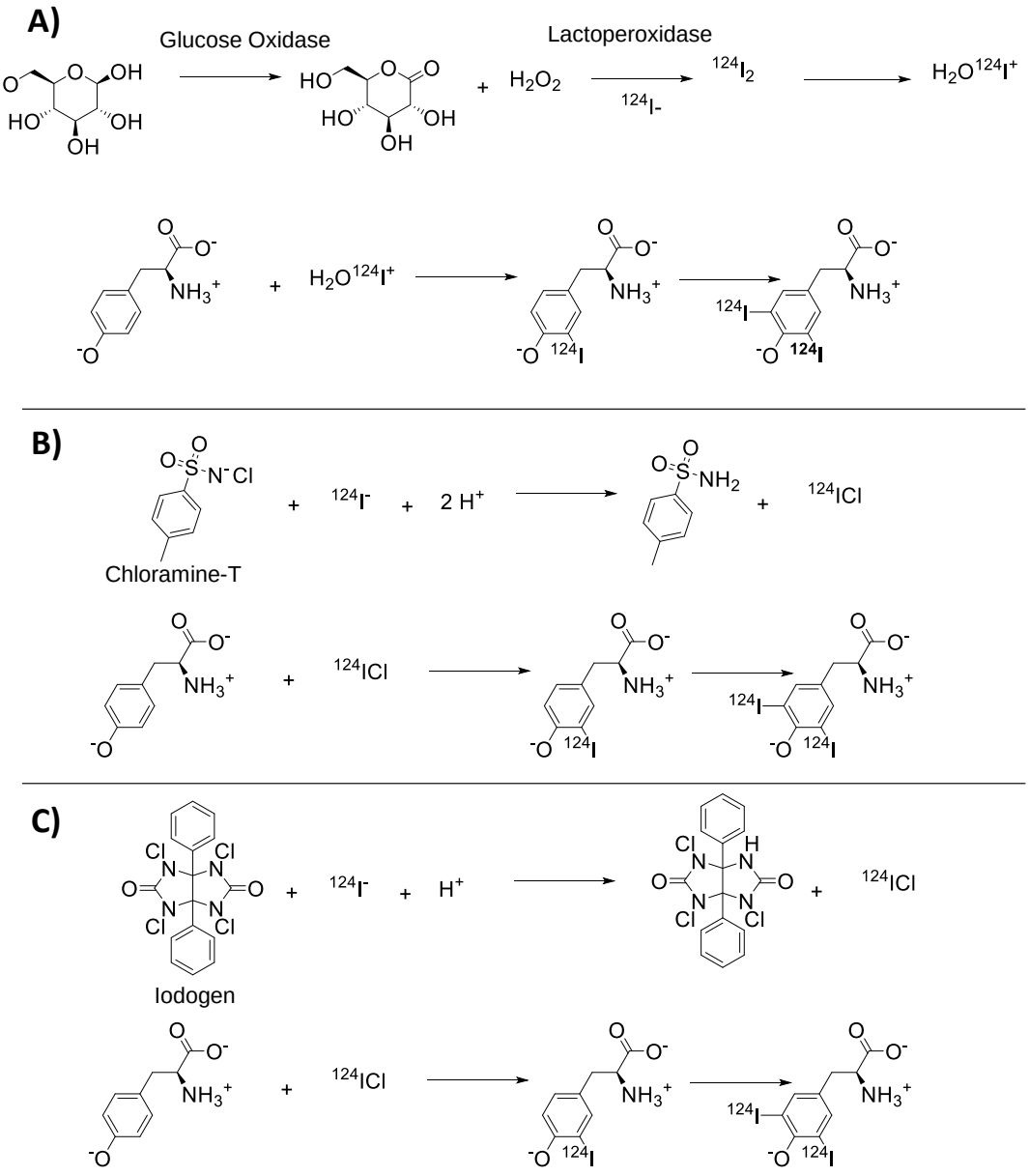

Figure 2. 4: Methods for radioiodination of tyrosine and peptides: A) oxidative enzymes. B) Chloramine-T. C) Iodogen.

In order to iodinate the tyrosine residue in siderophore antibiotic conjugates, many of the conventional harsh iodination approaches like halogen exchange reaction, use of Lewis acids is not compatible with gallium-siderophore coordination complexes. However, radioiodination of peptides and proteins can be achieved under comparatively mild reaction conditions that do not lead to degradation of the peptide or complex dissociation. Therefore, reagents like Chloramine T, Iodogen®, and various oxidative enzymes are useful oxidizing agents for the mild *in situ* oxidation of radioiodide for direct protein labeling (Figure 2.4).[106,107]

In this work, we introduce two novel Trojan horse constructs, **D6** and **D7** (Figure 2.2), which allow for the introduction of a ^{67}Ga and ^{124}I radio tags. Subsequently, we show that quantification of the individual radioisotope tagged constructs provides a quantitative readout for the internalization of iron-mimics, as well as the siderophore itself (Figure 2.3) and provides information on the distribution and metabolism of each component in vivo. A more comprehensive understanding of siderophore transport and metabolism will enable the improved, rational design of high efficacy diagnostics and Trojan horse antibiotics for in vivo applications.

2.3 Results and discussion

2.3.1 Synthesis of siderophore antibiotic conjugates D6 and D7

The structure of **D6** and **D7** (Figure 2.2) are inspired by the natural product albomycin [88] and salmycin[90] respectively; but incorporate a chemically easily modifiable antibiotic with a cytoplasmic inhibitory target such as ciprofloxacin. The structure also consists of a tyrosine linker to incorporate the radiotracer ^{124}I.

We employed structural connectivities similar to the natural product albomycin and our first-generation lead **D2** for synthesizing **D6**. The acetylated, amino protected linear desferrichrome precursor P5 was synthesized following previously established protocols by Miller and coworkers.[87,108,109] The tyrosine linker was introduced to the peptide precursor P5 by functionalizing ciprofloxacin with Fmoc-β-alanine, followed by N-terminal deprotection using diethylamine (DEA) and subsequent reaction of the free amine of B2 with Fmoc-Tyr(OtBu)-OH using standard 2-(1H-benzotriazol-1-yl)-1,1,3,3-tetramethyluronium hexafluorophosphate, Hexafluorophosphate Benzotriazole Tetramethyl Uronium (HBTU) solution phase coupling conditions. A second coupling step with the protected, linear desferrichrome derived building block P5 following Fmoc-deprotection of the tyrosine residue (Scheme 2.1A) was employed to link P5-β-alanine-tyrosine with the drug cargo precursor (2). The final product **D6** was attained in a < 2% over-all yield after 16 steps following final purification using reverse phase chromatography. To synthesize **D7**, we employed deferoxamine (DFO) as a commercially attainable surrogate of danoxamine and introduced tyrosine by reaction of the free amine of DFO with Fmoc-Tyr(OtBu)-OH using HBTU mediated amidation using a solution phase coupling approach. A second amidation step with the Fmoc deprotected DFO-Tyrosine was employed to link DFO-Tyrosine to succinate linked ciprofloxacin that was synthesized separately following our previously published protocol for first generation DFO conjugate **D1**.[87] The final product **D7** was attained in a < 6% over-all yield after 5 steps following final purification using reverse phase chromatography (Scheme 2.1B).

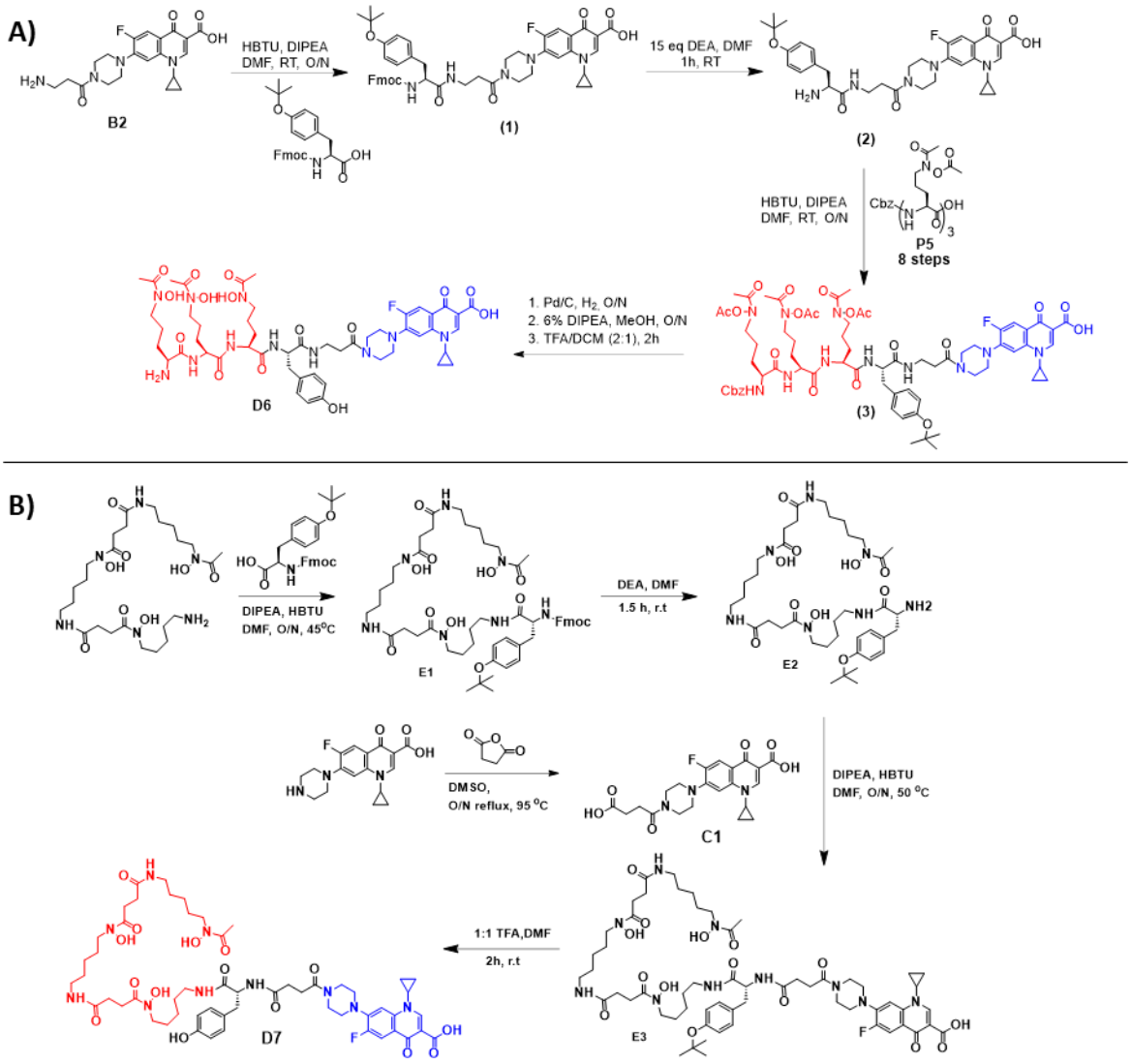

Scheme 2. 1: A) Functionalization of ciprofloxacin, subsequent conjugation to protected hydroxamate fragment P5 followed by sequential deprotection steps yields the Conjugate **D6**. B) Synthetic scheme of the deferoxamine based siderophore antibiotic **D7**.

2.3.2 Ga- and Fe-D6/D7 complex formation

Complexation with Ga(III) and Fe(III) salts formed Ga-**D6/D7** and Fe-**D6/D7** in aqueous, buffered media at pH 6 and pH 7. Further purification of Ga(III) and Fe(III) using reverse phase chromatography was carried out to isolate white and orange red complexes respectively.

Characterization via HPLC, HRMS and ICP-OES was employed to affirm purity and produce consistent complex concentrations for subsequent in vitro and in vivo studies based on the quantitation of metal content.

2.3.3 Growth inhibition in *wt* bacterial strains

With *apo*- (metal-free), Ga and Fe complexes of **D6** in hand, we next probed their ability to inhibit bacterial growth in a conventional mini-mum inhibitory concentration for 98% inhibited growth (MIC_{98}) assay. *E. coli* K12 and *P. aeruginosa* PA01 were selected as Gram-negative model organisms, and *S. aureus* RN4220 as the Gram-positive model organism. Fe-deficient media was prepared by the addition of DP to mimic the tightly iron controlled in vivo environment.[67,87,110] Results are summarized in Table 2.1 and Figure 2.5, 2.47, 2.48. The parent drug ciprofloxacin was utilized as a control, giving an MIC of 0.93 μM, which is consistent with literature values. The apo-**D6** and apo-**D7** constructs showed a MIC at >30 μM in wt *E. coli*, whereas Ga-**D6** was determined to have a MIC at 1.9 μM and Ga-**D7** MIC of 30 μM in wt *E. coli*, retaining some of the growth inhibitory action of ciprofloxacin and slightly less than the antibiotic activity of our first-generation conjugates Ga-**D2** and Ga-**D1** respectively (Figure 2.5, 2.47A, 2.48A, Table 2.1). In accordance with our previous findings, Fe(III) complexes remain significantly less active: Fe-**D6** showed a 15-fold decrease in activity in *E. coli* when compared to Ga-**D6**, with an MIC of >30 μM (Figure 2.46A, Table 2.1); Fe-**D7** was also found to be less active in comparison to Ga-D7 (Figure 2.47A, Table 2.1). In *P. aeruginosa*, the activity of apo-**D6** and Ga-D6 activity decreased 20-fold with an MIC value of >30 μM, while Fe-**D6** was inactive; apo-**D7** was demonstrated to be inactive and Ga-**D7** (MIC value of >30 μM) retained a diminished activity compared to E. coli, while Fe-**D7** demonstrated to be growth promoting at concentrations above 30 μM (Figure 2.46B,

2.47B, Table 2.1). Ga-**D6** also exhibited reduced activity in S. aureus with a MIC of 3.8 μM comparable to its activity in wt *E. coli*. apo-**D6** remained inactive, whereas Fe-**D6** produced growth promoting effects at concentration above 93 nM (Figure 2.5 A, Table 2.1); apo-**D7** has MIC of > 30 μM while Ga-**D7** has MIC of 30 μM, whereas Fe-**D7** is inactive (Figure 2.5 C, Table 2.1).

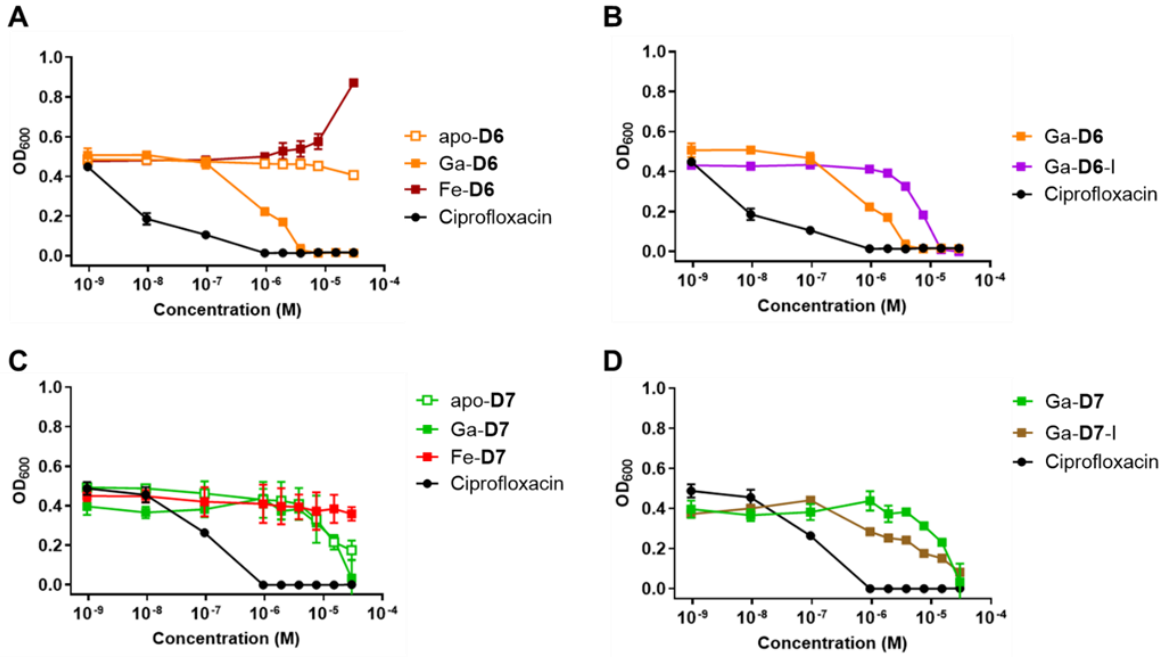

Figure 2. 5: **(A**) MIC assay of **D6** and its complexes in *S. aureus* (n =3x3). **(B)** MIC assay of Ga-**D6**-I in *S. aureus* shows 5-fold lower potency as compared with Ga-**D6** (n =3x3). **(C)** MIC assay of **D7** and its complexes in *S. aureus* (n =3x3). **(D)** MIC assay of Ga-**D7**-I in *S. aureus* shows comparable potency with Ga-**D7** (n =3x3).

Ga-**D6**-I and Ga-**D7**-I activities were also assessed in *S. aureus* and *E. coli*, the strains where both Ga-**D6** and Ga-**D7** showed the highest antibiotic potency. Ga-**D6**-I exhibited 5-fold and 10-fold reduced activity in *S. aureus* and *E. coli* as compared with Ga-**D6**, with a MIC of 15 μM and 30 μM respectively (Figure 2.5 B, 2.47 C, Table 2.1), whereas Ga-**D7**-I showed comparable activity to Ga-**D7** with a slightly lower MIC_{50} for *S. aureus* (Figure 2.5 D, 2.48 C, Table 2.1). Overall, our results indicate that the introduction of the tyrosine residue into the linker

affects the antibiotic potency of Ga-**D6** and Ga-**D7** when compared to their parent compounds, Ga-**D1** and Ga-**D2**.

Table 2. 1: Summary of MIC (μM) determined in *E. coli*, *S. aureus*, and *P. aeruginosa*. GP: Growth Promoting. ND: Not Determined.

Compound	E. coli	S. aureus	PA01
ciprofloxacin	0.93	0.93	0.93
apo-**D6**	Inactive	Inactive	Inactive
Ga-**D6**	1.9	3.8	Inactive
Fe-**D6**	Inactive	GP	Inactive
Ga-**D6**-I	30	15	ND
apo-**D7**	Inactive	Inactive	Inactive
Ga-**D7**	30	30	Inactive
Fe-**D7**	GP	Inactive	GP
Ga-**D7**-I	Inactive	Inactive	ND

2.3.4 Radiochemical labeling with ^{67}Ga

The formation of the ^{67}Ga-**D6** and ^{67}Ga-**D7** complexes was feasible under mild radiolabeling conditions (pH 7, 100 mM HEPES, 5 minutes) quantitatively with ligand concentrations of 10^{-6} M (Scheme 2.4, 2.5). The complexation was monitored using a radio-HPLC (Figure 2.49, 2.51). Radiolabeling of **D6**-I and **D7**-I with ^{67}Ga were also feasible but a reduction of overall radiochemical yield was observed (~ 15%) as purification was required to isolate ^{67}Ga-**D6**-I and ^{67}Ga-**D7**-I under the same mild conditions and specific activities used for the formation of ^{67}Ga-**D6** and ^{67}Ga-**D7** complexes (Figure 2.6, 2.52).

2.3.5 Radiochemical labeling with ^{124}I

Iodination of Ga-**D6** and Ga-**D7** was achieved in plastic tubes pre-coated with 1,3,4,6-tetrachloro-3alpha,6alpha-diphenylglycouril, in accordance with commonly utilized procedures for peptide and antibody labeling. After 45 min incubation at room temperature, at ~5 mM ligand concentration, a radiochemical yield of 15% was achieved, which also required chromatographic purification of the desired product to reduce loading of competing, parent Ga-**D6** and Ga-**D7** complexes, which could impede bacterial uptake experiments significantly by reduction of specific activity (Figure 2.6, 2.47). Isolated fractions were analyzed with radio-HPLC to affirm that purification and removal of the parent carrier was successful.

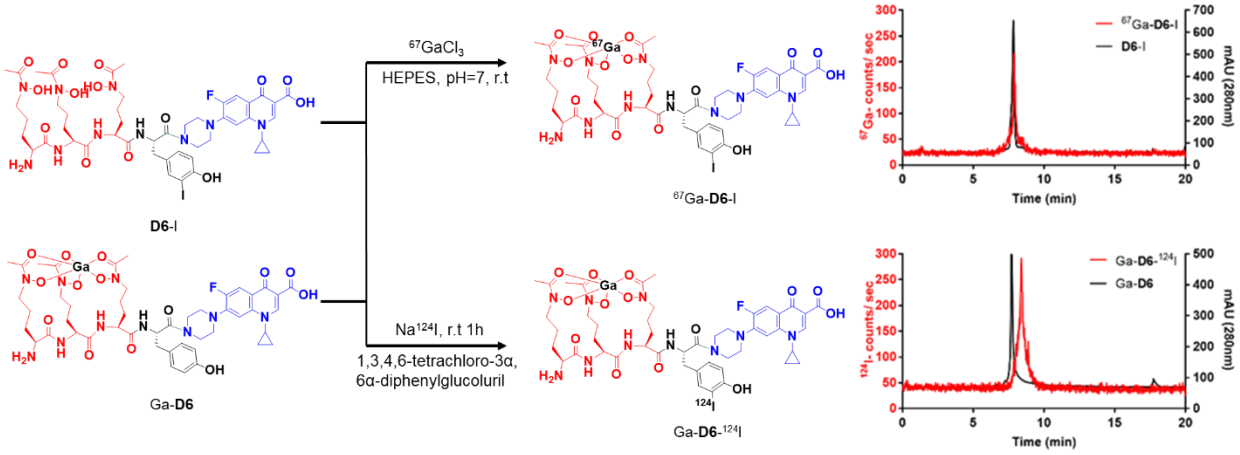

Figure 2. 6: (**Top**) Schematic description of the radiochemical complexation of **D6**-I with ^{67}Ga. ^{67}Ga-complexation proceeds in 5 min, 25 ∘C, pH 7. A representative radiolabeling HPLC trace for the characterization of ^{67}Ga-**D6**-I (t_R = 7.90 min, left axis, ^{67}Ga counts per second, method D), in comparison with HPLC characterization of the **D6**-I ligand (t_R= 7.83 min, right axis, absorbance at 280 nm, method D) is shown. Free ^{67}Ga elutes at 0.7 minutes. **(Bottom)** Schematic description of the radiolabeling of Ga-**D6** with ^{124}I. A representative radiolabeling HPLC trace for the characterization of Ga-**D6**-^{124}I (t_R = 8.40 min, left axis, ^{124}I counts per second, method C), in comparison with HPLC characterization of the Ga-**D6** ligand (t_R= 7.77 min, right axis, absorbance at 280 nm, method C) is shown. Free ^{124}I elutes at 1.03 minutes.

2.3.6 Radiochemical uptake experiments in wt bacterial strains.

The radiolabeled ^{67}Ga-**D6**-I/**D7** complexes were subsequently used to probe time-dependent compound uptake and quantification with ^{67}Ga-citrate as the control. For uptake experiments, ^{67}Ga-**D6**-I and ^{67}Ga-**D7**-I were used at an average specific activity of 1.9 MBq/μmol. *E. coli*, *S. aureus* and *P. aeruginosa* (3.2 x 10^8 CFU) were incubated in Fe-deficient LB with 0.18 MBq of ^{67}Ga-**D6**-I and 0.07 MBq of ^{67}Ga-**D7**-I at 37°C. Aliquots were removed at 10, 20, 30, 60, and 120 minutes, followed by separation of pellets from supernatant and counting of retained radioactivity in each fraction. For all tested strains, ^{67}Ga-**D6**-I shows reduced uptake compared to the first-generation conjugates ^{67}Ga-**D2**, with a maximum uptake of 5%, 7% and 13% for *E. coli*, *P. aeruginosa and S. aureus* respectively at 2 h (Figure 2.52, 2.53, 2.7 A, Table 2.2, 2.3, 2.3). In addition, ^{67}Ga-**D7**-I also demonstrated a decreased uptake in comparison to the first-generation ^{67}Ga-**D1**, with the maximum uptake of 3%, 20%, and 12% for *E. coli*, *P. aeruginosa and S. aureus* respectively at 2 h (Figure 2.54, 2.55, 2.7B, Table 2.5, 2.6, 2.7). The introduction of iodinated tyrosine reduces the uptake of ^{67}Ga-**D6**-I and ^{67}Ga-**D7**-I in most bacterial strains probably due to reduced binding affinity to the siderophore receptors in the bacterial membrane. To elucidate the effect of iodine on the uptake of Ga-**D6**-I and Ga-**D7**-I in different bacterial strains, uptake assays were also performed with non-iodinated ^{67}Ga-**D6** and ^{67}Ga-**D7**. The results show time-dependent increased uptake (20% at 2 h) for ^{67}Ga-**D6** in all three strains as compared to ^{67}Ga-**D6**-I affirming the adverse effect of iodination of the tyrosine residue, resulting in reduced uptake of the conjugate (Figure 2.52, 2.53, 2.7A, Table 2.2, 2.3, 2.3). Similar results were obtained for ^{67}Ga-**D7** which has a maximum uptake average uptake of ~ 10% at 2h time point. Overall, the uptake of ^{67}Ga-**D7**-I is decreased when compared to ^{67}Ga-**D7** in *E. coli*, but remains comparable in *S. aureus* (Figure 2.54, 2.55, 2.7B, Table 2.5, 2.6, 2.7).

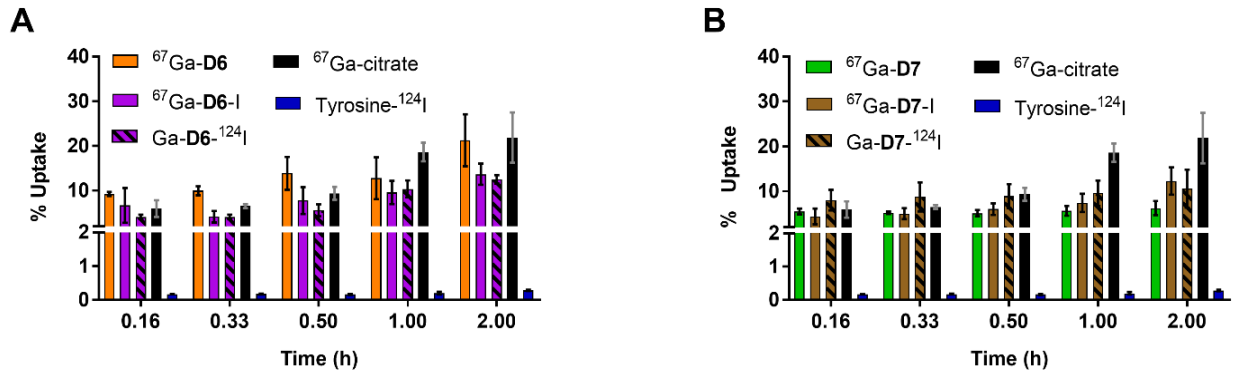

Figure 2. 7: **(A**) Time-dependent, radiochemical bacterial uptake studies in *S. aureus* RN4220 of ^{67}Ga-**D6**, ^{67}Ga-**D6**-I and Ga-**D6**-^{124}I in iron-depleted, DP-treated media, pH = 7.4 with controls ^{67}Ga-citrate and Tyrosine-^{124}I (n = 5x3). **(B)** Time-dependent, radiochemical bacterial uptake studies in *S. aureus* RN4220 of ^{67}Ga-**D7**, ^{67}Ga-**D7**-I and Ga-**D7**-^{124}I in iron-depleted, DP-treated media, pH = 7.4 with controls ^{67}Ga-citrate and Tyrosine-^{124}I (n = 5x3). Quantitation based on radioactive uptake.

For ^{124}I uptake experiments, Ga-**D6**-^{124}I, Ga-**D7**-^{124}I and Tyrosine-^{124}I (control) were prepared with a specific activity of 1.9 MBq/μmol. *E. coli*, *S. aureus* and *P. aeruginosa* (3.2 x 10^8 CFU) were incubated in Fe-deficient LB with 0.14 MBq of Ga-**D6**-^{124}I, 0.15 MBq of Ga-**D7**-^{124}I and Tyrosine-^{124}I (control) at 37 °C in direct analogy with experiments conducted for ^{67}Ga-labeled conjugates. Similar to ^{67}Ga-**D6**-I results, Ga-**D6**-^{124}I showed maximum time dependent uptake in *S. aureus* with a peak uptake of 13% at 2 h, followed by *E. coli* and *P. aeruginosa*. The uptake was comparable to ^{67}Ga-**D6**-I uptake providing quantitative readout for internalization of both the iron mimic ^{67}Ga and the siderophore antibiotic conjugate (Figure 2.52, 2.53, 2.7A, Table 2.2, 2.3, 2.3). The result for Ga-**D7**-^{124}I was also very similar, with Ga-**D7**^{124}I uptake comparing well to ^{67}Ga-**D7**-I in all bacterial strains; the maximum uptake is observed in *P. aeruginosa* ~ 20% at 2h time point; however, ^{67}Ga and ^{124}I radiolabeled **D7**-I still have an increased uptake in comparison to ^{67}Ga-**D7** in *P. aeruginosa* indicating that the introduction of iodine is not detrimental to receptor recognition. While this same structural modification is unfavorable for *E. coli* receptors, it does not seem to affect *S. aureus* receptors. In addition to the introduction of tyrosine and iodine

possibly reducing the uptake of Ga-**D6**-^{124}I and Ga-**D7**-^{124}I in bacterial strains, self-blocking is also a problem with Ga-**D6**-^{124}I and Ga-**D7**-^{124}I due to difficulty in separating the iodinated conjugate from cold Ga-**D6** and Ga-**D7** complexes resulting in diminished specific activities. However, Ga-**D7**-^{124}I uptake in *P. aeruginosa* seems to be an exception, as the increased uptake compared with ^{67}Ga-citrate and ^{67}Ga-**D7** indicates a possibly increased affinity for transport receptors in *P. aeruginosa* (Figure 2.54, 2.56, 2.7B, Table 2.5, 2.6, 2.7).

2.3.7 In-vivo biodistribution and pharmacokinetics in mice

With ^{67}Ga-**D6**-I, ^{67}Ga-**D7**-I, Ga-**D6**-^{124}I, Ga-**D7**-^{124}I, ^{67}Ga-**D6**, and ^{67}Ga-**D7** uptake validated in vitro using bacterial uptake assays, we investigated biodistribution of ^{67}Ga-**D6**/^{67}Ga-**D7** and Ga-**D6**-^{124}I / Ga-**D7**-^{124}I in vivo next. Naïve Balb/c mice (female, 8 weeks) were injected with ^{67}Ga-**D6**, ^{67}Ga-**D7**, ^{67}Ga-citrate, Ga-**D6**-^{124}I, Ga-**D7**-^{124}I, and Tyrosine-^{124}I intravenously,

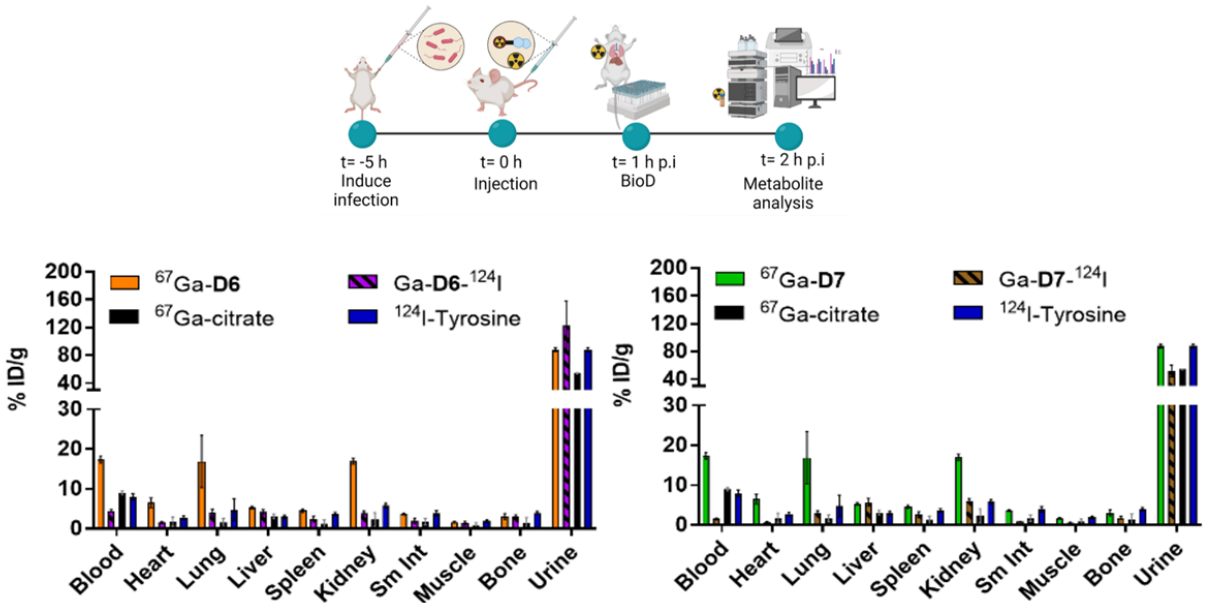

Figure 2. 8: **(Top panel**) Animal study experimental timeline. Comparative biodistribution of ^{67}Ga-**D6**/**D7**, ^{67}Ga-citrate, Ga-**D6**/**D7**-^{124}I and Tyrosine-^{124}I in naïve mice (n=3) shows a rapid renal clearance and no major off target uptake.

followed by biodistribution and analysis of metabolites in the urine using radio-HPLC at 1-hour post injection. Naïve ^{67}Ga and ^{124}I biodistribution revealed rapid, renal clearance of all conjugates: ^{67}Ga-**D6**, ^{67}Ga-**D7**, ^{67}Ga-citrate, Ga-**D6**-^{124}I, Ga-**D7**-^{124}I, and Tyrosine-^{124}I (Figure 2.8, Table 2.15, 2.16).

We next also probed the in vivo biodistribution of Ga-**D6**-^{124}I, Ga-**D7**-^{124}I, and Tyrosine-^{124}I in murine myositis models. Infection was established by i.m. injection of live or heat killed (90^{o}C, 30 minutes) inoculum of wt *S. aureus* owing to its higher in vitro uptake in *S. aureus*. Mice were inoculated with 10^{8} CFUs of wt *S. aureus* in the right triceps and with a tenfold higher (10^{9}) burden of heat-killed bacteria on the left triceps. The microbial infections were allowed to develop for 5 h before the injection of the radiolabeled constructs, followed by biodistribution of inflamed (heat killed), infected and control muscles 1h p.i. The biodistribution revealed specific, enhanced uptake for Ga-**D6**-^{124}I in infected muscle in comparison with heat killed, control muscle, and control conjugate Tyrosine-^{124}I (Figure 2.9, Table 2.17). Whereas for Ga-**D7**-^{124}I, the biodistribution demonstrated no significant uptake difference between the control, heat killed, infected muscle Ga-**D7**-^{124}I, and control Tyrosine-^{124}I (Figure 2.9, Table 2.17). Overall, it is likely

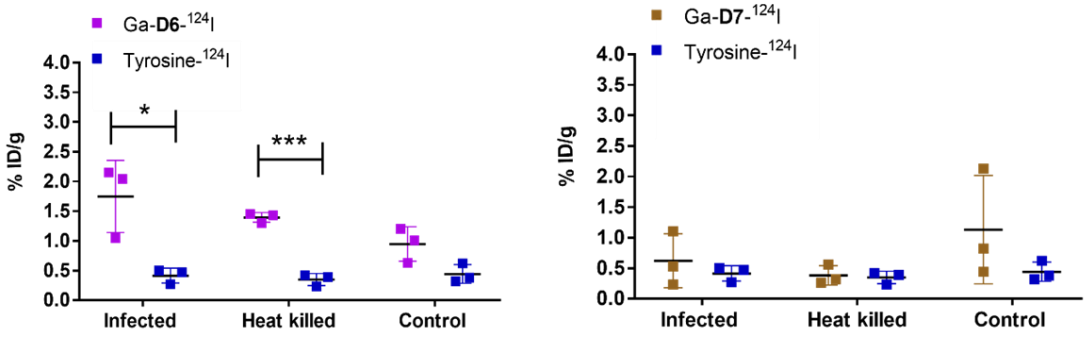

Figure 2. 9: Comparative biodistribution of ^{67}Ga-**D6**/**D7**, ^{67}Ga-citrate, Ga-**D6**/**D7**-^{124}I and Tyrosine-^{124}I in *S. aureus* in infected muscles of murine myositis models (n=3) shows a rapid renal clearance and no major off target uptake.

that the structural impact of the Tyrosine-^{124}I introduction hampered uptake as also indicated by the MIC assay results.

Finally, a urine metabolite study was also conducted. Previously investigated ^{67}Ga-labeled compounds have shown little integrity in the urine to date. Similarly, this study revealed 5% intact of detectable ^{67}Ga-**D6** (Figure 2.10A) and 0% intact ^{67}Ga-**D7** (Figure 10B) radiochemical complex in the urine, whereas Ga-**D6**-^{124}I was 45% intact (Figure 10A) and Ga-**D7**-^{124}I was 64% after an

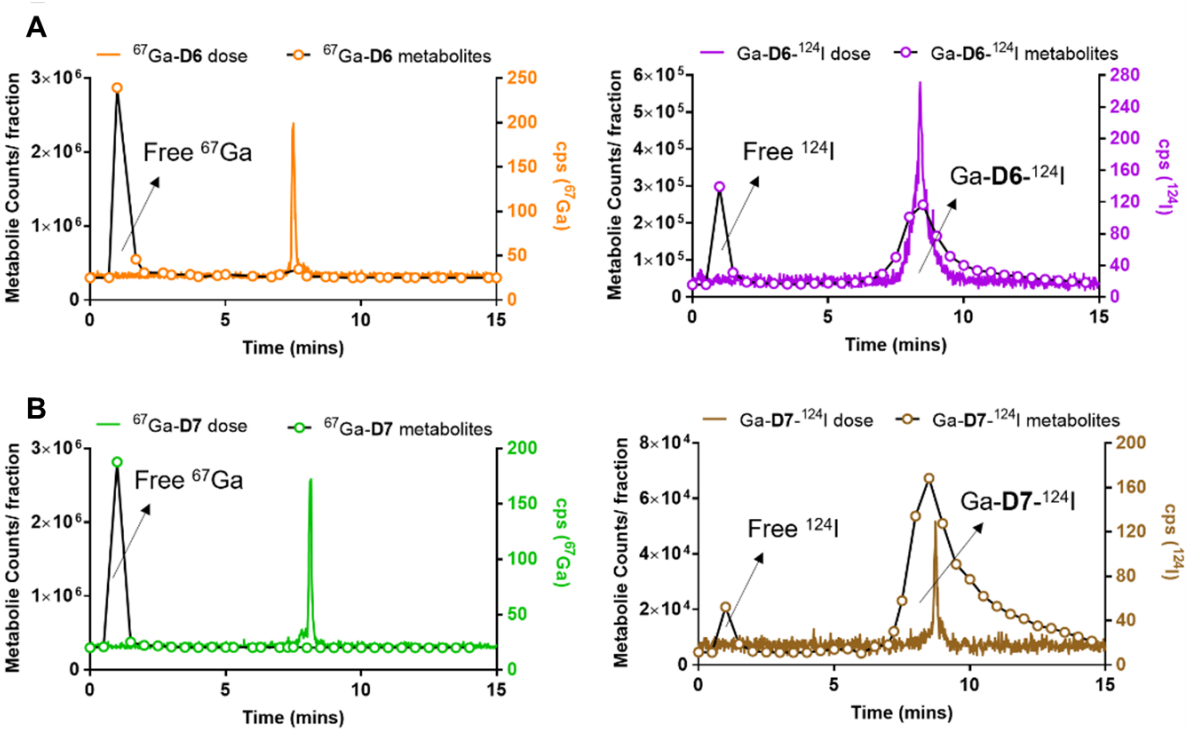

Figure 2. 10: Metabolite analysis of: **A)** ^{67}Ga-**D6** (open circles) shows a detectable intact complex (5 %) in the urine 1 h post injection. Radioanalytical HPLC trace of the ^{67}Ga-**D6** dose formulation prior to administration is shown as a reference (orange, right). Metabolite analysis of Ga-**D6**-^{124}I (open circles) shows a detectable intact complex (45 %) in the urine 1 h post injection. Radioanalytical HPLC trace of the ^{124}I-Ga-**D6** dose formulation prior to administration is shown as a reference (purple, left).**B)** Metabolite analysis of ^{67}Ga-**D7** (open circles) shows 0 % intact complex in the urine 1 h post injection. Radioanalytical HPLC trace of the ^{67}Ga-**D7** dose formulation prior to administration is shown as a reference (green, left). Metabolite analysis of Ga-**D7**-^{124}I (open circles) shows detectable intact complex (64 %) in the urine 1 h post injection. Radioanalytical HPLC trace of the Ga-**D7**-^{124}I dose formulation prior to administration is shown as a reference (brown, right).

hour (Figure 10B). The differential metabolite profile of ^{67}Ga-**D6**/ ^{67}Ga-**D7** and Ga-**D6**-^{124}I / Ga-**D7**-^{124}I shows that gallium dissociation is one of the primary sources of complex degradation in vivo due to the comparatively labile nature of Ga-LDFC and Ga-DFO complexes.

2.4 Summary and Conclusion

Here, we show for the first time that a multi-isotope, radiochemical approach can be employed to elucidate the metabolic fate of the metal and the ligand component of siderophore-conjugate. We utilized the complexation of the siderophore moiety of the conjugate with a long-lived SPECT isotope ^{67}Ga and radiochemical tagging of the ligand component with the long-lived PET isotope ^{124}I by incorporation of a tyrosine linker.

In this study, Ga-**D6** shows higher potency than the *apo*-conjugate in wt *E. coli* and *S. aureus* with an MIC value of 1.9 µM and 3.8 µM respectively, indicating synergistic effects of Ga complexation and siderophore-mediated transmembrane transport of the antibiotic, in accordance with previously evaluated compounds of this class. Ga-**D7** shows diminished potency, but some growth inhibitory activity is retained in S. aureus and E. coli and therefore the construct is still able to deliver the antibiotic cargo ciprofloxacin to the cytoplasm at a lower concentration. Ga-**D7** remained the most active in comparison to Fe-**D7** and **D7**, confirming findings reported for this compound class that Ga-complexation rescues antibiotic potency. While radiolabeling was feasible, the radiochemical yield for ^{124}I iodination and ^{67}Ga-labeling of **D6**-I and **D7**-I were low (15-20%) and necessitated purification of the radiochemically tagged constructs to remove reactive precursor. The ^{67}Ga-**D6** and ^{67}Ga-**D7** complexes show time dependent siderophore mediated active uptake in *wt* bacterial strains with an average uptake of ~20 % for all strains tested. Ga-**D6**-^{124}I and Ga-**D7**-^{124}I also showed siderophore mediated time dependent uptake, however the overall uptake

was lower for *E. coli* and *P. aeruginosa*. *S. aureus* showed the maximum uptake. Biodistribution and urine metabolite analysis reveal significantly improved integrity of the radioiodinated conjugate in contrast to the ^{67}Ga-labeled constructs. Finally, based on the higher in vitro uptake of Ga-**D6**-^{124}I and Ga-**D7**-^{124}I in *S. aureus*, a study of murine infection was performed. The study reveals significantly enhanced uptake in infected muscle for Ga-**D6**-^{124}I when compared to control tyrosine-^{124}I, which showed no specificity. The uptake of Ga-**D7**-^{124}I showed no statistical difference in uptake in any of the muscle tissues investigated.

In summary, Ga-**D6** and Ga-**D7** constitute the first xenometallomycins which enable tagging with two short-lived biomedical isotopes for direct quantification of individual components. Direct isotope quantification also allows for a more comprehensive picture of siderophore mediated internalization of antibiotic payloads, that can predict in vitro efficacy and enable the non-invasive identification, localization and monitoring of bacterial infection in vivo. We note that a correlation between enhanced uptake and growth inhibitory activity emerges among the 8 Ga(III) Trojan horse compounds investigated by us to date (Figure 2.10, Figure 2.64, 2.65), which, while by no means predictive, can further support drug discovery efforts and improve understanding of structure activity relationships of this compound class.

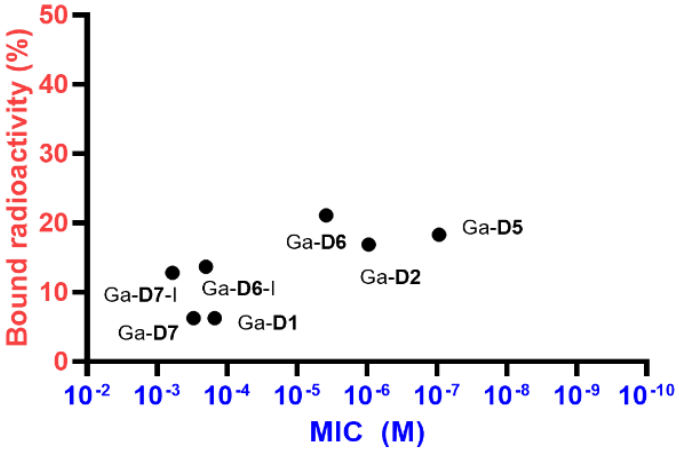

Figure 2. 11: Proposed correlation plot between bound radioactivity and MIC value in *S. aureus* for all gallium siderophore-base antibiotic conjugates tested, first, second, and third-generation. The Y-axis shows the highest bacteria uptake percentage, and X-axis shows the MIC concentration.

2.5 Experimental and supporting Information

2.5.1 Materials and Methods

All starting materials were purchased from Acros Organics, Alfa Aesar, Sigma Aldrich, or TCI America and used without further purification. NMR spectra (^{1}H and ^{13}C) were collected on a 700 MHz Advance III Bruker, 500 MHz or 400 MHz Bruker instrument at 25 °C and processed using TopSpin 3.5pl7. ^{19}F NMR were collected on a 400 MHz Bruker instrument at 25 °C using TFA as an internal standard (δ: -76 ppm). Chemical shifts are reported as parts per million (ppm). Mass spectrometry: low-resolution electrospray ionization (ESI) mass spectrometry and high-resolution (ESI) mass spectrometry was carried out at the Stony Brook University Institute for Chemical Biology and Drug Discovery (ICB&DD) Mass Spectrometry Facility with an Agilent LC/MSD and Agilent LC-UV-TOF spectrometers, respectively. UV-VIS spectra were collected with the NanoDrop 1C instrument (AZY1706045). Spectra were recorded from 190 to 850 nm in a quartz cuvette with 1 cm path length. HPLC: Preparative HPLC was carried out using a Shimadzu HPLC-20AR equipped with a Binary Gradient, pump, UV-Vis detector, manual injector on a Phenomenex Luna C18 column (250 mm×21.2 mm, 100 Å, AXIA packed). Method A (preparative purification method): A = 0.1% TFA in water, B = 0.1% TFA in MeCN. Gradient: 0-5 min: 95% A. 5-24 min: 5−95% B gradient. Method B (preparative purification method): A = 10 mM sodium acetate (pH = 4.5) in water, B = 100% MeCN. Gradient: 0-5 min: 95% A. 5-24 min: 5−95% B gradient. Analytical HPLC analysis was carried out using a Shimadzu HPLC-20AR equipped with a binary gradient, pump, UV-Vis detector, autoinjector and Laura radio detector on a Phenomenex Luna C18 column (250mm x 4mm, 10µm C18(2), 100 Å). Method C: A = 10 mM NaOAc (pH = 4.5), B = MeCN with a flow rate of 0.8 mL/min, UV detection at 254nm and 280nm. 0−2 min: 95% A. 2−5 min: 5−35% B.5-23 min: 35-70%. 23-25min:70-95%. Phenomenex Luna C18 column

(150mm × 3 mm, 100 Å, AXIA packed), method D (analysis of ^{67}Ga/Ga complexes): A = 10 mM sodium acetate (pH = 4.5) in water, B = 100% MeCN. Gradient: 0-2 min: 95% A. 2-14 min: 5−95% B gradient. 14-16 min: 95% B. 16-16.6 min: 95-5% B. 16.5-20 min: 5% B, UV detection at 254 and 280 nm. Purity of all intermediates and final products including radiochemical species was determined using analytical HPLC. High-resolution (ESI) mass spectrometry was carried out at the Stony Brook University Institute for Chemical Biology and Drug Discovery (ICB&DD) Mass Spectrometry Facility with an Agilent LC/MSD and Agilent LC-UV-TOF spectrometers; low-resolution LC-MS was carried out using the Agilent 1260 Infinity II LC system and Agilent Infinity Lab LC/MSD system, single quadrupole, spray ionization with a Phenomenex Luna C18 column (150mm × 3 mm, 100 Å, AXIA packed). A = 0.1% formic acid in water, B = 0.1% formic acid in MeCN with a flow rate of 0.8 mL/min, UV detection at 254 and 220nm. Gradient, method E: 0 - 3 min: 5% B, 3-10: 5-95%B, 10-13min: 95% B, 13-13.5 min: 95-5%B; 13.5-16 min: 5% B. All conjugates and complexes were ≥95% pure. ICP-OES was carried out using an Agilent 5110 ICP-OES. A 10-point standard with respect to gallium and iron was used and lines of best fit were found with R2 of 0.999. 5-(N-Acetyl-N-acetoxyamino)-2- {5-(N-acetyl-N-acetoxy-amino)-2-[5-(N-acetyl-N acetoxyamino) -2-(benzyloxy-carbonylamino) valerylamino] valerylamino) valeric acid (**P5**) and 7-(4-β-Alanyl-1-piperazinyl)-1-cyclopropyl-6-fluoro-4-oxo-1H-quinoline-3-carboxylic acid (**B2**) were synthesized according to previously published procedures.[74,111] A detailed account of the chemical synthesis of **D6** and **D7**, including NMR spectral assignments, HPLC traces, HRMS and corresponding data is provided in the supporting information.

2.5.2 Synthesis of coordination complexes of D6 and D7

Ga and Fe complexes of **D6** and **D7** were synthesized using the following protocol. **Ga-D6**. **D6** (0.010 g, 0.009 mmol, 1 eq) was dissolved in DMF (1 mL) and $Ga(NO_3)_3$ (0.007 g, 0.027 mmol, 3 eq) dissolved in 10mM CH_3COONa (pH =5) was added. The pH of the solution was adjusted to 6 by adding 0.1 M NaOH. The reaction mixture was stirred for 1h at 60°C and overnight at room temperature. Solvent was removed in vacuo and product was purified by preparative HPLC (Method A, product elutes at 43% B) to afford Ga-**D6** (0.006 g, 0.005 mmol, 62%) as a white solid. Calculated mass for Ga-**D6** ($C_{50}H_{65}FGaN_{11}O_{15}$): 1147.3; found 1048.3 $[M+H]^+$. Retention time (Method D): 7.65 min (purity/ peak area: > 99%). **Fe-D6**. **D6** (0.005 g, 0.004 mmol, 1 eq) was dissolved in DMF (1 mL) and $FeCl_3$ (0.002 g, 0.012 mmol, 3 eq) was added. The reaction mixture was stirred for 1h at room temperature. Solvent was removed in vacuo and the product was purified by preparative HPLC (Method A, product elutes at 48% B) to afford Fe-**D6** (0.006 g, 0.003 mmol, 87%) as a red solid. Calculated mass for Fe-**D6** ($C_{50}H_{65}FFeN_{11}O_{15}$): 1134.4; found 1135.4 $[M+H]^+$. Retention time (Method D): 7.48 min (purity/ peak area: > 99%) . **Ga-D7**. **D7** (7 mg, 0.006 mmol, 1 eq) was dissolved in DMF (1 mL) and Ga $(NO_3)_3$ (5.1 mg,0.018 mmol, 3 eq.) dissolved in 10mM CH_3COONa (pH =6) was added. The pH of the solution was adjusted to 6 by adding 1 M NaOH. The reaction mixture was stirred for 1h at 60°C and overnight at room temperature. Solvent was removed in vacuo and the product was purified by preparative HPLC (method D, product elutes at 50% B) to afford Ga-**D7** (0.0046 mmol, 5.6 mg, 78%) as a white solid. LC-MS: calculated mass for Ga-**D7** ($C_{55}H_{73}FGaN_{10}O_{15}$): 1202.46; found 1203.50 $[M+H]^+$. Retention time (method D): 8.19 min (purity/ peak area: > 90%). **Fe-D7**. **D7** (4 mg, 0.0035 mmol, 1 eq) was dissolved in DMF (1 mL) and $FeCl_3$ (0.0018 g, 0.011 mmol, 3 eq) was added. The pH of the solution was adjusted to 6 by adding 1 M NaOH. The reaction mixture was stirred for 1h at

60ºC and overnight at room temperature. Solvent was removed in vacuo and product was purified by preparative HPLC (method D, product elutes at 50% B) to afford Ga-**D7** (0.0048 mmol, 5.7 mg, 80%) as a white solid. LC-MS: calculated mass for Fe-**D7** ($C_{55}H_{74}FFeN_{10}O_{15}$): 1189.45; found 1190.40 $[M+H]^+$. Retention time (method D): 8.23 min (purity/ peak area: > 90%).

2.5.3 Antimicrobial activity assay

Antibacterial activity of *apo*-**D6** and **D7**, its corresponding Fe and Ga complexes and iodinated Ga-**D6** and Ga-**D7** was determined by measuring their minimum inhibitory concentrations (MIC) using the broth microdilution method according to the Clinical and Laboratory Standards Institute (CLSI) guidelines. All aqueous solutions and media were prepared using deionized water. All liquids and media were sterilized by autoclaving (220 °C, 1 h) before use. Iron deficient Mueller-Hinton broth (cation adjusted) was used for these assays. 5.25g of MHB was added to 250 mL of deionized water. Aqueous solutions of 1 M Ca^{2+} (0.418 mL) and 1 M Mg^{2+} (0.155 mL) to 250 mL of MHB was added to the broth. The broth was autoclaved for 1h at 220 °C. To make the broth iron-deficient, 4.06 mL of 1 mg/mL sterile (autoclaved) aq. solution of 2,2'-bipyridine (DP) was added to 250 mL of cation adjusted MHB.

In general, 0.3 mM stock solution of testing compounds were prepared. 10 µL solution of testing compound (0.3 mM) was added to the first well of the 96-well plate and serial dilutions were made down each row of the plate. 40 µL of growth media and 50 µL of diluted bacterial inoculum was also added to each well, resulting in a total volume of 100 µL and a concentration gradient of 0.3×10^{-4} M – 0.92×10^{-12} M. The dilution rate was adjusted keeping in mind the MIC of ciprofloxacin (positive control). The plates were incubated at 37 °C for 13 h and each plate was examined for bacterial growth using a plate reader (EPOCH2NS, Biotek microplate spectrometer).

The MIC was recorded as the lowest compound concentration (μM) required to inhibit >90% of bacterial growth as judged by the absorbance of the culture media relative to the negative control.

2.5.4 Radiolabeling with ^{67}Ga.

^{67}Ga-citrate was received from Jubilant Radiopharma at an average specific activity of 140.9 MBq/mL. The ^{67}Ga-citrate solution was converted to ^{67}Ga-chloride using a previously described protocol. The average specific activity of the resultant 67Ga-chloride solution used for radiolabeling was 137.2 MBq/mL. For radiolabeling of **D6** and **D7**, an aliquot of $^{67}GaCl_3$ (2.3 MBq, 15 μL) was mixed with a solution of **D6** (50 μL, 0.01 mM) and an aliquot of $^{67}GaCl_3$ (3.2 MBq, 30 μL) was mixed with a solution **D7**(40 μl, 0.003 mM) . The pH of the solution was adjusted with HEPES (100 mM, 80 μL) to 7.4. Complexation was monitored by radio-HPLC, method D. Radiolabeling was found to proceed after 5 minutes at room temperature. Radiochemical yield: >99%. ^{67}Ga-**D6**: R_t = 7.50 min (purity/peak area: 99%). ^{67}Ga-**D7:** R_t=8.11 min (purity/peak area: 99%). For radiolabeling **D6**-I, $^{67}GaCl_3$ (4.3 MBq, 20 μL) was mixed with a solution of **D6-I** (10 μL, 0.01 mM) in chelex resin treated water. The pH of the solution was adjusted with HEPES (100 mM, 40 μL) to 7.4. Complexation was monitored by radio-HPLC, method D. For **D7**-I, $^{67}GaCl_3$ (4.3 MBq, 20 μL) was mixed with a solution of **D7**-I (45μl,1.5 mM). Radiolabeling was found to proceed after 5 minutes at room temperature. Radiochemical yield: ~10%. ^{67}Ga-**D6**-I: R_t = 7.90 min (purity/peak area: 99%).^{67}Ga-**D7**-I: Radiochemical yield ~15%, R_t= 7.93 min (purity/peak area: >95%).

2.5.5 Bacterial Uptake of ^{67}Ga in wt bacterial strains

wt *E. coli* (Mg 1655), wt *S. aureus* (RN4220) and wt *P. aeruginosa* (PAO1) were grown overnight in 5 mL LB (Fe-deficient) at 37ºC. The overnight cultures were inoculated in 10 mL

iron deficient LB and incubated at 37 ºC until the OD_{600} reached 0.4. Uptake was initiated by adding ^{67}Ga complexes (10 µL, 0.11 MBq) to culture tubes containing 10 mL bacterial inoculum and incubating at 37ºC. Aliquots (1 mL) were removed after 10 min, 20 min, 30 min, 1h and 2h and centrifuged for 3 min (34000 rpm). The supernatant was removed, and the bacterial pellet was washed with DPBS (1mL, 3x). The assay was performed in five replicates and in parallel with a ^{67}Ga-citrate control. All tubes were counted using an automated gamma counter to quantify retained radioactivity in pellets in comparison to the 1 mL parent inoculum.

2.5.6 Radiolabeling with ^{124}I

^{124}I was received from 3D imaging at an average specific activity of 17131 MBq/mL, as an aqueous solution of NaOH. The stock solution was diluted with 100 µL water. The average specific activity of the resultant ^{124}I solution used for radiolabeling was 3515 MBq/mL. Direct radioiodination was carried out using Iodo-gen precoated iodination test tubes (Pierce 28601) at pH = 7.4, 25 °C for 45 min. In general, stock solutions of Tyrosine, Ga-**D6** and Ga-**D7** dissolved in buffer (HEPES, 100 mM, 100 µL) were added to the iodo-gen tube. An aliquot of ^{124}I (9.5 MBq, 3 µL) was added to the tube. The sample was vortexed for 5 mins and incubated at room temperature. After 45 mins, the conjugates were purified on radio HPLC to isolate the mono-iodinated product using method C. Radiochemical yield 15-20%. Tyrosine-^{124}I: t_R = 4.97 min, Ga-**D6**-^{124}I: t_R = 8.40 min, Ga-**D7**-^{124}I: t_R = 8.73 min, (purity/peak area: 99%).

2.5.7 Bacterial Uptake of ^{124}I in wt bacterial strains.

wt *E. coli* (Mg 1655), wt *S. aureus* (RN4220) and wt *P. aeruginosa* (PAO1) were grown overnight in 5 mL LB (Fe-deficient) at 37ºC. The overnight cultures were inoculated in 10 mL iron deficient LB and incubated at 37 ºC until the OD_{600} reached 0.4. The uptake was initiated by

adding ^{124}I complexes (10 µL, 0.14 MBq) to culture tubes containing 10 mL bacterial inoculum and incubating at 37^{o}C. Aliquots (1 mL) were removed after 10 min, 20 min, 30 min, 1h and 2h and centrifuged for 3 min (34000 rpm). The supernatant was removed, and the bacterial pellet was washed with DPBS (1mL, 3x). The assay was performed in five replicates and in parallel with a tyrosine-^{124}I control. All tubes were counted using an automated gamma counter to quantify retained radioactivity in pellets in comparison to the 1 mL parent inoculum.

2.5.8 Biodistribution of naïve Balb/c mice

All animal experiments were performed using protocols approved by the Institutional Animal Care and Use Committee (IACUC) at Stony Brook University accredited through Association for Assessment and Accreditation of Laboratory Animal Care International (AAALAC International, Federal assurance #A3011-01). 0.5- 0.7 MBq of ^{67}Ga-**D6**, ^{67}Ga-**D7**, ^{67}Ga-citrate (control) and 0.2- 0.4 MBq of Ga-**D6**-^{124}I, Ga-**D7**-^{124}I and Tyrosine-^{124}I (control) were intravenously injected via tail vein catheter in naïve mice. Mice were sacrificed 1h p.i. and select organs were harvested. Radioactivity was counted by using a gamma counter, and the radioactivity associated with each organ was expressed as % ID/g.

2.5.9 Biodistribution of infected Balb/c mice

Murine myositis models were established by intramuscular (i.m.) injection of live or heat killed (90^{o}C, 30 minutes) strains of wt *S.aureus*. Mice were inoculated with 10^{8} CFUs of wt *S. aureus* in the right triceps and with a tenfold higher (10^{9}) burden of heat-killed bacteria on the left triceps. The microbial infections were allowed to develop for 5 h. Subsequently, 0.2- 0.4 MBq of Ga-**D6**-^{124}I and Tyrosine-^{124}I (control) were injected. Mice were sacrificed 1h p.i. and select organs

were harvested. Radioactivity was counted by using a gamma counter, and the radioactivity associated with each organ was expressed as % ID/g.

2.5.10 Metabolite analysis

100 µL of urine was directly injected on radio HPLC. Eluate was collected in 30s increments from 0-15 minutes. Activity on each tube was quantified using a gamma counter. The counts were used to reconstruct the metabolite trace which was then compared to the HPLC traces of the original ^{67}Ga-**D6**, ^{67}Ga-**D7**, Ga-**D6**-^{124}I and Ga-**D7**-^{124}I complexes.

2.5.11 Chemical synthesis and characterization

2.5.11.1 Synthesis of D6

(1) (S)-7-(4-(3-(2-((((9H-fluoren-9-yl) methoxy) carbonyl)amino)-3-(4-(tert-butoxy)phenyl) propanamido)propanoyl)piperazin-1-yl)-1-cyclopropyl-6-fluoro-4-oxo-1,4-dihydro quinoline-3-carboxylic acid. Fmoc-O-tert-butyl-L-tyrosine (0.208 g, 0.518 mmol, 1 eq) was dissolved in DMF (5 mL) and DIPEA (270.7 µL, 1.554 mmol, 3 eq) was added. After 2 minutes, HBTU (0.294 g, 0.773 mmol, 1.5 eq) was added to the reaction mixture followed by 7-(4-β-Alanyl-1-piperazinyl)-1-cyclopropyl-6-fluoro-4-oxo-1H-quinoline-3-carboxylic acid (0.250 g, 0.621 mmol, 1.2 eq) dissolved in DMF (2 mL). The reaction mixture was stirred overnight at 40oC. Solvent was removed in vacuo and the product was purified using combiflash chromatography (product elutes at 90% B) to afford 1 (0.388 g, 0.460 mmol, 88%) as a yellow solid. Calculated mass for 1 ($C_{48}H_{50}FN_5O_8$): 843.3; found 844.3 $[M+H]^+$. ^{1}H NMR (700 MHz, DMSO- d_6): δ 1.16 (s, 9H, H-30, H-31, H-32, H-33, H-34, H-35, H-36, H-37, H-38), 1.11-1.13 (dd, 2H, H-4, H-5), 1.26-1.28 (dd, 2H, H-6, H-7), 2.64-2.79 (t, 2H, H-18, H-19), 2.80-2.95 (d, 2H,

H-24, H-25), 3.21-3.27 (m, 4H, H-10, H-11, H-12, H-13), 3.60-3.73 (m, 7H, H-3, H-14, H-15, H-16, H-17, H-20, H-21), 4.06-4.12 (m, 4H, H-23, H-40, H-41, H-42), 7.06 (d, 1H, H-8), 7.25-7.30 (m, 4H, H-26, H-27, H-28, H-29), 7.36-7.41 (m, 4H, H-44, H-45, H-48, H-49), 7.48-7.52 (m, H-43, H-50), 7.61-7.65 (m, 3H, H-46, H-47, H-9), 7.80-7.84 (s and s, 2H, H- 39, H-22), 8.61 (s, 1H, H-2), (s, 1H, H-1, not included in the spectrum). ^{19}F NMR (376 MHz, DMSO- d_6,): δ -122.68. Retention time (Method C): 12.87 min (purity/peak area: > 99%).

(2) (S)-7-(4-(3-(2-amino-3-(4-(tert-butoxy) phenyl) propanamido) propanoyl)piperazin-1-yl)-1-cyclopropyl-6-fluoro-4-oxo-1,4-dihydroquinoline-3-carboxylic acid. Compound 1 (0.338 g, 0.461 mmol, 1 eq) was dissolved in DMF (5 mL) and DEA (716 µL, 6.918 mmol, 15 eq) was added. The reaction was stirred at room temperature for 1 h. Solvent was removed in vacuo and product was purified using combiflash chromatography (product elutes at 55% B) to afford 2 (0.119 g, 0.192 mmol, 50%) as a yellow solid. Calculated mass for 2 ($C_{33}H_{40}FN_5O_6$): 621.3; found 622.3 [M+H]+. 1H NMR (700 MHz, DMSO- d_6):): δ 1.25 (s, 9H, H-30, H-31, H-32, H-33, H-34, H-35, H-36, H-37, H-38), 1.16-1.20 (dd, 2H, H-4, H-5), 1.29-1.33 (dd, 2H, H-6, H-7), 2.93 (d, 2H, H-24, H-25), 3.16-3.42 (m, 6H, H-10, H-11, H-12, H-13, H-20, H-21), 3.59-3.72 (m, 4H, H-14, H-15, H-16, H-17), 3.78-3.83 (t, 1H, H-23), 3.93-3.97 (t, 1H, H-3), 6.88-6.94 (d, 2H, H-26, H-29), 7.10-7.19 (d, 2H, H-27, H-28), 7.92 (d, 1H, H-9), 7.56 (d, 1H, H-8), 8.19 (s, 2H, H-39, H-40, H-9), 8.35 (t, 1H, H-22), 8.66 (s, 1H, H-2), 15.12 (s, 1H, H-1, not included in the spectrum). 19F NMR (376 MHz, DMSO- d_6,): δ -123.40. Retention time (Method C): 8.77 min (purity/peak area: > 99%).

(3) 7-(4-((8S,11S,14S,17S)-11,14-bis(3-(N-acetoxyacetamido) propyl)-4-acetyl-8-(((benzyloxy) carbonyl)amino)-17-(4-(tert-butoxy)benzyl)-2,9,12,15,18-pentaoxo-3-oxa-

4,10,13,16,19-penta azadocosan-22-oyl)piperazin-1-yl)-1-cyclopropyl-6-fluoro-4-oxo-1,4-dihydroquinoline-3-carboxylic acid. P5 (0.106 g, 0.134 mmol, 1 eq) was dissolved in DMF (2 mL) and DIPEA (93.4 µL, 0.536 mmol, 3 eq) was added. After 2 minutes, HBTU (0.021 g, 0.056 mmol, 1.5 eq) was added to the reaction mixture followed by compound 2 (0.762 g, 0.201 mmol, 1.2 eq) dissolved in DMF (2 mL). The reaction mixture was stirred overnight at 40oC. Solvent was removed in vacuo and product was purified by preparative HPLC (Method A, product elutes at 76% B) to afford 3 (0.037 g, 0.037 mmol, 18%) as a yellow solid. Calculated mass for 3 ($C_{68}H_{88}FN_{11}O_{20}$): 1397.2; found 1398.7 $[M+H]^+$. ^{1}H NMR (700 MHz, DMSO- d_6): 1.14-1.19 (dd, 2H, H-4, H-5), δ 1.22 (s, 9H, H-30, H-31, H-32, H-33, H-34, H-35, H-36, H-37, H-38), 1.28-1.32 (dd, 2H, H-6, H-7), 1.33-1.77 (m, 12H, H-40, H-41, H-42, H-43, H-54, H-55, H-56, H-57, H-68, H-69, H-70, H-71), 1.77-2.09 (broad s, 9H, H-46, H-47, H-48, H-63, H-64, H-65, H-74, H-75, H-76), 2.07-2.25 (broad s, 9H, H-49, H-50, H-51, H-66, H-67, H-68, H-77, H-78, H-79), 2.65-2.99 (m, 4H, H-18, H-19, H-24, H-25), 2.98-3.31 (m, 10H, H-10, H-11, H-12, H-13, H-14, H-15, h-16, H-17, H-20, H-21), 3.65-4.00 (m, 7H, H-74, H-73, H-58, H-59, H-44, H-45, H-3), 4.22-4.42 (m, 4H, H-67, H-53, H-87, H-23), 5.03 (s, 2H, H-80, H-81), 6.86-6.79 (m, 2H, H-39, H-22), 6.97 (d, 1H, H-9), 7.06-7.27 (m, 4H, H-26, H-27, H-28, H-29), 7.32-7.36 (m, 5H, H-82, H-83, H-84, H-85, H-86), 7.39-7.52 (m, 2H, H-66, H-52), 7.55-7.59 (d, 1H, H-78), 7.90-7.94 (d, H, H-8), 8.65 (s, 1H, H-2), 15.20 (s, 1H, H-1, not included in the spectrum). ^{19}F NMR (376 MHz, DMSO- d6,): δ -123.87. Retention time (Method C): 9.85 min (purity/peak area: 99%).

(D6) 7-(4-((7S,10S,13S,16S)-7-amino-3-hydroxy-10,13-bis(3-(N-hydroxyacetamido) propyl)-16-(4-hydroxybenzyl)-2,8,11,14,17-pentaoxo-3,9,12,15,18-pentaazahenicosan-21-oyl)piperazin-1-yl)-1-cyclopropyl-6-fluoro-4-oxo-1,4-dihydroquinoline-3-carboxylic acid.

Compound 3 (0.037 g, 0.037 mmol, 1 eq) was dissolved in MeOH (2 mL) and 10% Pd/C (0.003 g) was added to the flask. After purging the flask with H2, the reaction mixture was stirred for 5 h under H2-pressure (1 atm). The reaction mixture was filtered through a PVDF filter, the solvent was evaporated in vacuo, and the desired product was obtained as a yellow soil (0. 055 g, 0.046 mmol) and used without further purification immediately for next step. Calculated mass for C60H82FN11O18: 1263.5; found 1264.8 [M+H] +. Retention time (Method C): 8.87 min (purity/ peak area: 87.6%). The yellow oil was treated with 6% DIPEA in MeOH (1 mL) overnight at room temperature. Solvent was removed to afford yellow oil (0.047 g, 0.044 mmol), the product was again used without further purification for the next step. Calculated mass for $C_{54}H_{76}FN_{11}O_{15}$: 1137.5; found 1138.7 $[M+H]^+$. Retention time (Method C): 8.43 min (purity/ peak area: 86.3%).

The oil was dissolved into a solution of 2:1 TFA and DCM (1 mL). The reaction mixture was stirred overnight at room temperature. Solvent was removed in vacuo and the product was purified using preparative HPLC (Method A, product elutes at 44% B) to afford D6 (0.020 g, 0.020 mmol, 45%) as a yellow solid. Calculated mass for D6 ($C_{50}H_{68}FN_{11}O_{15}$): 1081.4; found 1082.7 $[M+H]^+$. Retention time (Method C): 7.67 min (purity/ peak area: > 99%). ^{1}H NMR (700 MHz, DMSO- d_6): 1.16-1.18 (dd, 2H, H-4, H-5), 1.22-1.24 (dd, 2H, H-6, H-7), 1.46-1.70 (m, 12H, H-33, H-34, H-35, H-36, H-45, H-46, H-47, H-48, H-59, H-60, H-61, H-62), 1.94-1.99(broad s, 9H, H-40, H-41, H-42, H-52, H-53, H-54, H-66, H-67, H-68), 2.03-2.08 (m, 2H, H-18, H-19), 2.29-2.46 (m, 4H, H-24, H-25, H-10, H-11), Under water peak (m, 4H, H-20, H-21, H-12, H-13, 3.57 + under water peak (m, 12H, H-3, H-56, H-14, H-15, H-16, H-17, H-37, H-38, H-49, H-50, H-63, H-64), 3.75-3.95 (m, 1H, H-44), 4.18-4.40 (m, 2H, H-22, H-32), 6.60-6.66 (m, 3H, H-27, H-29, H-8), 6.95-7.00 (m, 2H, H-26, H-28), 7.35 (d, 1H, H-57), 7.58 (d, 1H, H-58), 7.92-7.99 (d, 1H, H-

9), 7.98-8.10 (m, 4H, H-55, H-43, H-31, H-22), 8.68 (s, 1H, H-2), 11.05 (s, 3H, H-39, H-51, H-65), 15.20 (s, 1H, H-1, not included in the spectrum). ^{19}F NMR (376 MHz, DMSO- d_6,): δ -123.07. Retention time (Method C): 7.37 min (purity/peak area: > 99%).

(D6-I) 7-(4-((7S,10R,13S)-7-amino-3-hydroxy-16-(4-hydroxy-3-iodobenzyl)-10,13-bis(3-(N-hydroxyacetamido)propyl)-2,8,11,14,17-pentaoxo-3,9,12,15,18-pentaazahenicosan-21-oyl)piperazin-1-yl)-1-cyclopropyl-6-fluoro-4-oxo-1,4-dihydroquinoline-3-carboxylic acid. D6 (0.002 g, 0.001 mmol, 1 eq) was dissolved in 500 µL MeCN/H2O (1:1) and selectfluor (250 µL, 1 eq) and NaI (250 µL, 1 eq) dissolved in MeCN were added to the reaction mixture. The reaction mixture was stirred for 15 mins at room temperature. Solvent was removed in vacuo and product was purified using prep HPLC (Method A, product elutes at 46% B) to afford **D6**-I (0.001 g, 0.0008 mmol, 46%) as a white solid. Calculated mass for **D6**-I ($C_{50}H_{67}FIN_{11}O_{15}$): 1207.3; found 1206.7 $[M-H]^-$. Retention time (Method D): 7.83 min (purity/ peak area: > 99%).

2.5.11.2 Ga-D6-I complex formation

Ga-D6-I. Compound **D6**-I (0.002 g, 0.001 mmol, 1 eq) was dissolved in DMF (250 µL) and $Ga(NO_3)_3$ (0.001 g, 0.003 mmol, 3 eq) dissolved in CH3COONa (10 mM, pH = 5) was added to the reaction mixture. The pH of the solution was adjusted to 6 by adding 0.1 M NaOH. The reaction mixture was stirred for 1h at 60^{o}C and overnight at room temperature. Solvent was removed in vacuo and the product was purified by preparative HPLC (Method D, product elutes at 48% B) to afford Ga-**D6**-I (0.0005 g, 0.0003 mmol, 23%) as a white solid. Calculated mass for Ga-**D6**-I ($C_{50}H_{64}FGaIN_{11}O_{15}$): 1273.2; found 1292.2 $[M+NH4]^+$. Retention time (Method D): 7.97 min (purity/ peak area: > 99%).

2.5.11.3 HPLC traces of D6

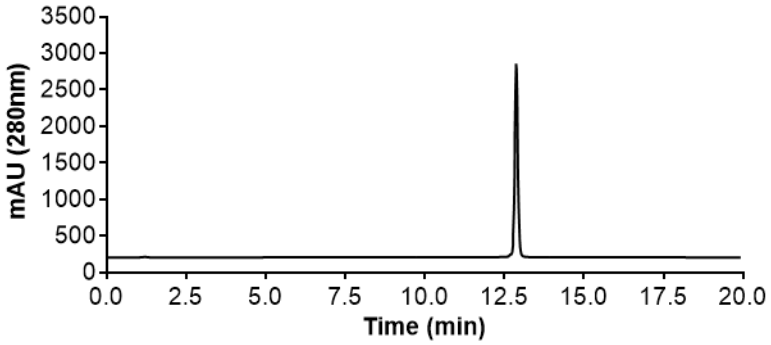

Figure 2. 12: HPLC chromatogram of compound **(1)**. Retention time (Method C): 12.87 min

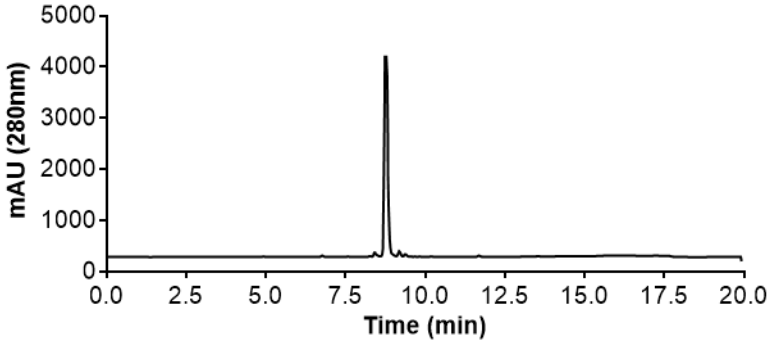

Figure 2. 13: HPLC chromatogram of compound **(2)**. Retention time (Method C): 8.77 min.

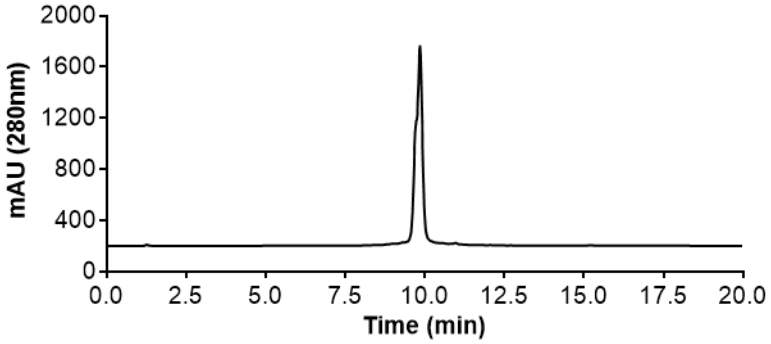

Figure 2. 14: HPLC chromatogram of compound **(3)**. Retention time (Method C): 9.85 min.

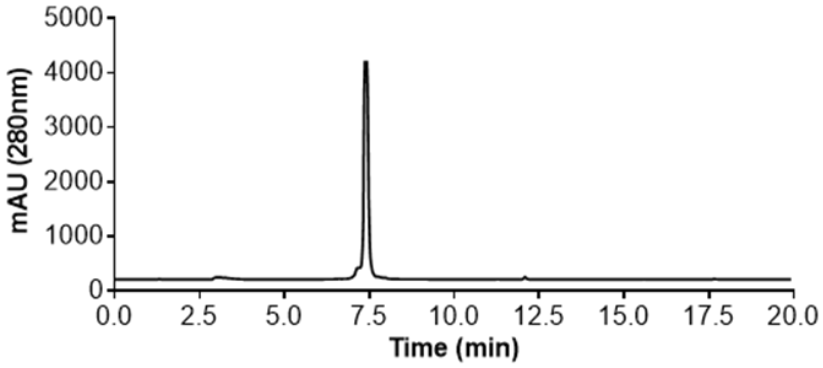

Figure 2. 15: HPLC chromatogram of compound **D6**. Retention time (Method C): 7.40 min.

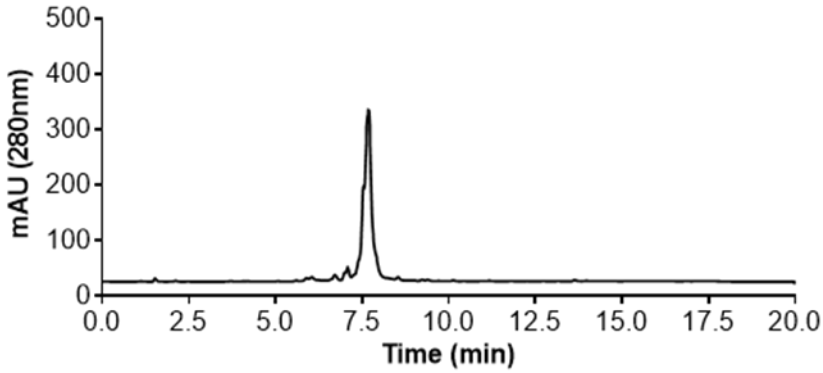

Figure 2. 16: HPLC chromatogram of compound Ga-**D6**. Retention time (Method D): 7.68 min.

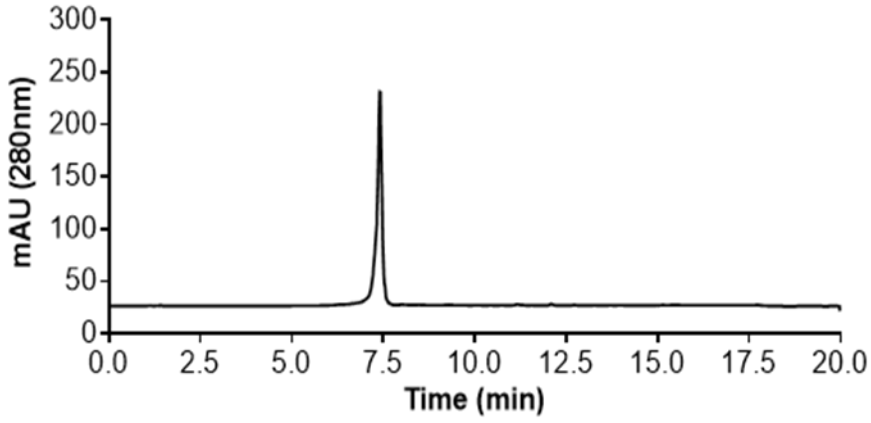

Figure 2. 17: HPLC chromatogram for Fe-**D6**. Retention time (Method D): 7.40 min.

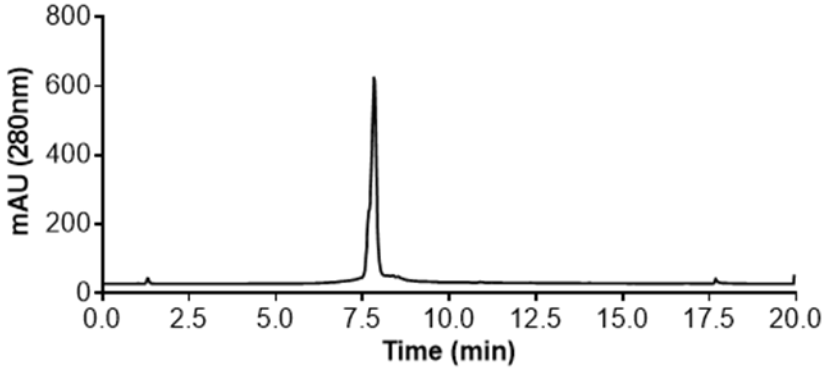

Figure 2. 18 :HPLC chromatogram of compound **D6**-I. Retention time (Method D): 7.83 min.

2.5.11.4 NMR data of D6

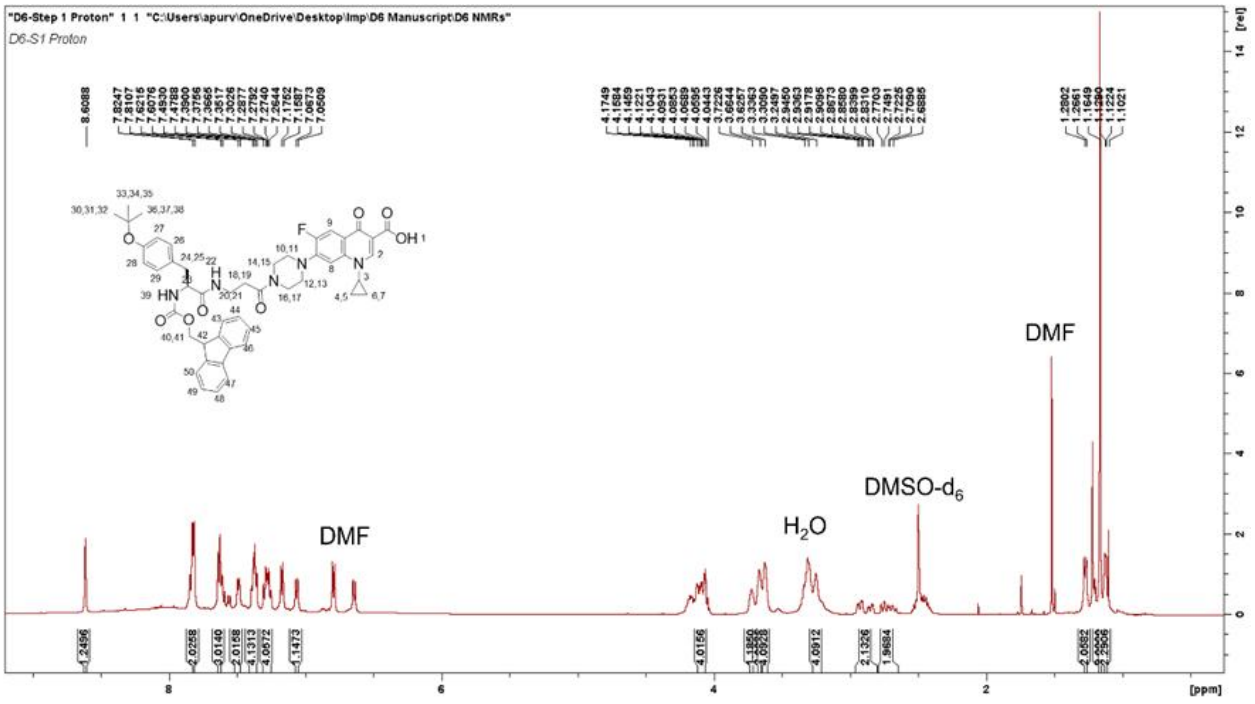

Figure 2. 19: ^{1}H-NMR spectrum of compound **(1)**. 700 MHz, DMSO-d_6.

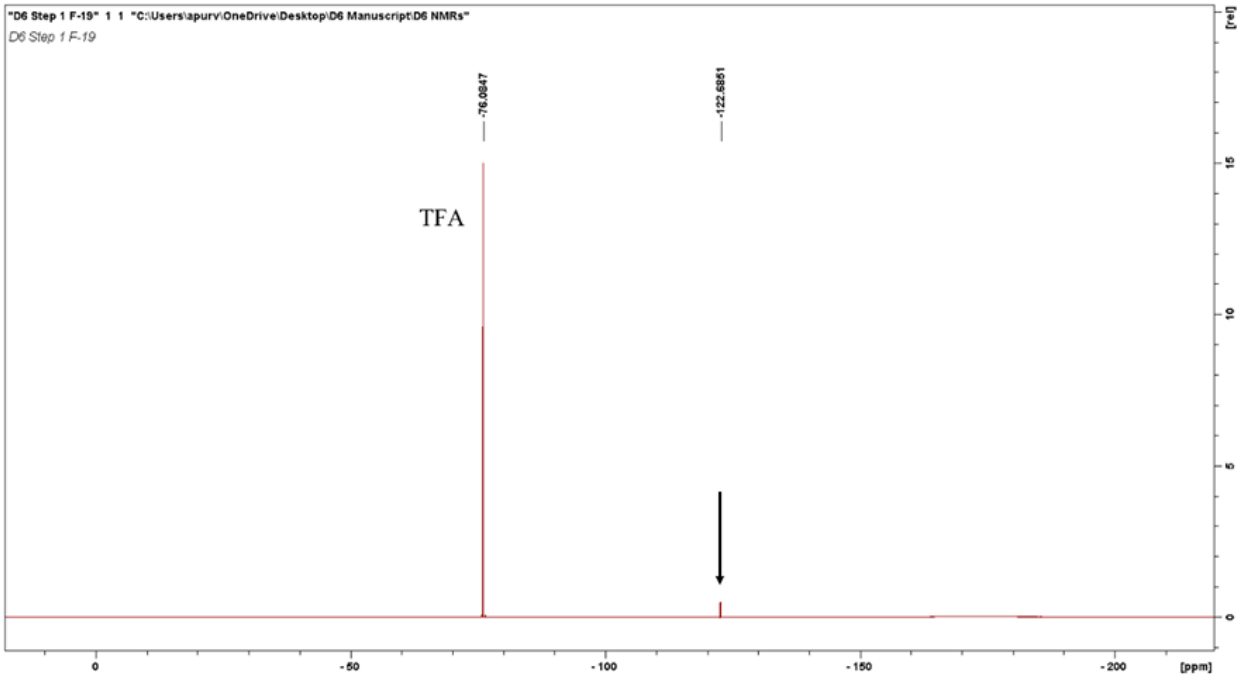

Figure 2. 20: ^{19}F-NMR spectrum of compound **(1)**. 376 MHz, DMSO-d_6.

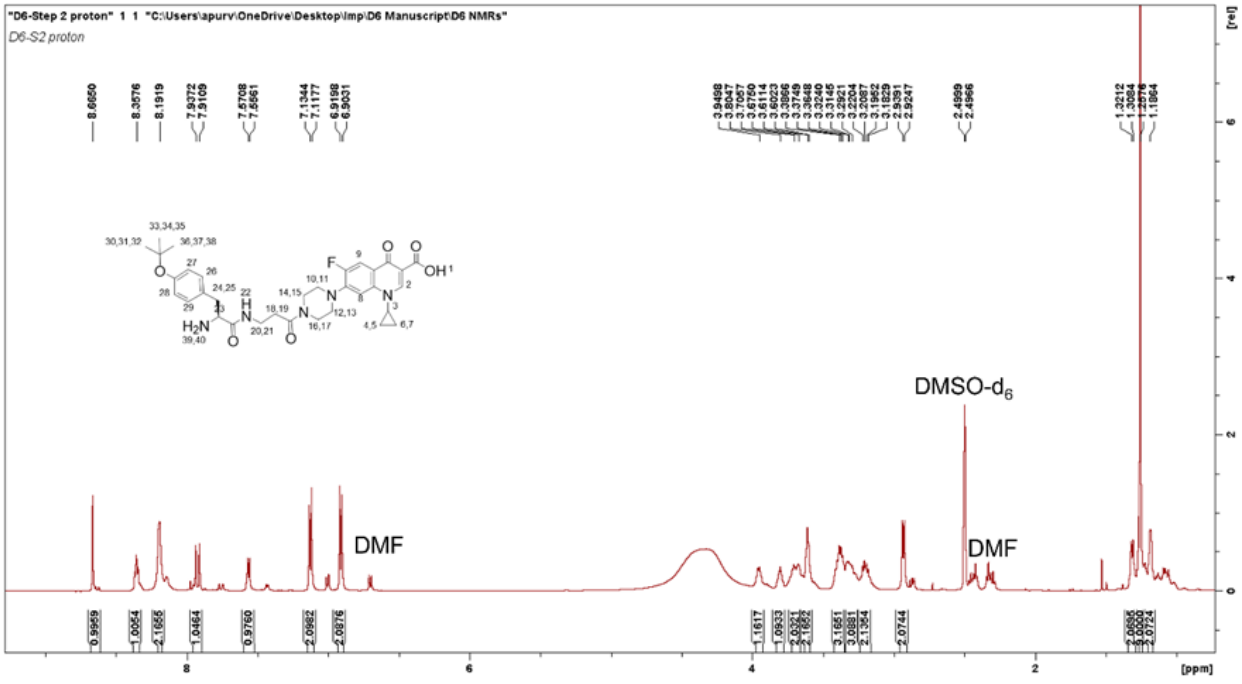

Figure 2. 21: ^{1}H-NMR spectrum of compound **(2)**. 700 MHz, DMSO-d_6.

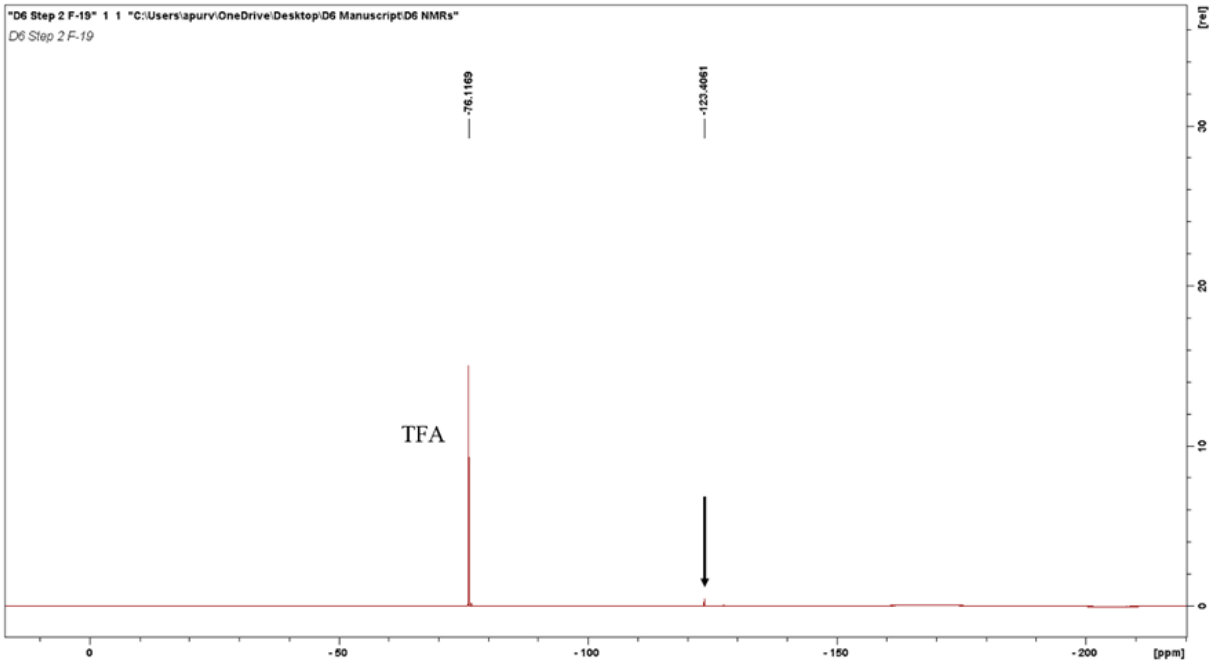

Figure 2. 22: ^{19}F-NMR spectrum of compound **(2)**. 376 MHz, DMSO-d_6.

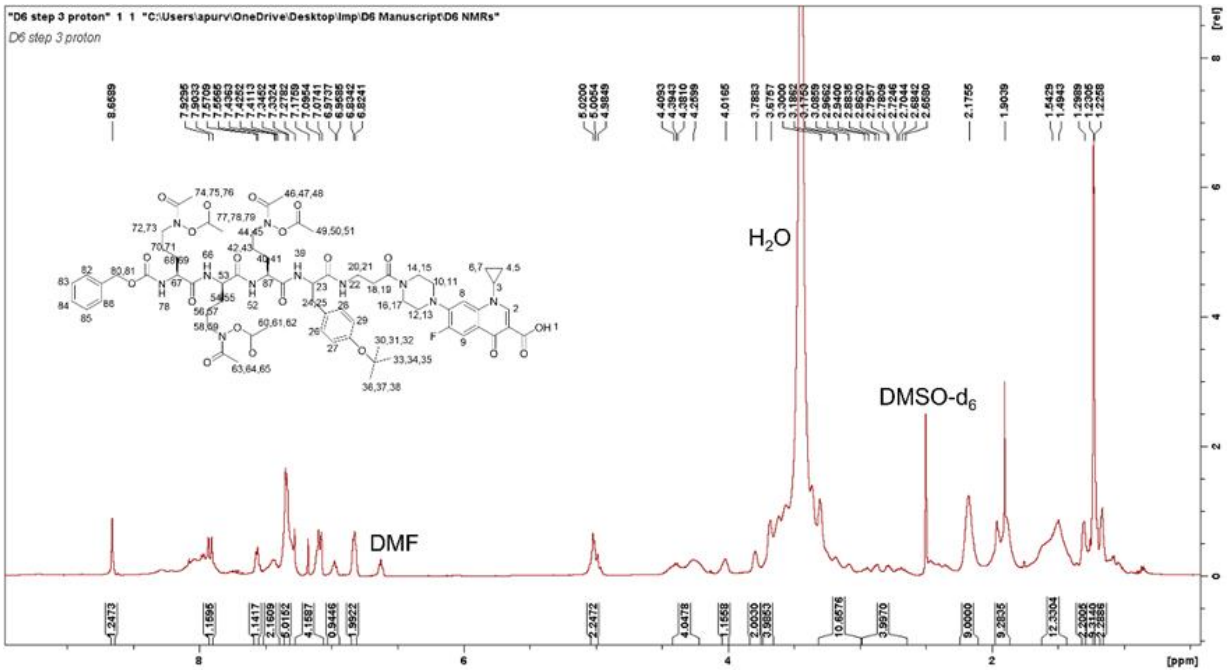

Figure 2. 23: ^{1}H-NMR spectrum of compound **(3)**. 700 MHz, DMSO-d_6.

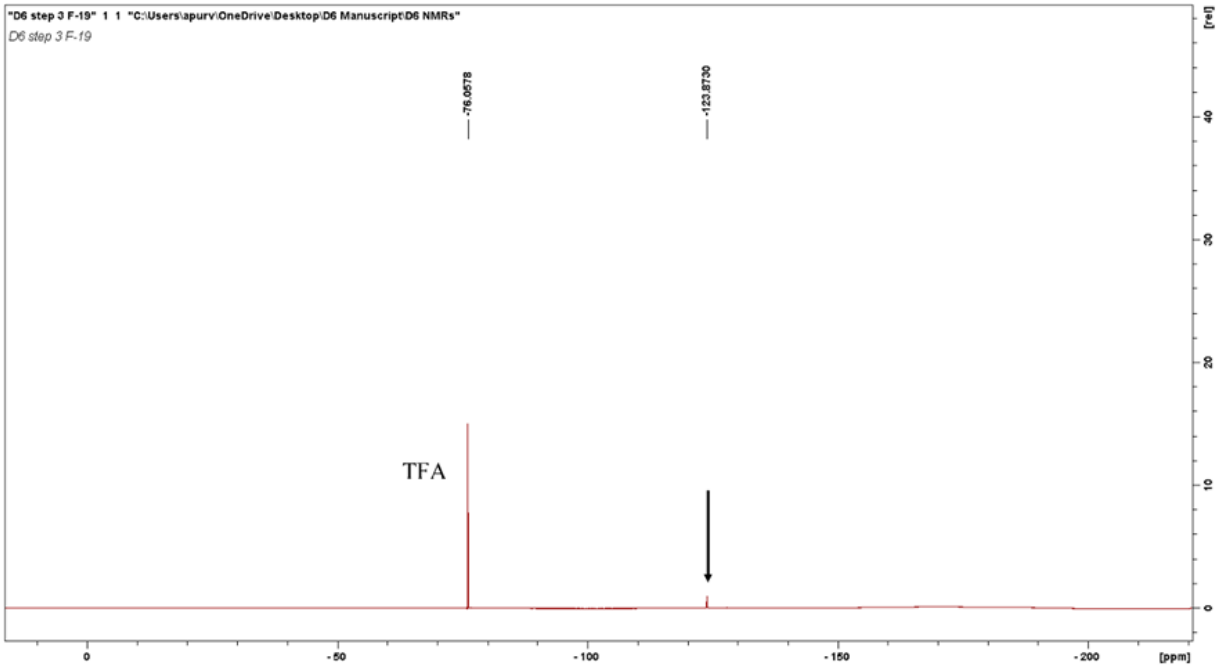

Figure 2. 24: ^{19}F-NMR spectrum of compound **(3)**. 376 MHz, DMSO-d_6.

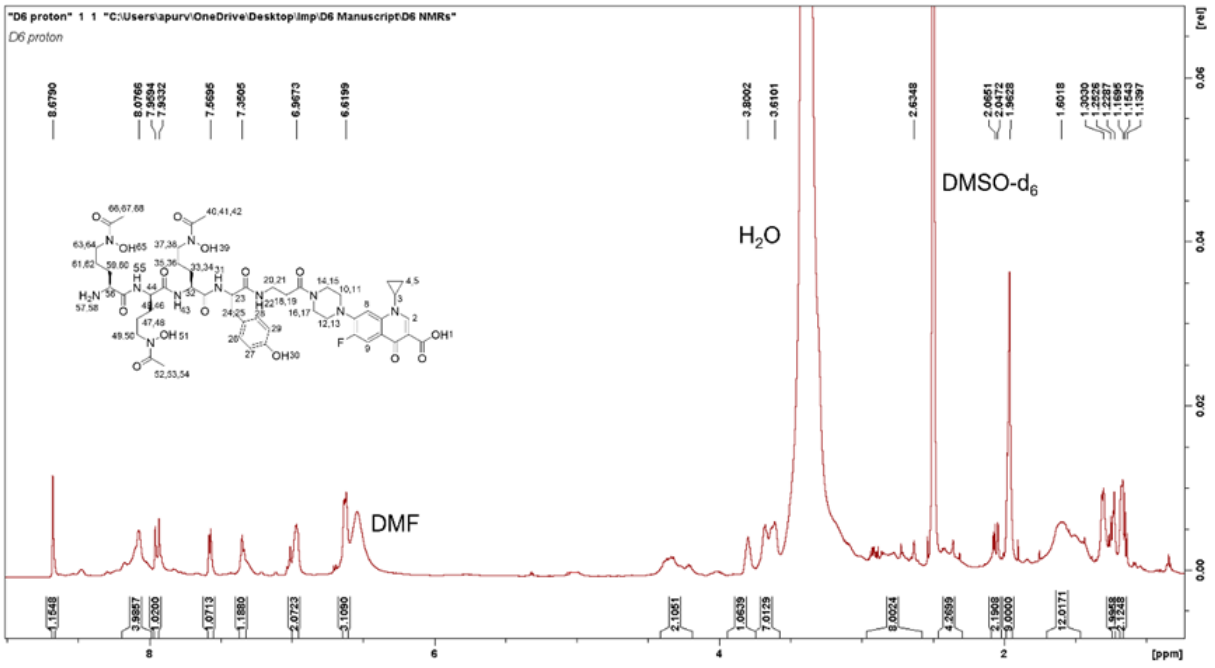

Figure 2. 25: ^{19}F-NMR spectrum of *apo*-**D6**. 376 MHz, DMSO-d_6.

2.5.11.5 HRMS and MALDI characterization for D6

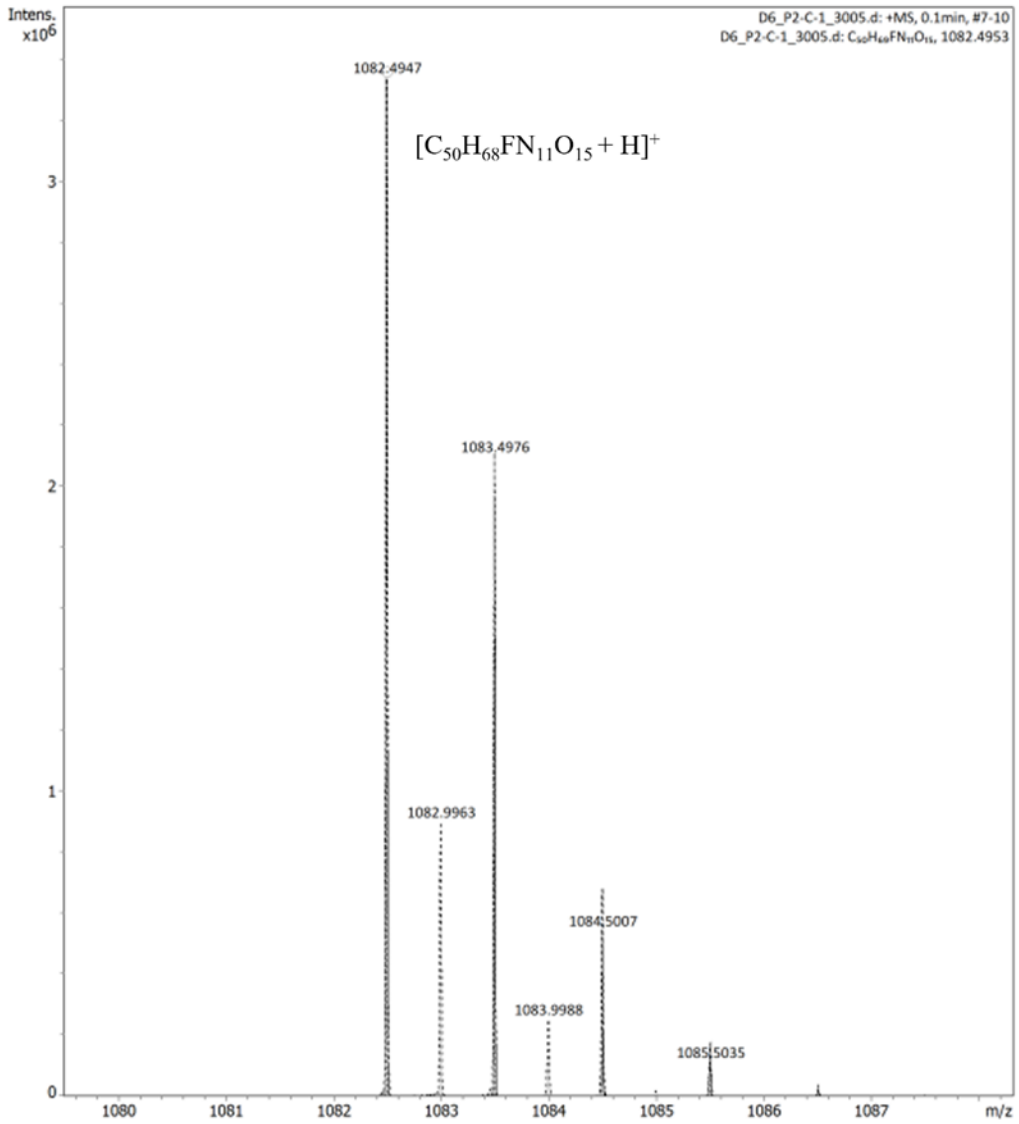

Figure 2. 26: High resolution mass spectrum of **D6**. HRMS calculated for $C_{50}H_{68}FN_{11}O_{15}$: 1081.4880; found 1082.4947 $[M+H]^+$.

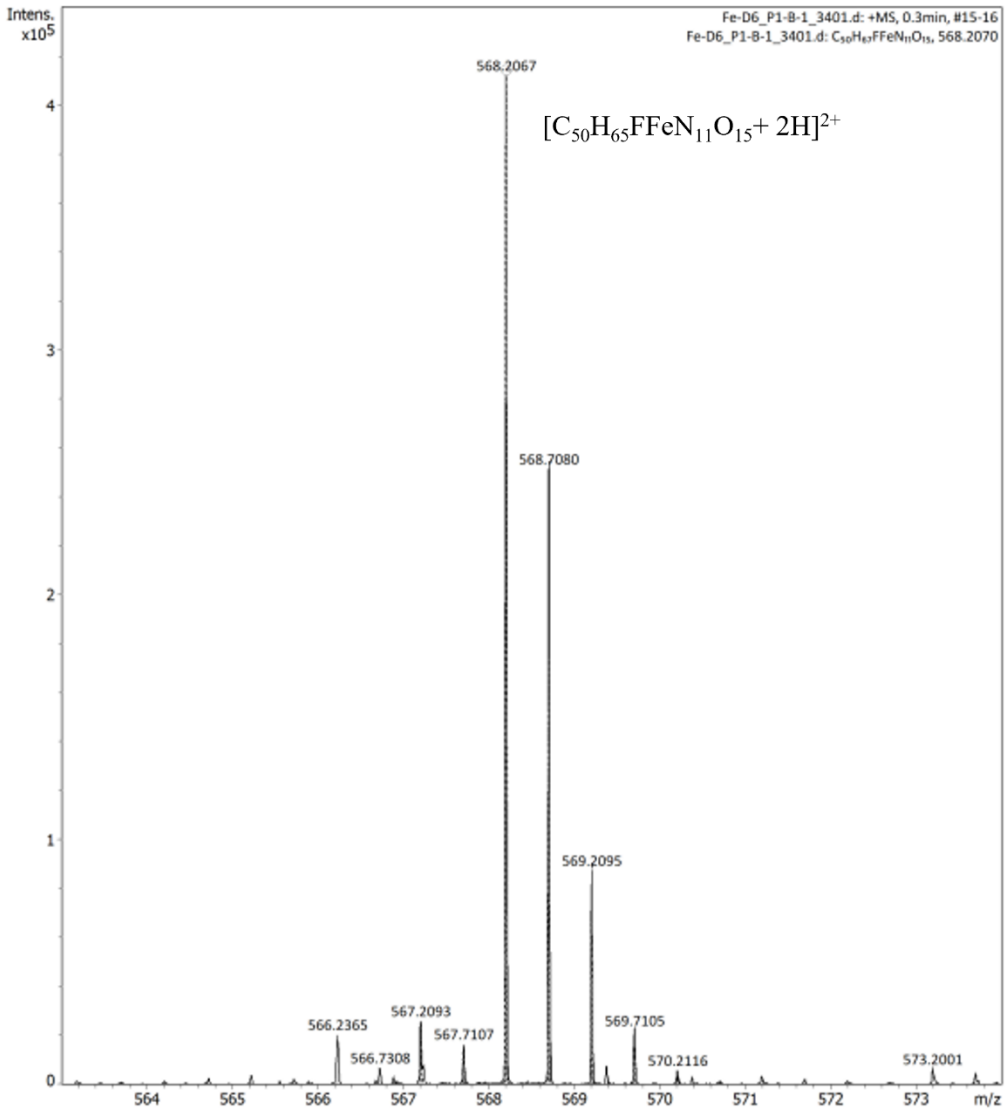

Figure 2. 27: High resolution mass spectrum of Fe-**D6**. HRMS calculated for $C_{50}H_{65}FFeN_{11}O_{15}$: 1134.3995; found 568.2067 $[M+2H]^{2+}$.

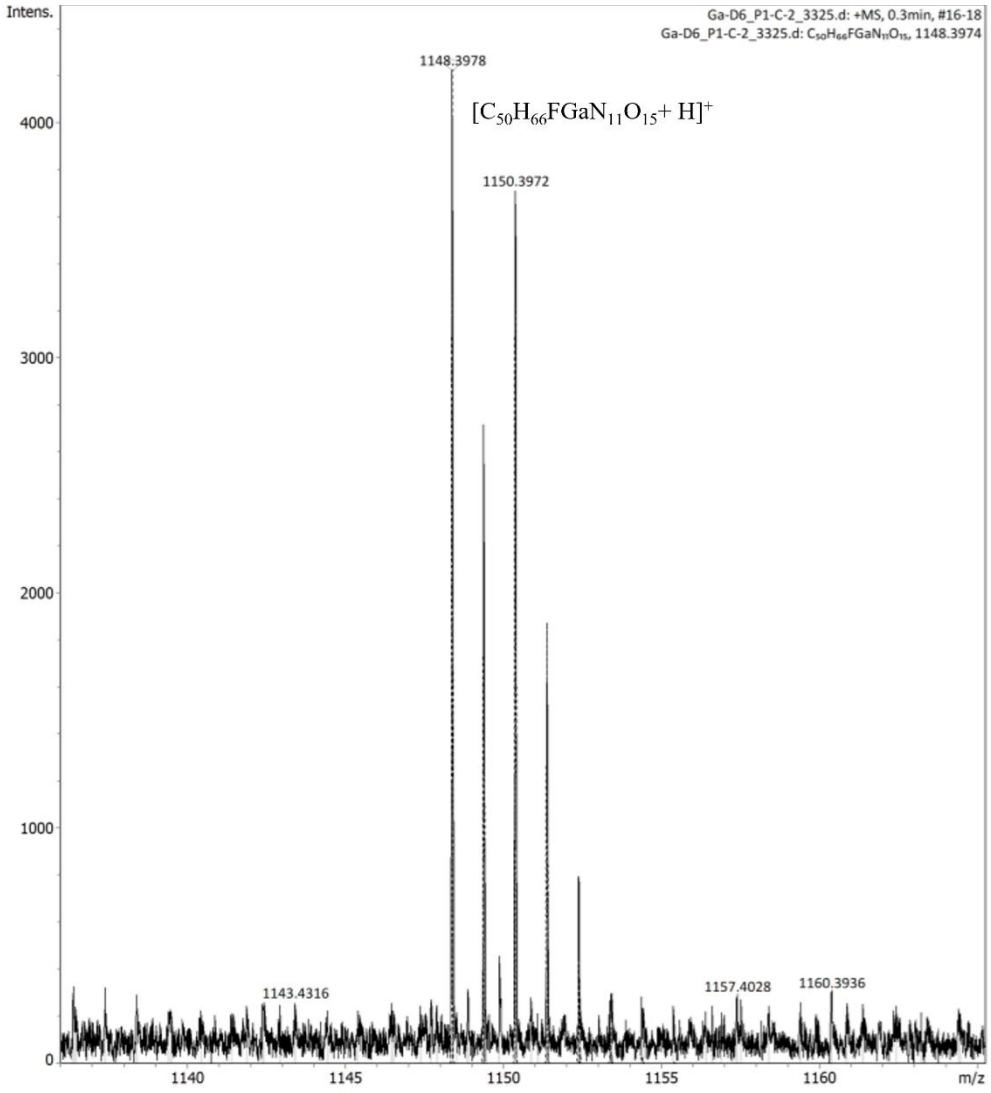

Figure 2. 28: High resolution mass spectrum of Ga-**D6**. HRMS calculated for $C_{50}H_{65}FGaN_{11}O_{15}$: 1147.3901; found 1148.3978 $[M+2H]^{2+}$.

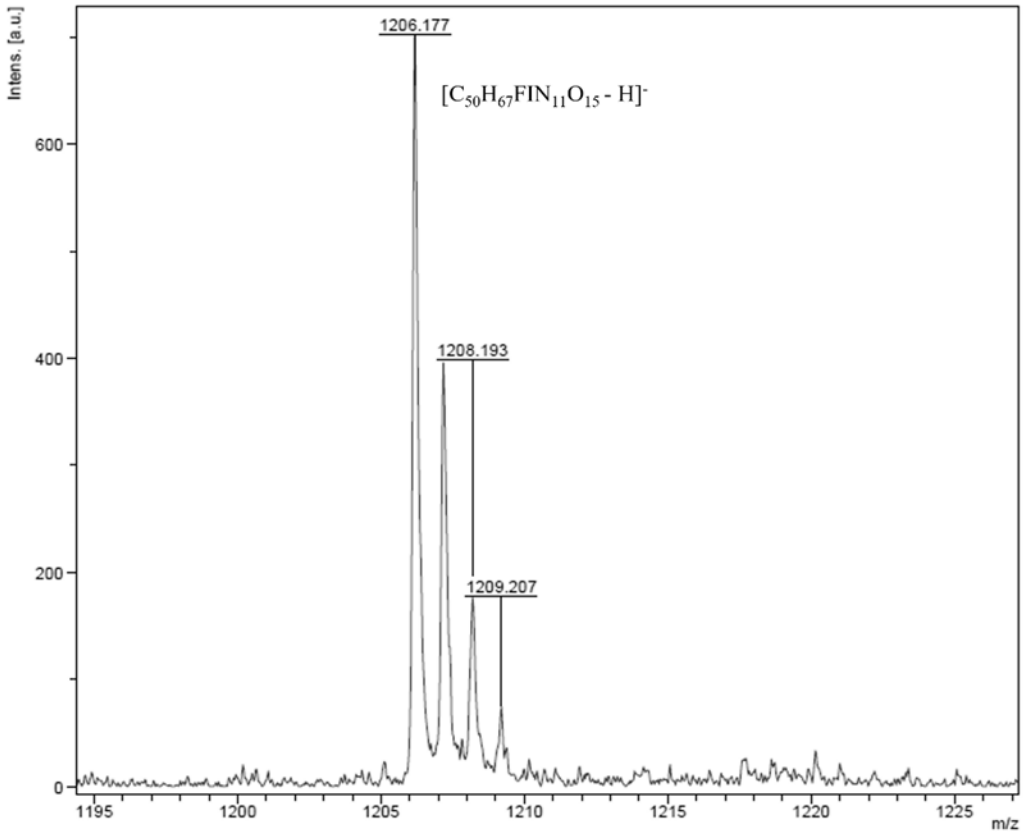

Figure 2. 29: MALDI analysis of **D6**-I. MS calculated for $C_{50}H_{67}FIN_{11}O_{15}$: 1207.3847; found 1206.177 $[M-H]^-$.

2.5.11.6 Synthesis of D7

7-(4-(3-carboxypropanoyl)piperazin-1-yl)-1-cyclopropyl-6-fluoro-4-oxo-1,4-dihydro quinoline-3-carboxylic acid, C1. Ciprofloxacin (1.0 g, 3.02 mmol) was suspended in dimethylsulfoxide (DMSO) (20 mL), followed by the addition of succinic anhydride (0.302 g, 0.302 mmol, 1 equiv). The reaction

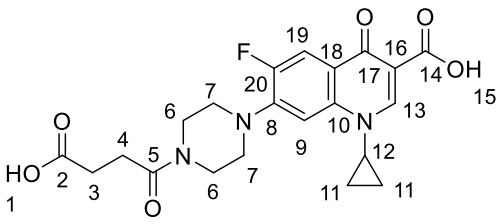

mixture was refluxed for 24 h at 95 ºC. After 24 h, the reaction crude precipitate was filtrated and washed with diethyl ether (Et_2O) and H_2O. The filtrate was lyophilized to afford a white solid **C1** (821 mg, 1.9 mmol, 63%) and used without further purification. LC-MS: calculated mass for **C1** ($C_{21}H_{22}FN_3O_6$): 431.15; found: 432.2 $[M+H]^+$.^{1}H NMR (DMSO-d_6, 500 MHz, ppm): δ 1.18 – 1.33 (d, 4H,H-11), 2.45 – 2.62 (m, 4H, H-3,H-4), 3.32 (s, 1H, H-7), 3.68-3.69 (d,2H, H-6), 3.80-3.83 (m,1H,H-12), 7.56-7.58 (d, 1H, H-9), 7.79-7.94 (d, 1H, H-19), 8.67 (s,1H, H-13),14.32 (s,1H,H-15).^{13}C NMR (DMSO-d_6, 500 MHz): δ 7.59 (2C,C-11), 27.41 (1C,C-2), 28.96 (1C,C-3), 35.87 (1C,C-12), 44.32 (2C,C-6), 49.20- 49.57 (2C, C-7), 106.57 – 106.75 (2C, C-9,C-19), 110.87-111.82 (1C,C-16), 118.74-118.82 (1C,C-18), 139.13 (1C,C-8), 144.86-144.96 (1C,C-10), 151.69 (1C,C-20), 165.88 (1C,C-14), 169.76 (1C,C-5), 173.93 (1C,C-17), 176.32 -176.35 (1C,C-2). ^{19}F NMR (DMSO-d_6, 400 MHz): δ -125.97-125.92. Retention time (method A): 8.32min.

(9H-fluoren-9-yl)methyl(R)-(34-(4-(tert-butoxy)phenyl)-3,14,25-trihydroxy-2,10,13, 21,24,32-hexaoxo-3,9,14,20,25,31-hexaazatetratriacontan-33-yl)carbamate, E1. N,N-Diisopropylethylamine (DIPEA) (3 mmol, 3 equiv) was added to a solution of Fmoc-Tyr(tBu)-OH (112.98 mg, 0.23 mmol, 1.5 equiv) in dry dimethylformamide (DMF). The reaction mixture was stirred for 10 min at room temperature. (2-(1H-benzotriazol-1-yl)-1,1,3,3-tetramethyluronium hexafluorophosphate (HBTU) (69.63 mg, 0.18 mmol, 1.2 equiv) in DMF was added to the reaction solution and allowed to stir for another 10 min. Deferoxamine mesylate (DFO) (100mg, 0.15 mmol) was dissolved in dry DMF and added to the stirring solution. The reaction mixture was stirred overnight at 50 ºC. The reaction

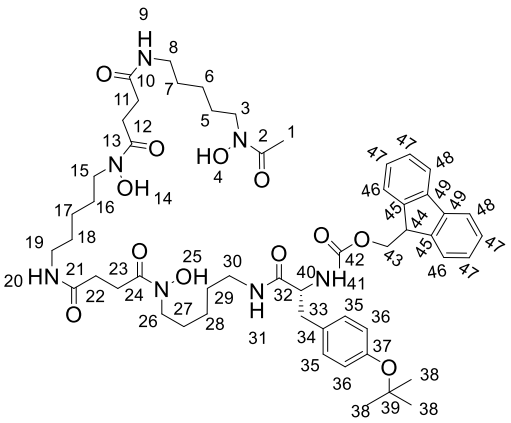

mixture was evaporated to dryness and purified over combi flash (method B, product elutes at 70% B) to afford E1 (73.9 mg, 0.07 mmol, 48% yield). LC-MS: calculated mass for **E1** ($C_{53}H_{75}N_7O_{12}$), 1001.55; found 1002.48 $[M+H]^+$, 501.98 $[M+2H]^{2+}$. ^{1}H NMR (DMSO-d6, 500 MHz, ppm): δ 1.74 – 2.04 (m, 31H, H-1,H-5,H-6,H-7,H-16,H-17,H-18,H-27, H-28,H-29,H-38), 2.79-2.82 (m, 4H, H-11,H-22), 3.11-3.13 (m, 4H, H-8,H-19), 3.52-3.54 (m, 6H, H-3,H-15,H-26), 3.97- 4.00 (m, 6H, H-8,H-19,H-30), 4.63- 4.70 (m, 6H, H-33,H-40,H-44,H-44), 7.32- 7.34 (d, 2H, H-36), 7.69 -7.71 (d, 2H, H-35), 7.81- 9.95 (d, 4H, H-42,H-47), 8.19 – 8.21 (d, 2H, H-45), 8.31 (s, 2H, H-9,H-20), 8.39-8.41 (d, 2H, H-48), 8.46-8.48 (s, 1H, H-31), 10.17 (s, 3H, H-4,H-14,H-25). ^{13}C NMR (DMSO-d6, 500 MHz, ppm): δ 20.36 (1C,C1), 23.49 – 29.96 (6C, C-5,C-6,C-16,C-17,C-27,C-28), 37.30 – 38.49 (3C,C-8, C-19,C-30,C-33), 46.62- 47.13 (4C,C-3,C-15,C-26,C-43), 56.36 (1C,C-32), 65.70 (1C,C-42), 77.56 (1C,C-32), 123.33 (1C,C-47), 127.06 (1C,C-36), 127.66 (1C,C-35), 132.75 (1C,C-34), 140.71 - 140.73 (1C,C-48), 143.81 (1C,C-44), 153.40 (1C,C-37), 170.21 (1C,C-2), 171.39 (1C,C-2), 172.03 (2C, C-21,C-24). Retention time (method A): 9.23 min.

(R)-N1-(5-(2-amino-3-(4-(tert-butoxy)phenyl)propanamido)pentyl)-N1-hydroxy-N4-(5-(N-hydroxy-4-((5-(N-hydroxyacetamido)pentyl)amino)-4-oxobutanamido)pentyl) succinamide, E2. Deprotection of the Fmoc group was performed by adding diethylamine (DEA) (108.6 µl,1.05 mmol, 15 equiv) to a solution of E1 (73.9 mg, 0.07 mmol) in DMF at room temperature for 2 h. The solution was evaporated to dryness and purified over CombiFlash chromatography (method B, product elutes at 50% B) to afford an oily liquid (43.1 mg, 0.06 mmol, 79% yield). LC-MS: calculated mass for **E2** $C_{38}H_{65}N_7O_{10}$, 779.48;

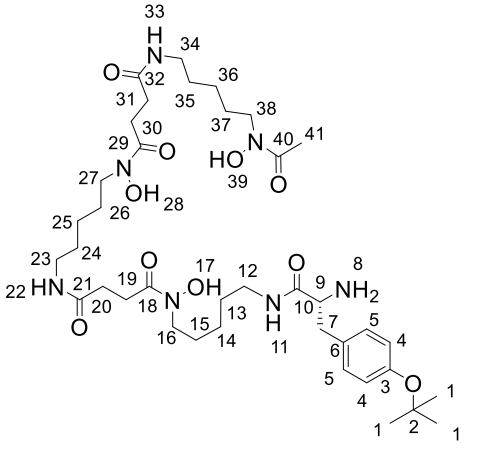

found 780.4 $[M+H]^+$, 390.8 $[M+2H]^{2+}$.^{1}H NMR (DMSO-d6, 500 MHz, ppm): 1.13-1.53 (m, 27H,H-1, H-13, H-14, H-15, H-24, H-25, H-26, H-35, H-36, H-37), 1.93 (s, 3H, H-41), 2.25-2.28 (m, 4H, H-20,H-31), 2.56-2.58 (m, 4H, H-19, H-30), 2.92-3.01 (m, 6H, H-12, H-23, H-34), 3.44-3.46 (m, 6H, H-12, H-23, H-34), 3.85-3.86 (m, 2H,H-7, H-9), 6.91- 6.92 (d, 2H, H-4), 7.09- 7.12 (d, 2H, H-5), 7.76-7.79 (m, 2H, H-8), 8.16-8.17 (d, 3H, H-11,H-22,H-33), 9.63 (broad singled, 3H, H-17,H-28,H-29). ^{13}C NMR (DMSO-d6, 500 MHz, ppm): δ 29.36 (C-41), 23.38-29.9 (C-14, C-15, C-25, C-26, C-36, C-37, C-1, C-19, C-20, C-30, C-3), 36.49- 30.56 (C-7, C-12, C-23, C-24), 46.78- 47.07 (C-16, C-27, C-38), 53.69 (C-9), 77,94 (C-2), 115.09 (C-4), 123.65 (C-6), 129.99 (C-5), 154.19 (C-3), 170.59- 171.96 (C-17, C-18, C-10, C-21). Retention time (method A): 8.32min 6.46 min.

(R)-7-(4-(33-(4-(tert-butoxy)benzyl)-3,14,25-trihydroxy-2,10,13,21,24,32,35-hept aoxo-3,9,14,20,25,31,34-heptaazaoctatriacontan-38-oyl)piperazin-1-yl)-1-cyclo propyl-6-fluoro-4-oxo-1,4-dihydroquinoline-3-carboxylic acid, E3. DIPEA (15.47 mg, 0.12 mmol, 3 3 equiv) was added to a stirring solution of C1 (25.8 mg,0.06 mmol, 1.4 3 equiv) in dry DMF. The reaction mixture was stirred for 10 min at room temperature. HBTU (18.19mg, 0.05 mmol, 1.2 equiv) in dry DMF was added to the reaction mixture and stirred for another 10 min. A solution of E2 (40 mg, 0.04 mmol) in DMF was added to the solution and stirred overnight at 45 ºC. The crude was evaporated to dryness and purified over the preparative HPLC (method C, product elutes at 55% B) affording E3 (10.30 mg, 0.008 mmol, 21.6% yield). LC-MS: calculated

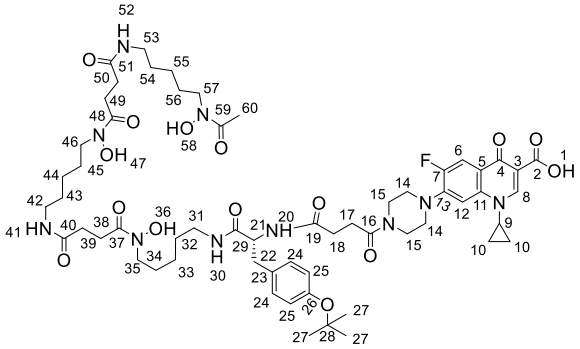

mass for **E3** ($C_{59}H_{85}FN_{10}O_{15}$): 1192.63. Found 1193.60 $[M+H]^+$, 597.4 $[M+2H]^{2+}$. ^1H NMR (DMSO-d6, 500 MHz, ppm): δ 1.18-1.48 (m, 27H, H-10, H-32, H-32, H-33, H-43, H-43, H-45, H-54, H-54, H-55, H-56). 1.96 (s, 3H, H-60), 2.25-2.57 (m, 10H, H-38,H-49,H-17,H-39,H-50,H-16,H-22), 2.97-2.99 (m, 6H, H-38, H-49,H-50), 3.29-3.46 (m,22H, H-14,H-15,H-22,H-31,H-35,H-43,H-46,H-53,H-57), 3.66 (s, 1H, H-9), 4.34-4.38 (m,1H, H-21), 6.84-6.85 (d, 2H, H-25), 7.11-7.13 (d, 2H, H-24), 7.82-7.84 (m, 2H, H-43,H-53), 8.15-8.17 (d, 3H, H-6,H-20,H-30),8.67(s, 1H, H-8), 9.60- 9.65 (broad singled, 3H, H-36,H-47,H-58). ^{13}C NMR (DMSO-d6, 500 MHz, ppm): δ 7.60 (C-10), 20.35 (C-60), 26.02- 30.36 (C-32, C-33, C-44, C-45, C-55, C-56, C-27, C-17, C-16, C-38, C-39, C49, C-50), 35.89 – 38.52 (C-9, C-22, C-32, C-42, C-53), 46.77- 54.26 (C-15, C-14, C-21, C-35, C-46, C-57), 77.57 (C-28), 106.77- 111.13 (C-3, C-6, C-12, C-25), 123.33 (C-5), 129.55 (C-24, C-23), 132.86 (C-7), 139.15 (C-11). ^{19}F NMR (DMSO-d_6, 400 MHz): δ -123.99 – -123.93. Retention time (method A): 8.07 min.

(R)-1-cyclopropyl-6-fluoro-4-oxo-7-(4-(3,14,25-trihydroxy-33-(4-hydroxybenzyl)-2,10,13,21,24,32,35-heptaoxo-3,9,14,20,25,31,34-heptaazaoctatriacontan-38-oyl) piperazin-1-yl)-1,4-dihydroquinoline-3-carboxylic acid, D7. E3

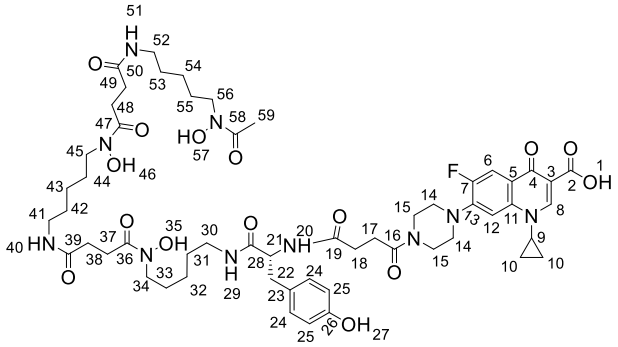

(10.3 mg, 0.01 mmol) was treated with a solution of 50% trifluoroacetic acid (TFA) in dichloromethane (DCM) for 2h at room temperature. The reaction mixture was evaporated to dryness. The crude was purified over preparative HPLC (method C, product elutes at 50% B) affording a white powder (7.6 mg, 0.007 mmol, 77.5 % yield).

LC-MS: calculated mass for **D7** ($C_{55}H_{77}FN_{10}O_{15}$): 1136.56. Found 1137.50 $[M+H]^{+,}$ 569.40 $[M+2H]^{2+}$.^{1}H NMR (DMSO-d6, 500 MHz, ppm): δ 1.19-1.49 (m, 20H, H-10, H-31, H-32, H-, H-33, H-42, H-43,H-44,H-53,H-54,H-55), 1.96 (s, 3H,H-59), 2.21- 2.61 (m, 12H, H-17, H-18, H-36, H-37, H-48, H-49), 2.56 - 3.44 (m, 22H,H-14,H-15,H-22,H-30,H-34,H-41,H-44,H-52,H-56), 3.69 (s,1H,H-9), 4.63 (m,1H, H-21), 6.62-6.63 (m, 2H,H-24),6.99-7.01(d,2H,H-24), 7.76- 7.78 (d, 4H, H-51, H-40), 7.92-7.94 (d, 4H, H-6,H-29),8.10-8.11(d,1H,H-20), 8.67 (s, 1H, H-8), 9.16 (s, 1H, H-27), 9.60-9.65 (broad singled, 3H, H-35,H-46, H-57), 15.12 (broad singled, 3H, H-35, H-46, H57). ^{13}C NMR (DMSO-d6, 500 MHz, ppm): δ 8.07 (C-10), 20.82 (C-59), 23.82 – 29.38 (C-31, C-32, C-43, C-44, C-54, C-55, C-31, C-42, C-55), 36.37- 50.05 (C-18, C-17, C-37, C-38, C-48, C-49, C-9, C-22, C-30, C-41, C-52, C-14), 107.12 -119.34 (C-6, C-12, C-25, C-5, C-23), 130.46 (C-24), 139.64 (C-13), 145.37-145.46 (C-13), 148.58 (C-11), 154.43 (C-7), 158.23-158.49 (C-26), 166.39 (C-2), 170.21- 176.87 (C-16, C-20, C-28, C-39, C58). ^{19}F NMR (DMSO-d_6, 400 MHz): δ – 124.49 – 124.44. Retention time (method D): 8.24 min

(R)-1-cyclopropyl-6-fluoro-4-oxo-7-(4-(3,14,25-trihydroxy-33-(4-hydroxy-3-iodobenzyl)-2,10,13,21,24,32,35-heptaoxo-3,9,14,20,25,31,34-heptaazaoctatria contan-38-oyl)piperazin-1-yl)-1,4-dihydro- quinoline-3-carboxylic acid, D7-I. NaI (H_2O/ MeCN 1:1, 8mM, 10 equiv) was added to a solution of D7 (H2O/ MeCN,1:1,10 mg, 0.0088 mmol) followed by the addition of selectfluor (H_2O/MeCN 1:1, 8 mM, 10 equiv). The reaction was stirred at room temperature for 1.5 hours. The crude was purified over preparative HPLC (method C, product eluted at 55% B) to afford a

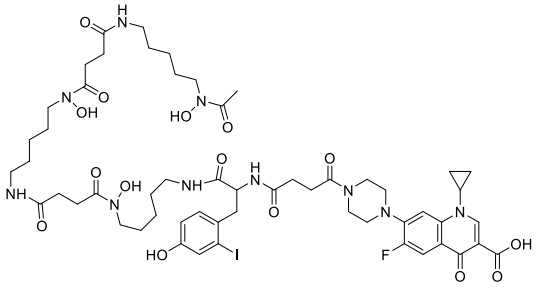

mixt of mono-iodinated D7 (MI) (1.5 mg, 15% yield) and di-iodinated D7 (DI). LC-MS: calculated mass for **D7-I** ($C_{55}H_{76}FIN_{10}O_{15}$) 1263.45; found: D7-MI 1263.36 $[M+H]^+$. Retention time(method D):8.54 min.

2.5.11.7 Ga-D7-I complex formation.

Ga-D7-I. Ga $(NO_2)_3$ (5.1 mg,0.018 mmol, 3 eq.) was added to a solution of **D7**-I (2mg, 0.0016 mmol, 1 eq.) in DMF. The pH of the solution was adjusted to pH 6 (NaOH, 1M). The reaction mixture was stirred at 60 ºC for 1 hour and overnight at room temperature. The crude was evaporated to dryness and purified over preparative HPLC (method D, product elutes at 50% B), affording Ga-**D7**-I (0.0011 mmol, 1.52 mg, 76% yield). LC-MS: calculated for $C_{55}H_{73}FGaIN_{10}O_{15}$: 1328.35; found: Ga-**D7**-I 1329.3 $[M+H]^+$. Retention time (method D): 8.53 min.

2.5.11.8 HPLC tracer for D7

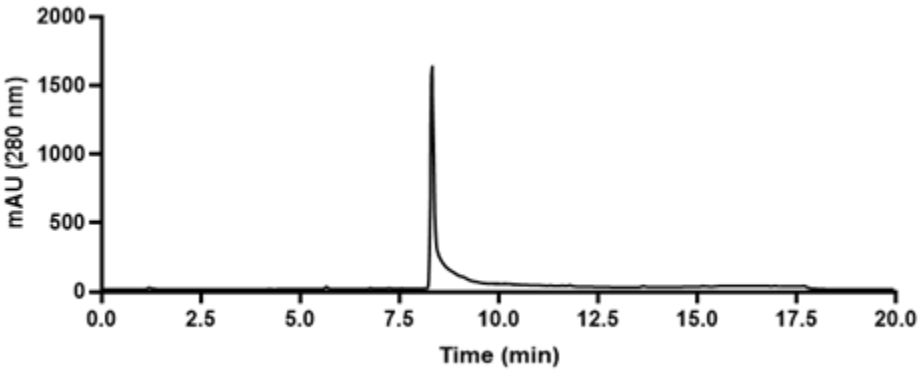

Figure 2. 30: HPLC chromatogram of compound **C1**. Retention time (Method D): 8.32 min.

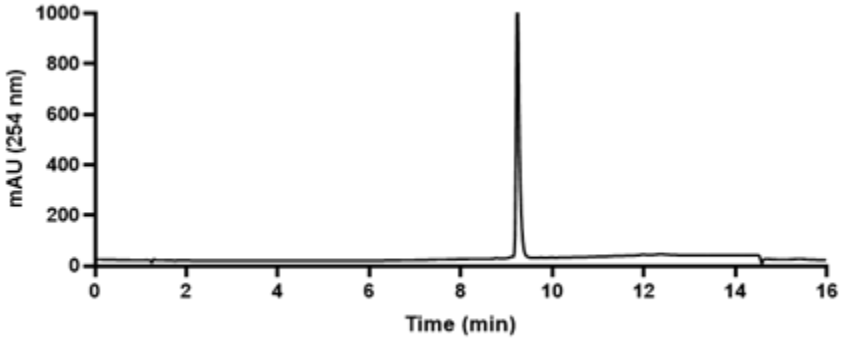

Figure 2. 31: HPLC chromatogram of compound **E1**. Retention time (Method A): 9.23 min.

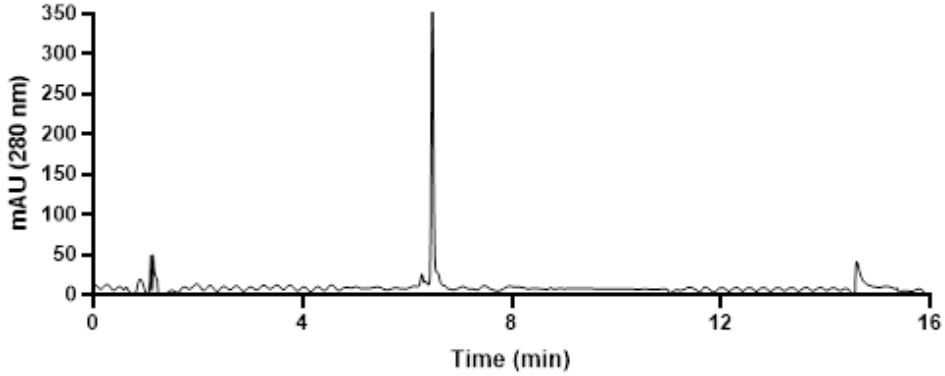

Figure 2. 32: HPLC chromatogram of compound **E2**. Retention time (Method A): 6.46 min.

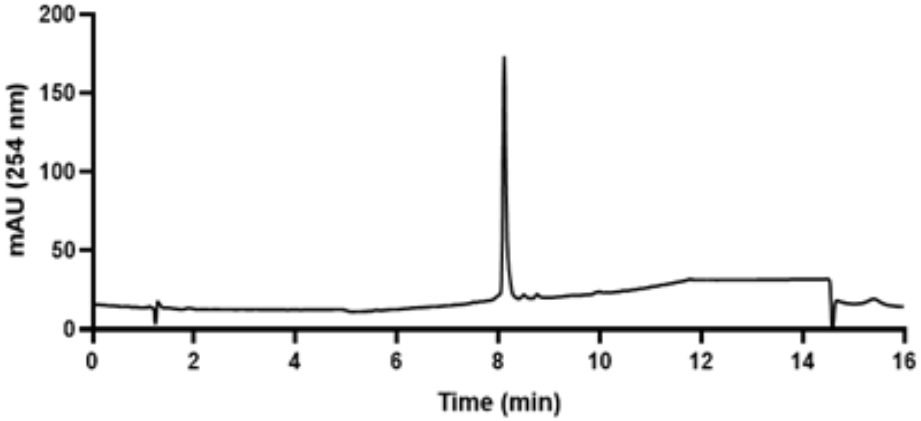

Figure 2. 33: HPLC chromatogram of compound **E3**. Retention time (Method A): 8.07 min.

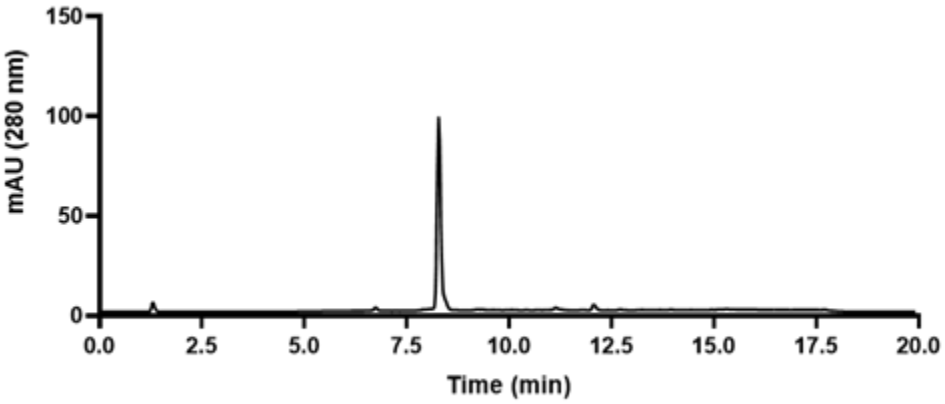

Figure 2. 34: HPLC chromatogram of compound **D7**. Retention time (Method D): 8.24 min.

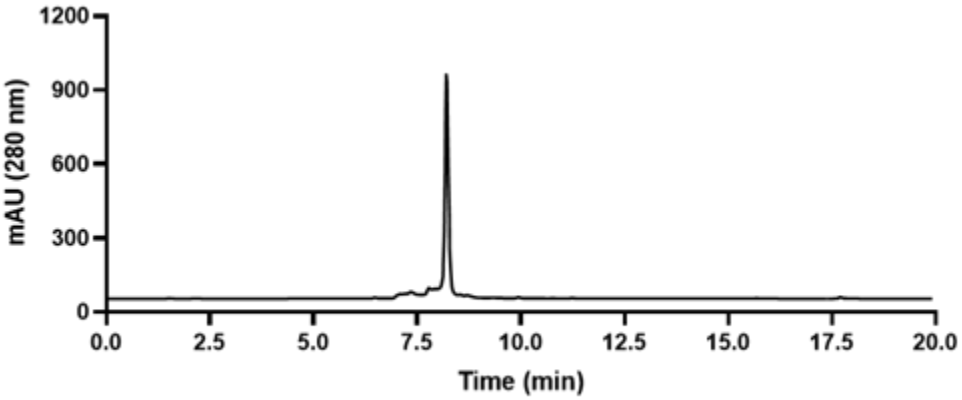

Figure 2. 35: HPLC chromatogram of compound **Ga-D7**. Retention time (Method D): 8.19 min.

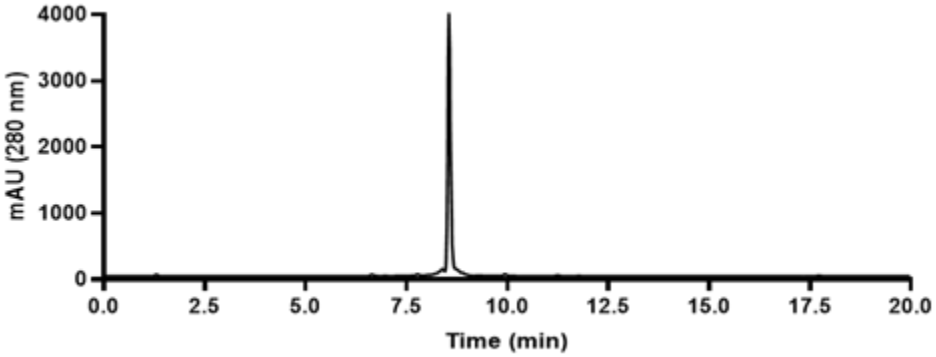

Figure 2. 36: HPLC chromatogram of compound Ga-D7-I. Retention time (Method D): 8.53min

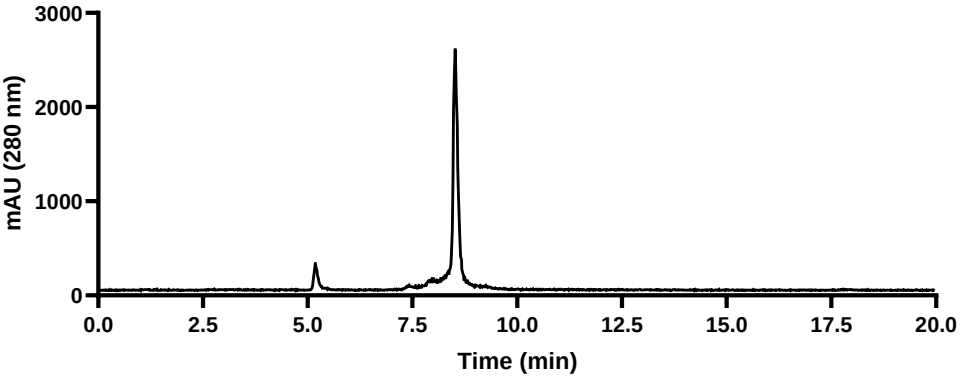

Figure 2. 37: HPLC chromatogram of compound Ga-**D7**-I. Retention time (Method D): 8.53min

2.5.11.9 NMR data for D7

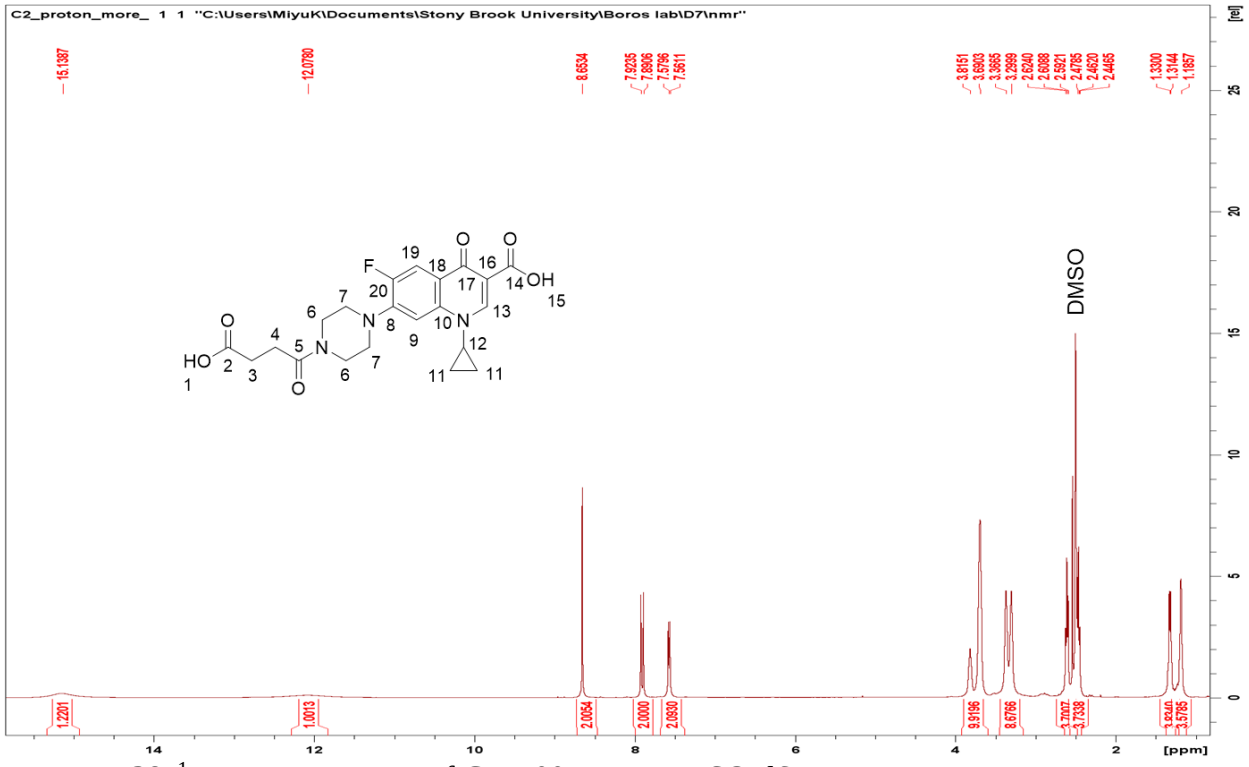

Figure 2. 38: ^{1}H-NMR spectrum of **C1**. 500 MHz, DMSO-d6.

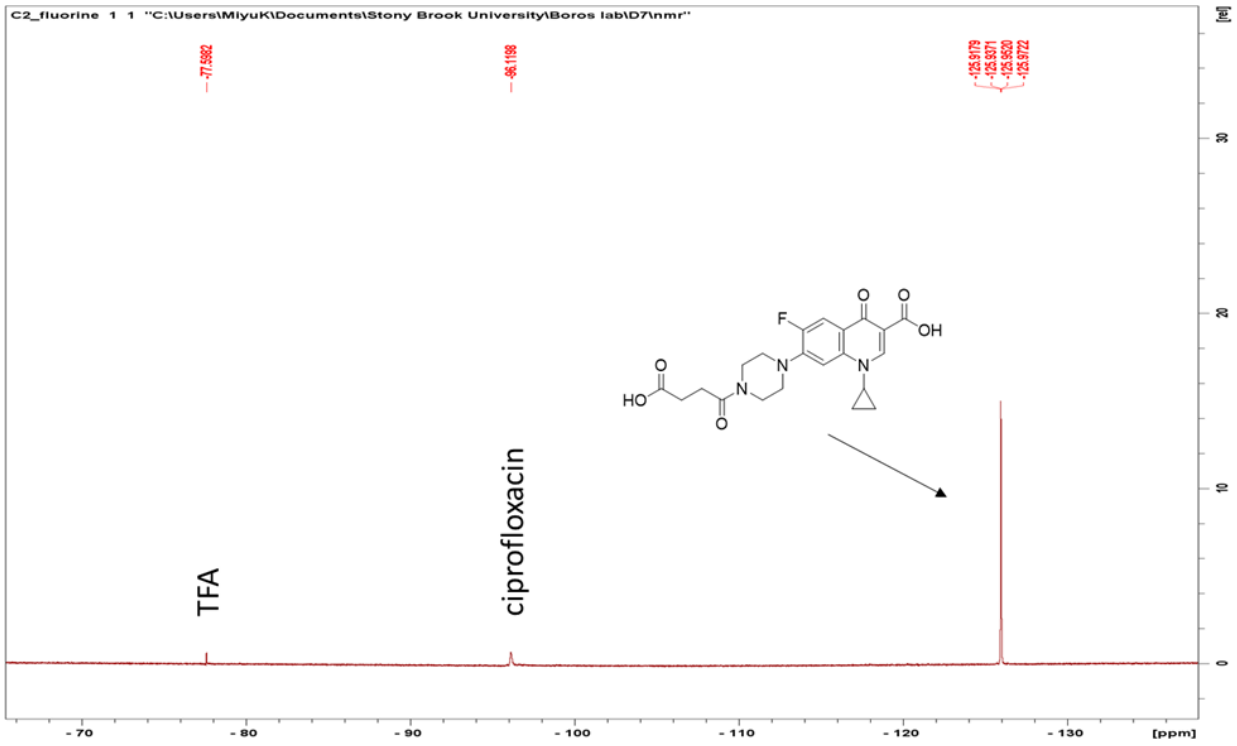

Figure 2. 39: ^{19}F-NMR spectrum of **C1**. 376 MHz, DMSO-d6.

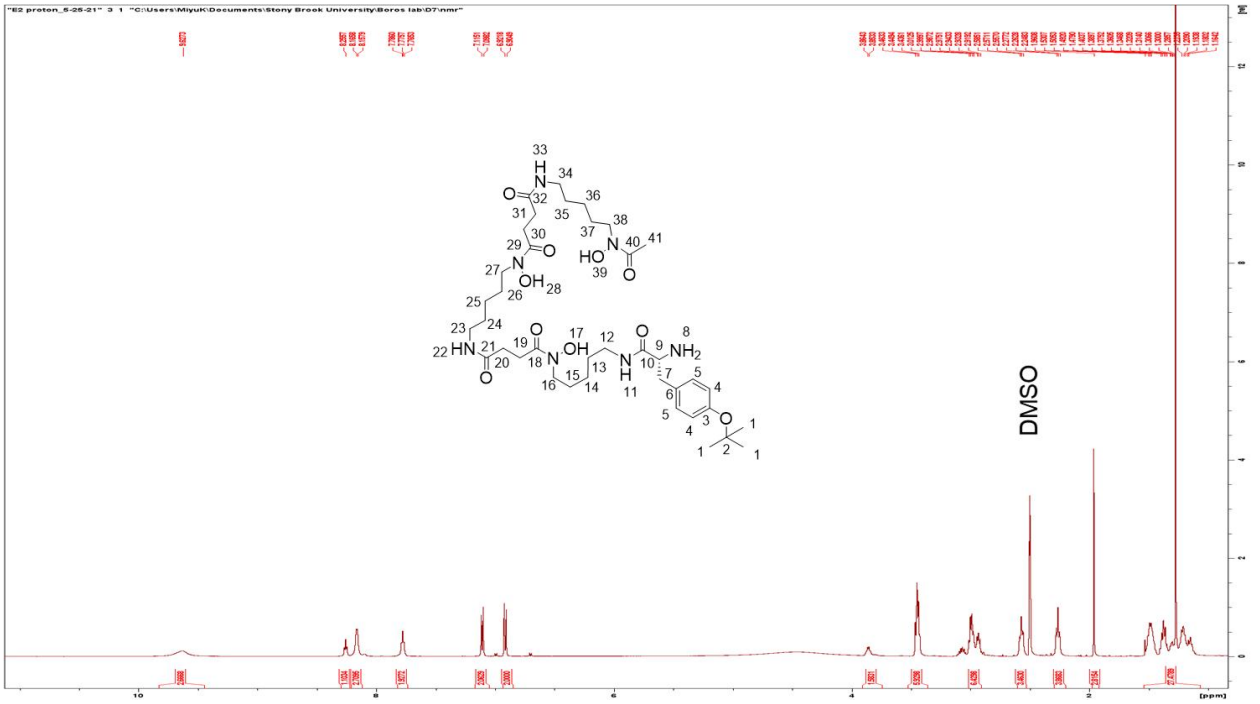

Figure 2. 40: ^{1}H-NMR spectrum of **E2**. 500 MHz, DMSO-d6.

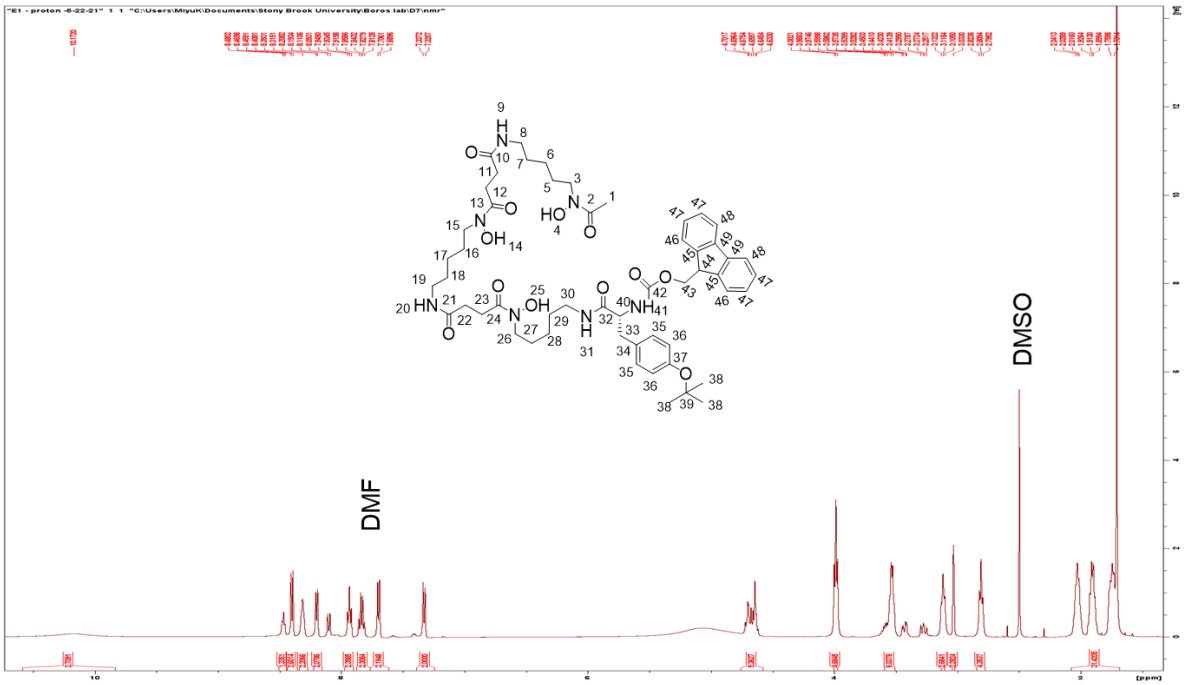

Figure 2. 41: ^{1}H-NMR spectrum of **E2**. 500 MHz, DMSO-d6.

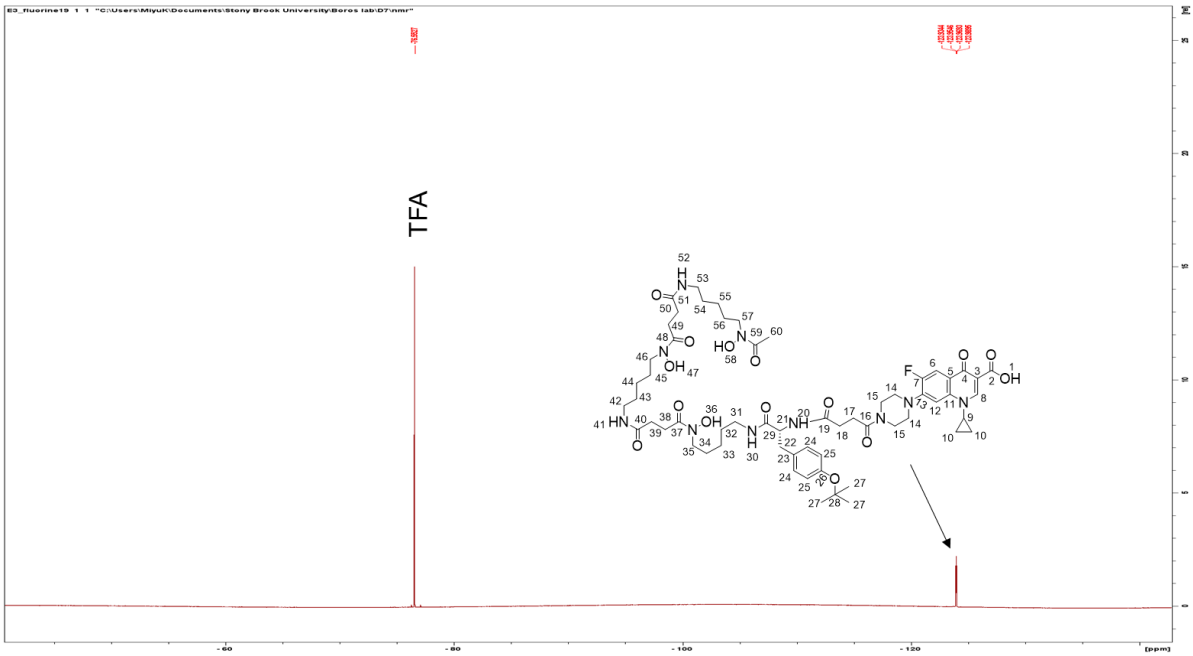

Figure 2. 42: ^{19}F-NMR spectrum of **E3**. 376 MHz, DMSO-d6.

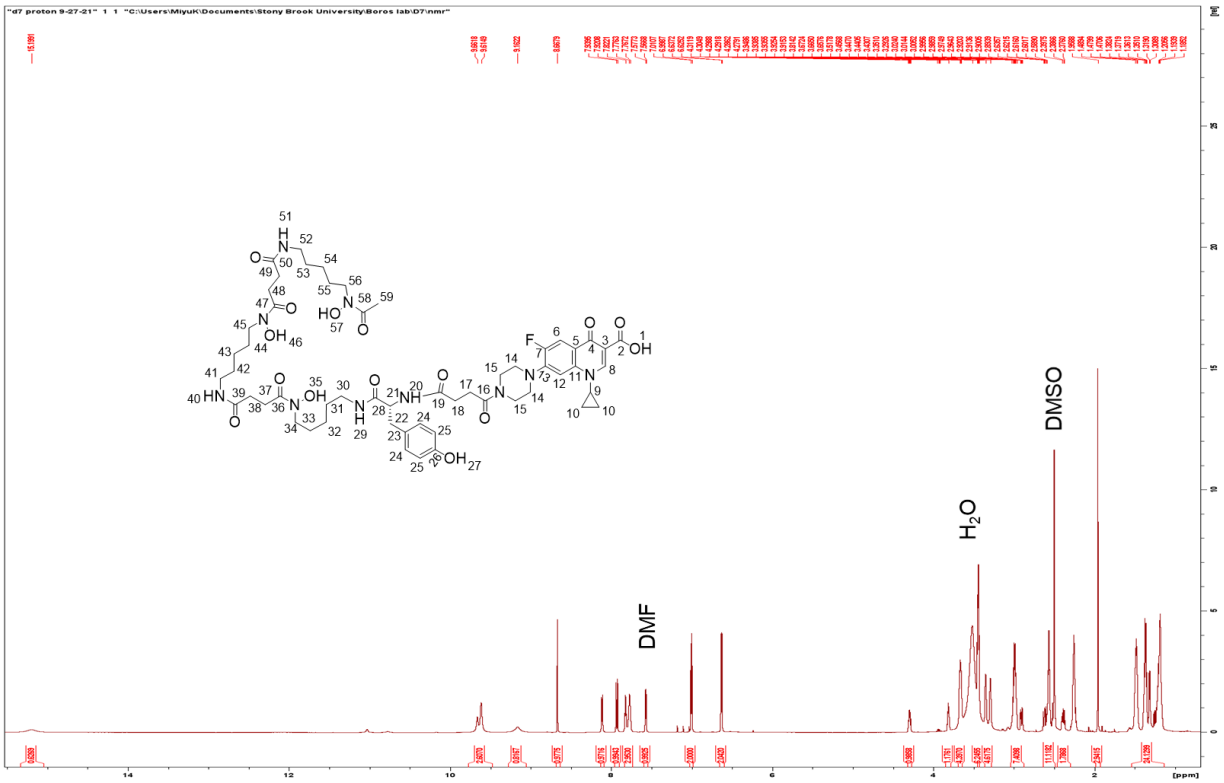

Figure 2. 43: ^{1}H-NMR spectrum of **D7**. 700 MHz, DMSO-d6.

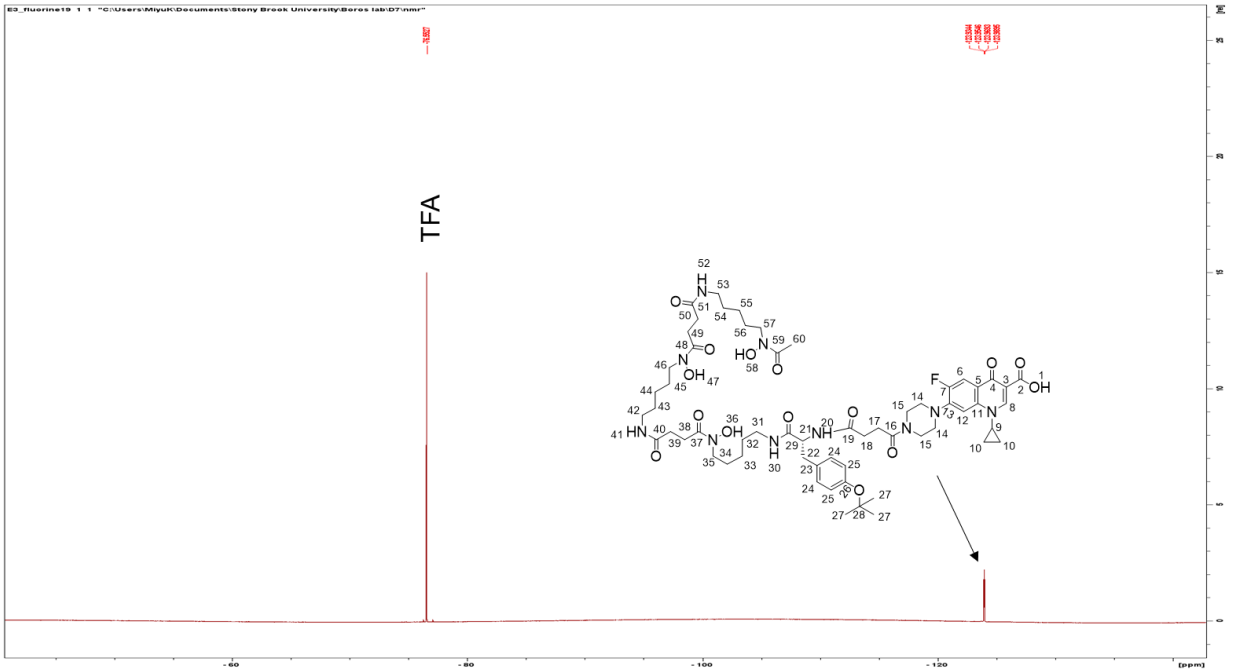

Figure 2. 44: ^{19}F-NMR spectrum of **D7**. 376 MHz, DMSO-d6.

2.5.11.10 HRMS and MALDI characterization data for D7

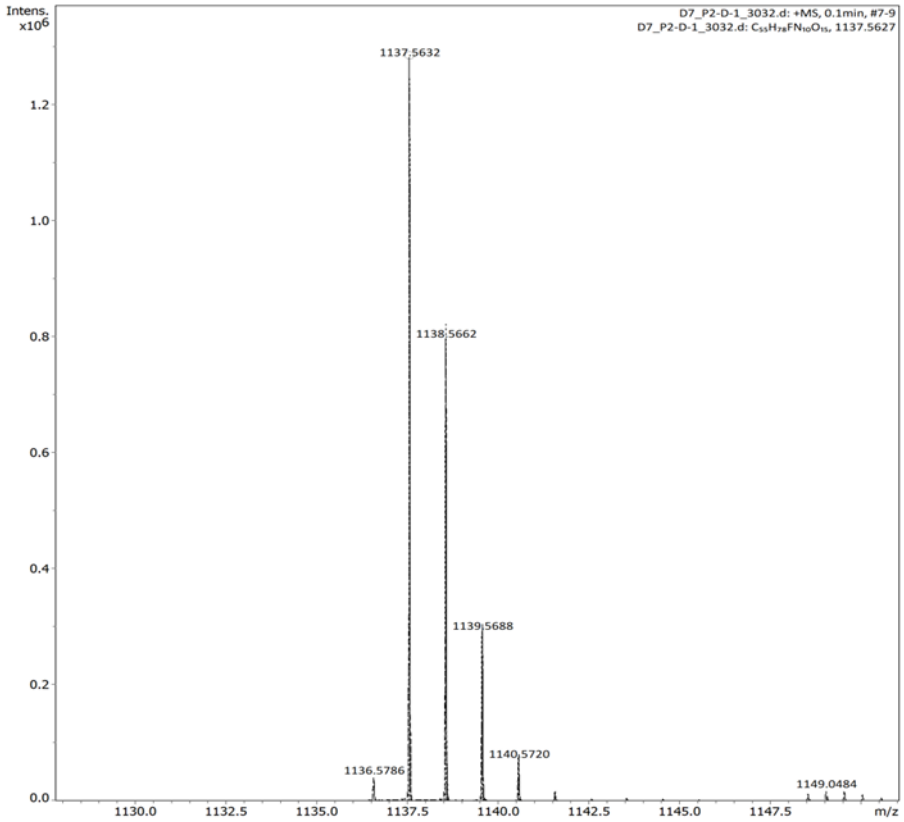

Figure 2. 45: High resolution mass spectrum of **D7**. HRMS calculated for $C_{55}H_{77}FN_{10}O_{15}$: 1136.5554; found 1137.5632 $[M+H]^+$.

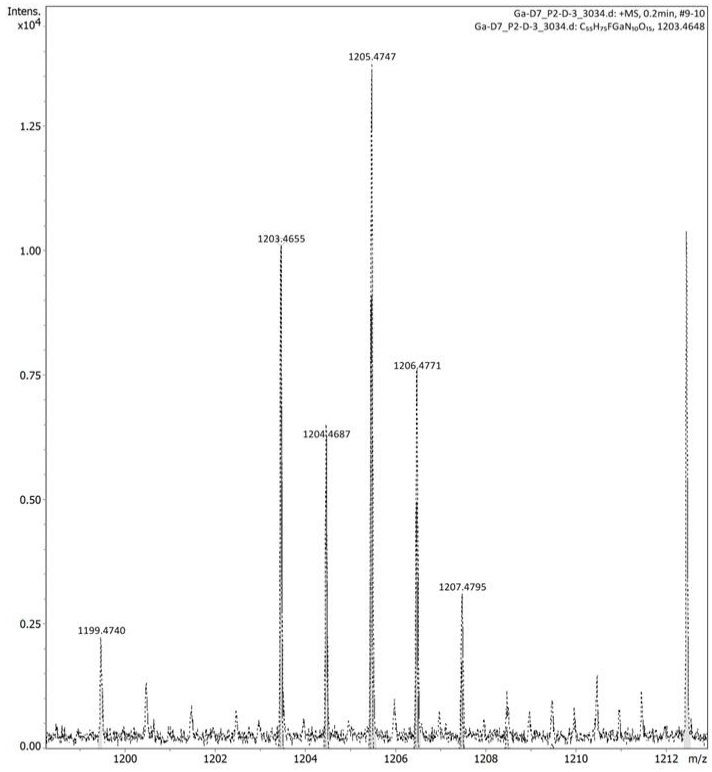

Figure 2.46: High resolution mass spectrum of **Ga-D7**. HRMS calculated for $C_{55}H_{73}FGaN_{10}O_{15}$: 1202.4575; found 1203.4655 $[M+H]^+$.

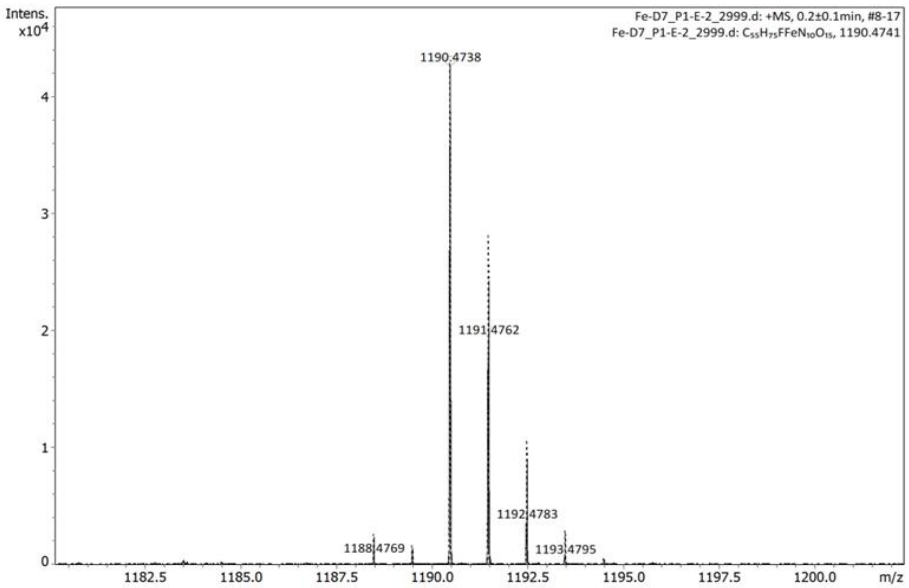

Figure 2. 47: High resolution mass spectrum of **Fe-D7**. HRMS calculated for $C_{55}H_{74}FFeN_{10}O_{15}$: 1189.4669; found 1190.4738 $[M+H]^+$.

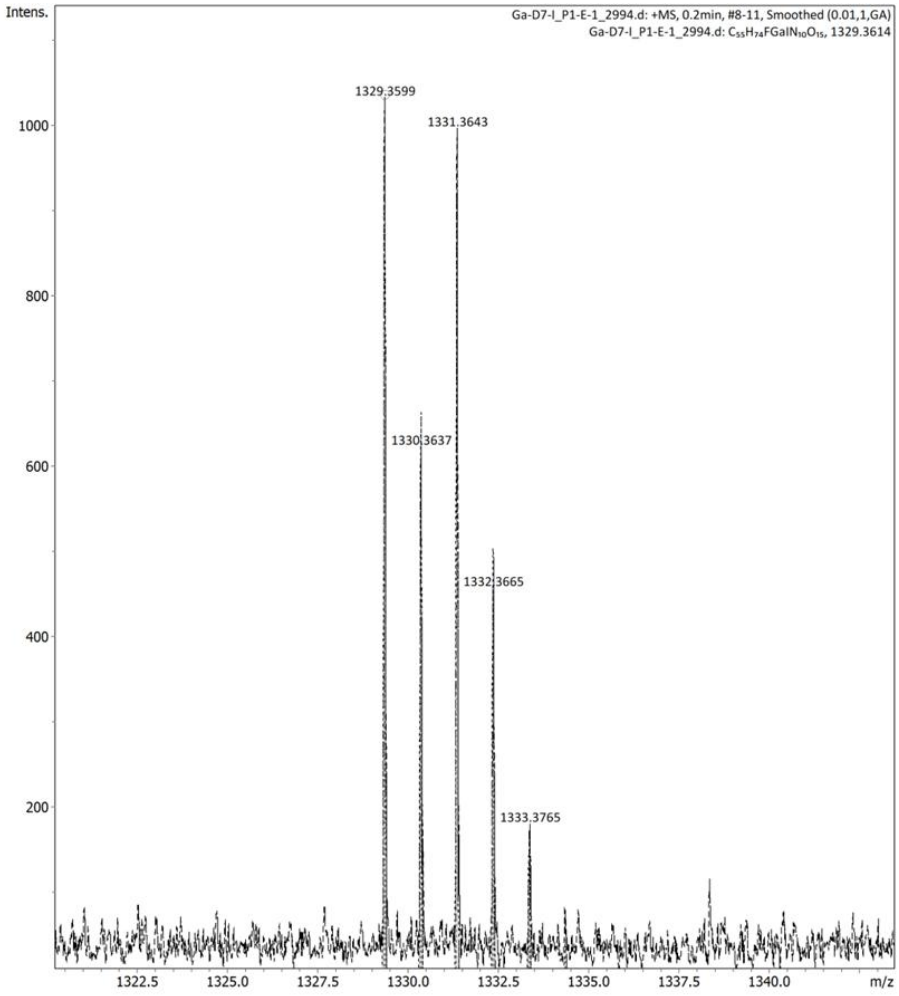

Figure 2. 48: High resolution mass spectrum of **Ga-D7-I**. HRMS calculated for $C_{55}H_{73}FGaI_1N_{10}O_{15}$: 1328.3541; found 1329.3599 [M+H] +.

2.5.12 Antibacterial Assessment Assays (MIC assays)

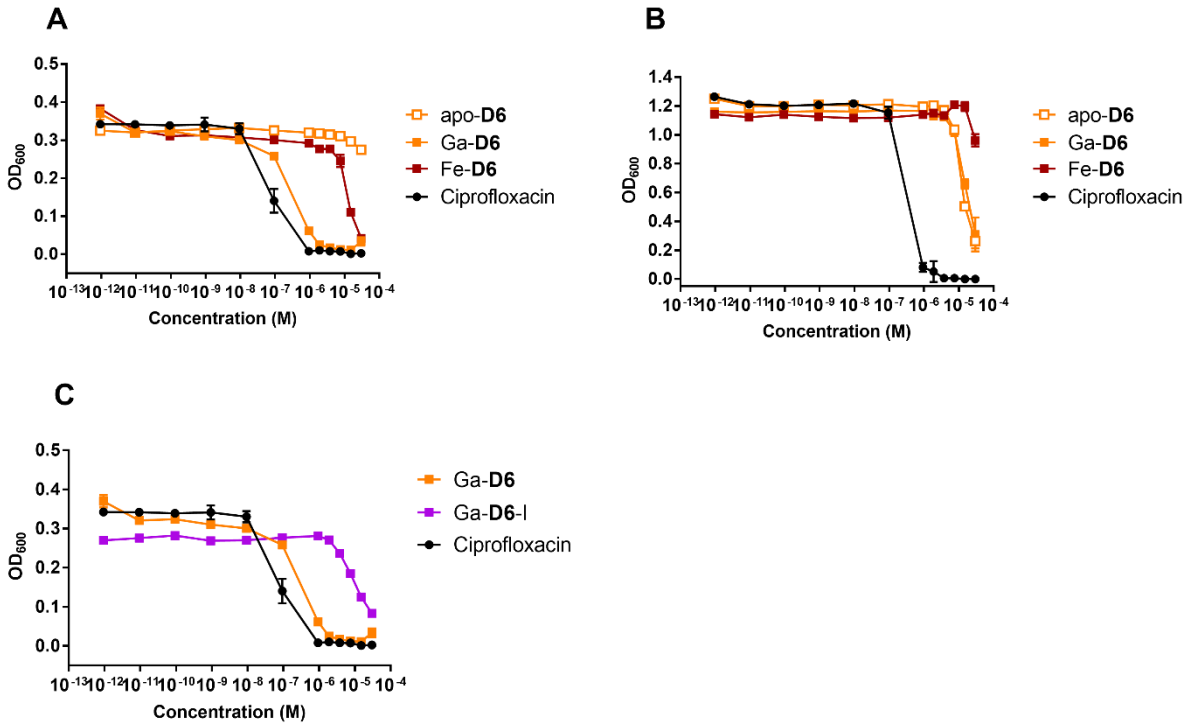

Figure 2. 49: **(A)** MIC assay of **D6** and its complexes in *E. coli* (n =3x3). **(B)** MIC assay of **D6** and its complexes in P. aeruginosa (n =3x3). **(C)** MIC assay of Ga-**D6**-I in *E. coli* (n =3x3)

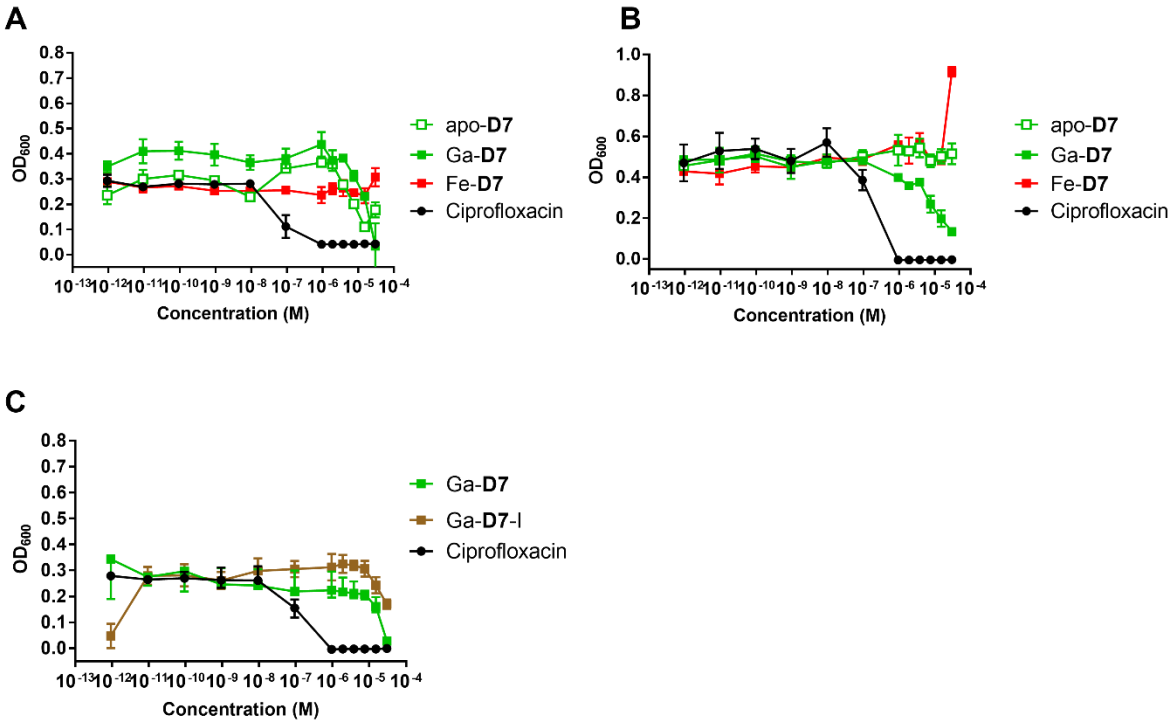

Figure 2. 50: **(A)** MIC assay of **D7** and its complexes in *E. coli* (n =3x3). **(B)** MIC assay of **D7** and its complexes in *P. aeruginosa* (n =3x3). **(C)** MIC assay of Ga-**D7**-I in *E. coli* (n =3x3).

2.5.13 Radiolabeling

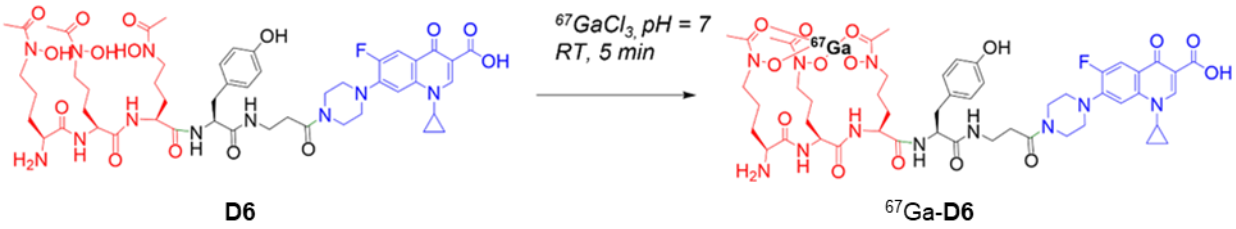

Scheme 2. 2: Schematic description of the radiochemical complexation of *apo*-**D6** with ^{67}Ga. ^{67}Ga-complexation proceeds in 5 min, 25 ∘C, pH 7.

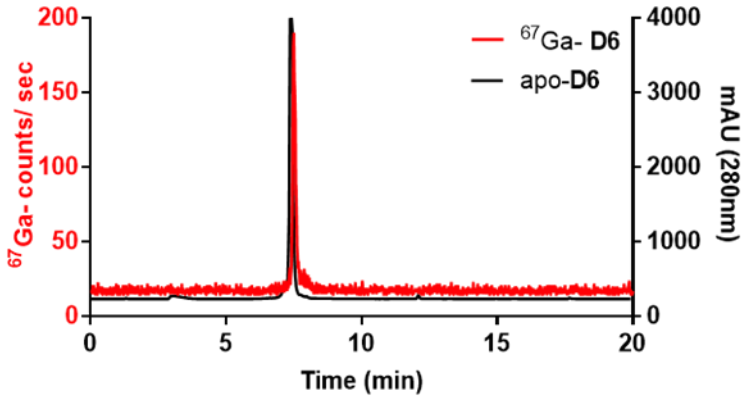

Figure 2. 51: A representative radiolabeling HPLC trace for the characterization of ^{67}Ga-**D6** (t_R = 7.50 min, left axis, ^{67}Ga counts per second), in comparison with HPLC characterization of the *apo*-**D6** ligand (t_R= 7.37 min, right axis, absorbance at 280 nm) is shown. Free ^{67}Ga elutes at 0.7 minutes.

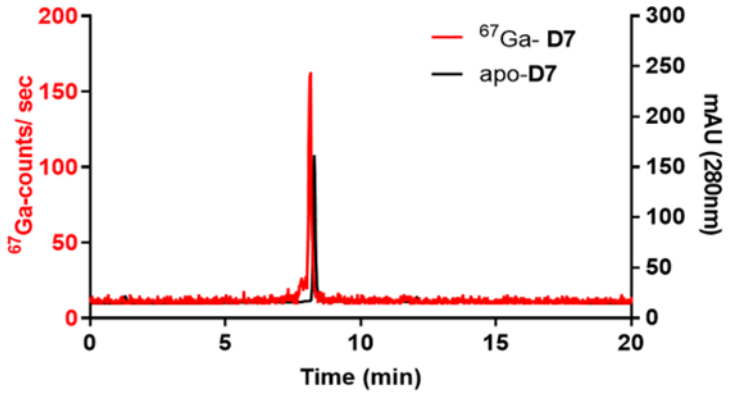

Figure 2. 52: A representative radiolabeling HPLC trace for the characterization of ^{67}Ga-**D7** (t_R = 8.12 min, left axis, ^{67}Ga counts per second) in comparison with HPLC characterization of the *apo*-**D7** ligand (t_R= 8.26 min, right axis, absorbance at 280 nm). Free ^{67}Ga elutes at 0.7 minutes.

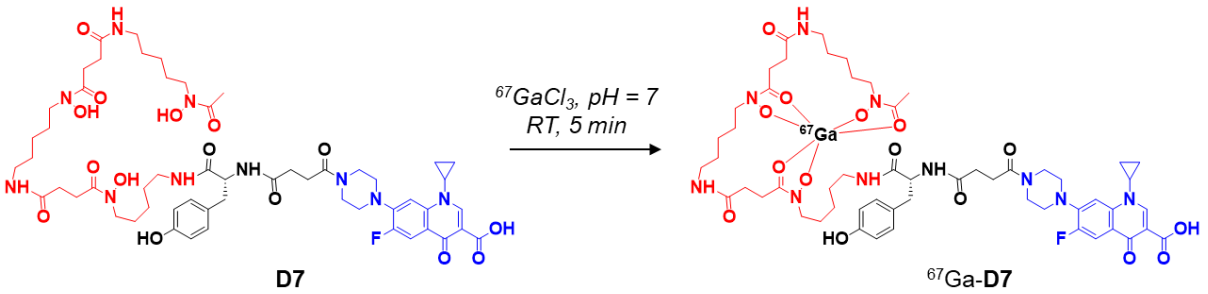

Scheme 2. 3: Schematic description of the radiochemical complexation of *apo*-**D7** with ^{67}Ga. ^{67}Ga-complexation proceeds in 5 min, 25 ∘C, pH 7.

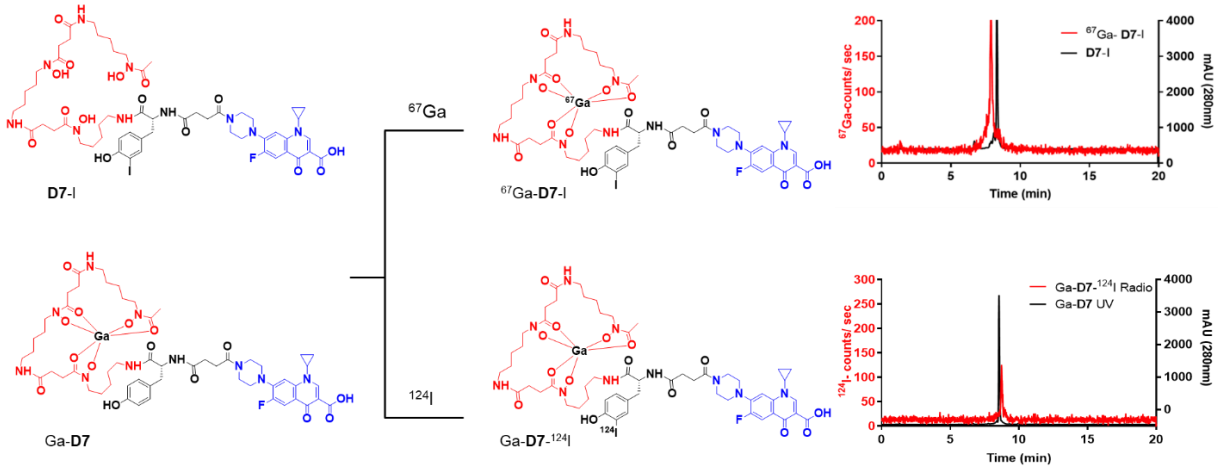

Figure 2. 53: **(Top)** Schematic description of the radiochemical complexation of **D7**-I radiolabeling with ^{67}Ga to form the Ga-**D7**-I complex. A representative radiolabeling HPLC trace for the characterization of ^{67}Ga-**D7**-I ((t_R = 8.29 min) in comparison with HPLC characterization of **D7**-I ligand (t_R= 8.54 min, right axis). **(Bottom)** Ga-**D7** radiolabeling with ^{124}I to afford Ga-**D7**-^{124}I. A representative radiolabeling HPLC trace for the characterization of Ga-**D7**-^{124}I ((t_R = 8.29 min) in comparison with HPLC characterization of **D7**-I ligand (t_R= 8.54 min, right axis).

2.5.14 Radiochemical uptake experiments in *wt* bacterial strains

The uptake was expressed as the % radioactivity found in the pellet:

$$\%\ uptake = \frac{cpm\ (pellet)}{cpm\ (1\ mL\ baterial\ inoculum)}$$

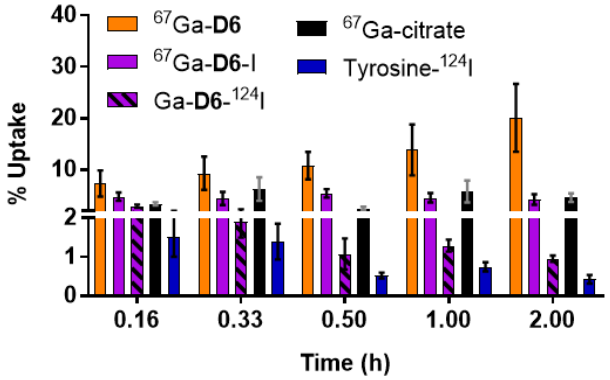

Figure 2. 54: Time-dependent, radiochemical bacterial uptake studies in *E. coli* K-12 of ^{67}Ga-**D6**, ^{67}Ga-**D6**-I and Ga-**D6**-^{124}I in iron-depleted, DP-treated media, pH = 7.4 with controls ^{67}Ga-citrate and Tyrosine-^{124}I.

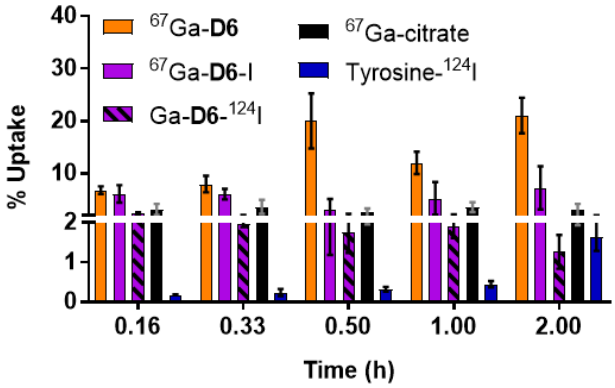

Figure 2. 55: Time-dependent, radiochemical bacterial uptake studies in *P. aeruginosa* PA01 of ^{67}Ga-**D6**, ^{67}Ga-**D6**-I and Ga-**D6**-^{124}I in iron-depleted, DP-treated media, pH = 7.4 with controls ^{67}Ga-citrate and Tyrosine-^{124}I.

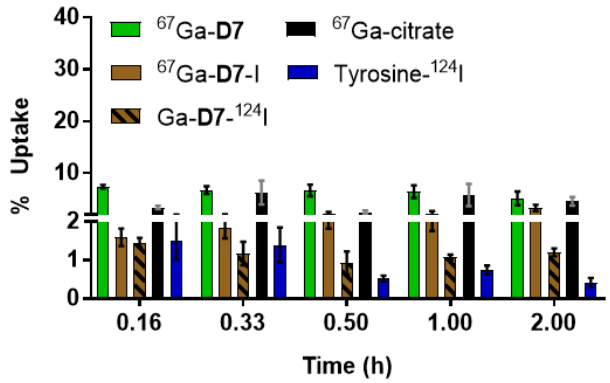

Figure 2. 56: Time-dependent, radiochemical bacterial uptake studies in *E. coli* K-12 of ^{67}Ga-**D7**, ^{67}Ga-**D7**-I and Ga-**D7**-^{124}I in iron-depleted, DP-treated media, pH = 7.4 with controls ^{67}Ga-citrate and Tyrosine-^{124}I.

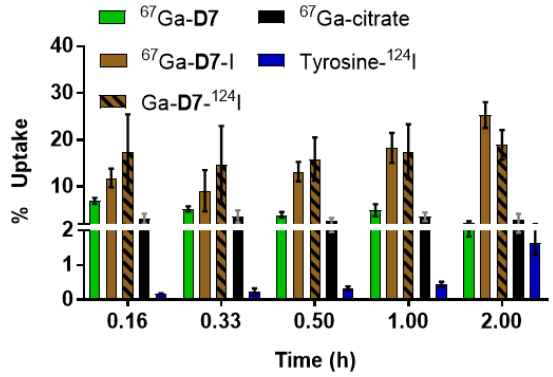

Figure 2. 57: Time-dependent, radiochemical bacterial uptake studies in *P. aeruginosa* PA01 of ^{67}Ga-**D7**, ^{67}Ga-**D7**-I and Ga-**D7**-^{124}I in iron-depleted, DP-treated media, pH = 7.4 with controls ^{67}Ga-citrate and Tyrosine-^{124}I.

Table 2. 2: Percentage of internalized ^{67}Ga-**D6**,^{67}Ga-**D6**-I, and Ga-**D6**-^{124}I in *E. coli* K-12 upon incubation in iron deficient bacterial culture (n=5).

Incubation Time (h)	^{67}Ga-**D6** (%)	^{67}Ga-**D6**-I (%)	Ga-**D6**-^{124}I (%)	^{67}Ga-citrate (%)	Tyrosine-^{124}I (%)
0.16	7.4±2.5	4.8±0.8	2.9±0.3	3.4±0.3	1.5±0.5
0.33	9.3±3.2	4.4±1.3	1.9±0.4	6.3±2.3	1.4±0.5
0.5	10.8±2.7	5.4±0.8	1.1±0.4	2.5±0.3	0.5±0.1
1	13.9±5.0	4.6±0.9	1.3±0.2	5.8±2.1	0.7±0.1
2	20.1±6.6	4.2±1.0	1.0±0.1	4.6±0.8	0.4±0.1

Table 2. 3: Percentage of internalized ^{67}Ga-**D6**,^{67}Ga-**D6**-I, and Ga-**D6**-^{124}I in *P. aeruginosa* PA01 upon incubation in iron deficient bacterial culture (n=5).

Incubation Time (h)	^{67}Ga-**D6** (%)	^{67}Ga-**D6**-I (%)	Ga-**D6**-^{124}I (%)	^{67}Ga-citrate (%)	Tyrosine-^{124}I (%)
0.16	7.4±2.5	6.1±1.7	2.4±0.2	3.2±1.0	0.2±0.0
0.33	9.3±3.2	6.1±1.0	2.0±0.1	3.6±1.3	0.2±0.1
0.5	10.8±2.7	3.2±2.0	1.8±0.5	2.6±0.7	0.3±0.1
1	13.9±5.0	5.3±3.1	1.9±0.3	3.6±0.9	0.4±0.1
2	20.1±6.6	7.3±4.1	1.3±0.4	3.1±1.1	1.6±0.4

Table 2. 4: Percentage of internalized ^{67}Ga-**D6**,^{67}Ga-**D6**-I, and Ga-**D6**-^{124}I in *S. aureus* RN4220 upon incubation in iron deficient bacterial culture (n=5).

Incubation Time (h)	^{67}Ga-**D6** (%)	^{67}Ga-**D6**-I (%)	Ga-**D6**-^{124}I (%)	^{67}Ga-citrate (%)	Tyrosine-^{124}I (%)
0.16	7.4±2.5	6.7±3.9	4.1±0.5	6.0±1.8	0.2±0.0
0.33	9.3±3.2	4.2±1.3	4.1±0.5	6.5±0.5	0.2±0.0
0.5	10.8±2.7	7.8±3.0	5.6±1.3	9.4±1.5	0.2±0.0
1	13.9±5.0	9.6±2.6	10.4±1.9	18.4±2.1	0.2±0.0
2	20.1±6.6	13.7±2.4	12.5±0.9	21.9±5.6	0.3±0.0

Table 2. 5:Percentage of internalized 67Ga-D7,67Ga-D7-I, and Ga-D7-124I in E. coli K-12 upon incubation in iron deficient bacterial culture (n=5).

Incubation Time (h)	^{67}Ga-**D7** (%)	^{67}Ga-**D7**-I (%)	Ga-**D7**-^{124}I (%)	^{67}Ga-citrate (%)	Tyrosine-^{124}I (%)
0.16	7.41±0.34	1.60±0.20	0.89±0.16	3.4±0.3	1.5±0.5
0.33	6.76±0.71	1.83±0.24	0.59±0.08	6.3±2.3	1.4±0.5
0.5	6.71±1.11	2.18±0.32	0.34±0.17	2.5±0.3	0.5±0.1
1	6.45±1.21	2.24±0.43	0.42±0.03	5.8±2.1	0.7±0.1
2	5.14±1.33	3.32±0.55	0.42±0.03	4.6±0.8	0.4±0.1

Table 2. 6:Percentage of internalized 67Ga-D7,67Ga-D7-I, and Ga-D7-124I in P. aeruginosa PA01 upon incubation in iron deficient bacterial culture (n=5).

Incubation Time (h)	^{67}Ga-**D7** (%)	^{67}Ga-**D7**-I (%)	Ga-**D7**-^{124}I (%)	^{67}Ga-citrate (%)	Tyrosine-^{124}I (%)
0.16	6.98±0.63	9.6±1.45	10.61±1.92	3.2±1.0	0.2±0.0
0.33	5.24±0.57	7.38±3.18	11.51±3.14	3.6±1.3	0.2±0.1
0.5	3.98±0.61	10.69±1.51	11.06±2.43	2.6±0.7	0.3±0.1
1	4.96±1.29	14.79±2.31	20.52±1.63	3.6±0.9	0.4±0.1
2	2.23±0.4	20.49±1.98	19.42±1.89	3.1±1.1	1.6±0.4

Table 2. 7: Percentage of internalized ^{67}Ga-**D7**,^{67}Ga-**D7**-I, and Ga-**D7**-^{124}I in *S. aureus* RN4220 upon incubation in iron deficient bacterial culture (n=5).

Incubation Time (h)	^{67}Ga-**D7** (%)	^{67}Ga-**D7**-I (%)	Ga-**D7**-^{124}I (%)	^{67}Ga-citrate (%)	Tyrosine-^{124}I (%)
0.16	5.54±0.65	4.43±1.56	6.73±1.92	6.0±1.8	0.2±0.0
0.33	5.22±0.28	5.06±1.09	8.86±3.06	6.5±0.5	0.2±0.0
0.5	5.15±0.71	6.07±1.15	10.55±3.50	9.4±1.5	0.2±0.0
1	5.68±1.10	7.45±1.83	9.73±1.57	18.4±2.1	0.2±0.0
2	6.28±1.57	12.30±2.72	10.11±2.41	21.9±5.6	0.3±0.0

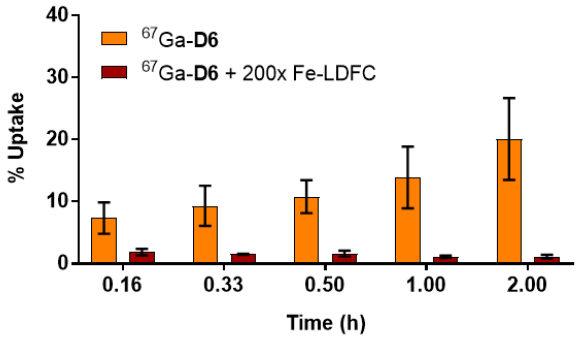

Figure 2. 58: In the presence of 200× excess Fe−LDFC, the uptake of ^{67}Ga-**D6** in *E. coli* K-12 is attenuated significantly after 10 min.

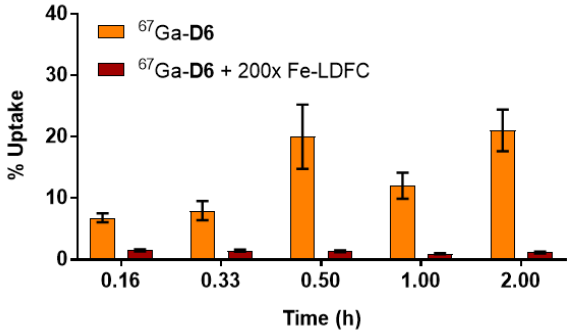

Figure 2. 59: In the presence of 200× excess Fe−LDFC, the uptake of ^{67}Ga-**D6** in *P. aeruginosa* PA01 is attenuated significantly after 10 min.

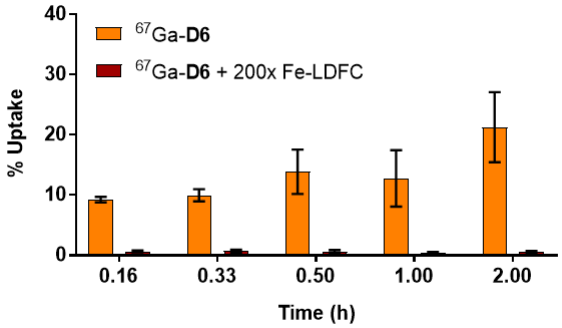

Figure 2. 60: In the presence of 200× excess Fe−LDFC, the uptake of ^{67}Ga-**D6** in *S. aureus* RN4220 is attenuated significantly after 10 min.

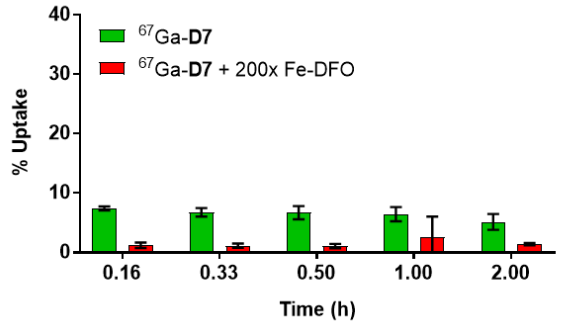

Figure 2. 61: In the presence of 200× excess Fe−DFO, the uptake of ^{67}Ga-**D7** in *E. coli* K-12 is attenuated significantly after 10 min.

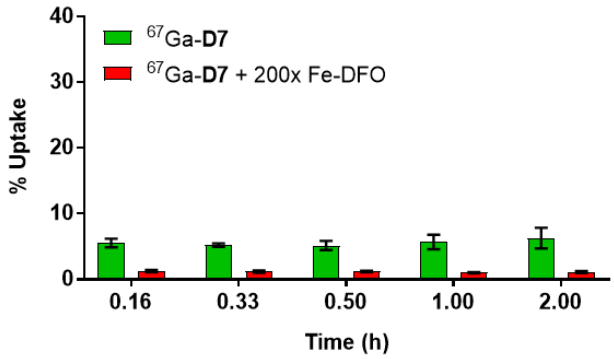

Figure 2. 62: In the presence of 200× excess Fe−DFO, the uptake of ^{67}Ga-**D7** in *S. aureus RN4220* is attenuated significantly after 10 min.

Table 2. 8: Percentage of internalized ^{67}Ga-**D6** and ^{67}Ga-**D6** + 200 x Fe-LDFC in *E. coli* K-12 upon incubation in iron deficient bacterial culture (n=5).

Incubation Time (h)	^{67}Ga-D6 (%)	^{67}Ga-D6 + 200x Fe-LDFC (%)
0.16	7.4±2.5	1.7±0.5
0.33	9.3±3.2	1.5±0.1
0.5	10.8±2.7	1.7±0.5
1	13.9±5.0	1.1±0.2
2	20.1±6.6	1.2±0.3

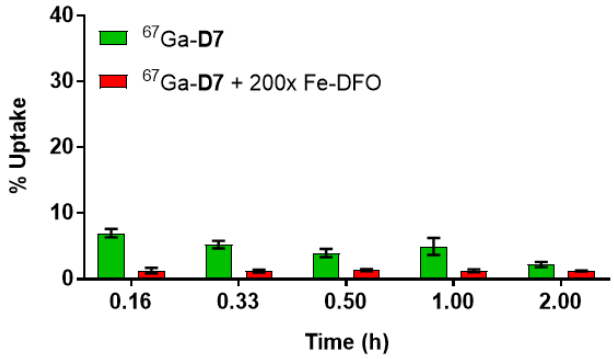

Figure 2. 63: In the presence of 200× excess Fe-DFO the uptake of ^{67}Ga-**D7** in *P. aeruginosa* PA01 is attenuated significantly after 10 min.

Table 2. 9:Percentage of internalized 67Ga-D6 and 67Ga-D6 + 200 x Fe-LDFC in *S. aureus* RN4220 upon incubation in iron deficient bacterial culture (n=5).

Incubation Time (h)	^{67}Ga-D6 (%)	^{67}Ga-D6 + 200x Fe-LDFC (%)
0.16	9.2±0.5	0.7±0.2
0.33	10.0±1.0	0.7±0.3
0.5	13.9±3.7	0.7±0.2
1	12.8±4.7	0.4±0.1
2	21.3±5.8	0.5±0.2

Table 2. 10: Percentage of internalized ^{67}Ga-**D6** and ^{67}Ga-**D6** + 200 x Fe-LDFC in *P. aeruginosa* PA01 upon incubation in iron deficient bacterial culture (n=5).

Incubation Time (h)	^{67}Ga-D6 (%)	^{67}Ga-D6 + 200x Fe-LDFC (%)
0.16	6.8±0.7	1.5±0.2
0.33	8.0±1.6	1.5±0.2
0.5	20.0±5.2	1.4±0.2
1	12.0±2.1	1.0±0.1
2	21.1±3.4	1.2±0.1

Table 2. 11: Percentage of internalized ^{67}Ga-**D7** and ^{67}Ga-**D7** + 200 x Fe-DFO in *E. coli* K-12 upon incubation in iron deficient bacterial culture (n=5).

Incubation Time (h)	^{67}Ga-D7 (%)	^{67}Ga-D7 + 200x Fe-DFO (%)
0.16	7.41±0.34	1.23±0.47
0.33	6.76±0.71	1.15±0.36
0.5	6.71±1.11	1.08±0.37
1	6.45±1.21	2.61±3.43
2	5.14±1.33	1.40±0.18

Table 2. 12: Percentage of internalized ^{67}Ga-**D7** and ^{67}Ga-**D7** + 200 x Fe-DFO in *S.aureus* RN4220 upon incubation in iron deficient bacterial culture (n=5).

Incubation Time (h)	^{67}Ga-D7 (%)	^{67}Ga-D7 + 200x Fe-DFO (%)
0.16	5.54±0.65	1.25±0.19
0.33	5.22±0.28	1.17±0.19
0.5	5.15±0.71	1.20±0.12
1	5.68±1.10	2.02±0.09
2	6.28±1.57	1.10±0.15

Table 2. 13: Percentage of internalized ^{67}Ga-**D7** and ^{67}Ga-**D7** + 200 x Fe-DFO in *P. aeruginosa* PA01 upon incubation in iron deficient bacterial culture (n=5).

Incubation Time (h)	^{67}Ga-D7 (%)	^{67}Ga-D7 + 200x Fe-DFO (%)
0.16	6.98±0.63	1.31±0.42
0.33	5.24±0.57	1.20±0.20
0.5	3.98±0.61	1.36±0.15
1	4.96±1.29	1.26±0.21
2	2.23±0.4	1.22±0.08

Table 2. 14: Summary of MIC (µM), ^{67}Ga-uptake (%) and concentration of ^{67}Ga-labeled ligand (nmol) used in the uptake studies. ND: Not Determined, GP: Growth Promoting.

	E.coli			*S.aureus*			*P.aeruginosa*		
Compound	MIC (µM)	^{67}Ga-Ligand Conc (nmol)	^{67}Ga-Uptake (%)	MIC (µM)	^{67}Ga-Ligand Conc (nmol)	^{67}Ga-Uptake (%)	MIC (µM)	^{67}Ga-Ligand Conc (nmol)	^{67}Ga-Uptake (%)
ciprofloxacin	0.93	-	-	0.93	-	-	0.93	-	-
apo-D6	Inactive	-	-	Inactive	-	-	Inactive	-	-
Ga-D6	1.9	94	20	3.8	94	21	>30	94	21
Fe-D6	Inactive	-	-	GP	-	-	Inactive	-	-
Ga-D6-I	30	94	5	15	94	13	ND	94	7
Ga-D2	0.23	0.15	14.5	0.94	0.15	16.9	3.8	0.15	12.8
apo-D7	Inactive	-	-	Inactive	-	-	Inactive	-	-
Ga-D7	30	36	5	30	36	2	Inactive	36	6
Fe-D7	GP	-	-	Inactive	-	-	GP	-	-
Ga-D7-I	Inactive	36	3	Inactive	36	12	ND	36	20
Ga-D1	1.9	0.15	13	0.094	0.15	9.5	15	0.15	13

2.5.15 In-vivo biodistribution and pharmacokinetics in naïve and infected mice

Naïve Balb/c mice (female, 8 weeks, n=3) were injected with ^{67}Ga-**D6**, ^{67}Ga-**D7**, ^{67}Ga-citrate, Ga-**D6**-^{124}I, Ga-**D7**-^{124}I and Tyrosine-^{124}I intravenously, followed by 1 hour post injection biodistribution. The infection was introduced into the soft tissue infection mouse model via intramuscular injection. As a source of infection, wild type *S. aureus* inoculum was injected into the right biceps, and inflammation was induced by heat-killed *S. aureus* (90 ^{o}C, 30 minutes, 10^9 CFUs). The microbial infections were allowed to grow for 5 hours prior to being administered with radiolabeled conjugates. Ex-vivo biodistribution was performed 1 hour after injection, and all organs collected were measured using a gamma-counter. We followed the published urine metabolite protocol.[1]

Table 2. 15: Biodistribution of Ga-**D6**-^{124}I and Ga-**D7**-^{124}I in Balb/c mice at 1h p.i. (n=3).

Organ	Ga-**D6**-^{124}I (%ID/g)	Ga-**D7**-^{124}I (%ID/g)	Tyrosine-^{124}I (%ID/g)
Blood	11.9±2.0	0.98±0.32	8.0±0.7
Heart	4.1±0.9	0.38±0.13	2.8±0.4
Lung	13.0±2.2	1.67±0.69	4.8±2.2
Liver	5.3±1.3	0.49±0.18	3.0±0.3
Spleen	4.8±1.3	2.06±1.38	3.7±0.3
Kidney	5.6±1.6	1.81±0.16	5.8±0.4
Small intestine	3.7±2.8	1.13±0.89	4.0±0.6
Muscle	0.9±0.3	0.38±0.16	1.9±0.2
Bone	3.2±3±.0	0.62±0.44	4.0±0.3
Urine	122.3±35.7	51.96±8.41	87.9±2.7

Table 2. 16: Biodistribution of ^{67}Ga-**D6** and ^{67}Ga-**D7** in Balb/c mice at 1h p.i. (n=3).

Organ	^{67}Ga-**D6** (%ID/g)	^{67}Ga-**D7** (%ID/g)	^{67}Ga-citrate (%ID/g)
Blood	17.4±0.8	15.63±4.23	9.1±0.4
Heart	6.5±1.2	4.97±1.17	1.8±1.2
Lung	16.9±6.5	16.65±11.29	1.7±0.9
Liver	5.3±0.3	61.89±8.68	3.1±0.6
Spleen	4.6±0.4	17.54±4.16	1.2±1.0
Kidney	17.0±0.8	6.25±0.42	2.3±1.8
Small intestine	3.7±0.2	6.81±0.65	1.7±0.8
Muscle	1.7±0.2	3.34±1.49	0.9±0.6
Bone	3.1±0.7	10.43±3.20	1.4±1.4
Urine	87.9±2.7	47.57±9.88	54.1±0.4

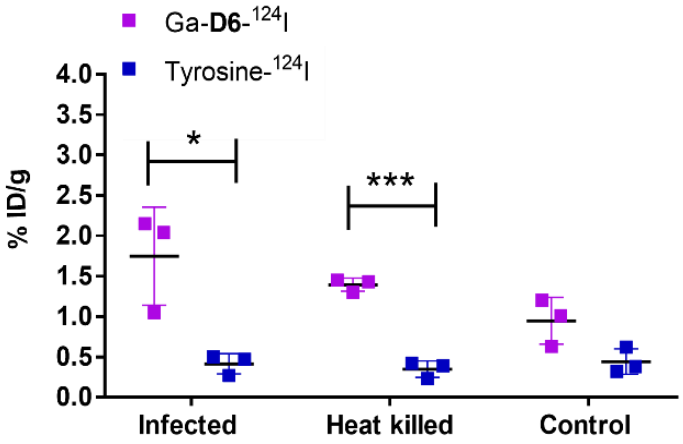

Figure 2.64: Comparative biodistribution of the infected muscles with *S. aureus* of Ga-**D6**-^{124}I and Tyrosine-^{124}I in murine myositis models. Pare t-test.

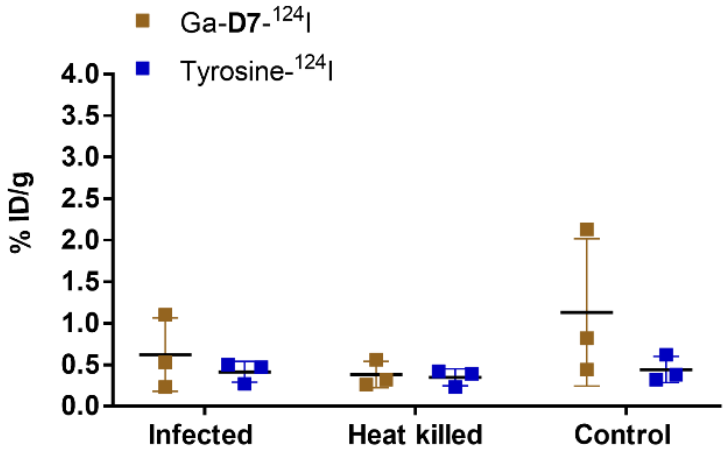

Figure 2. 65: Comparative biodistribution of the infected muscles with *S. aureus* of Ga-**D7**-^{124}I and Tyrosine-^{124}I in murine myositis models.

Table 2. 17: Biodistribution of Ga-**D6**-^{124}I and Ga-**D7**-^{124}I in infected Balb/c mice at 1h p.i.

Organ	Ga-**D6**-^{124}I (%ID/g)	Ga-**D7**-^{124}I (%ID/g)	Tyrosine-^{124}I (%ID/g)
Infected muscle	1.7±0.6	0.62±0.44	0.4±0.1
Inflamed muscle	1.4±0.1	0.38±0.16	0.3±0.1
Control muscle	0.9±0.3	1.13±0.89	0.4±0.2

2.5.16 Correlation plots

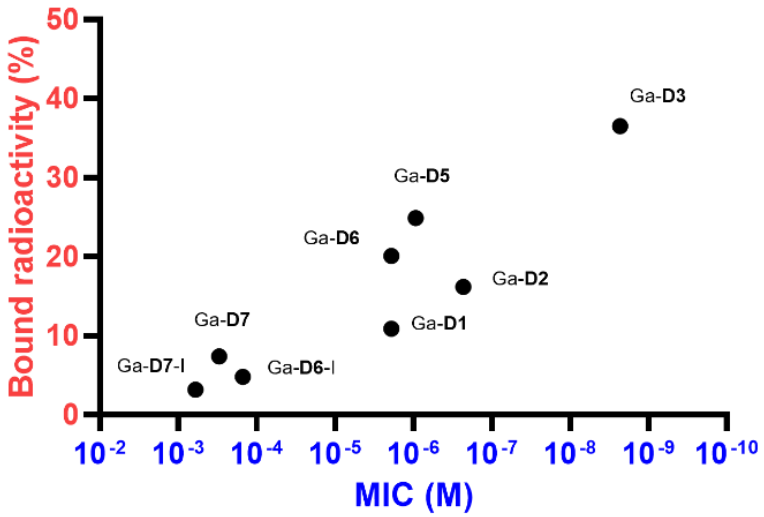

Figure 2. 66: Proposed correlation plot between bound radioactivity and MIC value in *E. coli* for all gallium siderophore-base antibiotic conjugates tested, first and second-generation. Y-axis is the highest bacteria uptake percentage and X-axis the MIC (M).

Chapter 3: Design and development of DFO-diazirine probes

Summary of this work

Crystal structure data was acquired by Inoketjis Josts and Hendrik Tidow. FoxA, used in the MS/MS analysis for Fe-DFO-azir01 and Fe-DFO-02, was purified by Inoketjis Josts. Grzegorz Sabat from the Mass Spectrometry Core Facility at UW-Madison performed MS/MS sample treatment and data acquisition. All other compound syntheses, characterization, and experiments were performed by Minhua Cao.

3.2 Introduction

3.2.1 Introduction to current diazirine photoaffinity probes

A comprehensive understanding of drug uptake and target interaction is crucial for the rational design of therapeutics and to enable drug optimization while mitigating off-target interactions that contribute to toxicity.[112] Traditional methodologies for investigating these interactions include affinity-based and expression cloning-based approaches, a strategy for isolating a gene encoding an uncharacterized protein relies on a known molecule or protein exhibiting high affinity for the target protein. Both methods rely on high target affinity for the small molecule substrate.[113] Photoaffinity probes (PAPs) offer significant advancement by facilitating the covalent capture of target proteins. Upon photoactivation at specific wavelengths, PAPs undergo irreversible binding via a photoreactive moiety, generating reactive intermediates that engage in covalent adduct formation with proximal molecules.[114] This is particularly valuable for identifying transient or weak interactions that may elude detection by conventional methods. The design of PAPs consists of three key components: (1) an affinity ligand, conferring selective, reversible binding to the target protein; (2) a photoreactive group, enabling photo-induced covalent

crosslinking; and (3) a reporter element, such as a fluorophore, radioisotope, or a substrate that is readily captured by high-affinity interactions, facilitating target identification and analysis.[115]

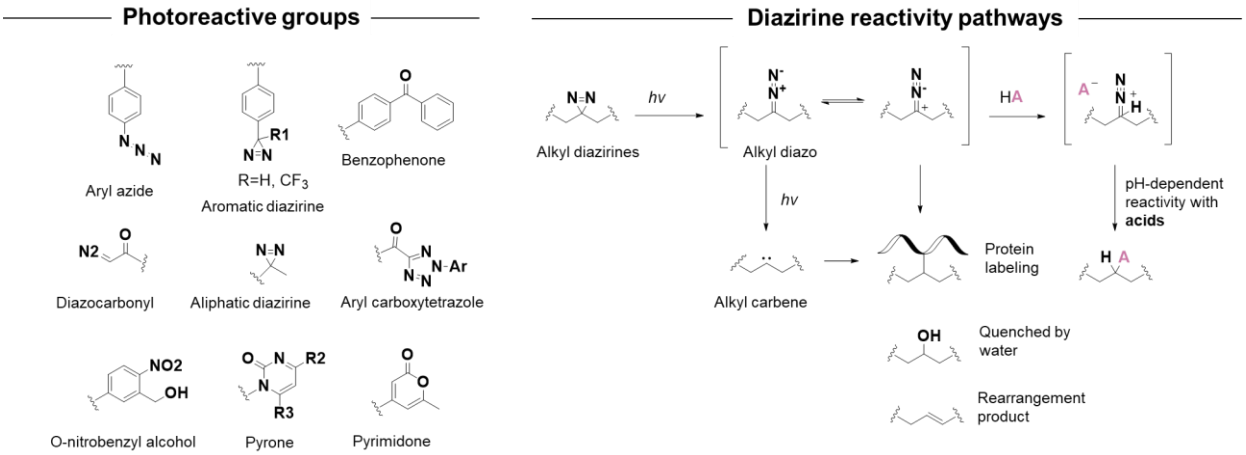

Figure 3. 1: (Left) Examples of photoreactive moiety. (Right) Pathways of diazirine photolysis. Beyond generating carbenes and diazo compounds for protein labeling, diazirines can be transformed into alkenes through a mechanism known as rearrangements in the excited state (RIES), quenched by water, and display pH-dependent reactivity with acids.

The selection of the photoreactive moiety is critical to the efficacy of PAPs. A variety of photoreactive moieties are employed in photoaffinity probes (PAPs), including aryl azides, phenyldiazirines, benzophenones, diazocarbonyls, enones, pyrones, pyrimidones, nitrobenzenes, and 2-aryl-5-carboxytetrazoles (Figure 3.1 left) .[113,116] Diazirines, characterized by their stable three-membered ring structure containing a carbon atom doubly bonded to two nitrogen atoms, have gained widespread adoption. Their commercial availability, coupled with an activation wavelength (250-365 nm) that minimizes interference with protein absorbance (280 and 200 nm), reduces photodamage and enhances compatibility with biomolecules.[115,117] Their mechanism of action relies on the formation of diazo intermediates that convert into carbenes. These carbenes can then participate in biomolecular conjugation, resulting in covalent bond formation, and be

quenched in the aqueous environment.[118] Experimental studies have also revealed a pH-dependent reactivity with acids, which influences the diazirine's preference for protein carboxylate groups (Figure 3.1 right) .[119]

Furthermore, the chemical stability of diazirines across a broad pH range makes them suitable for diverse experimental conditions. While aliphatic diazirines are favored for their compact size, minimizing steric and electronic ligand modification, aromatic diazirines exhibit superior photochemical stability, resulting in a higher yield of reactive carbenes, the key intermediates in covalent crosslinking.[117,119]

Aliphatic diazirine probes have been extensively explored for the capture of a diverse array of proteins by small molecule substrates.[120-123] Homan et al. successfully employed an aliphatic alkyne diazirine probe, HPAP, to map heme-protein interactions in HEK293T cells, demonstrating the feasibility of probing specific protein-ligand interactions. [124] Similarly, Woo et al. have developed a library of aliphatic diaziridine probes to investigate labeling preferences in protein biomolecules[119] and to facilitate interactome mapping by photoaffinity labeling. This approach, exemplified by the use of a photonaproxen probe, has enabled the characterization of NSAID binding sites, highlighting the power of aliphatic diazirines in elucidating small molecule-protein interactions. [125] Furthermore, Sieber et al. utilized a heme-containing diazirine library (heme probes 1-3) to

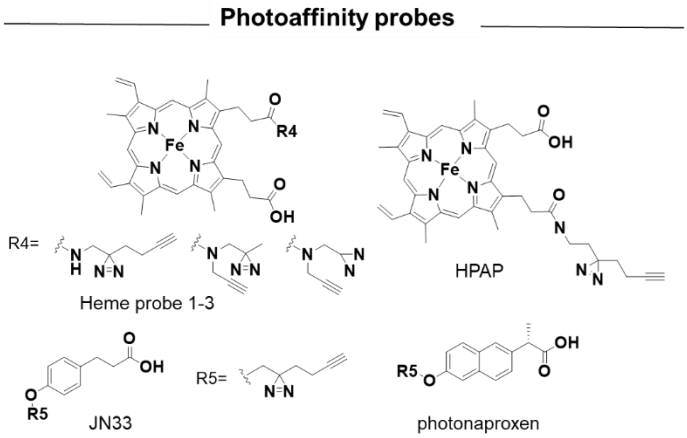

Figure 3. 2: Examples of photoaffinity probes containing aliphatic diazirine.

profile the heme-binding proteome in bacteria, showcasing the applicability of these probes to identify novel protein target beyond mammalian cells (Figure 3.2).[126]

3.2.2 Introduction to this work

Photoaffinity labeling (PAL) has emerged as an important technique for elucidating small molecule interactions, identifying target proteins, and quantifying interacting partners.[119] This approach has been extensively applied in target deconvolution and pharmacophore identification within diverse biological systems, including cancer [113] and bacterial cells, [126,127] demonstrating its broad utility. The aliphatic diazirines has gained considerable attention due to their compact size which minimize structural perturbation of the investigated small molecules and chemical stability in a diverse pH range.[113] The chemical properties and labeling preferences of aliphatic diazirines have been rigorously investigated by Woo et al.[119] and others,[115] providing valuable insights into their applicability.

While PAL utilizing aliphatic diazirines has proven particularly effective for characterizing small molecule targets, its application to metal-bound siderophores presents a unique opportunity to advance our understanding of bacterial transport mechanisms. A significant knowledge gap exists regarding the transport proteins responsible for the delivery of siderophore-metal complexes in various bacterial strains. The implementation of aliphatic diazirine-based PAL with siderophore conjugates could provide unprecedented access to the direct identification siderophore transport proteins. Elucidation of these uptake systems is critical, as it would directly inform the rational design of more potent siderophore-based antibiotics.

However, a significant challenge impedes the implementation of PAL in this context: siderophore transporters, which consist of membrane-associated barrel proteins possessing deeply

buried binding sites, present significant obstacles to efficient labeling. Consequently, covalent siderophore pulldown probes have been absent from literature. Alternative strategies employing affinity-based pulldown approaches have yielded limited success due to the inherently weak, non-covalent, and transient nature of coordinative and substrate-binding interactions.[128] Recent developments, specifically the synthesis and exploration of the first covalent metal complex tags, clickable heme-diazirines, have provided valuable insights into bacterial and mammalian transport and metabolism of this essential metal-containing cofactor [126,129] and the comprehensive studied indicating alkyl diazirine has preference for membrane proteins[116] demonstrate the potential feasibility of applying this technique to metal complex siderophore conjugates.

We report herein the rational design, optimization and synthesis of a first siderophore complex-photoaffinity probe library. This library was designed to systematically investigate the labeling preferences of diazirine-linked metal complexes with both single amino acids and proteins. Towards successful validation, we demonstrate that PAL can be employed to label FoxA, a siderophore transmembrane transporter in *P. aeruginosa*, within the putative metal complex binding site.

3.3 Results and discussion

3.3.1 Structural characterization of a Fe-DFO conjugate

The transmembrane siderophore transport machinery of most bacterial organisms is known to provide entry to various siderophore-linked molecules. This property provides the foundation for the Trojan horse siderophore-antibiotic drug strategy, which has been successfully employed by us and others.[74,86,130-132] We hypothesized that crystallographic identification of the binding mode of a siderophore-antibiotic conjugate could provide insight into suitable loci for the

incorporation of a covalent diazirine tag. To this end, we examined a co-crystal structure of Fe-D1,[74] a Fe-DFO complex linked to ciprofloxacin, with the previously characterized, *P. aeruginosa* outer-membrane siderophore binder *FoxA* (Figure 3.3). Comparison with previously obtained structural data with Fe-DFO[133] indicates that the functionalized siderophore retains binding mode and site. The chelate linker and appended ciprofloxacin occupy the channel leading to the siderophore binding locus inside the barrel and on top of the plug domain, informing on possible covalent tagging sites The substrate binding site and channel are lined with tyrosines, aspartic acids and glutamine residues that could provide suitable reactive partners to diazirine linked substrates. Based on reactivity profiling by Woo and coworkers,[119] we reasoned that the combination of an aliphatic diazirine with longer-wavelength irradiation (365 nm) would be more ideally suited to favor reactivity with tyrosine and aspartate sidechains. While this design was based on the FoxA protein, we note that other, previously crystallographically characterized siderophore binding proteins such as FhuA in complex with albomycin,[134] FhuA in complex with rifamycin, [135] and

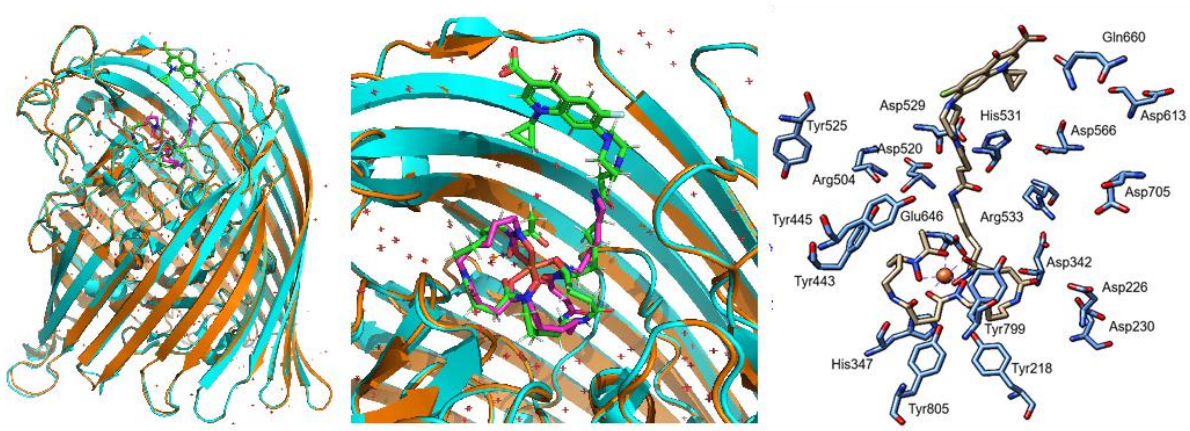

Figure 3. 3: Co-crystal structure overlays of Fe-DFO bound to FoxA (copper/magenta) and Fe-D1 bound to FoxA (turquoise/green) of the holo protein and substrate binding region (middle) demonstrate that Fe-DFO conjugates replicate the binding mode of the corresponding Fe-bound siderophore with high accuracy. Analysis of polar side-chain amino acids involved in binding and interaction with Fe-D1 (tan) indicates a prevalence of tyrosine and aspartic acid within the binding pocket, in addition to other polar amino acids (shown in blue).

FhuD in complex with coprogen[136] can also guide the design of siderophore affinity probes beyond deferoxamine.

3.3.2 Design and synthesis of DFO-diazirines

The design of DFO-based siderophore probes was guided by the structural insights provided by the co-crystal structure of Fe-D1 in FoxA. These findings informed potential modifications that a siderophore transmembrane transporter could tolerate specifically, we sought to incorporate the diazirine and alkyne into the linker moiety and vary the bond length between the desferoxamine NH_2 terminus and the diazirine reactive group. M-DFO-azir-01 was synthesized in a 2-step reaction for the apo-conjugate and a 3-step reaction for the Fe and Ga, employing a minimal design where the diazirine alkyne was directly coupled to the amine using a solution phase conjugation strategy (Scheme 3.1A). A second derivative, DFO-azir-02 incorporating a succinate linker between the siderophore amine terminus introduced the diazirine and alkyne functionalities as single amino acids. Accordingly, DFO-azir-02 was synthesized via solid-phase peptide synthesis (SPPS) (Scheme 3.1B). Metal complexation with Fe^{3+} and Ga^{3+} was achieved through a pre-formation strategy, wherein the metal complex was formed with DFO prior to its direct incorporation into the peptide during solid-phase synthesis. Both the Ga /Fe complexes and diazirine group exhibited stability throughout the resin cleavage process and were fully characterized using NMR spectroscopy and mass spectrometry (section 3.5.3).

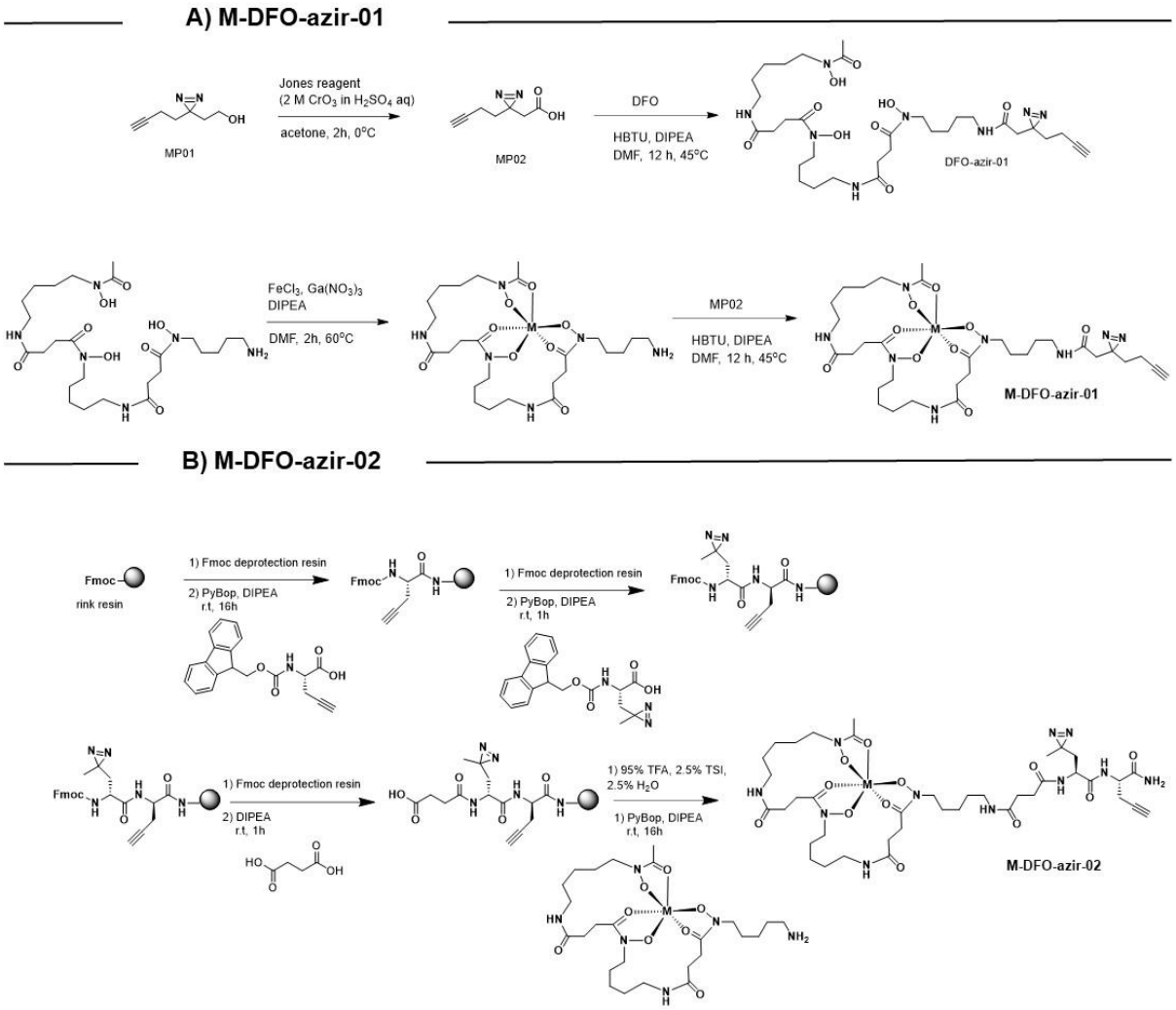

Scheme 3. 1: Synthesis of siderophore affinity probes, M-DFO-azir-01 (A) and M-DFO-azir-02 (B), consist of a deferoxamine affinity ligand, an aliphatic protective group, and an alkyne handle for reporter element conjugation.

3.3.3 Reactivity profiling of DFO-diazirines

In previous work by Woo and coworkers, reactivity profiling of aliphatic diazirine probes indicated that these compounds display preferences for tyrosine, glutamic acid, cysteine, and aspartic acid. [119] To investigate the reactivity of the two first-generation DFO-diazirines with amino acids, we conducted an amino acid side chain reactivity screen using acetyl and amino-protected amino acids, Ac-X-OMe amino acids (X = Tyr, Asp, Gln, Arg, His) with photoirradiation

at 365 nm. The conditions and amino acids were chosen in accordance with accessible sidechains within the *FoxA* binding pocket (Tyr, Asp), and incorporating other amino acids as reactivity controls with moderate (His) or poor reactivity (Arg, Gln). Ga- and Fe-DFO-azir-01 were anticipated to recapitulate reactivity trends reported with similar aliphatic, alkyl diazirines.[119] While the two complexes exhibited similar reactivity and comparable yields with Tyr and Asp (~ 12 and 3 % respectively), we also observed covalent modification of Gln, Arg and His (2-5%), with the Fe complex showing greater reactivity with the latter group when compared to the Ga complex. The linker extended derivatives Ga- and Fe-DFO-azir-02 showed comparable trends, with the Fe complex also retaining greater reactivity towards the second amino acid group (Figure 3.4). Over-all, our findings confirm that both DFO-diazirine probes should be reactive with Tyr and Asp which are well-represented within the FoxA binding pocket.

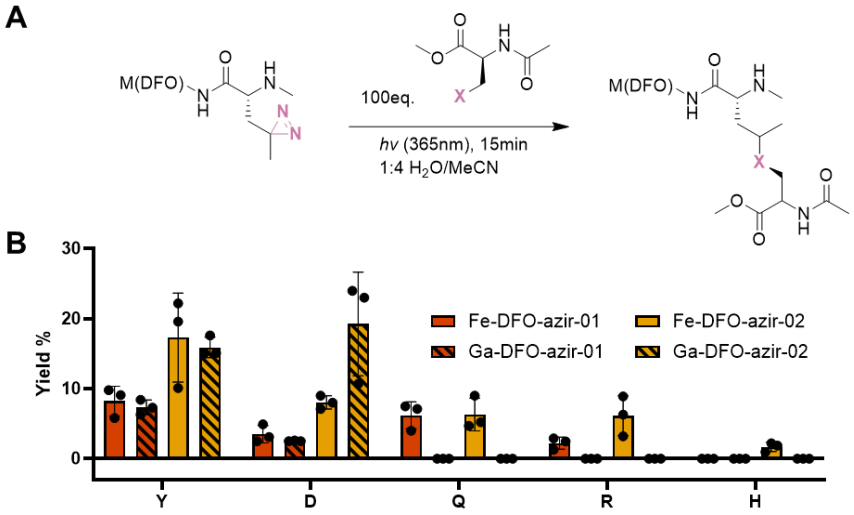

Figure 3. 4: A reactivity scheme for DFO-diazirine with N-acetyl, O-methyl protected amino acids. B) DFO-diazirine probes reactivity screening was performed with 5 N-acetyl, O-methyl protected amino acids (100 equivalents) in a 1:4 water: acetonitrile solution. Yield was calculated by LC-MS following UV-absorbance detection at 425 nm for Fe complexes and 280 nm for Ga complexes.

3.3.4 Covalent tagging of BSA and FoxA

To evaluate the compatibility of Ga- and Fe-DFO-azir-01/02 for protein labeling and subsequent copper-catalyzed azide-alkyne cycloaddition (CuAAC) with a fluorophore, we initially assessed non-specific conjugation to bovine serum albumin (BSA) in water. Optimization of CuAAC conditions yielded successful tagging, as evidenced by in-gel fluorescence visualization (Figure 3.5A) and MALDI mass spectrometry (Figures 3.71, 3.72). Following validation of the labeling chemistry, we proceeded to probe chemical crosslinking of FoxA in vitro. To this end, purified FoxA was incubated with 50 equivalents of M-DFO-azir-01 or -02 for 30 minutes, followed by 15 minutes of photo-irradiation. CuAAC conditions required further optimization to accommodate the transmembrane protein and the different buffer system (DBPS, 0.4% C8E4). For Fe/Ga-DFO-azir-01 and 02, probe-dependent fluorescence was observed, albeit with weak band intensities (Figure 3.5 B). We hypothesized that the presence of the metal ion could have a

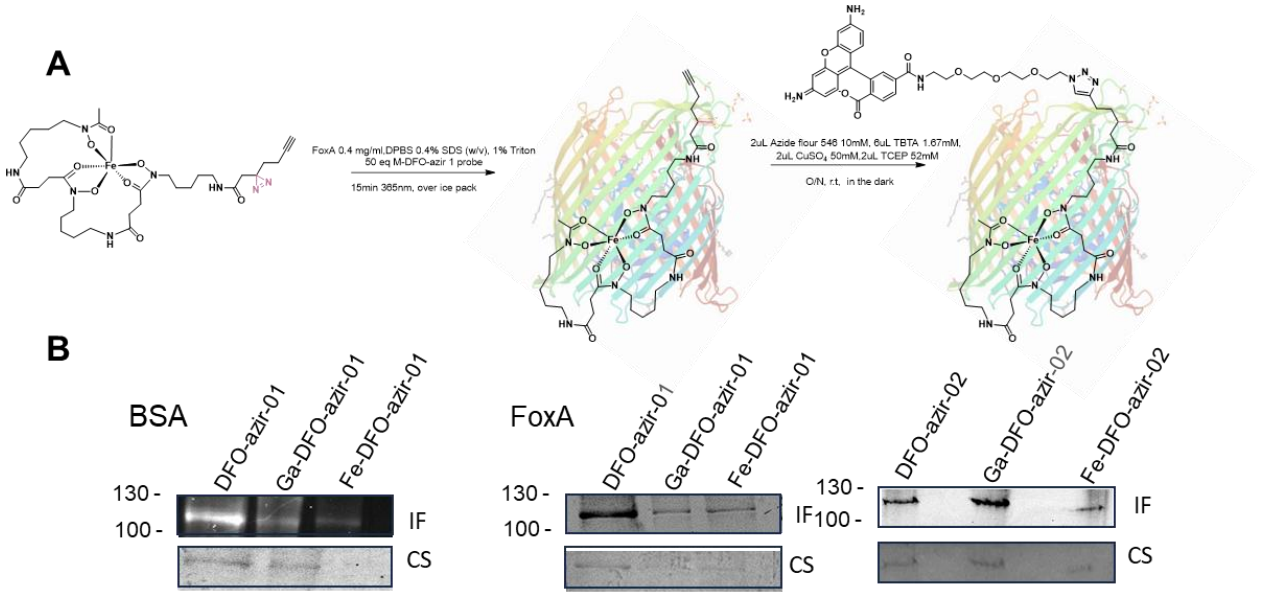

Figure 3. 5: A) Experimental schematic for PAL of proteins in vitro. B) In-gel fluorescence (IF) analysis evaluating the ability of M-DFO-azir-01 and M-DFO-azir-02 to label BSA and FoxA in vitro. Photo-irradiation (15 min) was performed prior to a 30-minute incubation for FoxA. (Full gel Figure 3.59). CS= Coomassie stain

quenching effect. Fe(III) complexes are well known to induce a non-radiative quenching effect on green-emissive fluorophores through photoelectron transfer.[137,138] Nevertheless, this should not be the case with Ga, yet we observed poor conversion to the desired product with all coordination complexes tested.

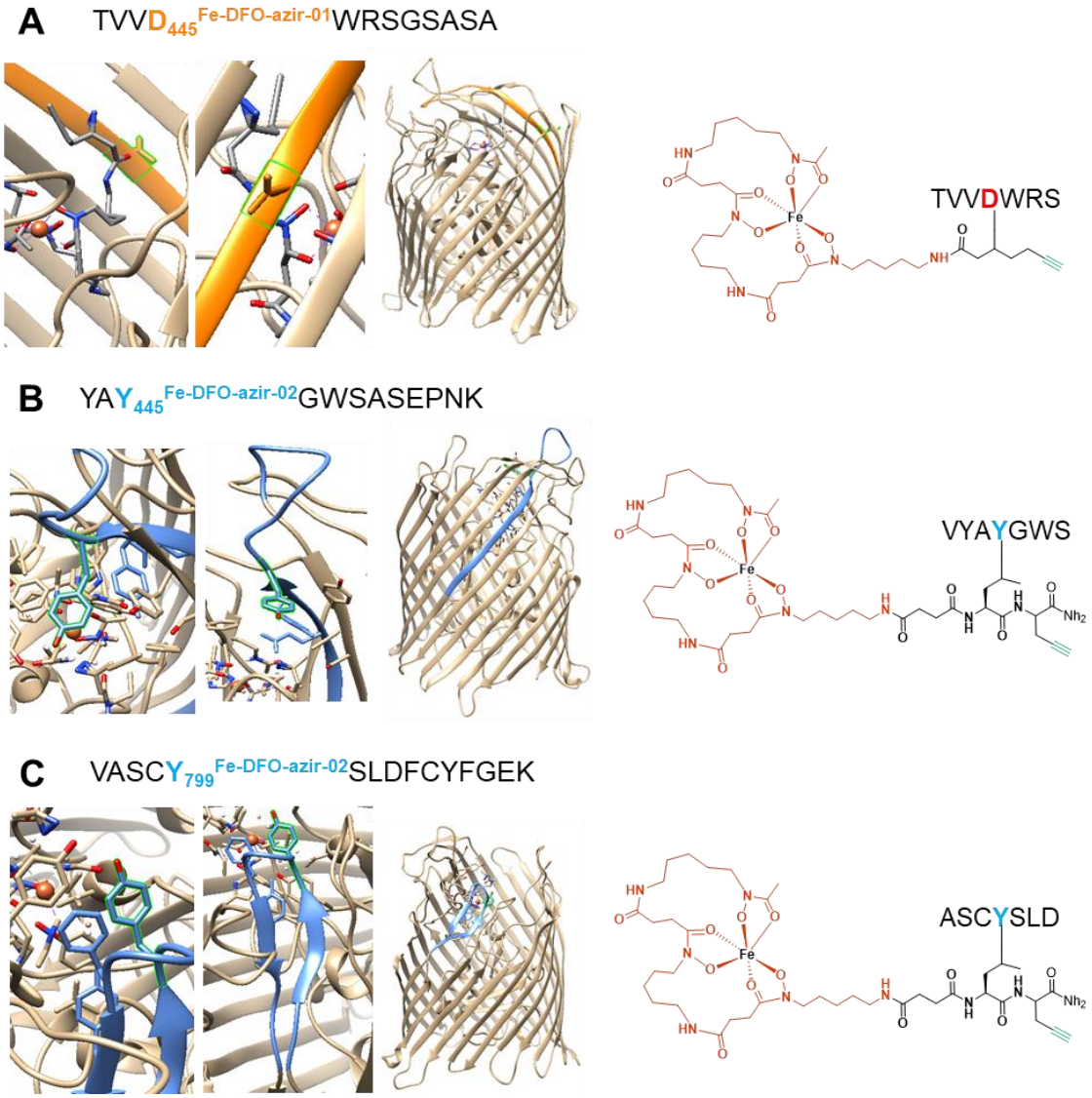

Figure 3. 6: Mass spectrometer results for photocrosslinking site of Fe-DFO-azir-01 and Fe-DFO-azir-02 in isolated FoxA. The labeled the amino acids indicated in orange and blue are shown in the FoxA co-crystal structure in complex with Fe-DFO-azir-01.

To further elucidate the identity, specificity, and potential labeling sites of DFO-diazirine probes, we performed MS/MS analysis of the photocrosslinked and CuAAC-modified FoxA. Despite the observed fluorescence of the reaction products, MS/MS analysis identified peptide fragments in FoxA only containing the covalently modified with Fe-DFO-01 and 02 without the clicked fluorophore. This is in line with what we observed with the in-gel fluorescence, indicating the click chemistry is suboptimal despite our optimization for this system. However, these fragments revealed distinct labeling preferences for Fe-DFO-azir-01 and -02. Specifically, Fe-DFO-azir-01 preferentially reacted with aspartic acid D_{502}, located within a beta-sheet at the top of the barrel (Figure 3.6A), whereas Fe-DFO-azir-02 labeled tyrosine residues Y_{445} and Y_{799}, situated within the protein binding pocket, and aspartic acid D_{512}, located in the outer loop region (Figure 3.6 B, 3.7 and C, 3.68-70). It is important to note that while Fe-DFO-azir-01 and -02 appeared intact during MS/MS analysis, iron dissociation may occur during the process, leading to subsequent chelation of trace iron present in solvents and instrumentation.

These differential tagging profiles within FoxA demonstrate the important role of linker length in achieving selective amino acid labeling within the immediate vicinity of the Fe-DFO binding site. Indeed, crystallographic analysis of Fe-DFO-azir-01 in FoxA following photocrosslinking attempts revealed no evidence of covalent tagging within the target binding site (Figure 3.66). Conversely, Fe-

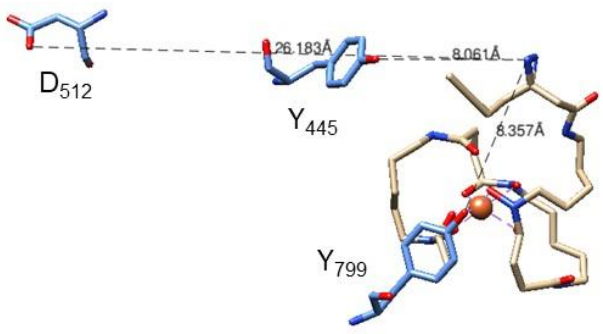

Figure 3. 7: Amino acids labeled by Fe-DFO-azir-02 shown in the FoxA in complex with Fe-DFO-azir-01 co-crystal structure. Distance between Y_{445} OH to diazirine N_{05} 8.06 Å, Y_{799} OH to diazirine N_{05} 8.35 Å, and D_{512} O_{D1} to diazirine N_{05} 26.183 Å.

DFO-azir-02 successfully labeled tyrosine residues within close proximity to the substrate binding site.

Given that Fe-DFO-azir-02 targeted amino acids deeply embedded within the protein binding site of this transmembrane receptor, we hypothesized that the alkyne group's accessibility within the barrel protein was insufficient, hindering fluorophore conjugation. To address this limitation, we synthesized M-DFO-azir-03 (Scheme 3.3), incorporating a PEG2 linker to increase alkyne handle distance to improve click chemistry accessibility. However, despite this modification, the longer linker did not improve fluorophore conjugation. We were unable to identify suitable CuAAC conditions that facilitated efficient conjugation with the M-DFO-azir-03 probes.

3.3.5 Design and synthesis of DFO-diazirines with pre-linked optical tags and pulldown tags

To circumvent the requirement for post-photocrosslinking conjugation with DFO-diazirine probes, we synthetically incorporated optical tags and biotin into the DFO-diazirine scaffold prior to photocrosslinking. This led to the synthesis of a second-generation of probes, M-DFO-azir-04 and -05, via solid-phase peptide synthesis (SPPS) (Schemes 3.6, 3.7). These probes maintained the linker length and diazirine position of the first-generation DFO-azir-02 but incorporated coumarin fluorophores: 7-(diethylamino)coumarin-3-carboxylic acid (Ex = 415 nm, Em = 465 nm) and coumarin 343 (Ex = 444 nm, Em = 480 nm), respectively. These fluorophores were selected due to their structural similarity to the fluoroquinolone ciprofloxacin, which we had previously characterized crystallographically in the form of the Fe-D1 in complex with FoxA. Additionally, we also synthesized M-DFO-azir-06 (Scheme 3.8), incorporating an extended lysine linker

attached to biotin, to enable the identification of labeled proteins of interest through biotin-streptavidin enrichment.

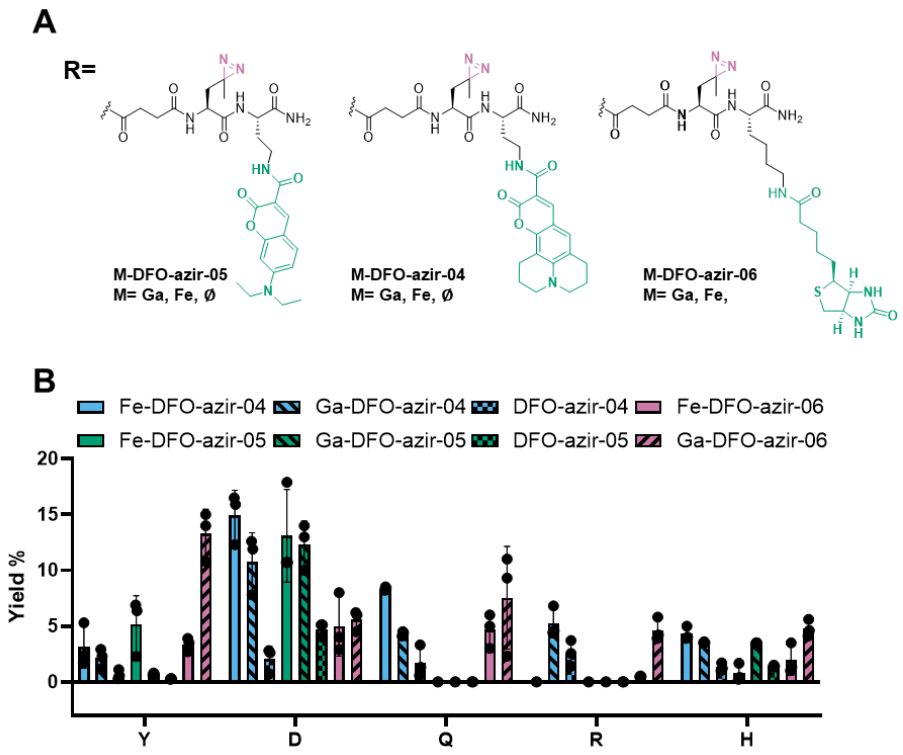

Figure 3. 8: A) Structures of M-DFO-azir-04, M-DFO-azir-05, and M-DFO-azir-06. B) Probe reactivity was assessed with 5 N-acetyl, O-methyl protected amino acids (100 equivalents) in a 1:4 water: acetonitrile solution. Yield was calculated by LC-MS following UV-absorbance detection at 425 nm for Fe complexes and 280 nm for Ga complexes.

The second-generation probes recapitulated the reactivity observed with the first-generation compounds M-DFO-azir-01/02, exhibiting similar trends in amino acid residue screening. M-DFO-azir-04 and 05 demonstrated a preference for aspartic acid (~ 10%), but with diminished yield for tyrosine (~ 2% yield) compared to the first generation (~12% yield). This could be in part due to the pre-linked strategy. Notably, the non-metallated, apo compounds displayed diminished reactivity in comparison to their corresponding metalated versions. In contrast, M-DFO-azir-06 exhibited a higher reactivity with tyrosine than aspartic acid, particularly Ga-DFO-azir-06 (~13% yield). The Fe-DFO-azir-06 probe (3% yield) displayed lower reactivity

compared to its Ga counterpart (Figure 3.8). Putatively, metalated compounds exhibited increased reactivity due to the capping of polar, hydroxamate functional groups that can interfere with intermolecular diazirine-induced cross-linking. However, this amino acid residue preference appears not to be exclusive to the DFO-diazirine probes. The control azir-06, which lacks the DFO moiety, also exhibited a preference for tyrosine, aspartic acid, and glutamic acid (Figure 3.9, 3.68).

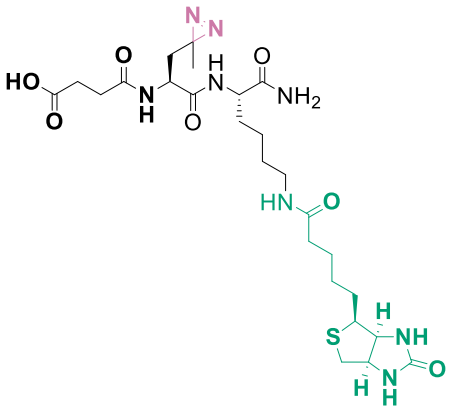

Figure 3. 9: Structure of azir-ctrl.

3.3.6 Reactivity profiling of DFO-diazirines with pre-linked optical and pulldown tags

The second-generation DFO-diazirine probe strategy effectively addressed the challenges encountered with the first-generation probes, notably enhancing the visualization of protein labeling in vitro with both BSA and FoxA through in-gel fluorescence and Western blotting (Figure 3.10 A and B). However, the blue-shifted excitation wavelength of M-DFO-azir-04 proved suboptimal for our available instrumentation, hindering efficient excitation and visualization.

Subsequent MS/MS analysis of Fe-DFO-azir-06 revealed targeting of Tyr_{525} and Tyr_{700}, located at the top of the FoxA beta-barrel, alongside Glu_{316} at the barrel's base and Glu_{257} within the cork domain. While Ga-DFO-azir-06 also targeted Glu_{257}, its detection as Fe-DFO-azir-06 confirmed our suspicion of metal dissociation during sample processing, followed by reformation of the complex with trace iron. Although M-DFO-azir-06 probes did not target amino acids situated as closely to the FoxA binding pocket as Fe-DFO-azir-02 (Figure 3.7), they still recapitulated the reactivity profile observed with single amino acid residues (Figure 3.10 C).

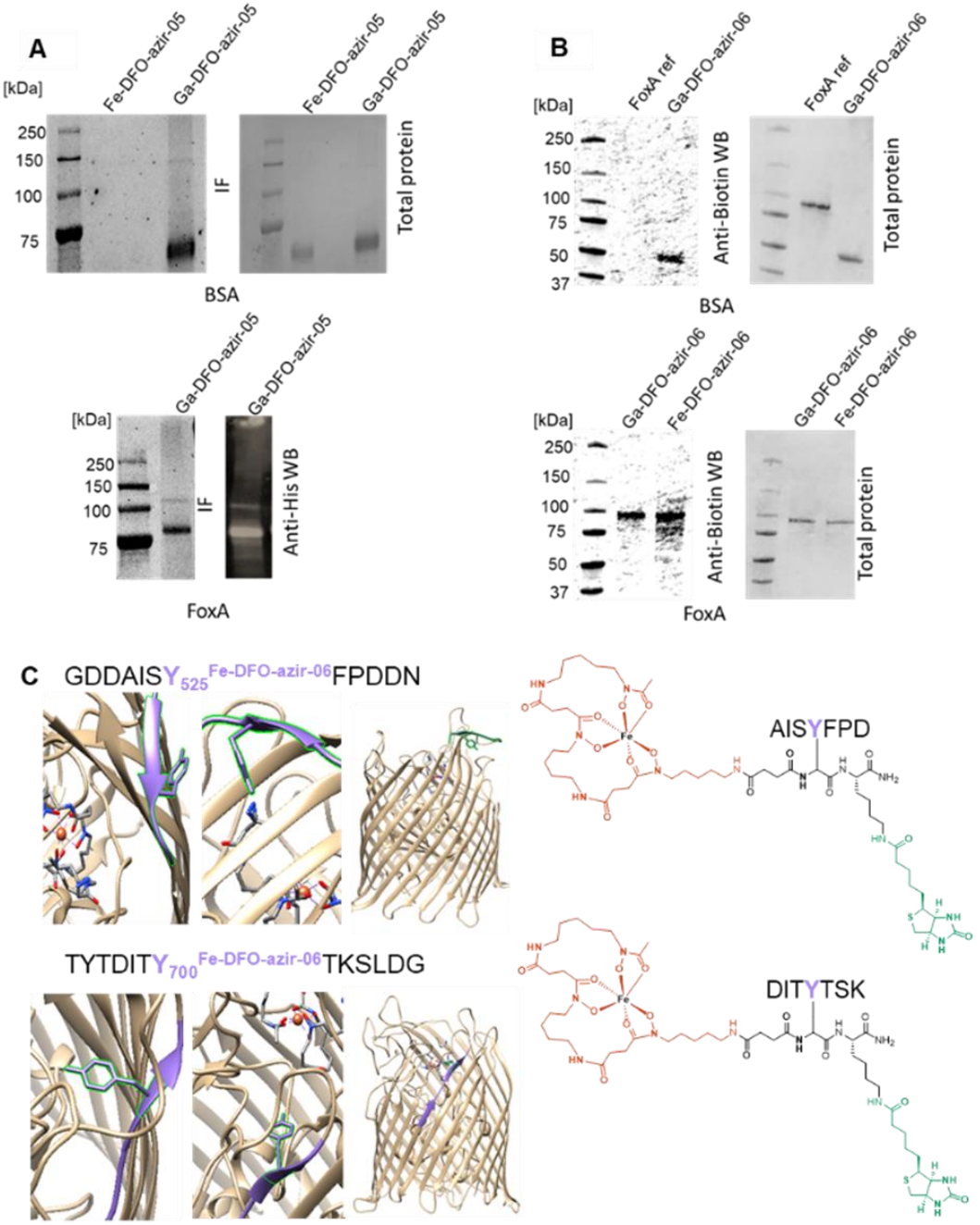

Figure 3. 10: A) M-DFO-azir-05 labeling of BSA and FoxA in vitro. Photo-irradiation (15 min) was performed prior to a 30-minute incubation for FoxA and with no incubation for BSA. B) In the FoxA co-crystal structure with Fe-DFO-azir-01, amino acids labeled with Fe-DFO-azir-06 are highlighted in green, and the protein fragment is shown in blue and orange.

3.4 Summary and conclusion

This study presents a systematic approach to the rational design and optimization of photoaffinity probes, specifically targeting the siderophore outer membrane transporter FoxA in *P. aeruginosa*. Leveraging the structural insights from the Fe-D1/FoxA co-crystal structure, we achieved a targeted selection of a photoreactive group, ensuring optimal compatibility with the putative siderophore transporter's binding pocket. Mass spectrometry validated the design strategy, demonstrating that the DFO-diazirine probes successfully conjugated to the same amino acid residues identified through single amino acid screening. This highlights the power of structure-guided design in developing photo-affinity probes. Our investigations further confirm the critical role of linker length in achieving effective labeling. As demonstrated, precise control over this parameter is important to ensure probe accessibility and reactivity within the binding pocket.

Acknowledging the challenges associated with CuAAC chemistry for the alkyne-functionalized probes, we explored a pre-linked strategy in our second-generation probes. This approach, while it is not as compact and minimal as the first-generation probe design including click-reactive alkynes, offers a viable pathway to circumvent limitations posed by post-crosslinking conjugation to install a fluorophore or affinity tag. This strategy is supported by precedent in the field where siderophores conjugated with biotin and fluorophores have been employed to study select high-affinity binding proteins.[139,140] Moving forward, we will be validating the efficacy of these siderophore photoaffinity probes in live cell experiments, aiming to demonstrate their ability to label known and unknown siderophore-binding proteins in live cells. This research demonstrates that photo affinity labeling can be applied to siderophores to enable the prospective identification of known and unknown bacterial binding proteins.

3.5 Experimental and supporting information.

3.5.1 General materials

All starting materials were purchased from Sigma-Aldrich, Ambeed, Fisher, Iris Biotech GmbH, TCI America, or Thermofisher and used without further purification. The UV-light was obtained from Waveform (realUV™ LED Flood Light, 365nm, 20W).

3.5.2 General methods and characterization

Nuclear magnetic resonance: ^{1}H and ^{13}C NMR spectra were collected on a 700 or 500 MHz AVANCE III Bruker instrument or a Bruker Advance 500 MHz (DCH cryoprobe) or 600 MHz (TCl-F cryoprobe) at 25 °C. Data were acquired under automation with iconNMR and processed with MestRenova. Chemical shifts are reported in parts per million (ppm).

Mass spectrometer methods: High-resolution mass spectrometry was performed on a Bruker Impact II QTOF or at the UW-Madison Chemistry Paul Bender Chemical Instrumentation Center Facility using a Thermo Q Exactive™ Plus (electrospray ionization-quadrupole-ion trap) mass spectrometer. Low-resolution LC-MS was conducted using an Agilent 1260 Infinity II LC system coupled with an Agilent InfinityLab LC/MSD system, equipped with a single quadrupole and spray ionization source. A Phenomenex Luna C18 column (250 mm × 21.2 mm, 100 Å, AXIA packed) was used. The mobile phase consisted of 0.1% formic acid in water (Method A), and 0.1% formic acid in acetonitrile (Method B), with a flow rate of 0.8 mL/min. UV detection was performed at 254 and 220 nm. The gradient method was as follows: 0-3 min, 5% B; 3-10 min, 5-95% B; 10-13 min, 95% B; 13-13.5 min, 95-5% B; 13.5-16 min, 5% B. MALDI measurements were carried out on a Bruker. Microflex LRF MALDI TOF. Samples were prepared by

concentrating the protein, dissolving it in 50% acetonitrile in water (containing 0.1% formic acid), and mixing with SA (sinapic acid) matrix in a 1:1 and 1:3 ratio for analysis.

Liquid chromatography methods: Preparative HPLC was performed using either a Shimadzu HPLC-20AR equipped with a binary gradient pump, UV-vis detector, and manual injector, or an Agilent 1260 Infinity II system equipped with a binary gradient pump, UV-vis detector, and manual injector. A Phenomenex Luna C18 column (250 mm × 19 mm, 100 Å, AXIA packed) was used. For preparative purification (Method B), the mobile phase consisted of 0.1% formic acid in water (A) and 0.1% formic acid in acetonitrile (B), with a flow rate of 15 mL/min. UV detection was performed at 190 and 220 nm for the ligand and Ga complex of DFO-azir-01, 02, 03, and 06, and at 280 and 425 nm for the Fe complex and DFO-azir-04 and 05 at 280 and 425 nm. The Analytical HPLC was performed using an Agilent 1260 Infinity II system equipped with a binary gradient pump, UV-vis detector, and autoinjector. A Phenomenex Luna C18 column (150 mm × 3 mm, 100 Å, AXIA packed) was used. source. A Phenomenex Luna C18 column (250 mm × 21.2 mm, 100 Å, AXIA packed) was used. For gradient (Method C), the mobile phase consisted of 0.1% formic acid in water (A) and 0.1% formic acid in acetonitrile (B), with a flow rate of 0.8 mL/min. UV detection was performed at 254 and 220 nm. The gradient was as follows: 0-5 min, 95% A; 5-24 min, 5-95% B. Phenomenex Yarra-2000 size exclusion column using an isocratic gradient (Method D) 3 μm, 145 Å, 150 × 7.8 mm; Solvent: 30 mM MOPS (3-(N-morpholino)propanesulfonic acid), 100 mM KCl, pH = 7.0; with a flow rate of 0.8 mL/min).

Compound concentration determination: Concentrations of Ga and Fe metal complexes were determined using an Agilent 5110 ICP-OES. A seven-point standard calibration curve was generated for gallium and iron, with R^2 values of 0.999. Sample concentrations were determined

based on this calibration curve. Ligand compound concentrations were determined through iron titration monitored by UV-Vis spectroscopy using the Fe-DFO absorbance band (ε = 2460 $cm^{-1}M^{-1}$ at 425 nm)[141] or by following the reported absorbance of the fluorophore for M-DFO-azir-04 (ε = 34000 $cm^{-1}M^{-1}$ at 409 nm), [142] and M-DFO-azir-05 (ε = 43000 $cm^{-1}M^{-1}$ at 445 nm). [143]

Bacterial culture OD_{600}: Bacterial culture OD600 was determined using a BioTek Epoch 2 microplate reader and Gen5 data analysis software.

Imager: Gel fluorescent imaging was obtained using either an iBright™ FL1500 Imaging System or a Typhoon 9400 Variable Mode Imager.

3.5.3 Synthesis and characterization of DFO-diazirine probes

3.5.3.1 Synthesis of DFO-diazirine probes

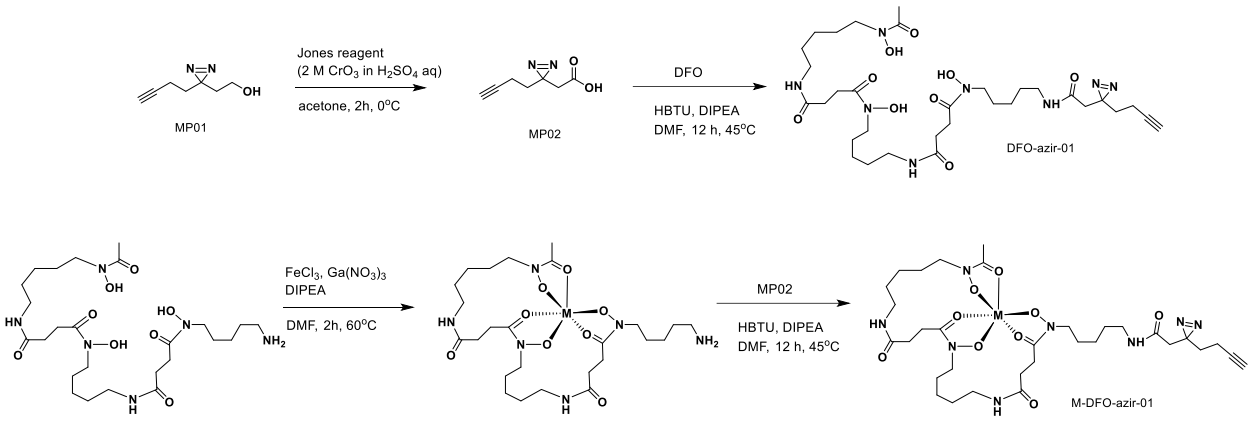

Scheme 3. 2: Synthetic scheme of M-DFO-azir-01.

MP01: *2-(3-(But-3-yn-1-yl)-3H-diazirin-3-yl) acetic acid*: ones reagent (1 mL, 2 M CrO_3 in aqueous H_2SO_4) was added dropwise to a stirred solution of 2-(3-(but-3-yn-1-yl)-3H-diazirin-3-yl)ethanol (AmBeed CAS# 1450754-41-2) (50.0 mg, 0.365 mmol, 1.00 eq) in acetone (5 mL) at 0

°C. The reaction mixture was stirred at room temperature for 2 h and then quenched with isopropanol (3 mL). The mixture was filtered through filter paper,[144] dried with Na_2SO_4, and evaporated to dryness. The crude product was used without further purification. Calculated mass MP01 ($C_7H_8N_2O_2$): 152.15; found 151.0 $[M-H]^-$.

DFO-azir-01: N1-(5-(2-(3-(but-3-yn-1-yl)-3H-diazirin-3-yl)acetamido)pentyl)-N1-hydroxy-N4-(5-(N-hydroxy-4-((5-(N-hydroxyacetamido)pentyl)amino)-4-oxobutanamido)pentyl) succinimide : N,N-Diisopropylethylamine (DIPEA, 4 eq, 1.46 mmol, 254 µL) was added to a stirring solution of MP01 in dry dimethylformamide (DMF). The mixture was stirred for 10 min before adding benzotriazol-1-yloxytripyrrolidinophosphonium hexafluorophosphate (PyBOP, 1 eq, 0.365 mmol, 189.9 mg). After an additional 10 min, deferoxamine (DFO, 1 eq, 0.365 mmol, 204 mg) was added, and the reaction was stirred overnight at 45 °C. The reaction mixture was evaporated to dryness and purified by preparative HPLC (method B) to afford DFO-azir-01 in 6% yield. Calculated mass DFO-azir-01 ($C_{32}H_{51}N_8O_9$): 694.40; found 695.41 $[M+H]^+$. Retention time (Method A): 7.23 min.

^{1}H NMR (700 MHz, DMSO) δ 9.65-9.61 (H=l, 2H), 7.88 (H=k, 1H), 7.78,-7.77 (H=j, 2H), 3.46-3.44(H=i, 6H), 3.05- 2.97 (H=h, 6H), 2.82-2.81 (H=e, 1H), 2.77-2.54 (H=f, 4H), 2.27-2.21 (H=g, 4H , m), 2.19 (H=d, 2H), 1.97- 1.96 (H=c, 3H, S), 1.64-1.62 (H=m, 2H), 1.51-1.34 (H=b, 14H m), 1.23-1.18 (H=a, 6H m).

^{13}C NMR (500 MHz, DMSO) δ 171.94-171.28 (C=j, 2C), 170.11 (C=l, 3C), 166.92, 157.81, 157.64, 82. 75 (C=o, 1C), 71.77 (C=o, 1C), 38.41 (C=h, 3C), 38.38 (C=g, 2C), 31.87 (C=b, 2C), 29.86 (C=f, 3C), 28.81, 28.65 (C=e, 2C), 27.55, 26.69, 26.02 (C= d, 1C), 25.96 (c=a, 1C), 23.40 (c=a, 1C).

M-DFO: DFO (60 mg, 0.108 mmol, 1 eq.) was dissolved in DMF (2 mL). In a separate vial, $Ga(NO_3)_3$ (41.42 mg, 0.162 mmol, 1.5 eq) or $FeCl_3$ (26.1 mg, 0.162 mmol, 1.5 eq) was dissolved in DMF followed by the addition of DIPEA (3 eq). The resulting solution was added to the DFO solution, and the mixture was stirred for 1 h at 60 °C and 1 h at room temperature. The reaction mixture was used without purification in the subsequent reaction.

M- DFO-azir-01: Compound MP02 (15 mg, 0.108 mmol, 1 eq) was dissolved in DMF (3 mL). DIPEA (75.25 µL, 0.432 mmol, 4 eq) was then added, and the mixture was stirred for 10 min. PyBOP (1 eq., 0.365 mmol, 189.9 mg) was subsequently added, followed by another 10 min of stirring. A solution of Fe-DFO or Ga-DFO (66.25 mg, 0.108 mmol, 1 eq) in dry DMF was then introduced, and the reaction mixture was stirred at 45 °C overnight. The solvent was removed under vacuum, and the product was purified by preparative HPLC (Method B) to yield M-DFO-azir-01 as a white solid (Ga complex) or reddish orange solid (Fe complex) in 13% yield.Calculated mass for Fe-DFO-azir-01 ($C_{32}H_{51}FeN_8O_9$): 747.65; found 748.32 $[M+H]^+$. Retention time (Method A): 6.91 min. Ga-DFO-azir-01 ($C_{32}H_{51}GaN_8O_9$):761.53; found 761.31 $[M+H]^+$. Retention time (Method A): 6.94 min.

^{1}H NMR Ga-DFO-azir-01 (700 MHz, DMSO) δ 7.89-7.87 (H=k, 1H m), 7.60-7.57 (H=j, 2H s), 3.88-3.41 (H=i, 6H m), 3.02-2.85 (H=h, 6H), 2.82-2.81 (H=e, 1H m), 2.66-2.34 (H=f, g), 2.20-2.17 (H=d, 2H s), 2.04-2.03 (H=c, 3H s), 1.73-1.60 (H=a, 6H m), 1.41-1.09 (H=b, 14H m).

^{13}C NMR Ga-DFO-azir-01 (500 MHz, DMSO) δ 174.53 (C=j, 2C), 170.52, 170.28 (C=t, 1C), 166.95, 166.93, 163.05, 162.55, 161.03 (C=l, 3l), 83.24 (C=o, 1C), 71.75 (C=n, 1C), 38.44 (C=h, 4C), 37.52 (C=g, 3C), 31.88 (C=m, 1C), 30.43 (C=b, 2C), 30.36 (C=f, 3C), 26.72 (C=e, 2C), 25.39 (C=c, 5C), 23.26, 21.99 (c=a, 1C).

M-DFO-azir-02,03,04,05, and 06 solid phase peptide synthesis: Probes M-DFO-azir-03, 04, 05, and 06 were synthesized on a 0.093 mmol scale using Rink Amide (RA) resin (100 mg, 0.62 mmol/g, 1 eq.). The RA resin was swollen in DCM (3 mL) and DMF (3 mL) for 1 min, repeated three times for each solvent. The first amino acid (153, 0.124 mmol, 2 eq) was loaded onto the resin using PyBOP (48.4 mg, 0.092 mmol, 1.5 eq) as a coupling reagent in the presence of DIPEA (43.2 µL, 0.248 mmol, 4 eq.). The first coupling reaction proceeded at room temperature for 16 hours. A standard capping step was performed using an acetic anhydride/pyridine mixture (3:2) for 30 min. The Fmoc group was subsequently removed by treating the resin with 20% piperidine in DMF (3 mL) for 20 min. The 4-methyltrityl (Mtt) group was deprotected by washing with 50 mL of 1% TFA in DCM until the wash solution was colorless. Subsequent amino acids were coupled using the same procedure until the full sequences were assembled. Succinic anhydride was loaded onto the resin in the presence of DIPEA (43.2 µL, 0.248 mmol, 4 eq.) for 1 h at room temperature. The Fmoc group on the N-terminus was then deprotected, and DFO or M-DFO (0.0761 mmol, 2 eq) was coupled using PyBOP (48.4 mg, 0.092 mmol, 1.5 eq) as a coupling reagent in the presence of DIPEA (43.2 µL, 0.248 mmol, 4 eq.) for 16 h. The compound was cleaved from the resin by treating it with a mixture of TFA/TIS/H_2O (95%/2.5%/2.5%) for 1 h at room temperature. The product was precipitated in cold 1:1 hexane/diethyl ether, dissolved in water/acetonitrile, and purified by preparative HPLC (method B) to yield M-DFO-azir-02 (21% yield), M-DFO-azir-03 (41% yield), M-DFO-azir-04 (21% yield), M-DFO-azir-05 (18% yield), and M-DFO-azir-06 (19% yield) (S.I. Schemes 2, 3, and 4).

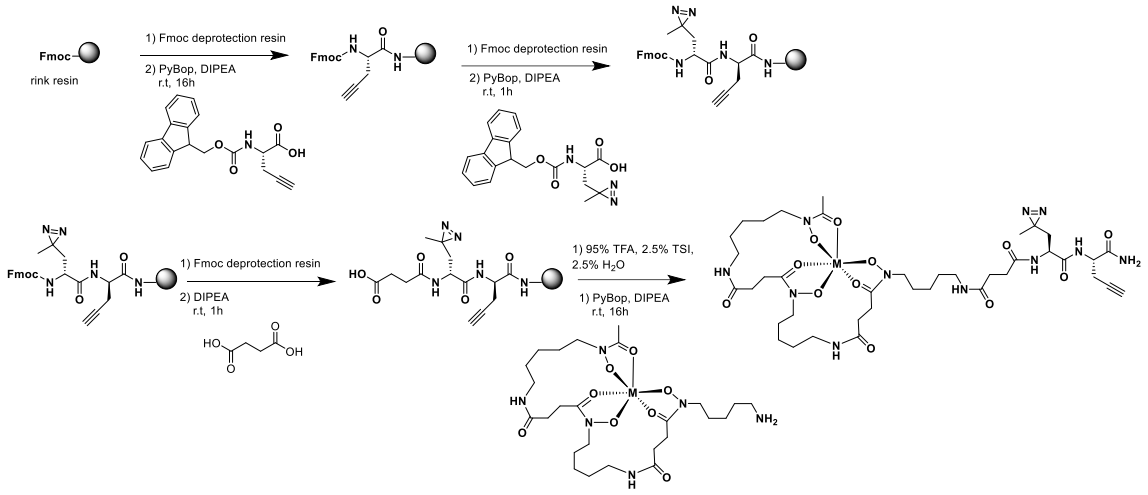

Scheme 3. 3: Solid phase peptide synthesis of M-DFO-azir-02.

Calculated mass ($C_{39}H_{65}N_{11}O_{12}$): 879.48; found 902.4706 $[M+Na]^+$, retention time (method A): 8.1min. Calculated mass Fe-DFO-azir-02 ($C_{39}H_{62}FeN_{11}O_{12}$: 932.39; found 933.4001 $[M+H]^+$, retention time (method A): 6.78 min. Calculated mass Ga-DFO-azir-02 ($C_{39}H_{62}GaN_{11}O_{12}$: 945.38; found 946.4001 $[M+H]^+$, retention time (method A): 7.61 min.

DFO-azir-02 ^{1}H NMR (500 MHz, DMSO) δ 9.73 (H=l, 3H), 8.36-8.12 (H=k, 2H d), 7.93-7.80 (H= j, 3H m), 7.17-7.13 (H=n, 2H s), 4.24-4.02 (H=q, 2H m), 3.46- 3.44 (H=i, 6H), 3.00-2.86 (H=h,6H m), 2.8 (H=p, 1H),2.59-2.5 (H=f, 8H m), 2.38-2.36 (H= g, 6H m), 1.96 (H=c, 3H S), 1.96-1.88 (H=e, 2H) 1.51-1.36 (H=b, 12H m), 1.25-1.20 (H=a, 6H m), 1.01 (H=m, 3H s).

DFO-azir-02 ^{13}C NMR (500 MHz, DMSO) δ 172.51 (C=w, 1C), 172.0 (C=j, 3C)2, 171.65-171.49 (C=r, 2C), 170.95 (C=l, 3C) , 80.90 (C=o, 1C), 72.87(C=p, 1C), 51.87(C=q, 2C), 49.28, 47.24, 46.93, 40.29 , 38.68, 38.56 (C=h, 4C), 36.00 (C=g, 3C), 31.05 (C=e, 4C), 28.95, 28.88 (C=f, 7C) , 27.76, 26.19 (C=d, 1C), 24.65, 23.71, 23.66 (C=a, 1C), 21.37, 20.51(C= K, 1C).

Ga-DFO-azir-02 ^{1}H NMR (500 MHz, DMSO) δ 8.36-8.35 (H=k, 1H), 7.93-7.91 (H=j, 3H), 7.59-7.57 (H= j, 2H),7.18-7.11 (H=n, 2H d), 4.23-4.00 (H=q, 2H m), 3.58-3.41(H=i, 6H m),3.02-2.87(H=h, 6H m), 2.82- 2.81 (H=p, 1H), 2.63-2.52 (H=g, 6H t), 2.42- 2.13 (H=f, 8H m), 2.02 (H=c, 3H S), 1.91-1.88 (H=e, 2H d), 1.73- 1.06 (H=a , b, 20H m) 1.01(H=m, 3H s).

Ga-DFO-azir-02 ^{13}C NMR (500 MHz, DMSO) δ 172.40 (C=j, 2C), 171.48 (C=w, 1C), 171.39-170.21 (C=r, 2) , 80.76 (C=o, 1C), 72.75 (C=p, 1C) , 51.72 (C=q, 2C), 38.58 (C=h, 6C), 35.80 (C=g, 2C), 30.88 (C=b, 2C), 30.59 (C=f, 3C), 28.78 (C=e, 6C), 26.57 (C= d, 1C), 24.50 (C=c, 7C), 21.20 (c=a, 1C), 19.65 (C=k, 1C).

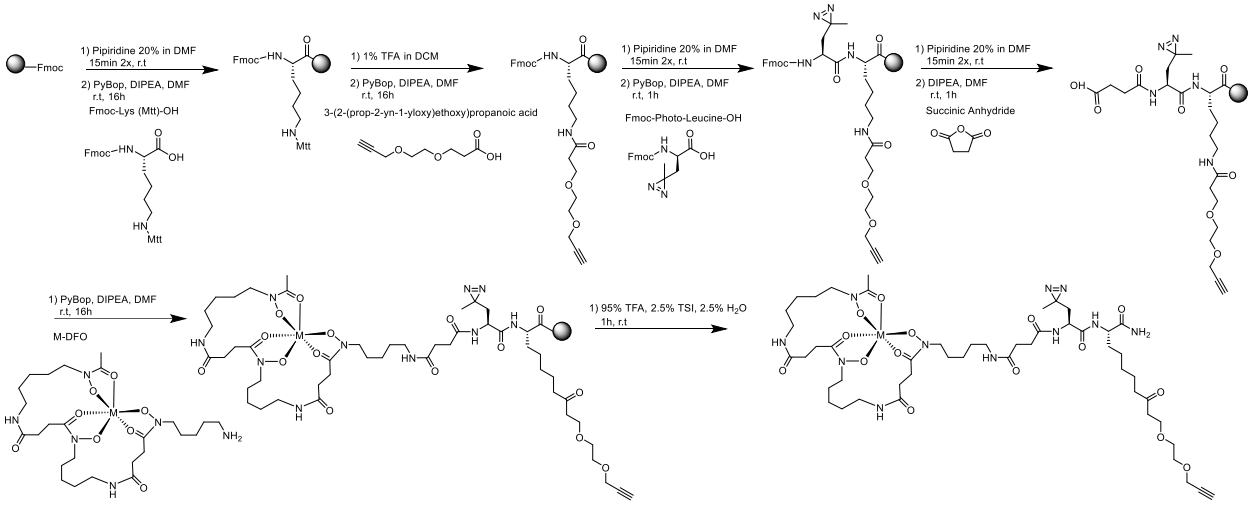

Scheme 3. 4: Solid phase peptide synthesis of M-DFO-azir-03

Calculated mass DFO-azir-03 ($C_{48}H_{82}N_{12}O_{15}$): 1067.25; found 1067.6079 $[M+H]^{+}$, retention time (method A): 8.2 min. Calculated mass Fe-DFO-azir-03 ($C_{48}H_{79}FeN_{12}O_{15}$: 1120.07; found 1120.5213 $[M+H]^{+}$, retention time (method A): 8.10 min. Calculated mass Ga-DFO-azir-03 ($C_{48}H_{79}GaN_{12}O_{15}$: 1133.95; found 1153.4929 $[M+Na]^{+}$, retention time (method A): 7.93 min.

DFO-azir-03 ^{1}H NMR (500 MHz, DMSO) δ 9.64 (H=l, 3H), 8.29-8.27 (H=k, 2H m), 7.91-7.79 (H=j, 3H),7.03-6.98 (H=n, 2H m), 4.13-4.12 (H=s, 2H d), 4.07-4.01(H=q, 2H m), 3.59-3.48 (H=d,

6H m), 3.46-3.43 (H=i,6H m), 3.40-3.39 (H=p, 1H t), 3.01-2.97 (H=h, 8H m), 2.59-2.56 (H=g, 6H m), 2.42-2.25 (H=f, 8H m), 1.96 (H=c, 3H s), 1.92-1.89 (H=o, 2H), 1.73-1.64 (H=r, 2H m),1.54-1.31 (H=b, 14 H m, 1.24-1.18 (H=a, 8H m), 1.01 (H= m, 3H s).

Ga-DFO-azir-03 DFO-azir-03 ^{13}C NMR DFO-azir-03 (500 MHz, DMSO) δ 173.54 (C=w, 1C), 172.24 (C=j, 4C), 171.96-171.39 (C=r, 2C), 170.69 (C=l, 3C) ,80.32 (C=t, 1C), 77.06 (C=s, 1C), 69.22 (C=o, 2C), 66.84 (C=n, 2C), 57.48 (C= p, 1C), 52.68 C=q, 2C), 49.08, 38.52 (C=h, 4C), 35.83 (C=g, 3C), 30.59 (C=e, 4C), 29.91(C=f, 7C) ,28.73 (C=m, 1C), 27.57 (C=c, 3C), 26.03(C=d, 1C), 23.50 (C=a, 1C), 20.34 (C= K, 1C).

Ga-DFO-azir-03 ^{1}H NMR (500 MHz, DMSO) δ 8.50-8.33 (H=k, 2H), 7.97-7.95 (H=j, 3H), 7.79 (H=v, 1H), 7.03-6.98 (H=n, 2H m), 4.13 (H=s, 2H d), 4.05-4.03 (H=q, 2H m), 3.59-3.38 (H= i ,d, 13H m), 3.01-2.97 (H=h, 8H m), 2.74-2.54 (H=g, 6H m), 2.42- 2.27 (H=f, 8H m), 2.03 (H=c, 3H s), 1.92-1.88 (H=e, 2H m), 1.61-1.16 (H= a, b, r, 24H m), 1.01(H= m, 3H s).

^{13}C NMR Ga-DFO-azir-03 (500 MHz, DMSO) δ 173.69 (C=j, 3C), 172.41 (C=w, 1C), 171.53-170.36 (C=r, 2C), 165.83 (C=l,3C), 80.48(C=t, 1C), 77.23 (C=s, 1C), 69.37 (C=o, 2C), 67.00 (C=n, 2C), 57.64 (C= p, 1C), 49.26 (C=q, 2C), 38.74 (C=h, 5C), 35.98 (C=g, 3C), 31.28 (C=b, 2C), 31.09 (C=m, 1C), 30.77(C=f, 3C), 28.94 (C=e, 5C), 26.72 (c=d, 2C), 24.67 (C=c, 5C), 23.09 (c=a, 1C), 19.80 (C= K, 1C), 16.97.

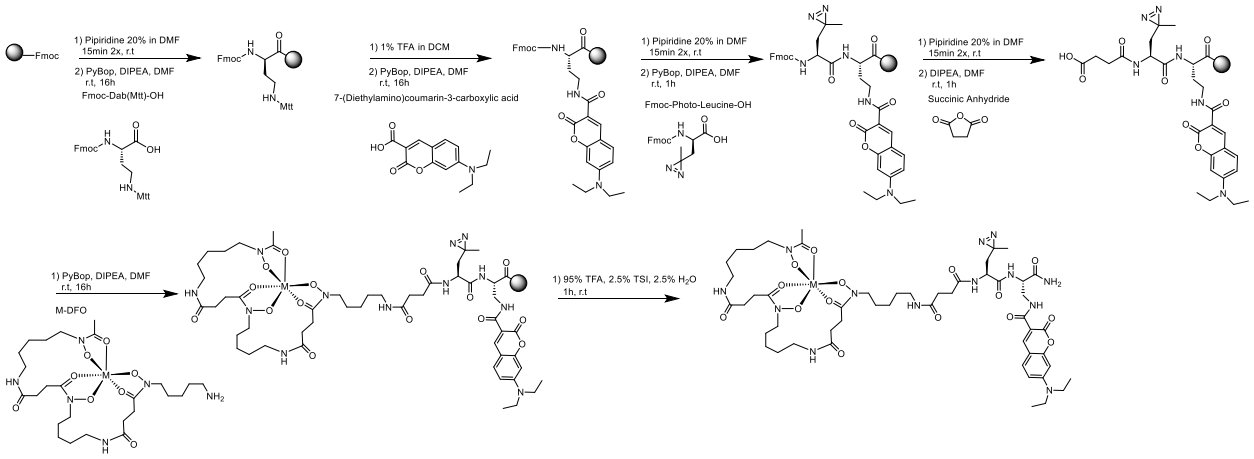

Scheme 3. 5: Solid phase peptide synthesis of M-DFO-azir-04.

Calculated mass DFO-azir-04 ($C_{52}H_{81}N_{13}O_{15}$): 1128.30; found 1128.6060 $[M+H]^+$, retention time (method A): 9.31 min. Calculated mass Fe-DFO-azir-04 ($C_{52}H_{78}FeN_{13}O_{15}$: 1181.12; found 1203.4964 $[M+Na]^+$, retention time (method A): 9.13min. Calculated mass Ga-DFO-azir-04 ($C_{52}H_{78}GaN_{13}O_{15}$: 1195.00; found 1216.4890 $[M+Na]^+$, retention time (method A): 9.20min.

DFO-azir-04 ^{1}H NMR (500 MHz, DMSO) δ 9.69-9.65 (H=l, 3H), 8.66-8.29 (H=k, 3H), 8.08-7.74 (H=j, 3H), 7.69-7.66 (H=u, 1H), 7.12-7.06 (H=n, 2H), 6.81-6.79 (H=s, 1H d), 6.62- 6.61 (H=t, 1H s), 4.15-4.03 (H=q, 2H), 3.50-3.41 (H= r,i, 12H m) 3.01-2.97 (H=h, 6H m), 2.56-2.53 (H=f, 6H), 2.43-2.24 (H=g, 8H m), 1.94 (H=c, 3H s), 1.92-1.88 (H=e, 2H m),1.58-1.36 (H=b, 12 H m), 1.23-1.19 (H=a, 6H m), 1.15-1.12 (H=o, 6H t), 1.01(H=m, 3H s).

DFO-azir-04 ^{13}C NMR (500 MHz, DMSO) δ 173.12 (C=w, 1C), 172.32 (C=j, 3C), 171.42 (C=r,1C), 170.80 (C=l, 3C), 162.27(C=i,C), 157.22 (C=p, 1C), 152.42 (C=v, 1C), 147.62 (C=z, 1C), 131.55 (C=s, 1C), 110.11 (C=o, 2C), 109.43 (C=t, 1C), 107.63, 95.87 (C=y, 1C), 50.80(C=q, 2C), 44.32 (C=x, 2C), 38.51 (C=h, 4C), 31.58(C=m, 1C), 30.97, 30.62(C=e, 4C), 28.80 (C=f, 7C), 28.71, 27.62(C=c, 3C), 26.03(C=d, 1C), 23.50 (C=a, 2C), 20.35(C= K, 1C), 12.3 (C=u, 2C).

Ga-DFO-azir-04 ^{1}H NMR (500 MHz, DMSO) δ 8.66-8.24 (H=k, 4H), 8.06-7.67 (H=j,3H), 7.57 (H=u, 1H), 7.11-7.06 (H=n, 2H d), 6.81-6.79 (H=s, 1H d), 6.62-6.61 (h=t, 1H s), 4.16-4.03 (H=q, 2H m), 3.57-3.46 (H=r, 6H m), 3.27-3.02 (H=i, 6H m), 3.00-2.82 (H=h, 6H m), 2.78-2.58 (H=g, 6H m), 2.45-2.13 (H=f, 8H), 2.02 (H=c , 3H s), 1.95-1.91 (H=e, 2H m), 1.83-1.22 (H= a,b, 18H m), 1.15-1.11 (H=0, 6H t), 1.02 (H=m, 3H s)

Ga-DFO-azir-04 ^{13}C NMR (500 MHz, DMSO) δ 173.08 (C=j, 2C), 172.34 (C=w, 1C), 171.41(C=v, 1C), 170.18 (C=r, 2C), 162.25 (C=i,C), 159.87 (C=l,3 C), 157.21 (C=v, 1C), 147.62 (C=z, 1C), 131.56 (C=s, 1C), 110.11 (C=o, 2C), 109.42 (C=t, 1C), 95.85 (C=y, 1C), 62.33 (C=n, 1C), 50.78 (C=q, 2C), 38.58 (C=h, 4C), 37.04, 35.74 (C=g, 2C), 31.58 (C=b, 2C), 30.96 (C=m, 1C), 30.61 (C=f, 3C), 28.75 (C=e, 6C), 26.55 (c=d, 2C), 24.52 (C=c, 6C), 21.50 (c=a, 1C), 19.63 (C= k, 1C), 12.30 (C=u, 2C).

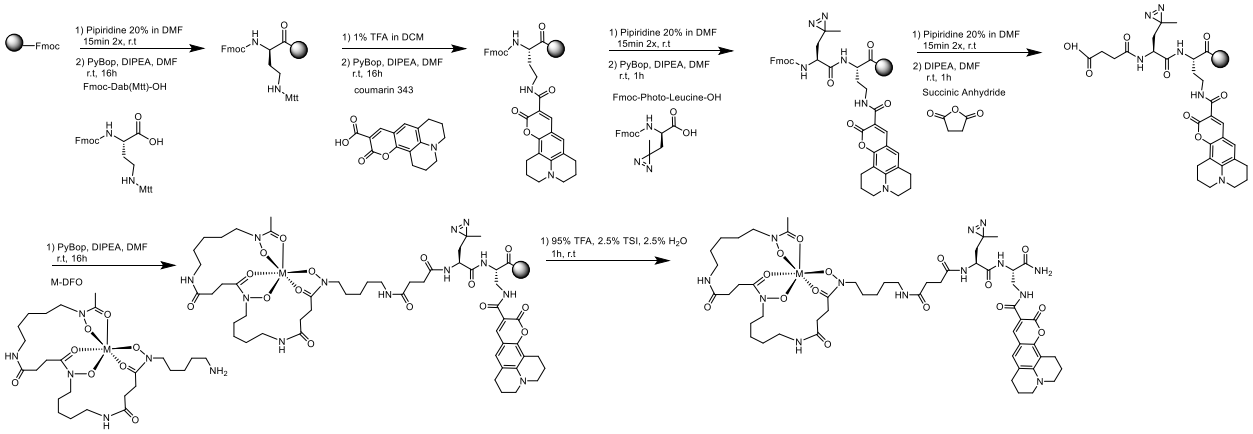

Scheme 3. 6: Solid phase peptide synthesis of M-DFO-azir-05.

Calculated mass DFO-azir-05 ($C_{54}H_{81}N_{13}O_{15}$): 1152.32; found 1174.5872 $[M+Na]^{+}$, retention time (method A): 9.31 min. Calculated mass Fe-DFO-azir-05 ($C_{54}H_{78}FeN_{13}O_{15}$: 1205.14; found 1205.5167 $[M+H]^{+}$, retention time (method A): 9.13 min. Calculated mass Ga-DFO-azir-05 ($C_{54}H_{78}GaN_{13}O_{15}$: 1219.02; found 1240.4892 $[M+Na]^{+}$, retention time (method A): 9.12min.

DFO-azir-05 ^{1}H NMR (500 MHz, DMSO) δ 9.72 (H=l, 3H), 8.67-8.49 (H=k, 3H m), 8.07-7.75 (H=j, 3H m), 7.26 (H=p, 1H s), 7.20-7.05 (H=n, 2H d), 4.14-4.02 (H=q, 2H m), 3.46-3.41 (H=r, 4H m), 3.01-2.97 (H=i, 6H m), 2.96-2.70 (H=h, 8H m), 2.62-2.55 (H= s, 4H m), 2.43- 2.33 (H=g, 6H m), 2.27-2.07 (H=f, 6H m), 1.96 (H= c, 3H s), 1.91-1.75 (H=e, 8H m),1.53-1.33 (H=b, 12H m), 1.28- 1.17 (H=a, 8H m), 1.01 (H=m, 3H s).

DFO-azir-05 ^{13}C NMR (500 MHz, DMSO) δ 173.60 (C=w, 1C), 172.82 (C=j, 3C), 171.90 (C=v, 1C), 171.78-171.24 (C=r, 1C), 170.59 (C=l,3C), 163.02 (C=j,1 C), 162.28 (C=i, 1C), 152.55 (C=u, 1C), 147.92 (C=y, 2C), 127.62(C=z, 2C), 119.90-119.09 (C=x, 1C),107.84 (C=o,1C), 51.30 (C=n,1C), 50.01 (C=q, 2C), 49.62 (C=p, 2C), 39.00 (C=h, 4C), 36.22 (C=g, 4C), 32.08 (C=m, 1C), 29.28 (C=e, 4C), 29.19 (C=f, 7C), 27.29(C=c, 3C), 26.51(C= d, 2C), 22.56 (C=a, 1C), 21.02 (C=t, 2C), 20.08 (C= K, 1C).

Ga-DFO-azir-05 ^{1}H NMR (500 MHz, DMSO) δ 8.68- 8.27(H=k, 3H), 8.03-7.66 (H=j, 3H m), 7.58(H=p, 1H s), 7.16-7.06 (H=n, 2H d), 4.40, 4.16-4.02 (H=q, 2H m),3.82-3.52 (H=r, 4H m), 3.51-3.44 (H=i, 6H m), 3.2-3.17 (H= h, 8H), 3.05- 2.98 (H=s, 4H m), 2.76-2.52(H=g, 6H m), 2.44-2.05 (H=f, 6H m), 2.02 ((H= c, 3H s), 1.91-1.76 (H=e, 8H m), 1.54-1.35 (H=b, 12H m), 1.26-1.17 (H=a, 8H m), 1.01 (H=m, 3H s).

Ga-DFO-azir-05 ^{13}C NMR (500 MHz, DMSO) δ 173.10 (C=j, 2C), 172.35 (C=w, 1C), 171.41(C=r, 2C), 170.18 (C=v, 1C), 162.51 (C=i, 1C), 159.89 (C=l,4 C), 152.02 (C=u, 1C), 147.42 (C=y, 2C), 127.13 (C=z, 2C), 119.41 (C=x, 1C), 107.95 (C=o,1C), 63.06 (C=n,1C), 50.80 (C=q, 2C), 49.51 (C=p, 2C), 38.57 (C=h, 4C), 35.71(C=g, 3C), 31.58 (C=m, 1C), 31.26 (C=b, 2C), 30.60(C=f, 3C), 29.00 (C=s, 1C), 28.74(C=e, 5C), 26.54(C= d, 2C), 24.51(C=c, 6C), 23.20 (c=a, 1C), 20.52 (C=t, 2C),19.58 (C=k, 1C).

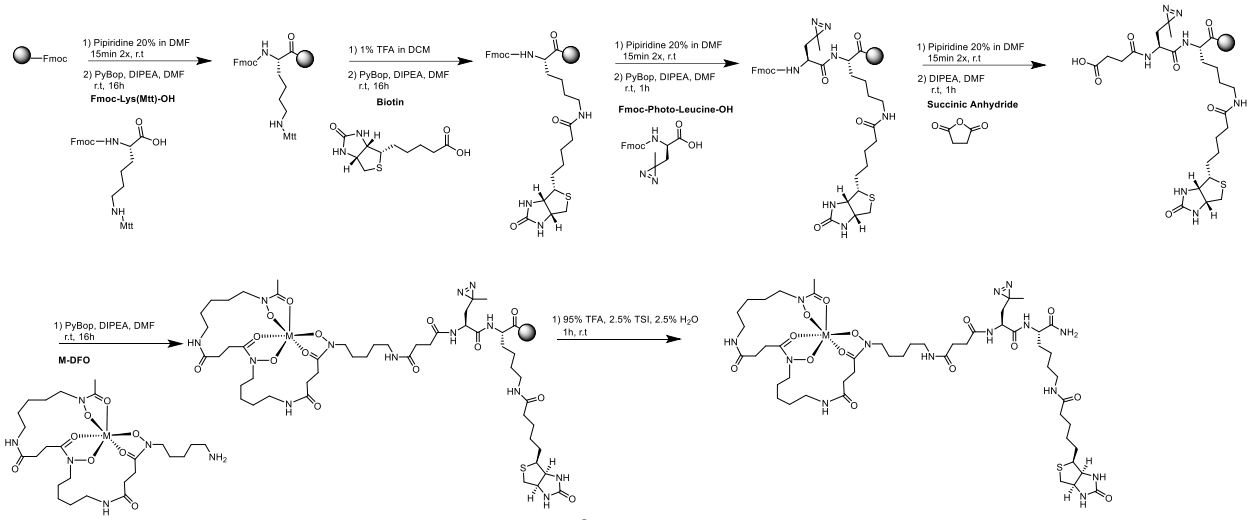

Scheme 3. 7: Solid phase peptide synthesis of M-DFO-azir-06.

Calculated mass Fe-DFO-azir-06 ($C_{50}H_{83}GaN_{14}O_{14}S$: 1206.08; found 1214.5176 $[M+Na]^+$, retention time (method A): 7.66 min. Calculated mass Ga-DFO-azir-06 ($C_{50}H_{83}GaN_{14}O_{14}S$: 1337.21; found 1227.5078 $[M+Na]^+$, retention time (method A): 7.59 min.

Ga-DFO-azir-06 ^{1}H NMR (500 MHz, DMSO) δ 8.30-8.29 (H=k, 2H), 7.94-7.72(H=j, 3H), 7.02-6.98 (H=n, 2H d), 6.41-6.35 (H=p, 2H), 4.32-4.29 (H=s, 1H m),4.14-4.11 (H=t, 1H m),4.07-4.01 (H= q, 2H m), 3.59-3.54 (H= o, 3H m), 3.10-2.80 (H= h,i, 14 H), 2.78-2.56 (H=g, 6H m), 2.42-2.33 (H=f, 6H m), 2.07-2.04 (H=d, 2H m) ,2.03 (H=c, 3H s), 1.92-1.88 (H=e, 2H m), 1.60-1.17 (H= a, b, r, 32H) , 1.00 (H= m, 3H s).

Ga-DFO-azir-06 ^{13}C NMR (500 MHz, DMSO) δ 173.51 (C=j, 2C), 172.24 (C=w, 1C), 171.79(C=v, 2C),171.36-170.63 (C=r, 2C), 162.69 (C=p, 1C), 159.85 (C=l,3 C), 61.02(C=n,2C), 59.18 (C= u, 1C), 55.39 (C=s,1C), 52.70 (C=q, 2C), 38.56 (C=h, 6C), 35.78 (C=g, 2C), 35.17(C=t, 1C), 31.12 (C=b, 2C), 30.34 (C=f, 3C), 28.85 (C=e, 5C), 28.20(C= o, 1C), 28.00 (C=m, 1C), 26.54 (C= d, 3C), 26.29(C=c, 6C), 25.27 (C=x, 1C), 22.95 (c=a, 1C), 19.59 (C=k, 1C).

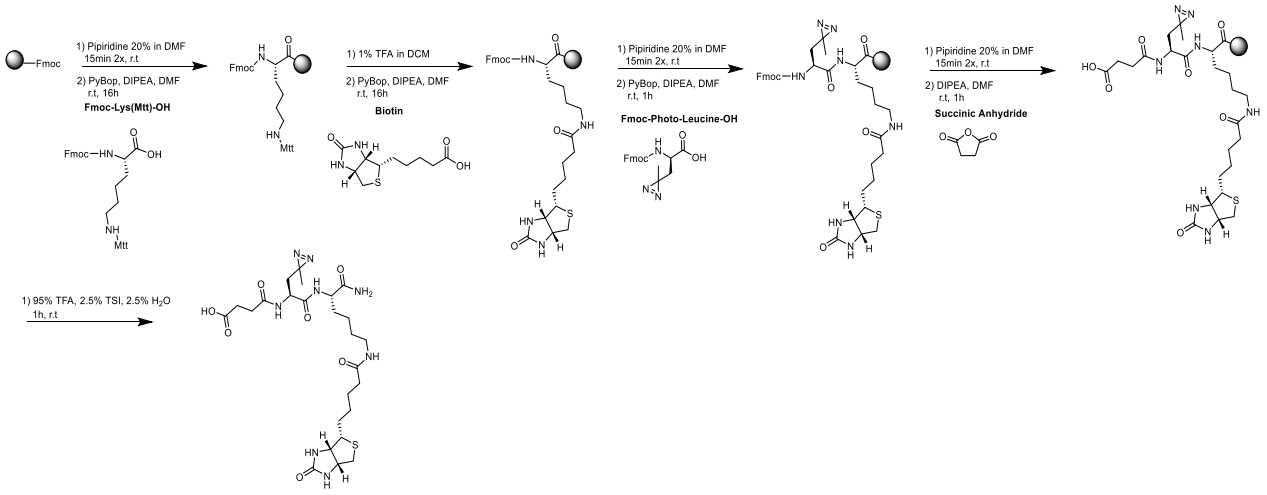

Scheme 3. 8: Solid phase peptide synthesis of azir-ctrl.

Calculated mass azir-ctrl ($C_{25}H_{40}N_8O_7S$: 595.2669; found 595.2663 $[M-H]^-$, retention time (method A): 6.90 min.

Azir-ctrl ^1H NMR (500 MHz, DMSO): δ 8.16-8.14 (H=k, 2H), 7.81-7.79 (H=C, 1H), 7.-7.18(H=n, 2H),6.37-6.29 (H=p, 2H), 4.28-4.23 (H=s, 1H m), 4.17-4.0 (H= q, 3H m), 3.01-2.75 (H= o, 3H m)**,** 2.43-2.33 (H=f, 4H m), 2.01-1.97 (H=d, 2H m) , 1.84-1.78 (H=e, 2H m), 1.50-1.13 (H= a, b, r, 10 H) , 1.00 (H= m, 3H s).

Azir-ctrl ^{13}C NMR (500 MHz, DMSO) δ 173.93 (C=c, 1C), 173.41(C=w, 1C), 171.83 (C=v, 1C), 171.41-170.53 (C=r, 2C), 162.71 (C=p, 1C), 129.64, 61.03 (C=n,1C), 59.19 (C= u, 1C), 55.39 (C=s,1C), 52.54 (C=q, 2C), 38.27 (C=h, 2C), 36.28, 35.19 (C=t, 1C), 28.86 (C=e, 3C), 28.71, 28.67, 28.54, 28.20 (C= o, 1C), 28.00 (C=m, 1C), 26.59-26.55 (C= d, 2C), 25.28 (C=x, 1C), 19.58 (C=k, 1C).

3.5.3.2 HRMS and HPLC tracer

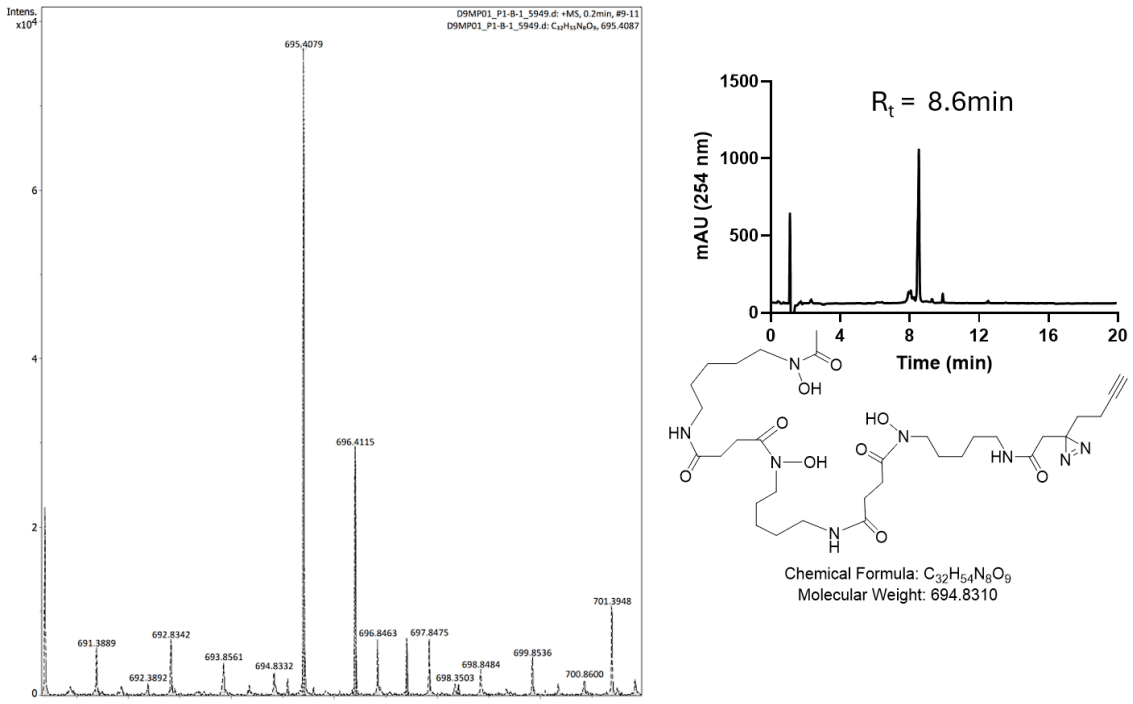

Figure 3. 11: DFO-azir-01's HRMS and HPLC trace (Method D).

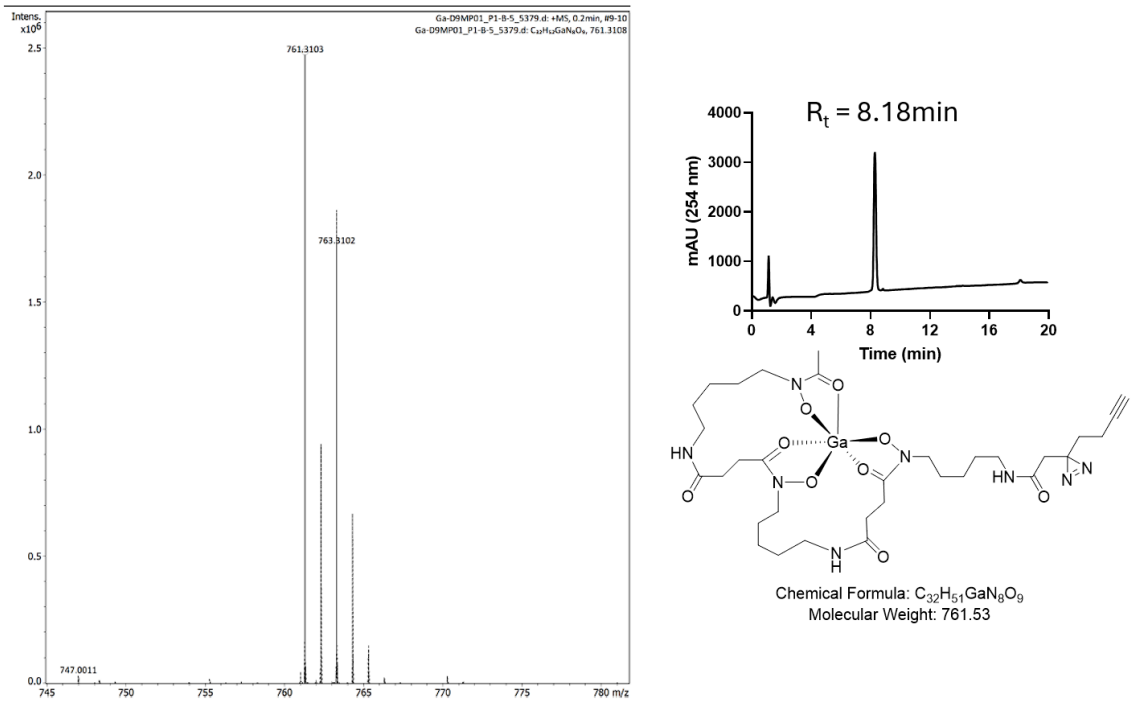

Figure 3. 12: Ga-DFO-azir-01's HRMS and HPLC trace (Method D).

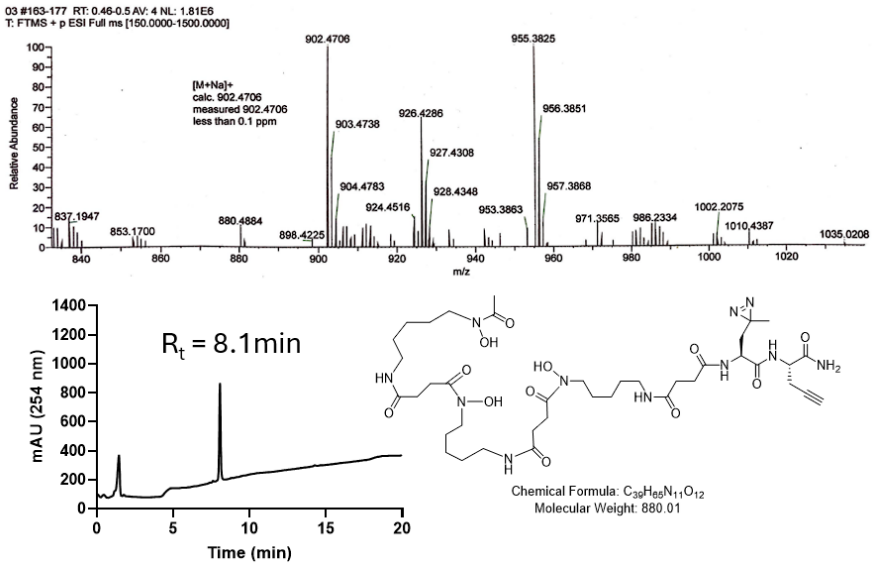

Figure 3. 13: DFO-azir-02's HRMS and HPLC trace (Method D).

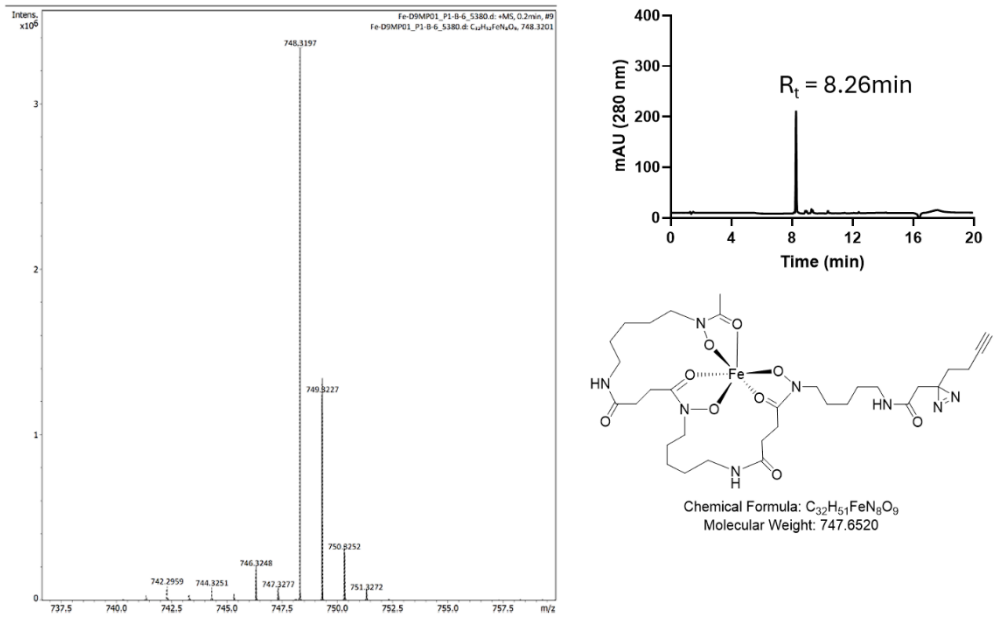

Figure 3. 14: Fe-DFO-azir-01's HRMS and HPLC trace (Method D).

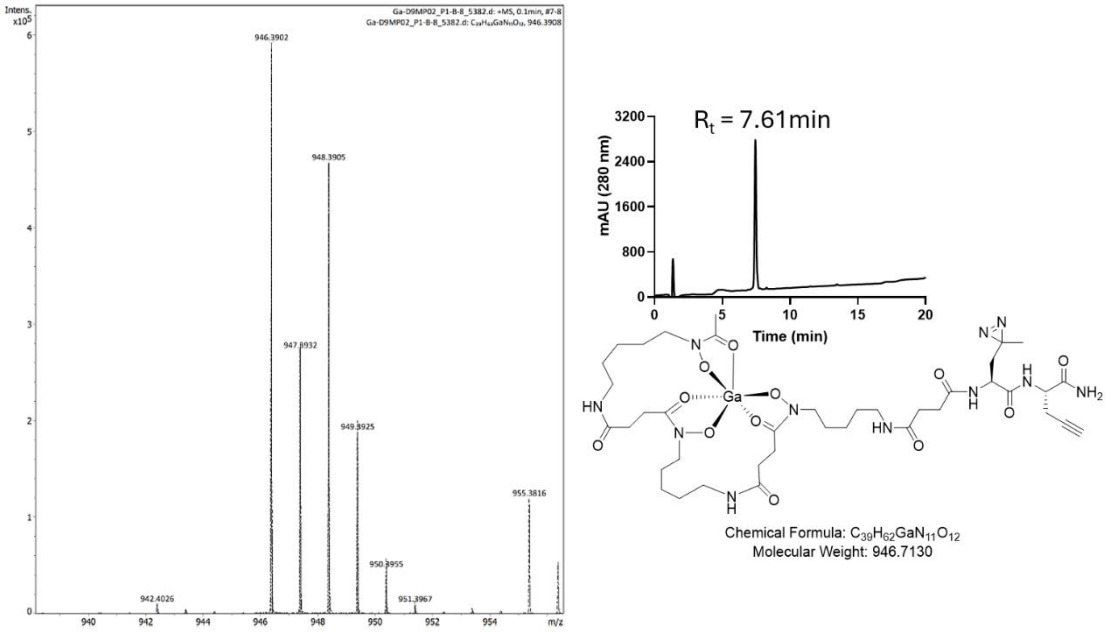

Figure 3. 15: Ga-DFO-azir-02's HRMS and HPLC trace (Method D).

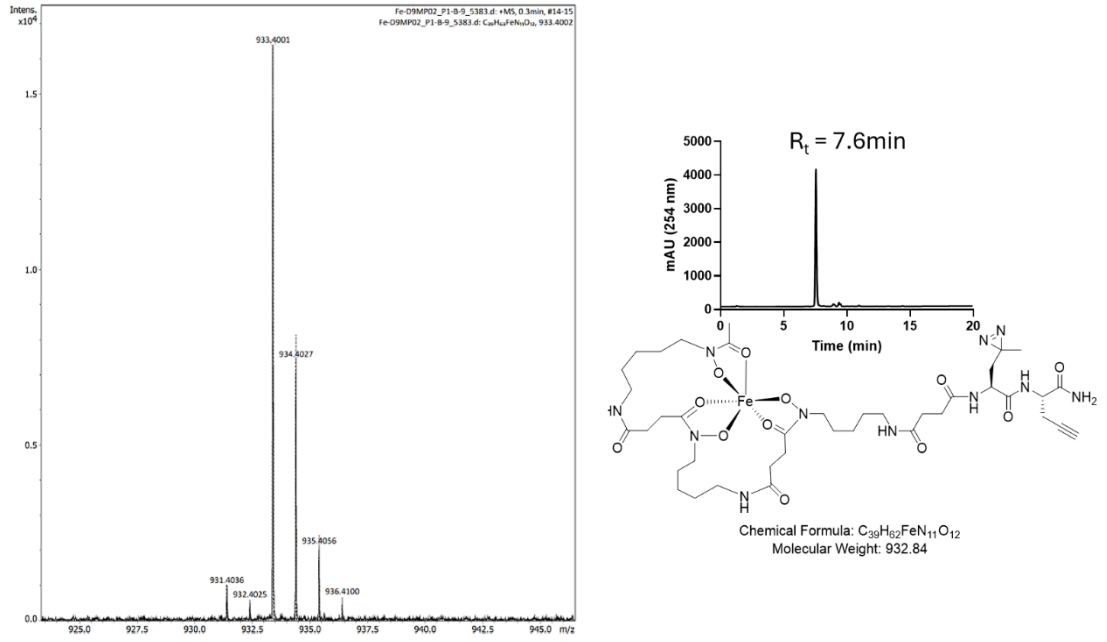

Figure 3. 16: Fe-DFO-azir-02's HRMS and HPLC trace (Method D).

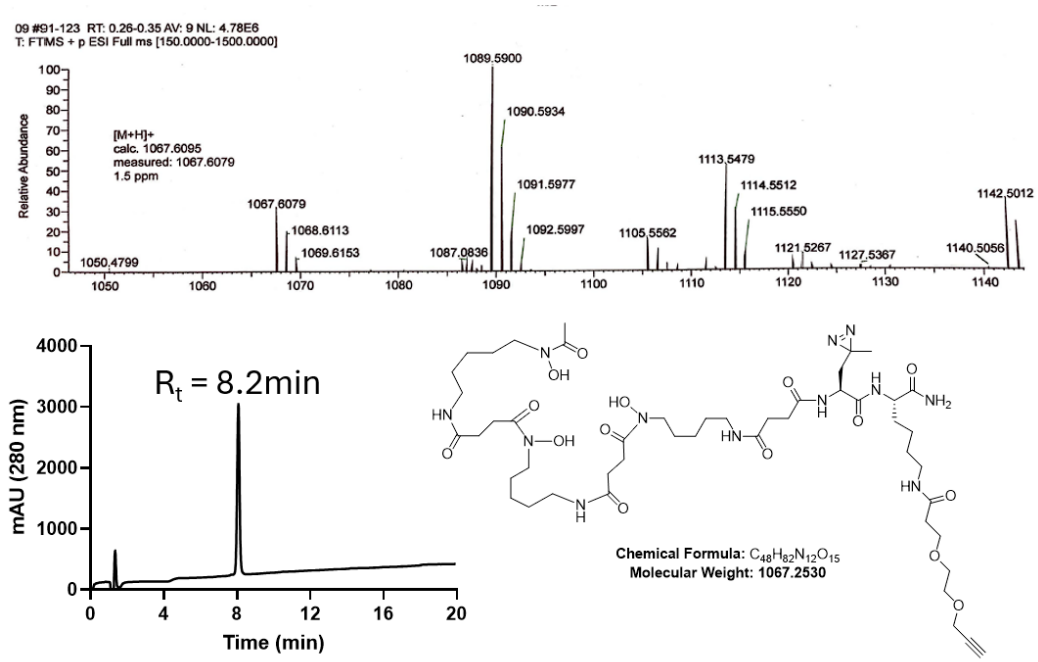

Figure 3. 17: DFO-azir-03's HRMS and HPLC trace (Method D).

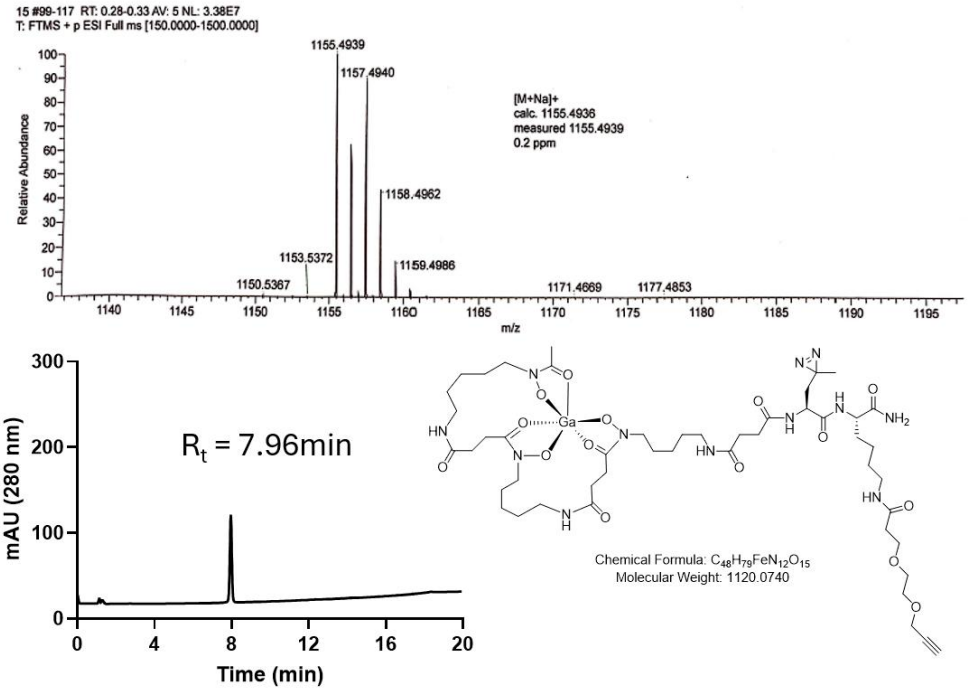

Figure 3. 18: Ga-DFO-azir-03's HRMS and HPLC trace (Method D).

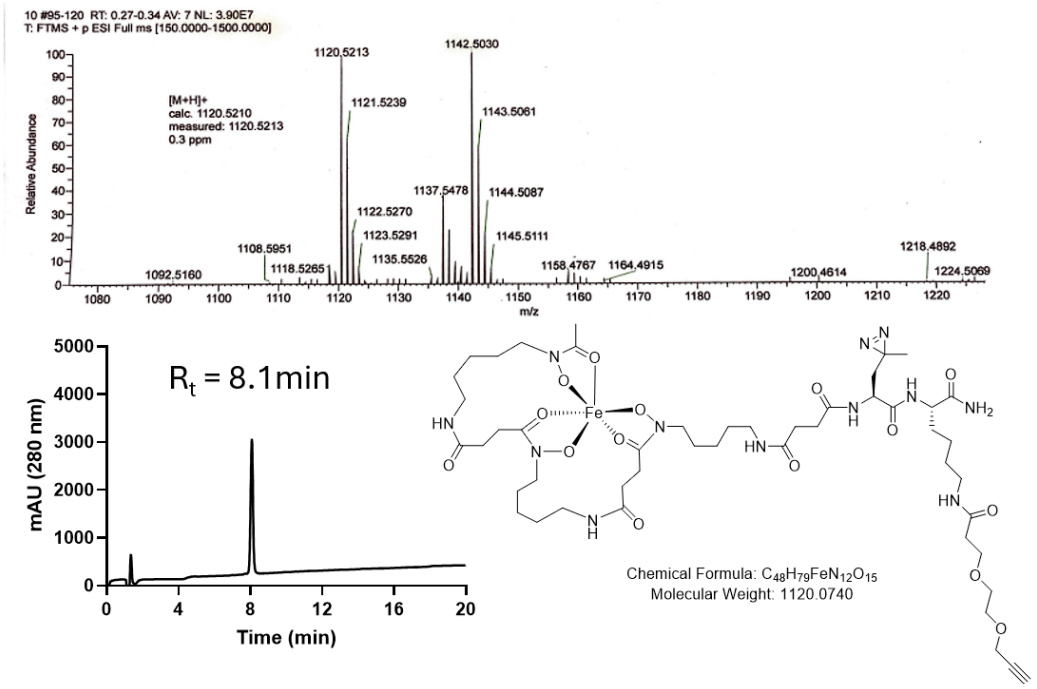

Figure 3. 19: Fe-DFO-azir-03's HRMS and HPLC trace (Method D).

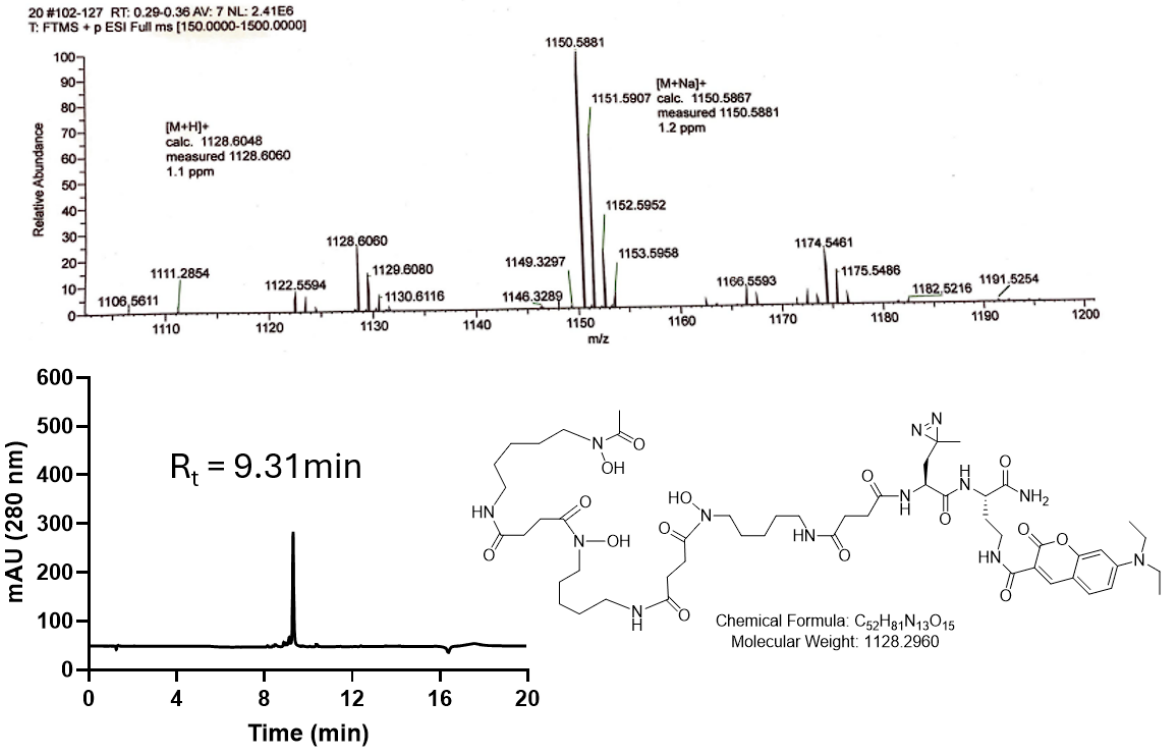

Figure 3. 20: DFO-azir-04's HRMS and HPLC trace (Method D).

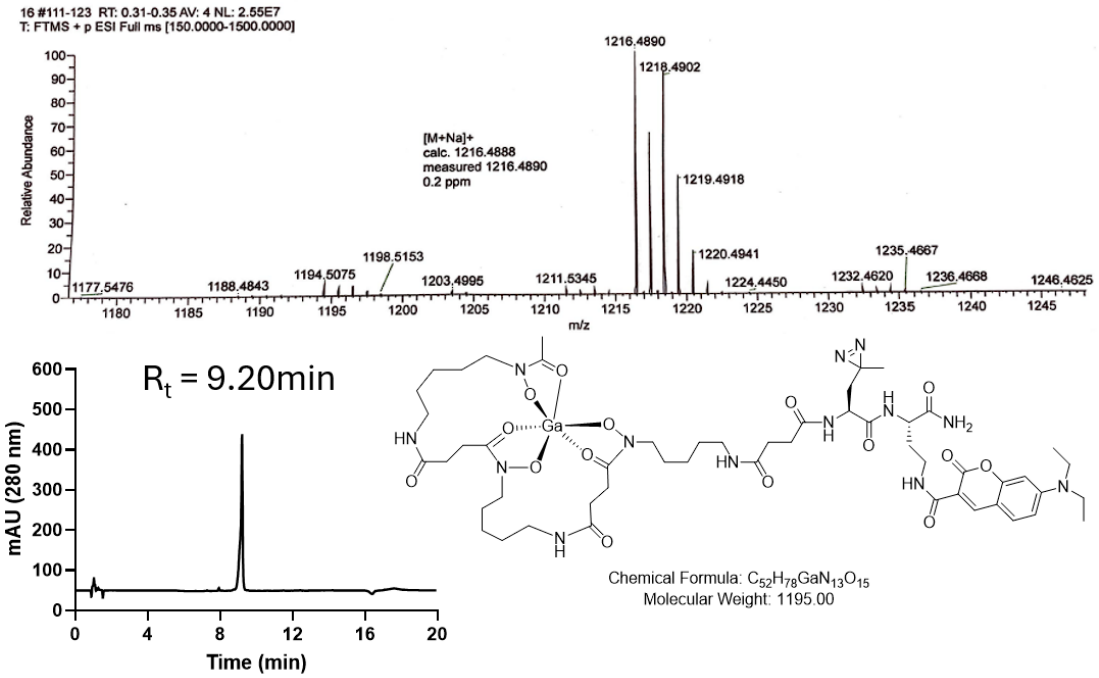

Figure 3. 21: Ga-DFO-azir-04's HRMS and HPLC trace (Method D).

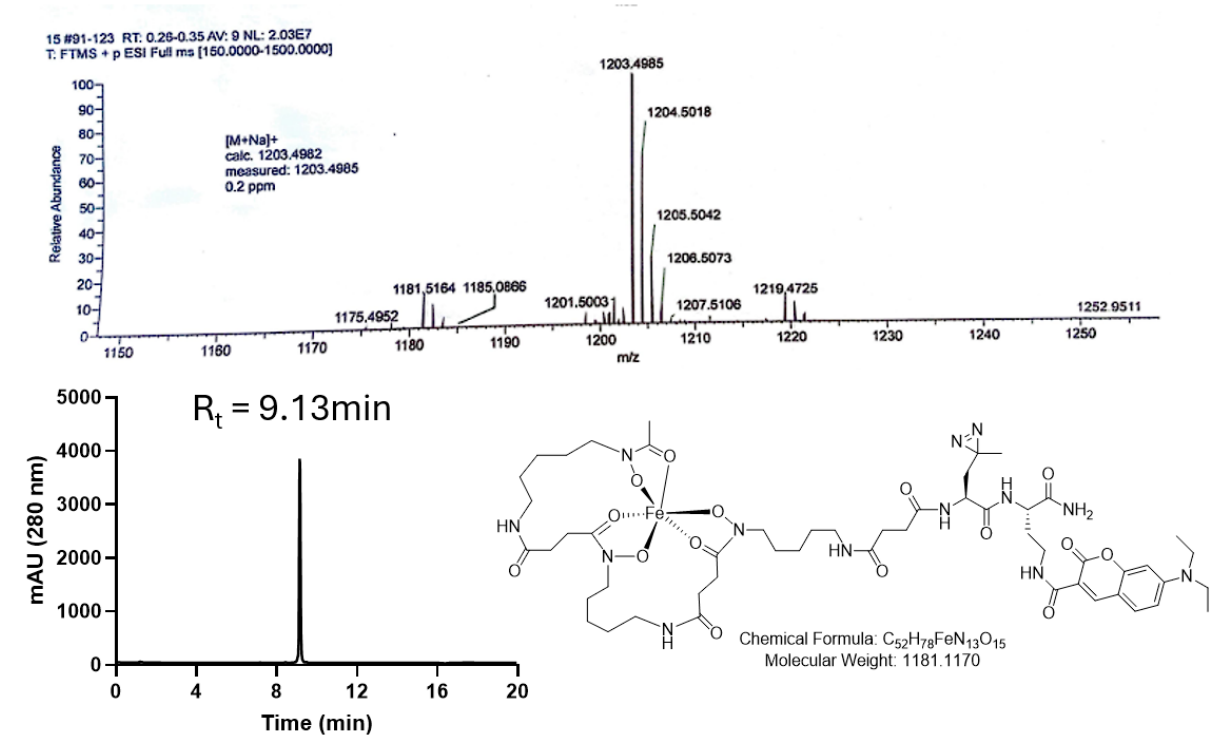

Figure 3. 22: Fe-DFO-azir-04's HRMS and HPLC trace (Method D).

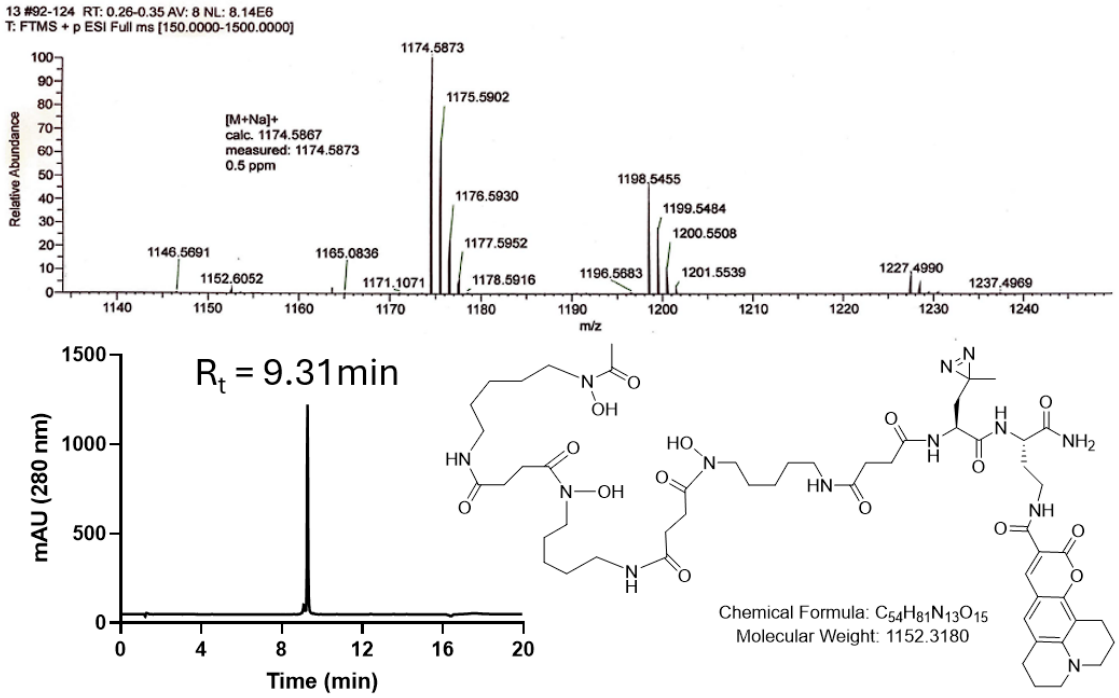

Figure 3. 23: DFO-azir-05's HRMS and HPLC trace (Method D).

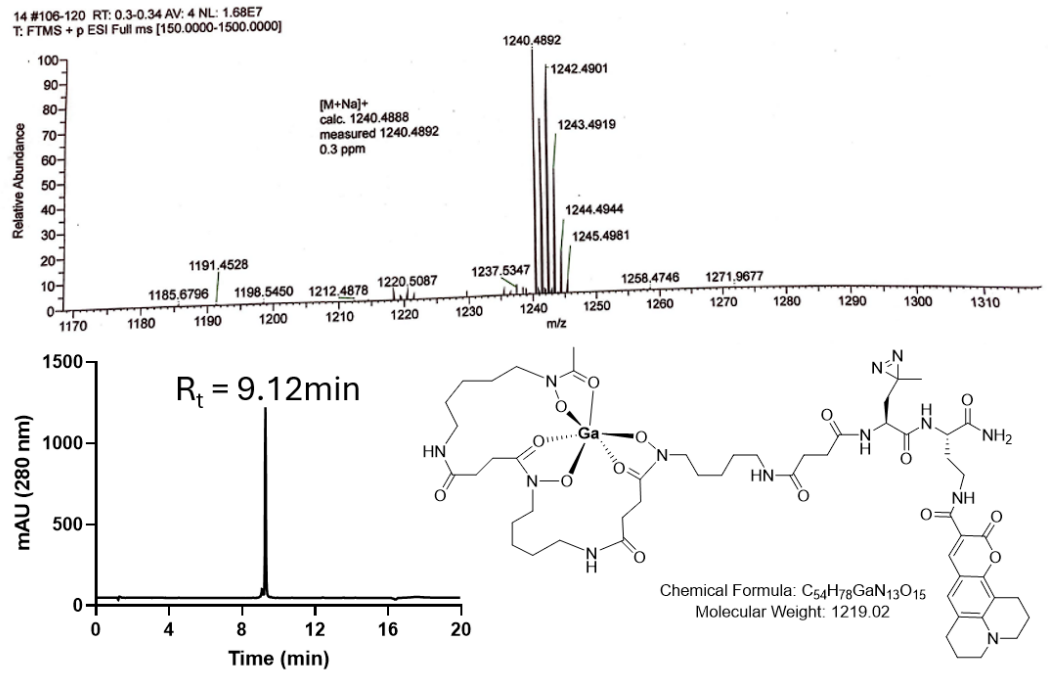

Figure 3. 24: Ga-DFO-azir-05's HRMS and HPLC trace (Method D).

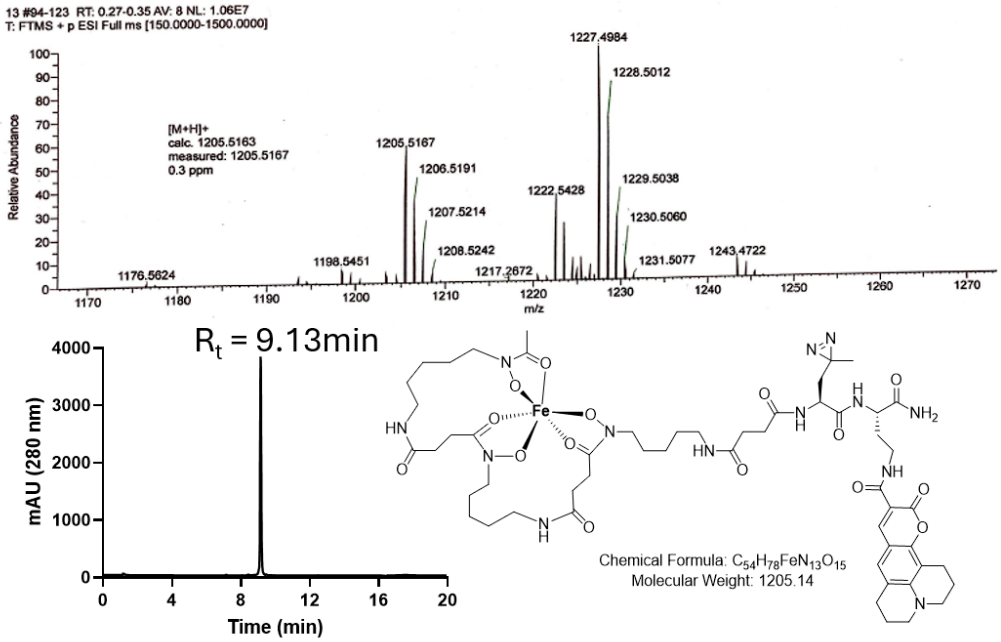

Figure 3. 25: Fe-DFO-azir-05's HRMS and HPLC trace (Method D).

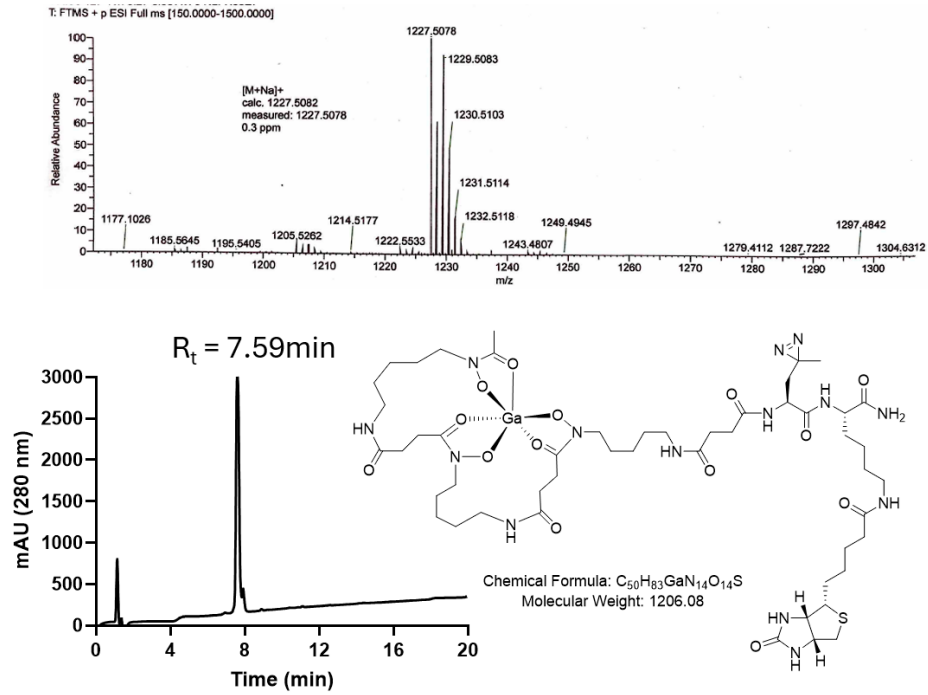

Figure 3. 26: Ga-DFO-azir-05's HRMS and HPLC trace (Method D).

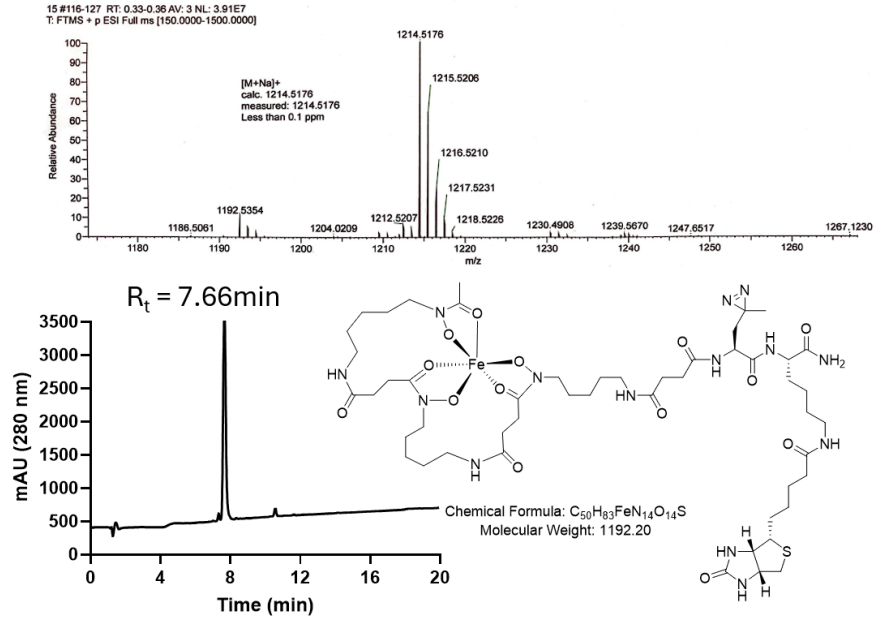

Figure 3. 27: Fe-DFO-azir-05's HRMS and HPLC trace (Method D).

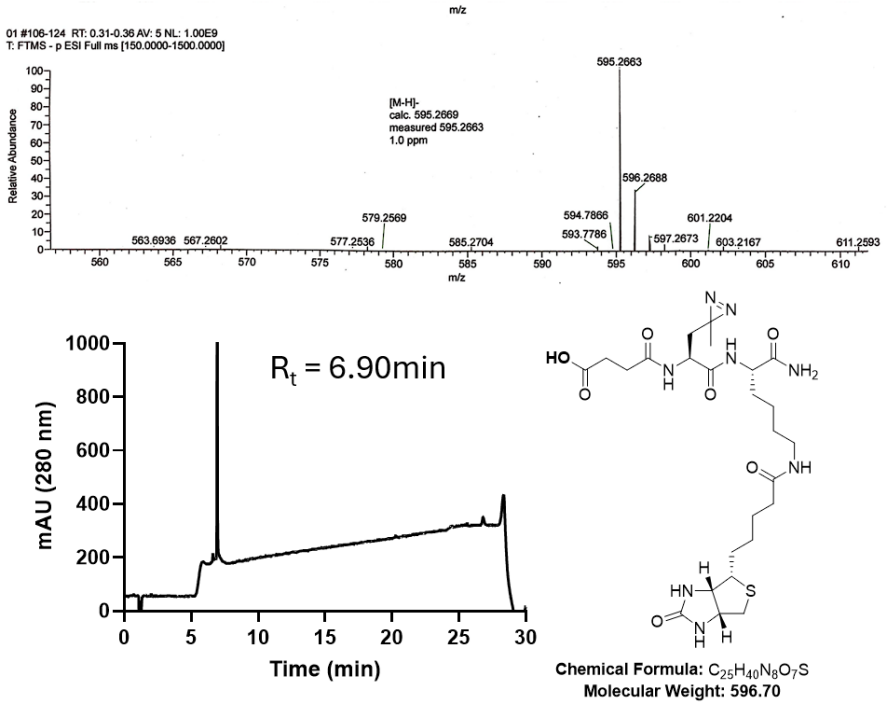

Figure 3. 28: azir-ctrl's HRMS and HPLC trace.

3.5.3.3 NMR spectra

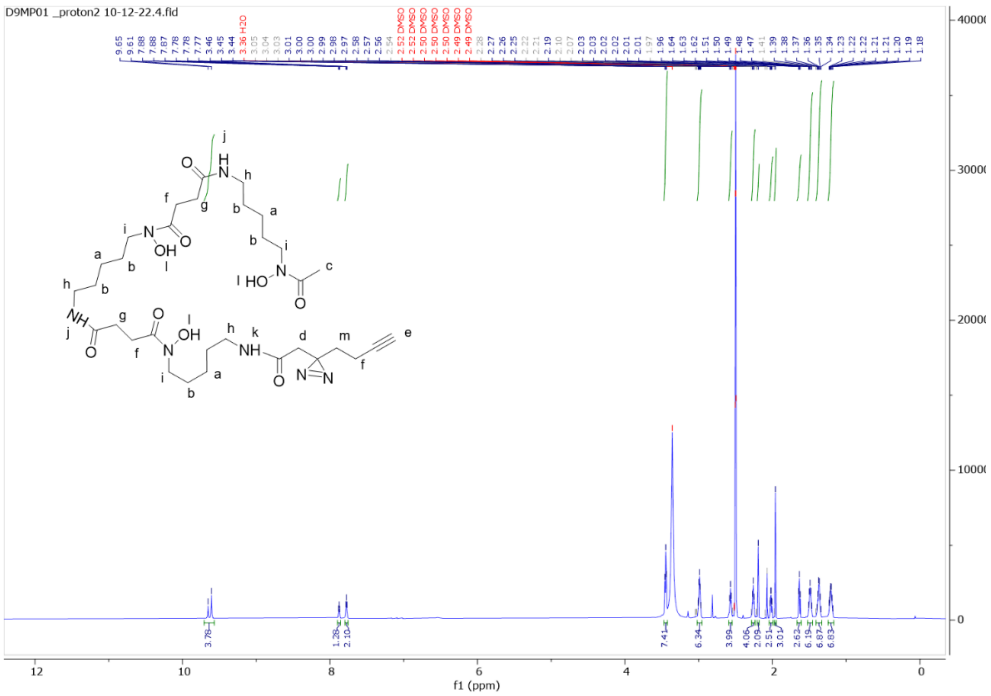

Figure 3. 29: ^{1}H-NMR spectrum of DFO-azir-01. 500 MHz, DMSO-d_6

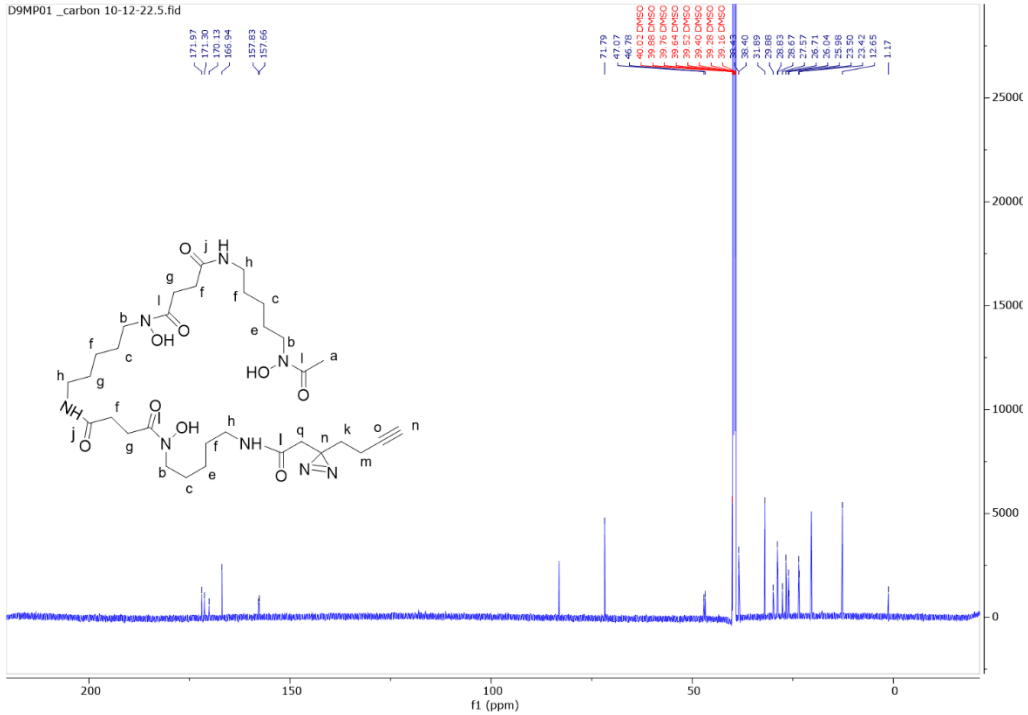

Figure 3. 30: ^{13}C-NMR spectrum of DFO-azir-01. 500 MHz, DMSO-d_6.

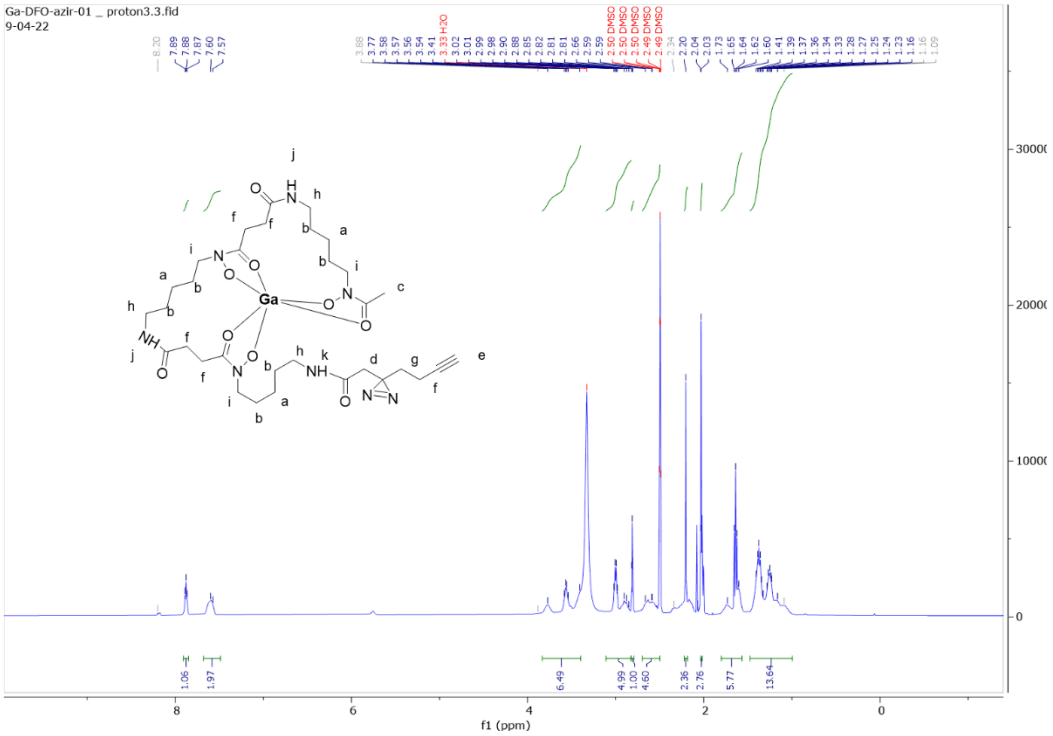

Figure 3. 31: 1H-NMR spectrum of Ga-DFO-azir-01. 500 MHz, DMSO-d6.

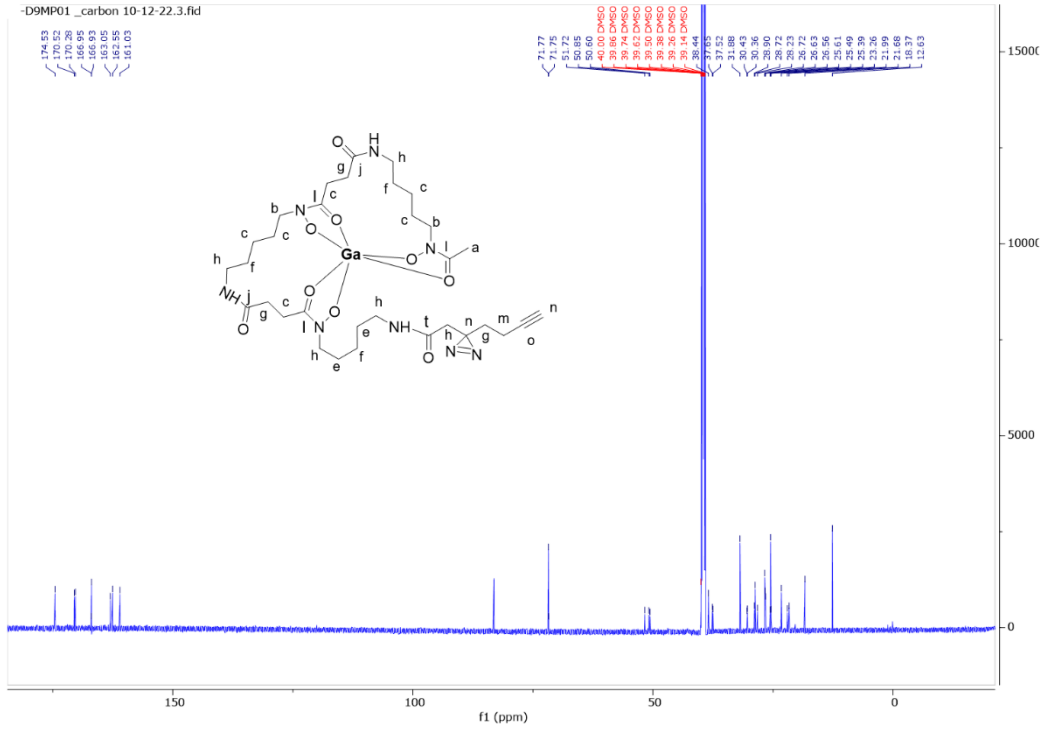

Figure 3. 32: ^{13}C-NMR spectrum of Ga-DFO-azir-01. 500 MHz, DMSO-d_6.

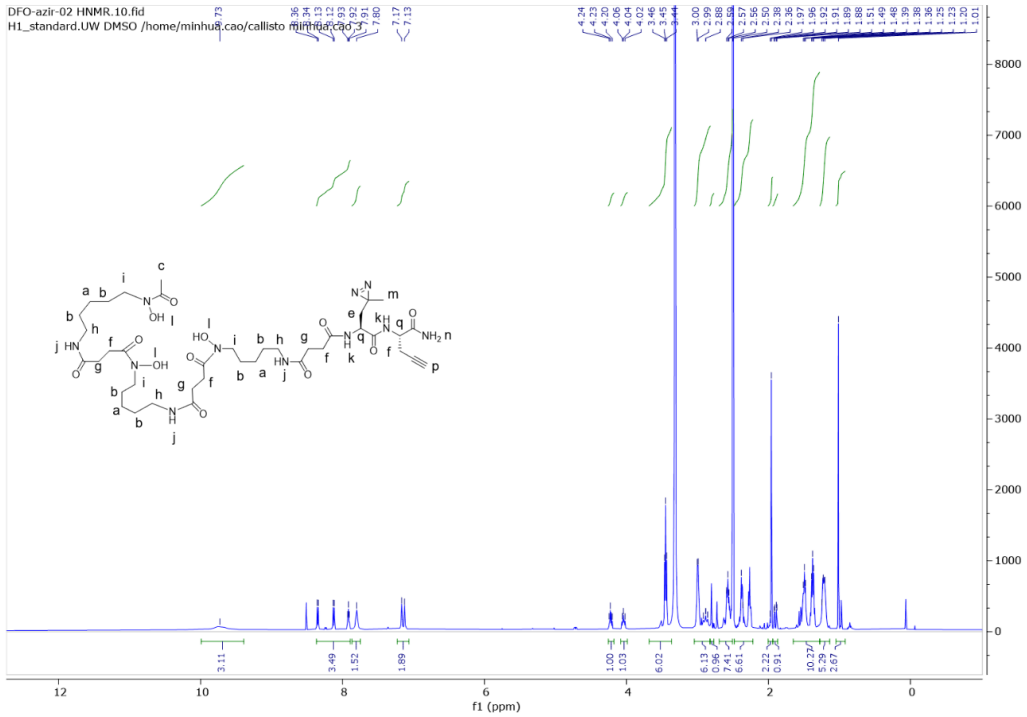

Figure 3. 33: ^{1}H-NMR spectrum of DFO-azir-02. 500 MHz, DMSO-d6.

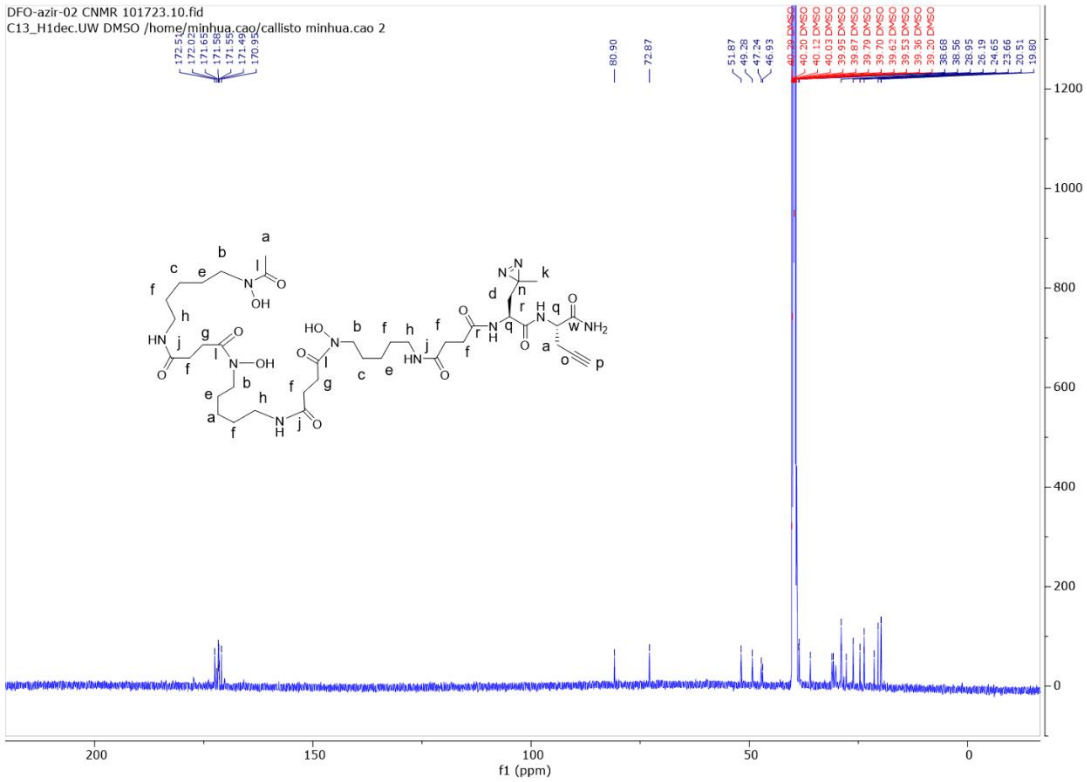

Figure 3. 34: ^{13}C-NMR spectrum of DFO-azir-02. 500 MHz, DMSO-d_6.

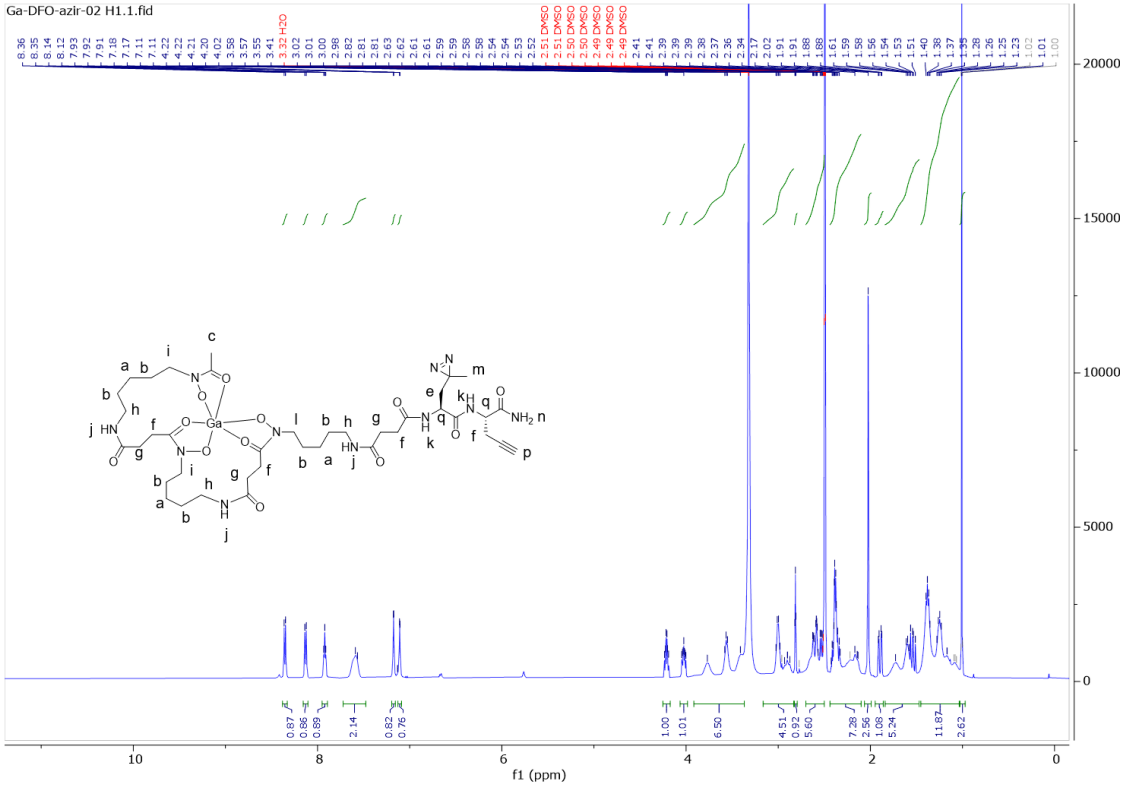

Figure 3. 35: ^{1}H-NMR spectrum of Ga-DFO-azir-02. 500 MHz, DMSO-d6.

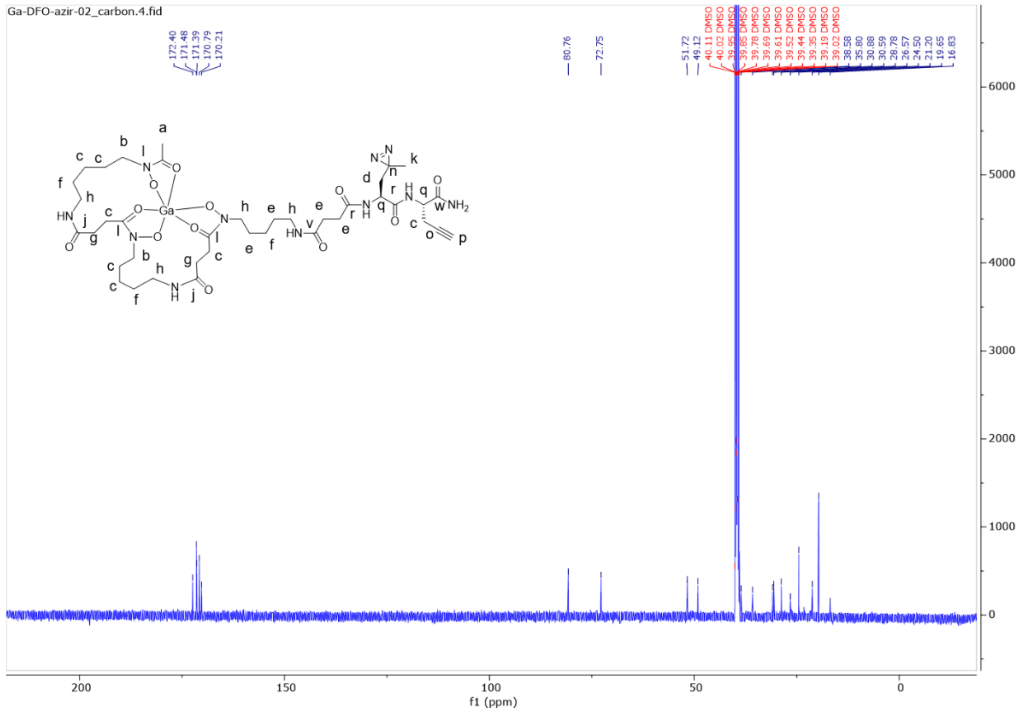

Figure 3. 36: ^{13}C-NMR spectrum of Ga-DFO-azir-02. 500 MHz, DMSO-d_6.

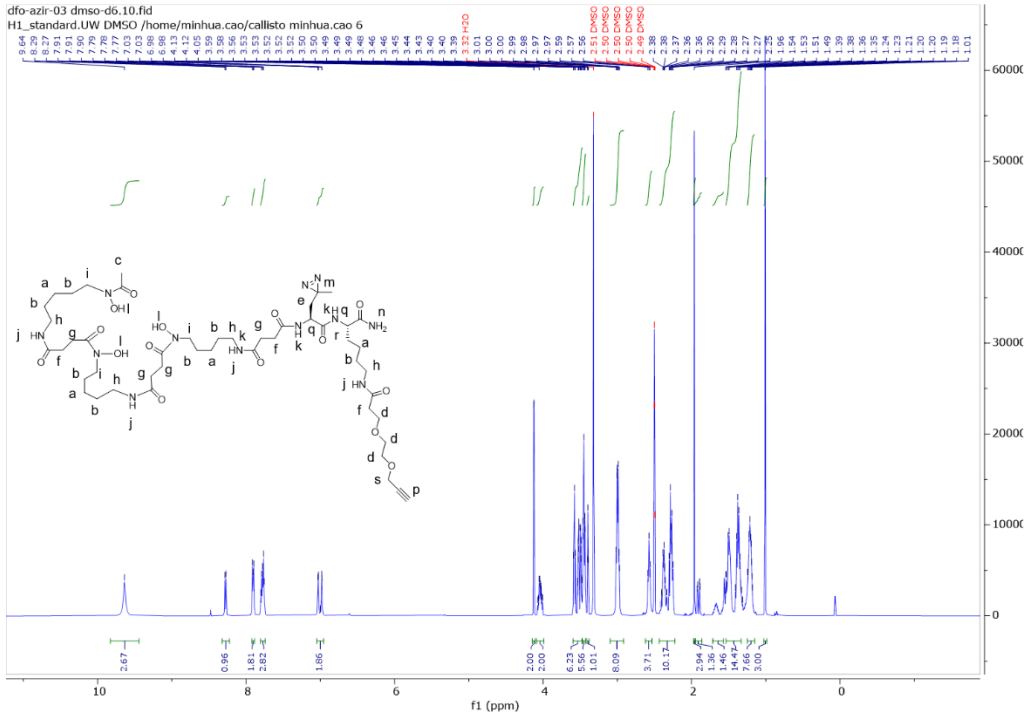

Figure 3. 37: ^{1}H-NMR spectrum of DFO-azir-03. 500 MHz, DMSO-d6.

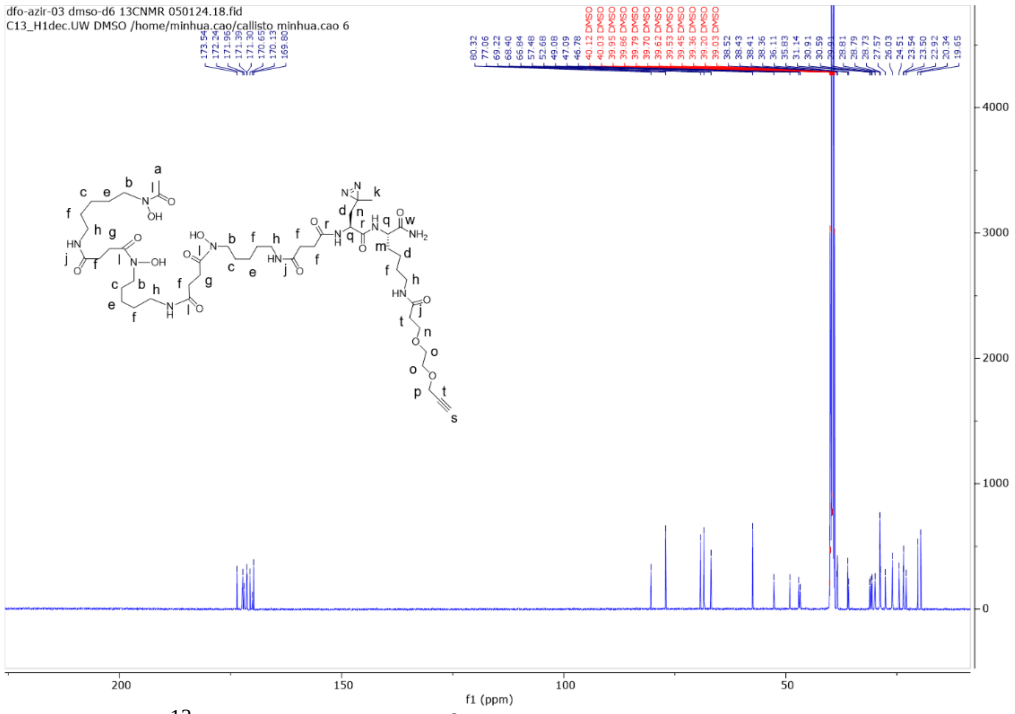

Figure 3. 38: ^{13}C-NMR spectrum of DFO-azir-03. 500 MHz, DMSO-d_6.

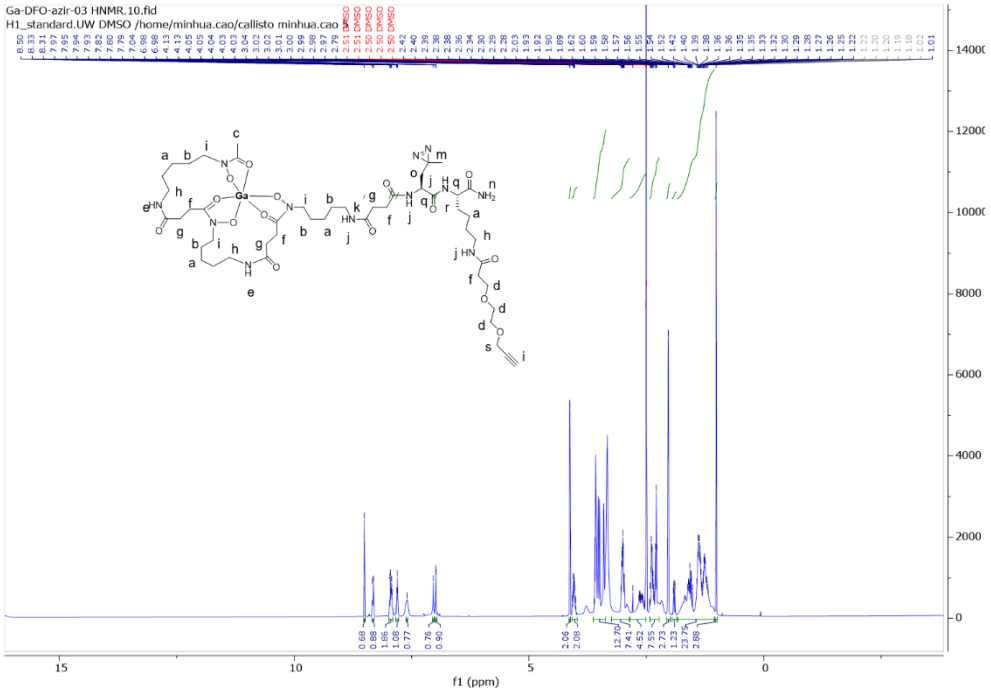

Figure 3. 39: ^{1}H-NMR spectrum of Ga-DFO-azir-03. 500 MHz, DMSO-d_6.

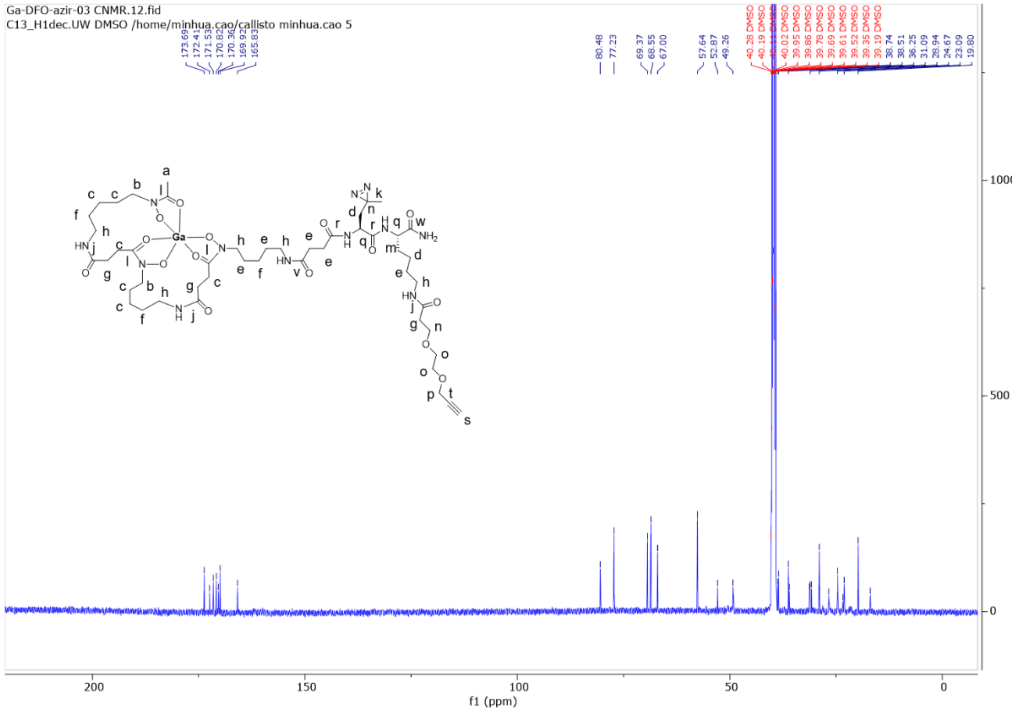

Figure 3. 40: ^{13}C-NMR spectrum of Ga-DFO-azir-03. 500 MHz, DMSO-d_6.

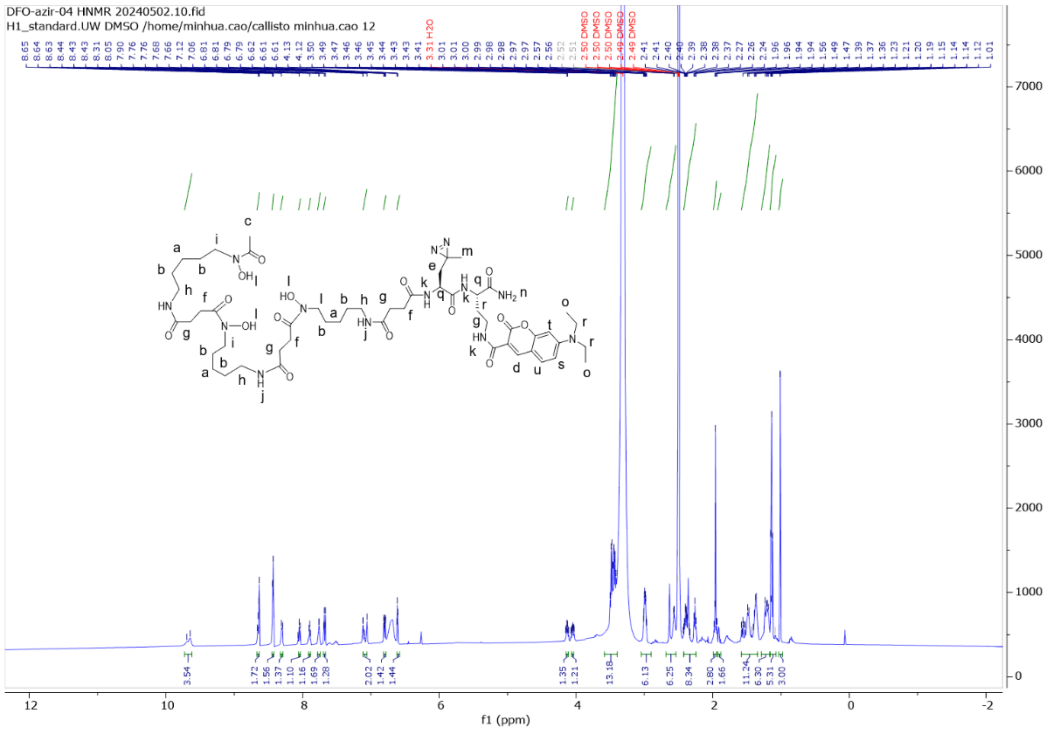

Figure 3. 41: ^{1}H-NMR spectrum of DFO-azir-04. 500 MHz, DMSO-d6.

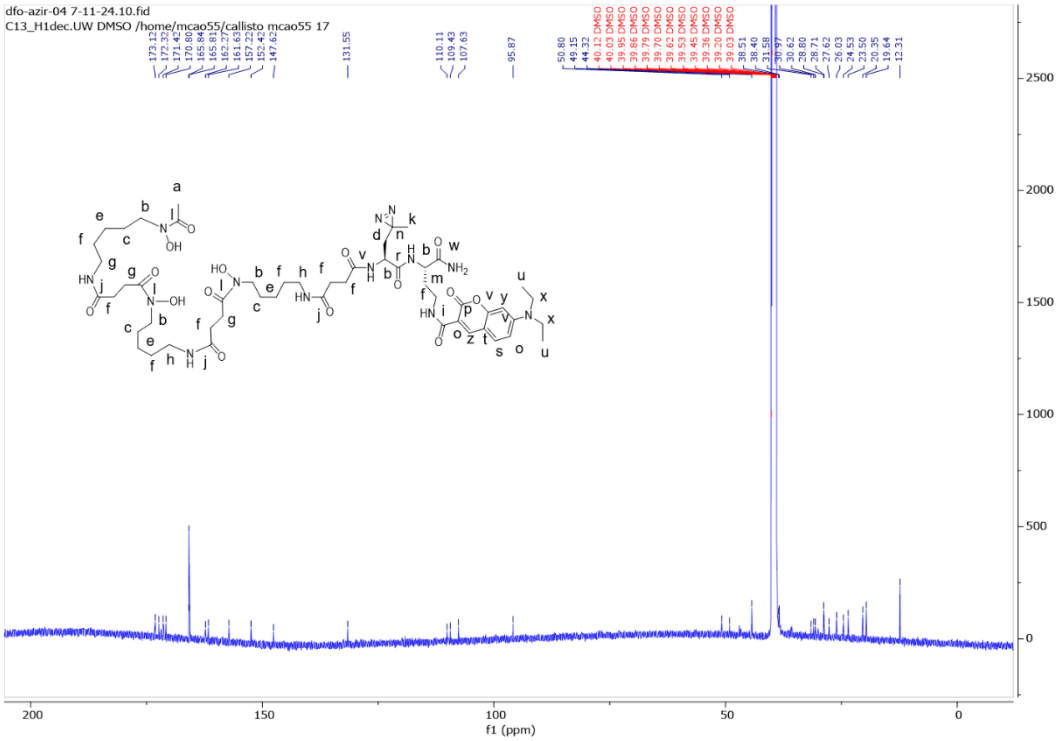

Figure 3. 42: ^{13}C-NMR spectrum of DFO-azir-04. 500 MHz, DMSO-d_6.

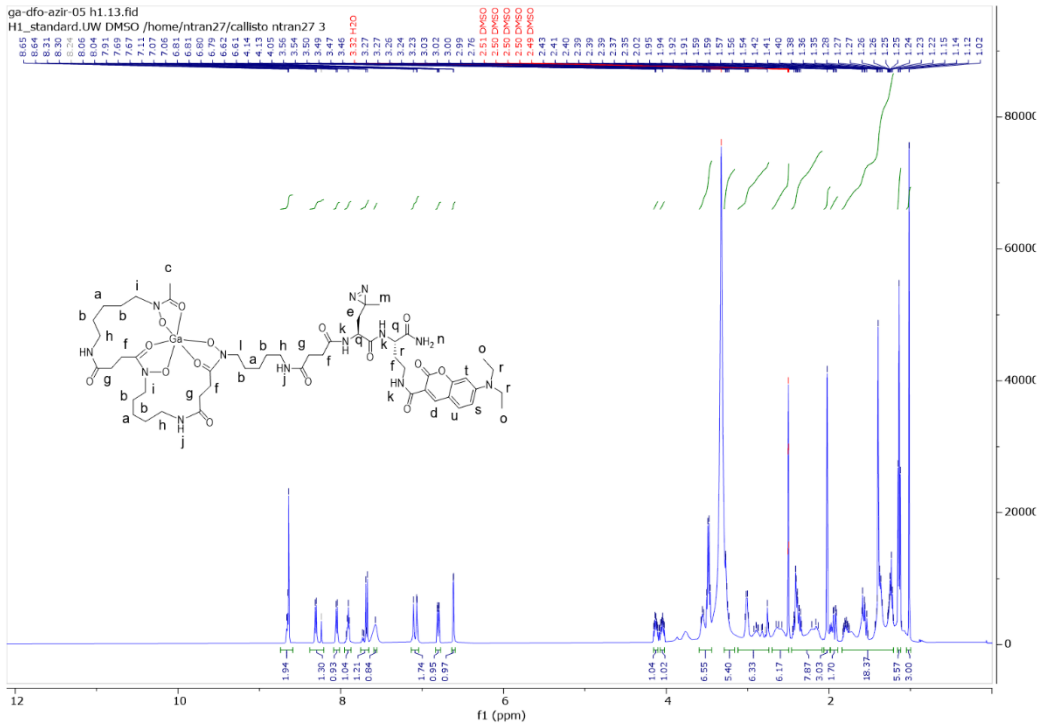

Figure 3. 43: ^{1}H-NMR spectrum of Ga-DFO-azir-04. 500 MHz, DMSO-d_6.

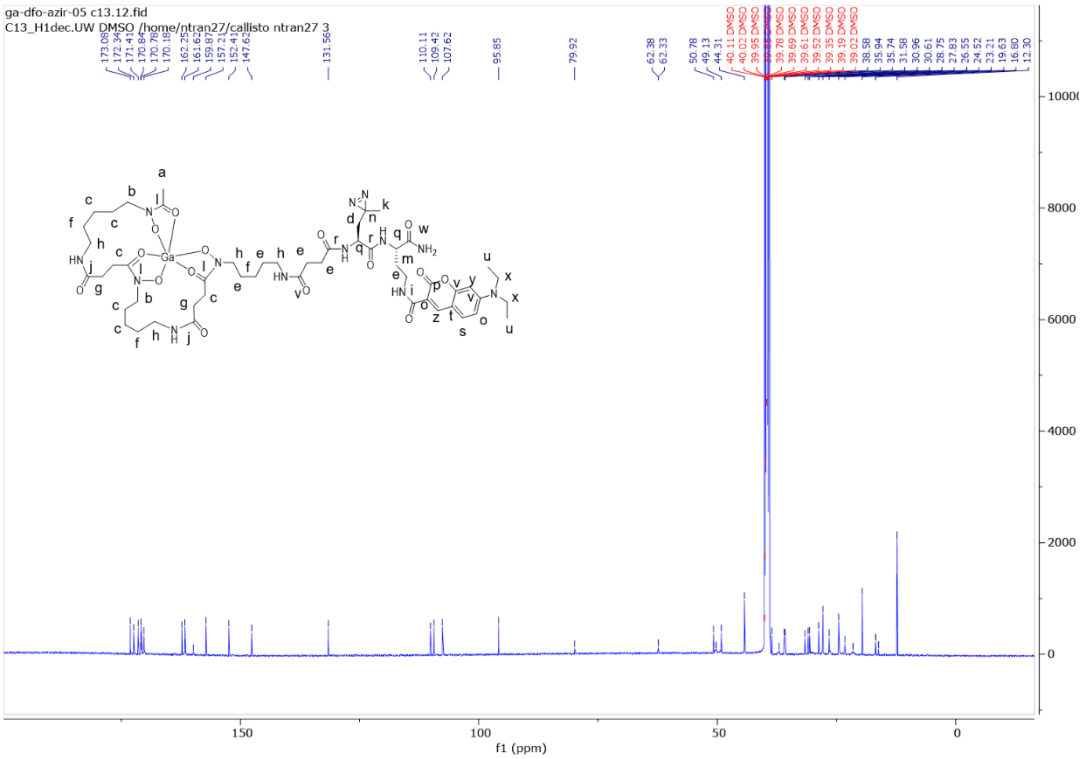

Figure 3. 44: ^{13}C-NMR spectrum of Ga-DFO-azir-04. 500 MHz, DMSO-d_6.

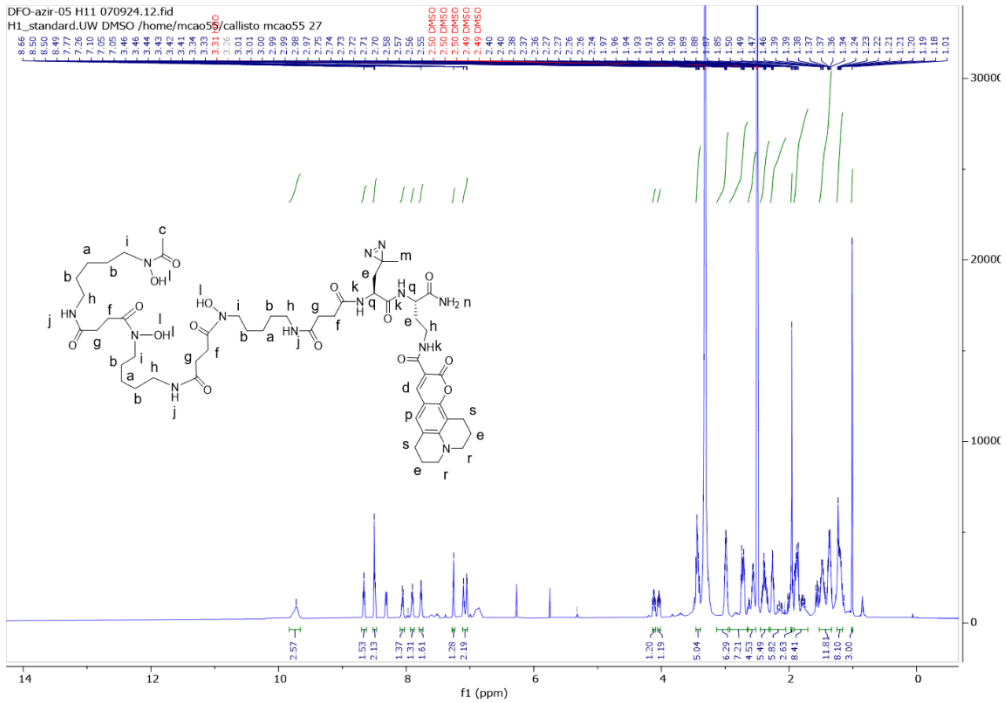

Figure 3. 45: ^{1}H-NMR spectrum of DFO-azir-05. 500 MHz, DMSO-d_6.

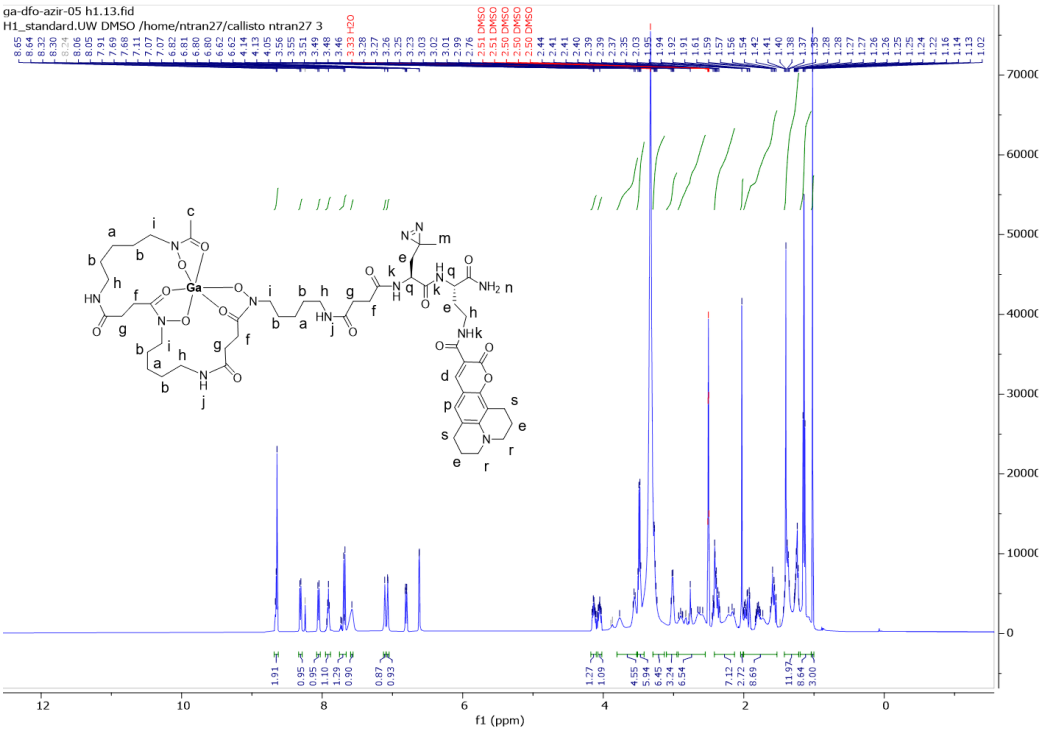

Figure 3. 46: ^{1}H-NMR spectrum of Ga-DFO-azir-05. 500 MHz, DMSO-d_6.

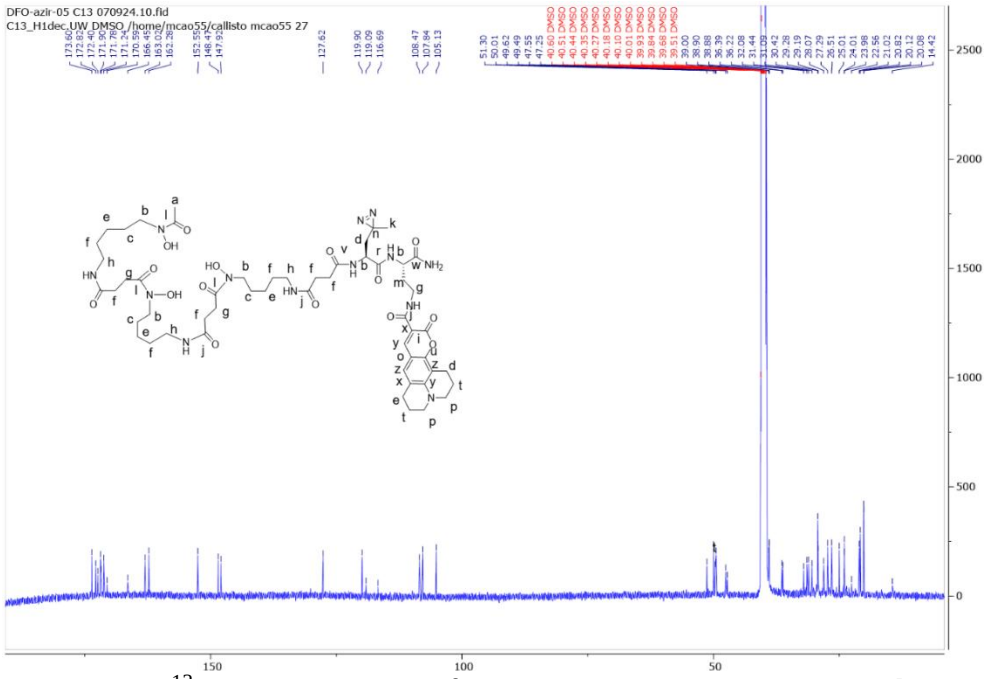

Figure 3. 47: ^{13}C-NMR spectrum of DFO-azir-05. 500 MHz, DMSO-d_6.

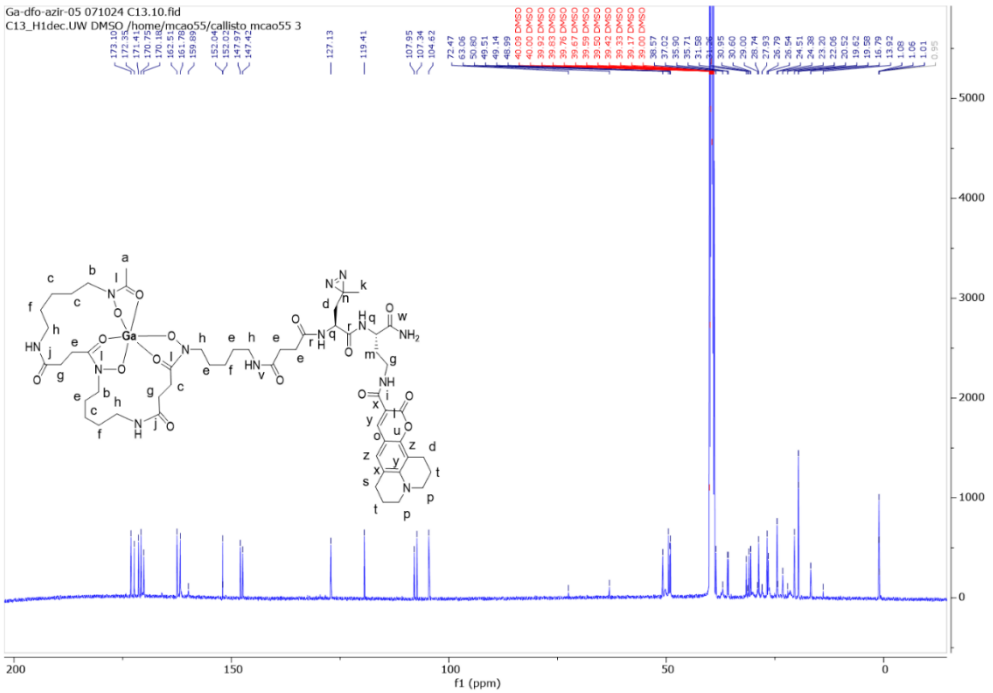

Figure 3. 48: ^{13}C-NMR spectrum of Ga-DFO-azir-05. 500 MHz, DMSO-d_6.

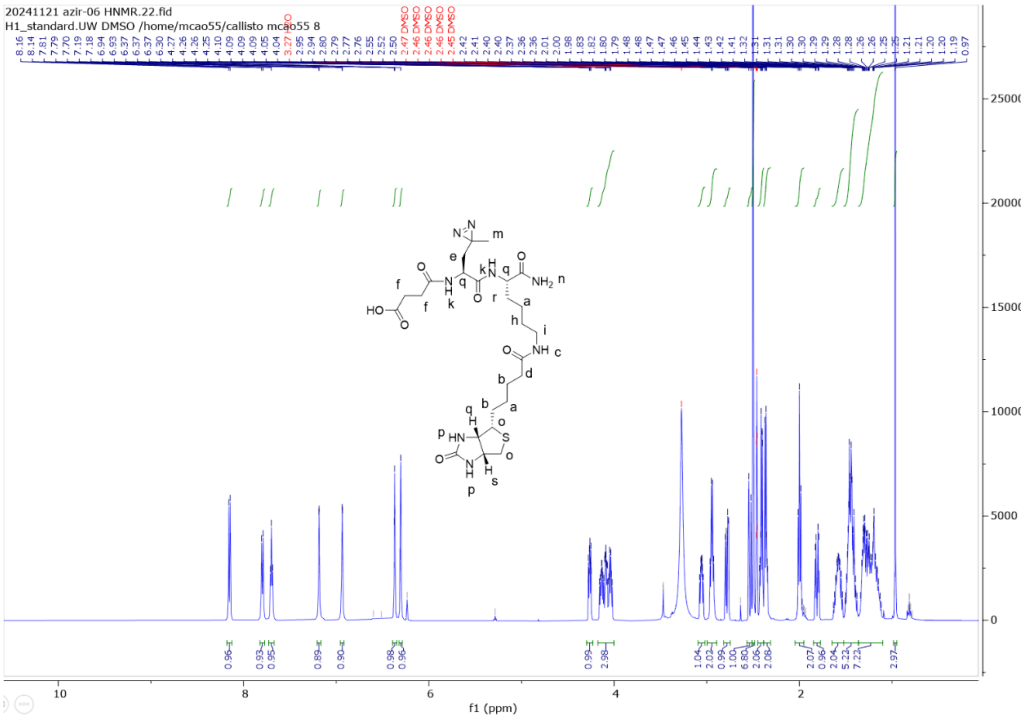

Figure 3. 50: ^{1}H-NMR spectrum of azir-ctrl. 500 MHz, DMSO-d_6**.**

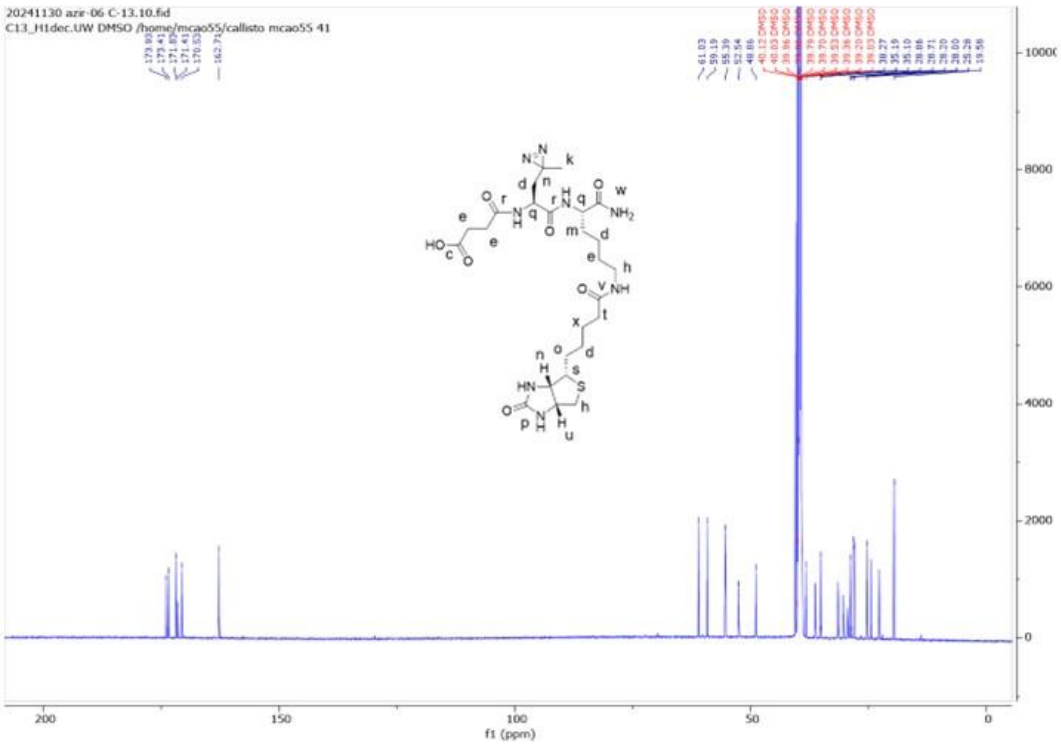

Figure 3. 49: ^{13}C-NMR spectrum of azir-ctrl. 500 MHz, DMSO-d_6**.**

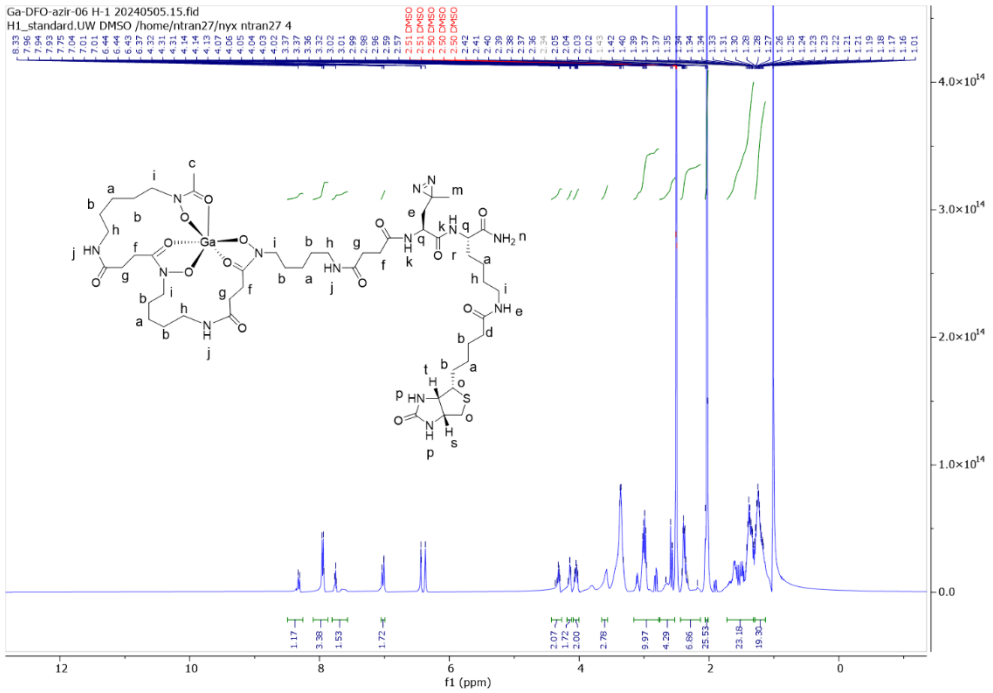

Figure 3. 51: ^{1}H-NMR spectrum of Ga-DFO-azir-06. 500 MHz, DMSO-d$_6$.

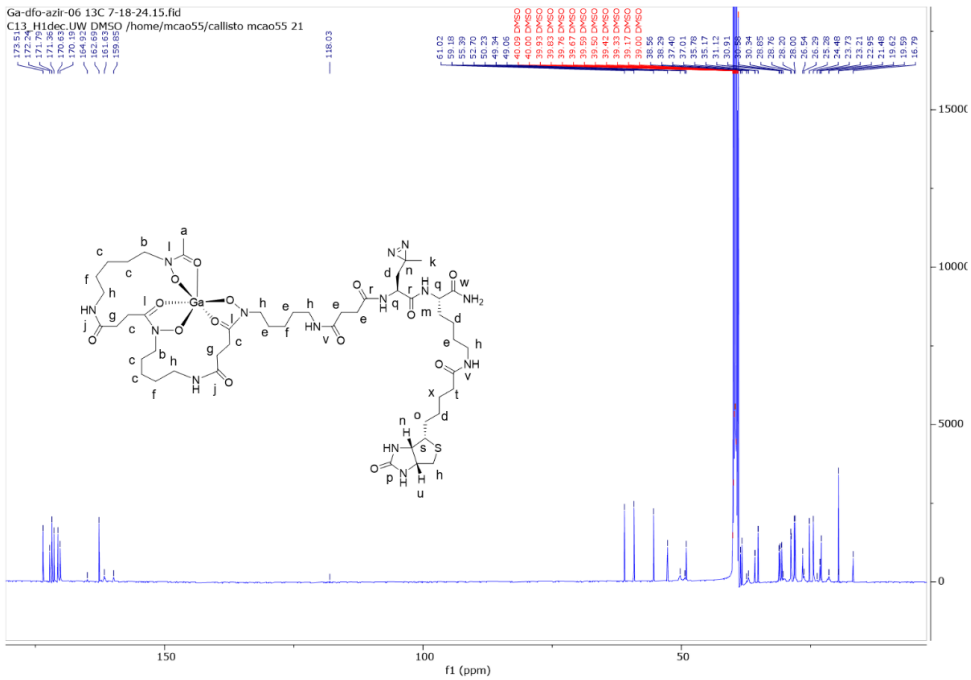

Figure 3. 52: ^{13}C-NMR spectrum of Ga-DFO-azir-06. 500 MHz, DMSO-d$_6$.

3.5.4 Amino acid reactivity screaming

Photo cross-link reaction with single amino acid: Stock solutions of the Ac-x-Ome (X= Tyr, Aps, Gln, Arg, and His 19mM) prepared acetonitrile or DMSO and M-DFO-azir-01,02,04,05,or 06 (M= apo, Ga, Fe) (0.4 mM) were prepared in 50% acetonitrile in water. M-DFO-azir-01,02,04,05,and 06 (5.00 µL, 1 equiv) and the amino acid (20.0 µL, 100.00 equiv) were added in sequence to a 96 well plate in triplicate and were irradiated with a broadband UV lamp (365 nm LED) over ice pack for 15 min. Samples were filtered and injected into the LC-MS (method C).

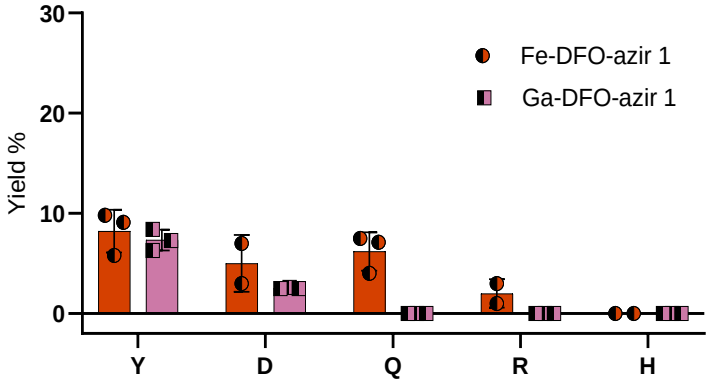

Figure 3. 53: Probe reactivity with single Ac-X-Ome amino acids.

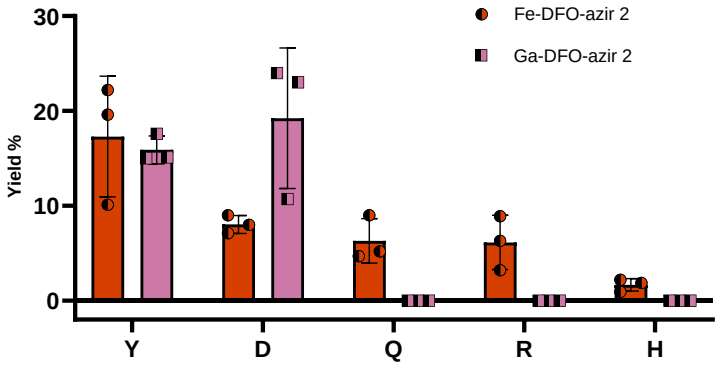

Figure 3. 54: Probe reactivity with single Ac-X-Ome amino acids.

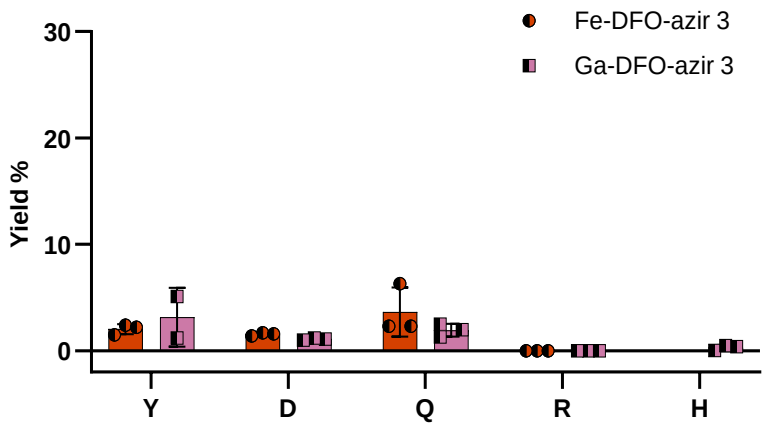

Figure 3. 55: Probe reactivity with single Ac-X-Ome amino acids.

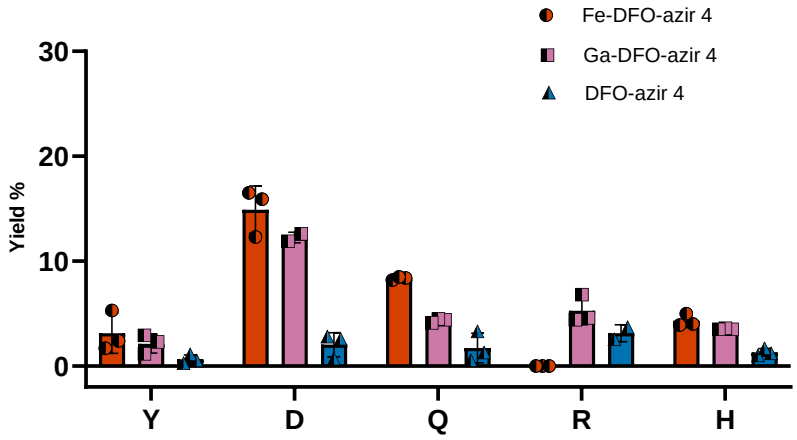

Figure 3. 56: Probe reactivity with single Ac-X-Ome amino acids.

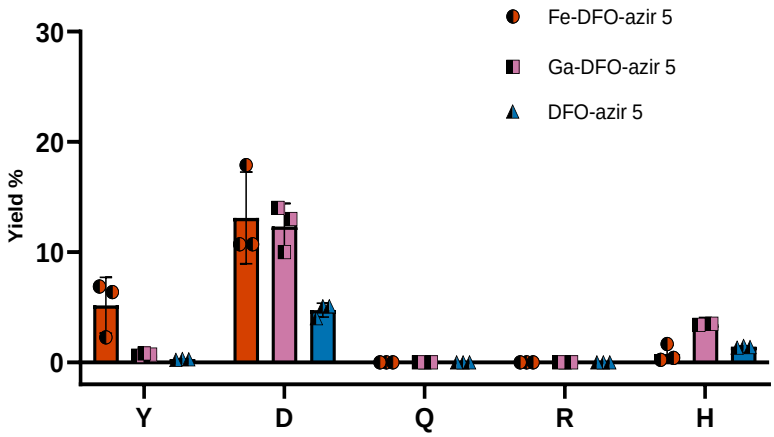

Figure 3. 57: Probe reactivity with single Ac-X-Ome amino acids.

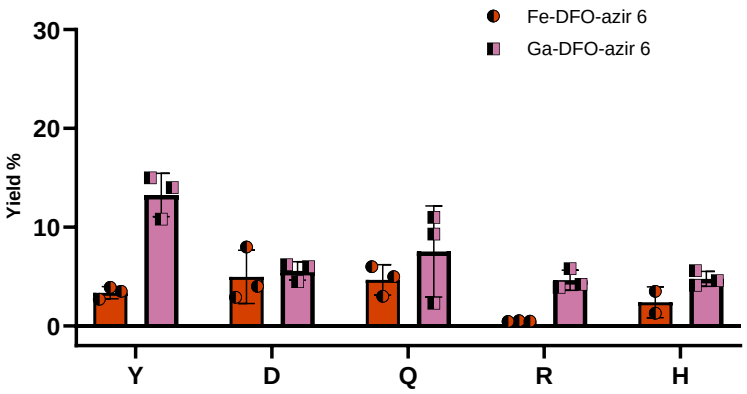

Figure 3. 58: Probe reactivity with single Ac-X-Ome amino acids.

3.5.6 Co-crystal structure

Crystallization and structure determination. For crystallization, FoxA (10 mg/ml) was mixed with 3-4-fold excess ligand (Fe-D1 or Fe-DFO-azir-01) and incubated on ice for approximately 30 min. Crystals of FoxA-Fe-D1 complex were grown in 1.6-2.0 M ammonium sulfate, 0.1 M HEPES pH 7, 0.6% β-octyl glucopyranoside (β-OG). For crystallization of FoxA-Fe-DFO-azir-01 complex the sample was irradiated with a UV-lamp (365 nm) for 15 min on ice

and crystals were grown in 2.0 M ammonium sulphate, 0.1 M Tris pH 8.5 (or 0.1M BICINE pH 9.0), 0.4-0.8% β-octyl glucopyranoside. All crystals appeared after 3-5 days and grew to 20-100 μm maximum size.

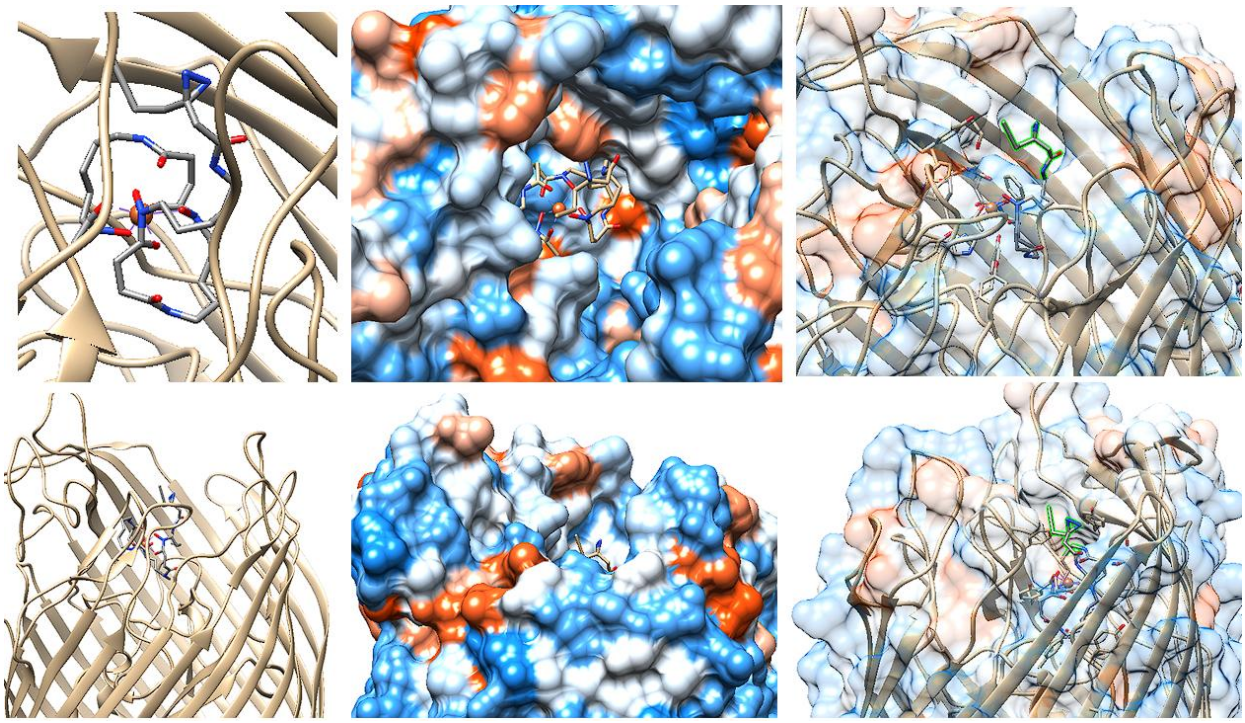

Figure 3. 59: Co-crystal structure of FoxA in complex with Fe-DFO-azir-01

3.5.7 Biochemical assays

Photo cross-link reaction with BSA and FoxA: BSA was prepared in DPBS (0.4% C8E4), and FoxA was prepared in DPBS (0.4% C8E4). M-DFO-azir-0x were dissolved in water for metal complexes or DMSO for the apo-ligand. For each reaction, 7.5 μL of probe (0.4 mM, 100 eq) and 7.5 μL of either BSA or FoxA (0.4 mg/mL, 1 eq) were sequentially added to a 96-well plate, followed by the addition of 15 μL of DPBS buffer. FoxA samples were incubated in the dark at room temperature for 30 minutes. Subsequently, they were photoirradiated with a 365 nm UV lamp over an ice pack for 15 minutes. The samples were then transferred to small conical vials and

washed twice with 15 µL of DPBS buffer. BSA samples were precipitated with acetone at -80 °C three times and then centrifuged at 21,000 g for 10 minutes to remove excess unreacted probe and realized in water. The BSA conjugation was analyzed by MALDI and western blot. FoxA samples were confirmed by western blot and submitted directly for MS/MS analysis without further treatment.

Fluorophore conjugation: Photo cross-linked labeled BSA or FoxA was dissolved in DPBS (pH 7.3, 25 mM, 1% SDS, 1% Triton-X). For the CuAAC reaction, the following cocktail was added: Azide Fluor 545 (10 mM, 2 µL), a premixed solution of $CuSO_4$ (50 mM, 2 µL) and TBTA (1.67 mM, 6 µL), and tris(2-carboxyethyl)phosphine (TCEP, 52 mM, 2 µL). The reaction mixture was stirred overnight in the dark at room temperature.

SDS-PAGE 1 method: Protein samples were mixed with loading buffer (5% β-mercaptoethanol in 2x Laemmli buffer) at a 1:1 or 1:3 sample-to-buffer ratio and heated to 95 °C for 2 minutes. The samples were then subjected to electrophoresis using 8–16% Mini-PROTEAN® TGX Stain-Free™ Protein Gels (10-well, 30 µL, #4568103) at 220 volts for 30 minutes in 1X TGS buffer (Tris/Glycine/SDS, #1610732). PageRuler™ Prestained Protein Ladder (180-10 kDa, # 26616) or Precision Plus Protein™ All Blue Prestained Protein Standards (250-10 kDa, #1610373) were used as molecular weight markers. Following electrophoresis, the gels were fixed in a solution of 50% ethanol and 10% acetic acid in water, washed with DI water for 10 minutes, and then imaged using a Typhoon 9400 Variable Mode Imager for fluorescence or stained with Coomassie R-250.

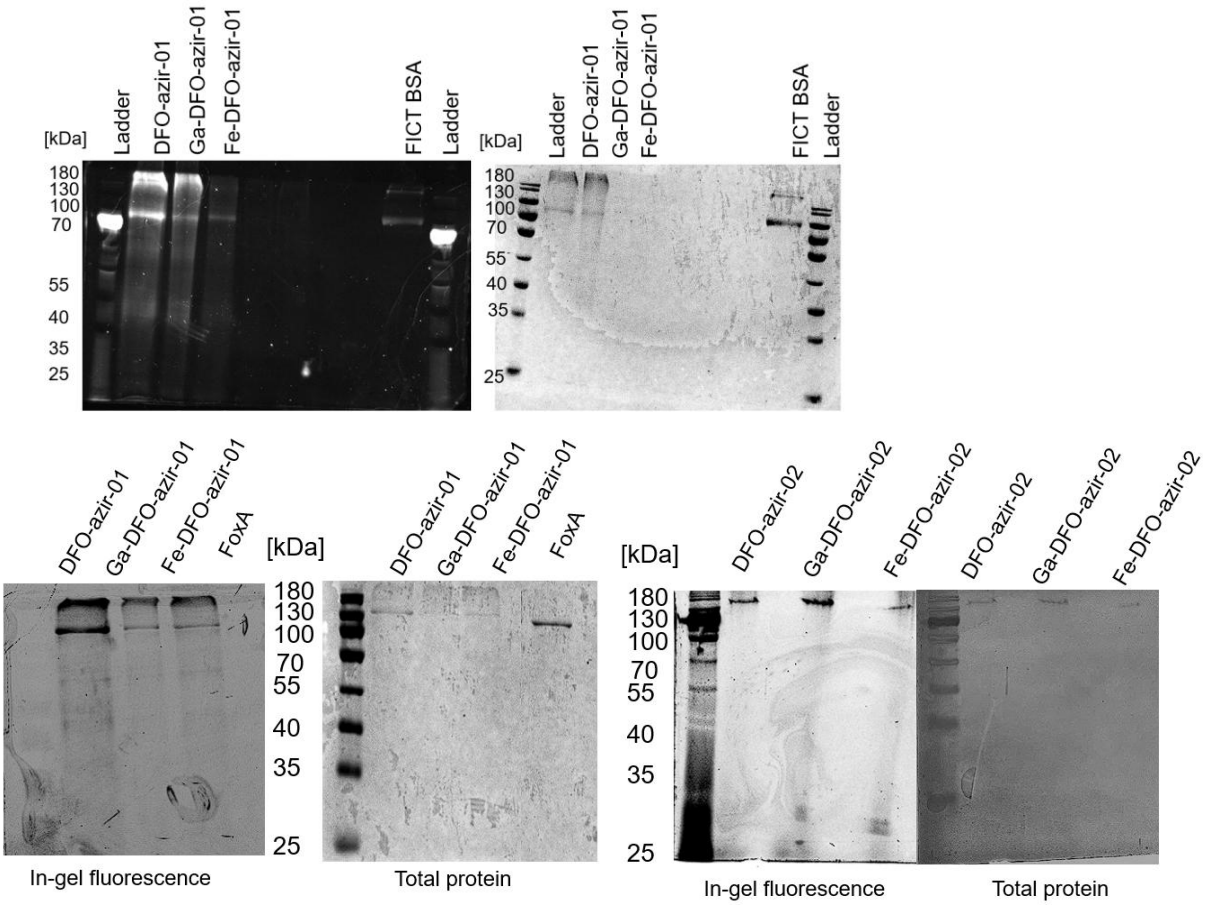

Figure 3. 60: Top panel: Purified BSA protein tagged with M-DFO-azir-01 and M-DFO-azir-02 and conjugated to Azide Fluor 545 were visualized by gel-based fluorescent imaging (left panel) and total protein staining (right panel).Botton panel: Purified FoxA protein tagged with M-DFO-azir-01 and M-DFO-azir-02 and conjugated to Azide Fluor 545 were visualized by gel-based fluorescent imaging (left panel) and total protein staining (right panel).

3.5.8 MS/MS for Fox site labeling identification

3.5.8.1 NanoLC-MS/MS

Peptides were analyzed by nanoLC-MS/MS using the Agilent 1100 nanoflow system (Agilent) connected to a hybrid linear ion trap-orbitrap mass spectrometer (LTQ-Orbitrap Elite™, Thermo Fisher Scientific) equipped with an EASY-Spray™ electrospray source (held at constant 35ºC). Chromatography of peptides prior to mass spectral analysis was accomplished using capillary

emitter column (PepMap® C18, 3µM, 100Å, 150x0.075mm, Thermo Fisher Scientific) onto which 3µl of extracted peptides was automatically loaded. NanoHPLC system delivered solvents A: 0.1% (v/v) formic acid , and B: 99.9% (v/v) acetonitrile, 0.1% (v/v) formic acid at 0.50 µL/min to load the peptides (over a 30 minute period) and 0.3µl/min to elute peptides directly into the nano-electrospray with gradual gradient from 0% (v/v) B to 30% (v/v) B over 80 minutes and concluded with 5 minute fast gradient from 30% (v/v) B to 50% (v/v) B at which time a 4 minute flash-out from 50-95% (v/v) B took place. Total run time of 150 minutes encompassed column conditioning at 95% B for 1 minute and equilibration at 100% A for 30 minutes. As peptides eluted from the HPLC-column/electrospray source survey MS scans were acquired in the Orbitrap with a resolution of 120,000 followed by CID-type MS/MS with 2.0 AMU isolation and 10 msec activation time with 35% normalized collision energy fragmentation of 30 most intense peptides detected in the MS1 scan from 350 to 1800 m/z; redundancy was limited by dynamic exclusion. Monoisotopic precursor selection and charge state screening were enabled and +1 and undefined charge states were rejected.

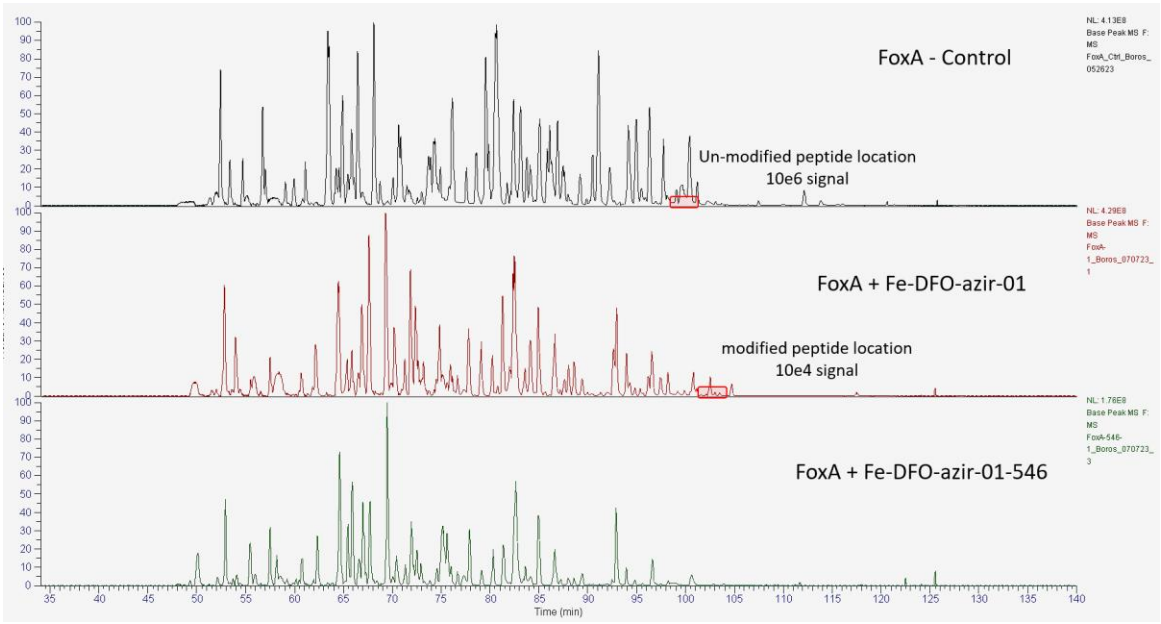

Figure 3. 61: Fe-DFO-azir-01 conjugated to azide-flour 545 base peak chromatogram traces of FoxA tryptic digest.

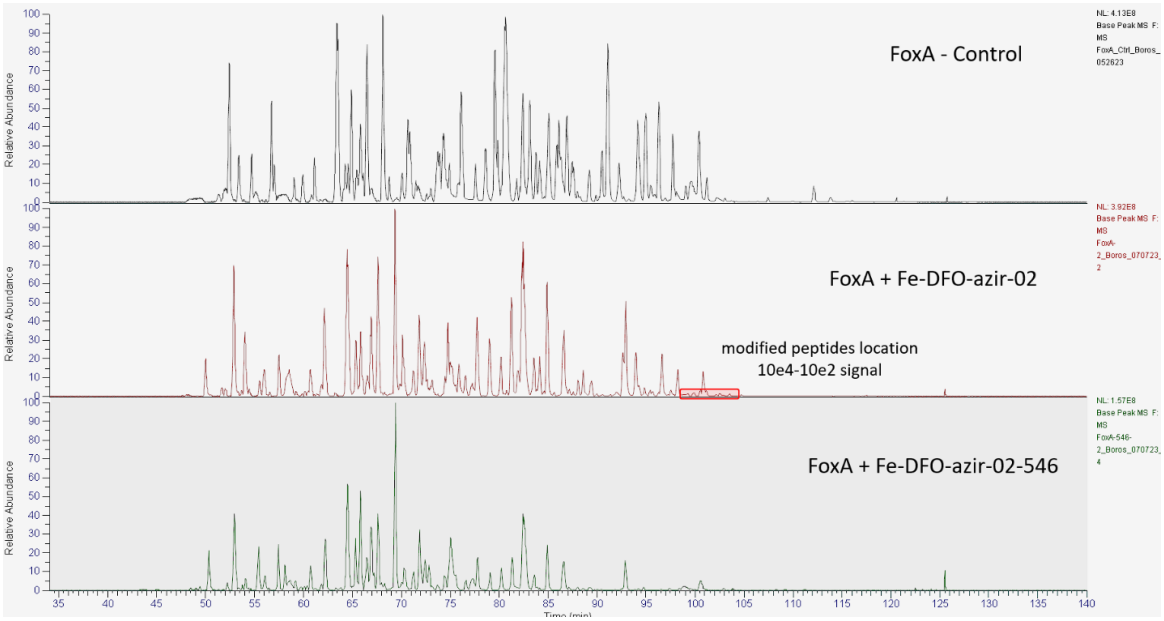

Figure 3. 62: Fe-DFO-azir-02 conjugated to azide-flour 545 base peak chromatogram traces of FoxA tryptic digest.

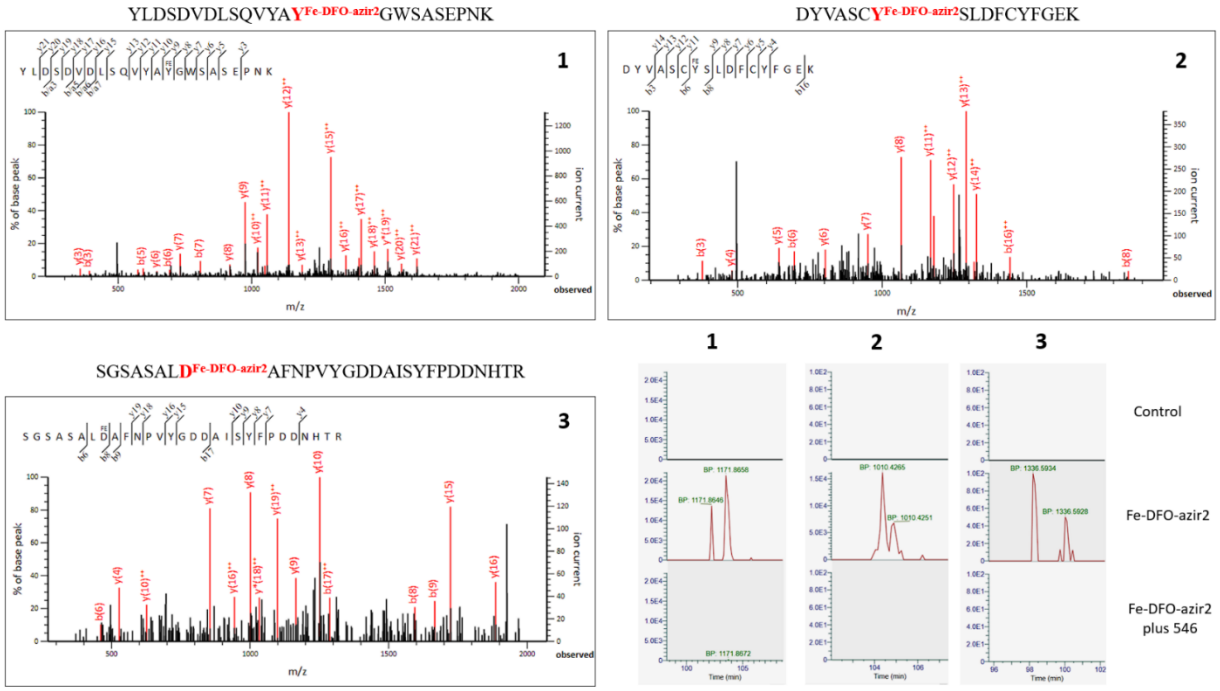

Figure 3. 63: Site of labeling by Fe-DFO-azir-02 photocrosslinked to pure FoxA in solution.

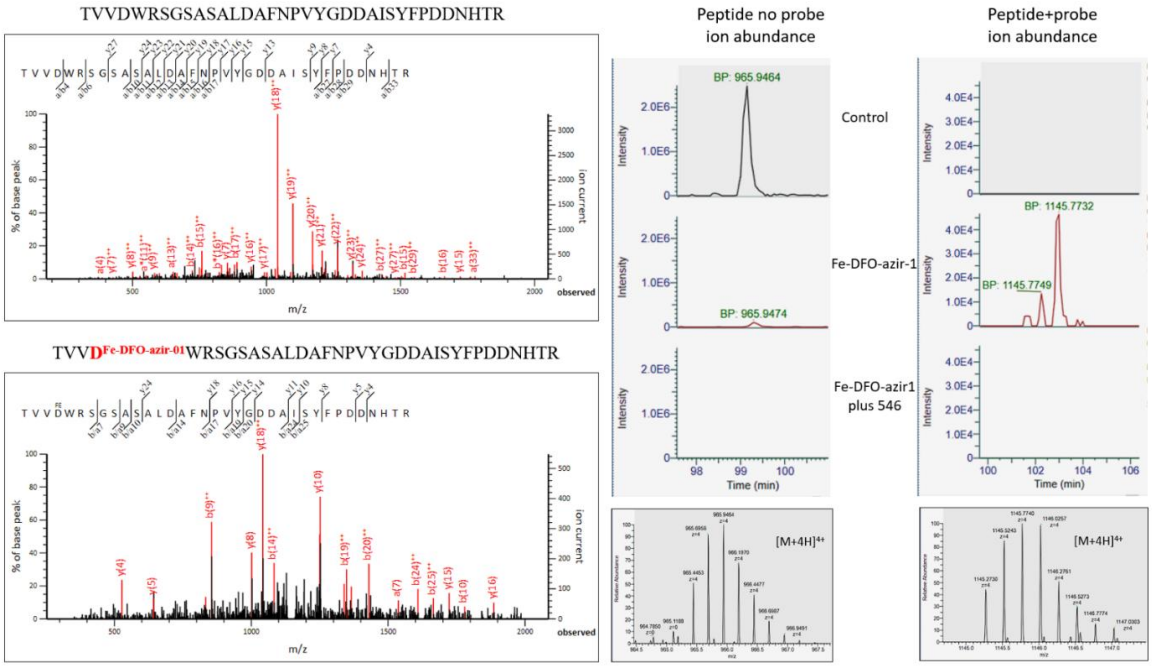

Figure 3. 64: Site of labeling by Fe-DFO-azir-01 photocrosslinked of pure FoxA in solution..

Figure 3. 65: FoxA sites with probe modification after reacting with 50 eq of probes followed by 15min photo-irradiation at 365nm.

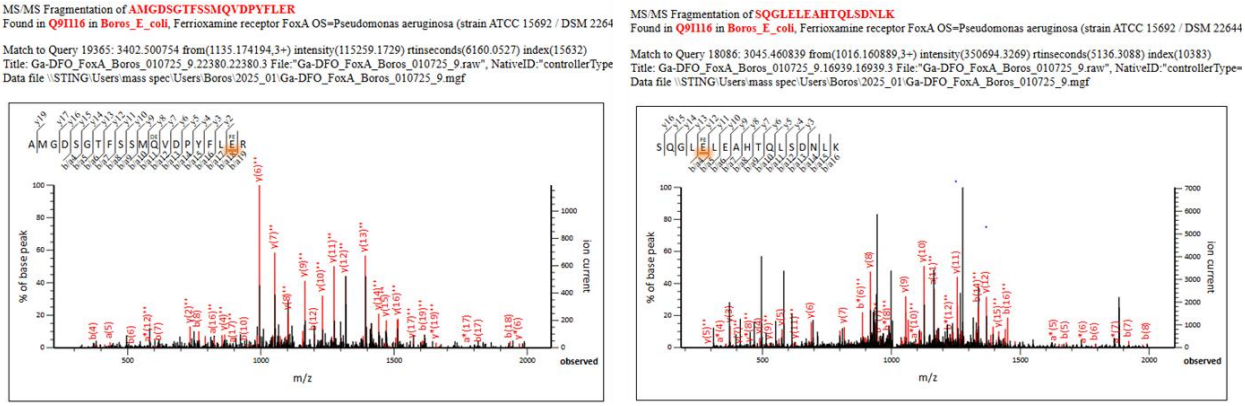

Figure 3. 66: Site of labeling by Ga-DFO-azir-06 photocrosslinked of pure FoxA in solution found as Fe-DFO-azir-06.

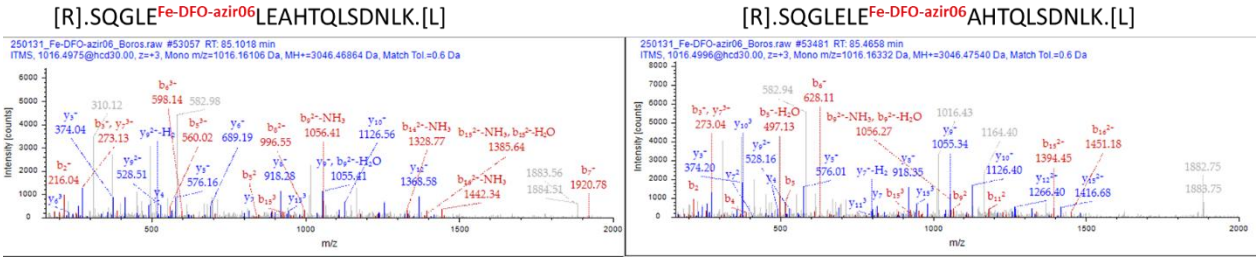

Figure 3. 67: Site of labeling by Fe-DFO-azir-06 photocrosslinked of pure FoxA in solution.

3.5.9 MALDI

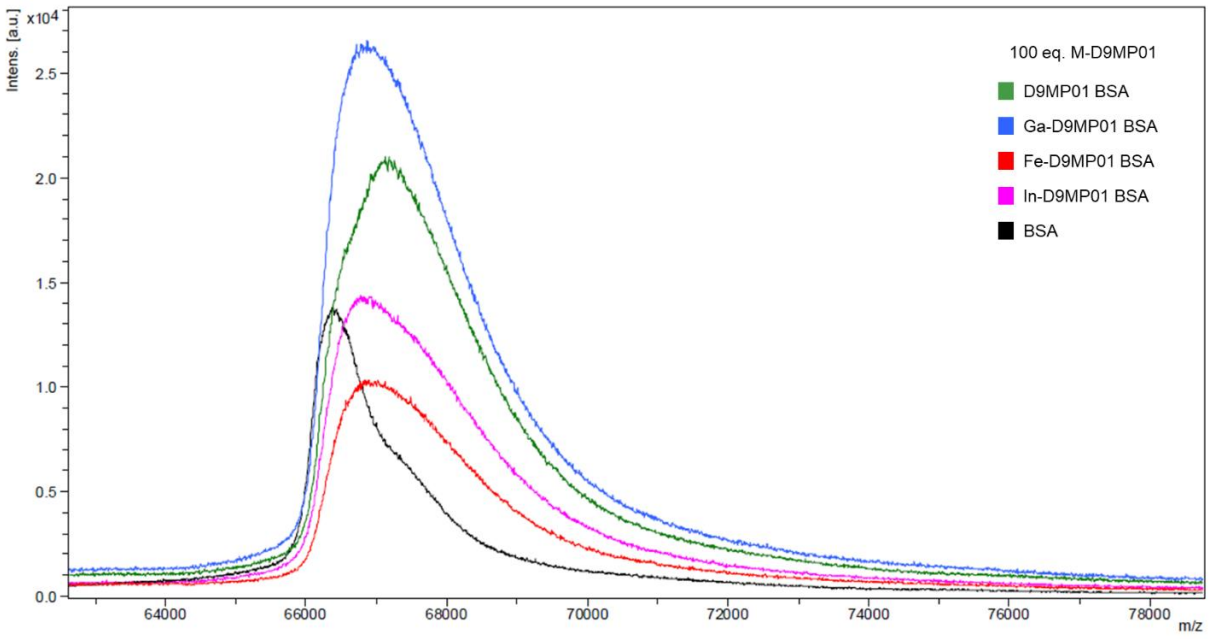

Figure 3. 68: MALDI chromatogram of M-DFO-azir-01 series cross-linked to BSA. .

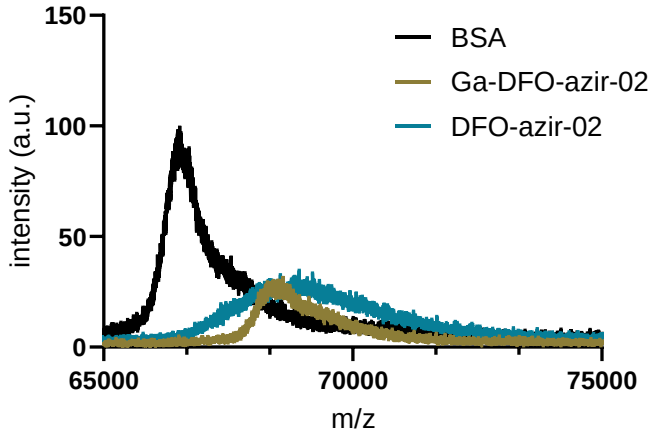

Figure 3. 69: MALDI chromatogram of Ga and DFO-azir-02 cross-linked to BSA. Intensity normalized.

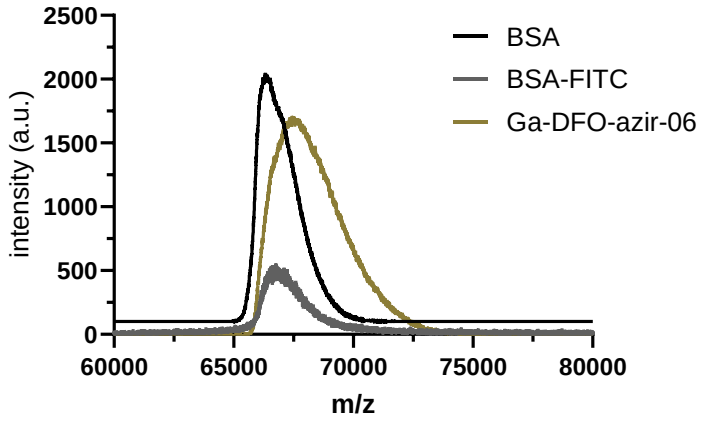

Figure 3. 70: MALDI chromatogram of Ga -DFO-azir-06 cross-linked to BSA. Intensity normalized.

Chapter 4: A multimodal chemical tagging strategy for identification siderophore-transporters

4.1 Summary this work

E. coli Lemo 21 C43(DE3) overexpressing FoxA strain was designed and produced by Inoketjis Josts and Hendrik Tidow. Grzegorz Sabat from the Mass Spectrometry Core Facility at UW-Madison performed MS/MS sample treatment and data acquisition. All compound synthesis, characterization, and other experiments were performed by Minhua Cao.

4.2 Introduction

4.2.1 Introduction of siderophore transporter identification

Siderophore conjugates can readily hijack the iron-siderophore import systems present in microbes to selectively deliver cargos to the bacterial peri- and cytoplasm.[75] An application of this concept has been validated by the FDA approval of the first synthetic siderophore antibiotic conjugate cefiderocol, a catechol-linked beta-lactam, for clinical use. Despite these advances, a lack of understanding remains regarding the siderophore uptake pathways for many known, but less studied, siderophores.

This lack of understanding stems, in part, from the intricate uptake pathways of siderophores, as each siderophore type can utilize differential, siderophore-binding transmembrane transport mechanisms. For instance, *E. coli* possesses at least six known iron transport systems, dedicated to the uptake of ferrichrome (FhuA), enterobactin (FepA), aerobactin (IutA), rhodotorulic acid, coprogen (FhuE), salmochelin (iroN), and yersiniabactin (FyuA) (Figure 4.1). [6,27] Furthermore, several siderophores may also be taken up by additional, duplicate transport systems with lower structural selectivity: for instance, pathogenic *E. coli* strains also uptake catechols through CirA and Fiu, two outer-membrane transporters uptake of catecholate siderophores.[145] Experimental studies demonstrated that Fiu and CirA function as transporters for enterobactin breakdown products such as 2,3-dihydroxybenzoyl-l-serine (DHBS) in complex with iron and other monomeric catecholate iron complexes.[146] The efficiency and selectivity of recognition and uptake of siderophores, are also strain-dependent and hint the existence of a larger family of transport proteins with highly variable affinity for the metal-bound siderophore substrate than previously estimated. [79,147] Therefore, tools that efficiently and rapidly identify such

transporters could provide unprecedented insight into metal homeostasis and virulence of commensal and pathogenic bacterial strains.

Current documented methods in siderophore protein identification rely on: 1) biosynthetic cluster mining to obtain genetic information about siderophore proteins, combined with Fur titration assay (FURTA) to identify clusters of Fur-regulated genes involved in siderophore biosynthesis across different bacterial strains and species.[148-150] 2) mutational analysis, often implemented to determine if the deletion of known siderophore proteins affects the uptake of siderophore antibiotics, by examining MIC and growth phenotype analyses of mutants.[49,151,152] 3) fluorescent sensors, created by modifying known siderophore proteins, to detect, discriminate, and quantify apo- and ferric siderophores.[153] 4) pull-down probes using biotin-enterobactin to identify interacting proteins from whole-cell lysates.[140] 5) affinity chromatography, utilizing an immobilized siderophore metal complex to capture siderophore proteins in whole cell extracts.[128,154]

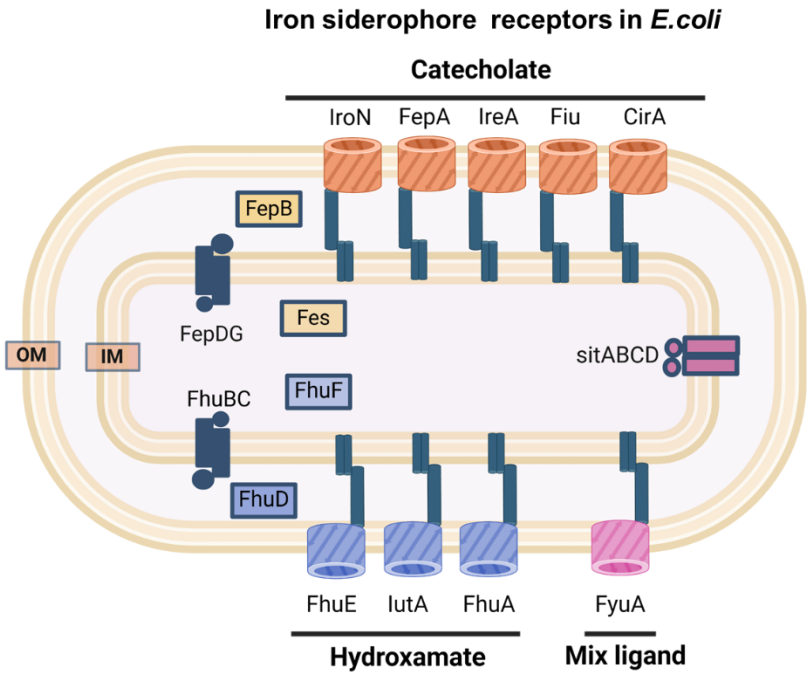

Figure 4. 1: In *E. coli*, the import of iron-siderophore complexes relies on specific outer membrane (OM) receptors, each responsible for the uptake of different siderophore classes, such as catecholates, hydroxamates, and mixed-ligand siderophores. Inner membrane (IM) transport is facilitated by components like the SitABCD cassette, FhuD, and FepB.

4.2.2 Introduction to the current work

Targeted siderophore antibiotic compound design is hindered by a critical knowledge gap: the identification of transmembrane transport proteins responsible for the critical import and cytoplasmic delivery of xenometal siderophore conjugates. This knowledge gap forces many synthetic siderophore conjugates to target periplasmic components as a workaround,[57,132] significantly complicating the development of effective semi-synthetic xenometal siderophore conjugates in Gram-negative bacteria.

The commonly employed methods to identify siderophore transport proteins each have several limitations, but each share the requirement for a high affinity binding mechanism between

the siderophore-substrate and the transmembrane protein.[155] This results in a bias towards such proteins with high selectivity, while overlooking proteins with lower affinity and selectivity, which are considered a likely source of xenosiderophore uptake to optimize iron piracy in the host and bacterially dense habitats.

To address this limitation, we sought to leverage the power of photoaffinity labeling. Recent advancements have demonstrated its efficacy in mapping protein-ligand interactions, particularly for metal complexes, within bacterial cells, offering a more comprehensive view of cellular interactions.[126] In Chapter 3, we investigated the reactivity profile of a new class of siderophore affinity probes, specifically DFO-diazirines, with single amino acid residues and the isolated siderophore periplasmic binding protein FoxA. These studies demonstrated the ability of our probes to effectively label protein of interest at the binding pocket, demonstrating the potential for targeted protein identification.

In this study, we evaluated if the previously established and validated diazirine-linked siderophore complexes can identify proteins that interact with xenometal siderophores in live cell culture. We validated our lead probes by covalently tagging FoxA, a known *P. aeruginosa* outer membrane siderophore-binding protein expressed in a plasmid-containing *E. coli* strain *E. coli* Lemo21. Furthermore, our experiments provide insight into *E. coli*'s mechanism of uptake of Ga-DFO-linked compounds, for which no equivocal transmembrane transporter has been identified to date.

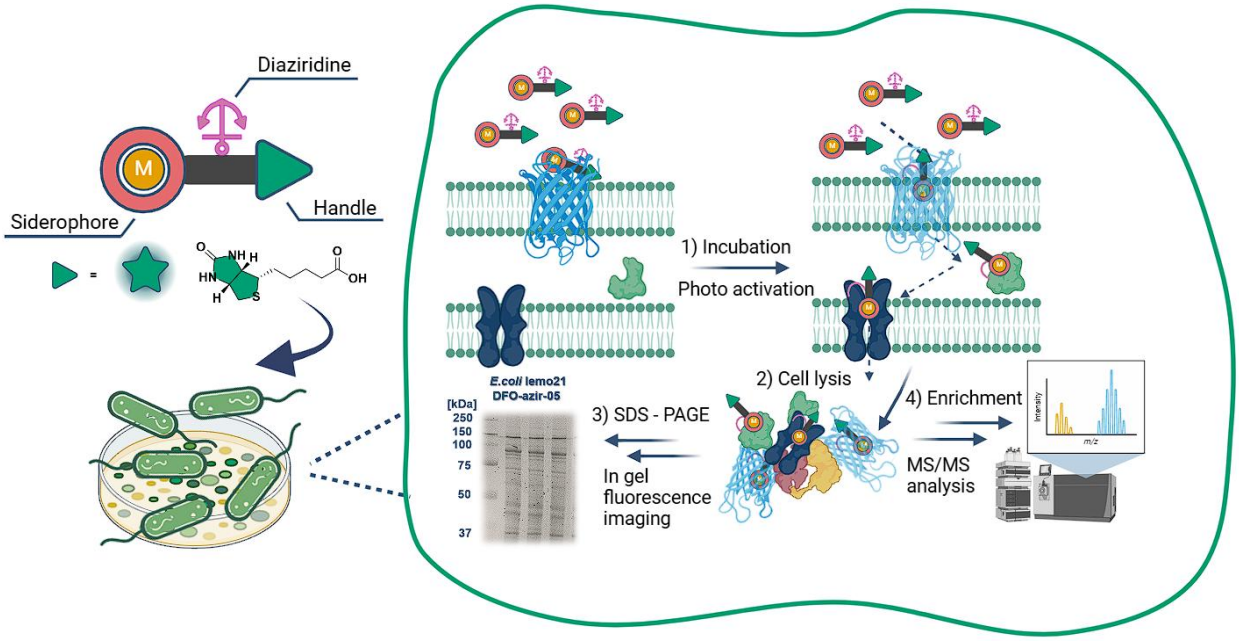

Figure 4. 2: A schematic for the application of siderophore photoaffinity probes: The probes, feature a photoactive diazirine moiety and a handle for the direct or post-labeling introduction of a reporter element, can be utilized for live bacterial cell labeling. The siderophore component of the probe directs it to the vicinity of siderophore-binding proteins. Upon UV activation, the diazirine moiety covalently crosslinks the probe to the protein of interest (1). The cells are lysis and reporter element, such as a fluorophore, allows for visualization (2-3), while a biotin reporter enables enrichment for subsequent protein identification (4).

4.3. Result and discussion

4.3.1 Radioactive assay to probe DFO-Diazirine probe internalization

To investigate DFO-diazirine internalization in bacterial cells, we utilized radiolabeling with ^{67}Ga to track compound uptake. Radiolabeled ^{67}Ga-DFO-azir-01 was incubated with *E. coli* Lemo21 cells overexpressing FoxA, an outer membrane receptor from *P. aeruginosa*. Following cell lysis and electrophoresis, the gel was exposed to a phosphor imaging plate for analysis. The experimental results indicated that the probe was internalized into the *E. coli* Lemo21 cells and appeared to label a protein with a molecular weight approximately 100-180kDa (Figure 4.3 A).

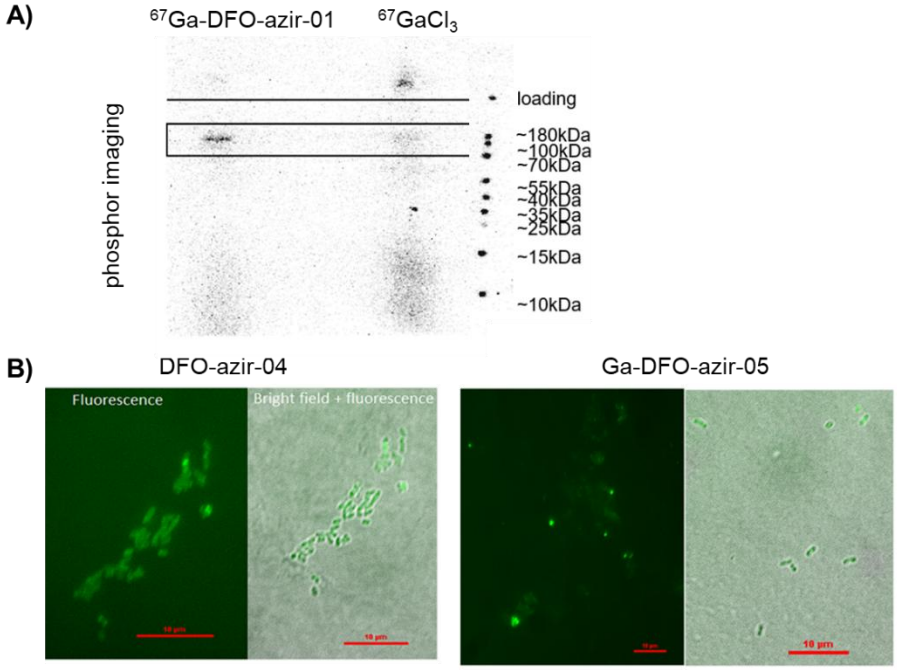

Figure 4. 3: A) Gel phosphor imaging from live cell labeling of *E. coli* Lemo21 cells with ^{67}Ga-DFO-azir-01, using 67GaCl3 as a control. B) Fluorescence microscopy of *E. coli* Lemo21 cells to visualize the internalization of compounds DFO-azir-04 and Ga-DFO-azir-05 with no photo-irradiation to conjugate the probe. Left fluorescence image and right bright field overlay with fluorescence image.

To complement these radiolabeling studies and enable visualization, second-generation DFO-diazirine probes, M-DFO-azir-04 and M-DFO-azir-05, incorporating a pre-conjugated coumarin fluorophore, were utilized for fluorescence microscopy (Figure 4.3B). The relative fluorescence quantum yields of the gallium complexes, Ga/DFO-azir-04 and Ga/DFO-azir-05, compared well with the parent fluorophore (quantum yield: 0.5 and 0.6 respectively), producing quantum yields of 0.8 and 0.48 respectively. Conversely, the iron complexes, Fe-DFO-azir-04 and Fe-DFO-azir-05, demonstrated significant fluorescence quenching upon Fe-complex formation, yielding near-negligible relative quantum yields (Figures 3.57-64). This observation is consistent with established literature reporting the fluorescence quenching of fluorophores by Fe-DFO, thereby preventing the utilization of these iron complexes for imaging applications.[83]

Further studies were conducted to investigate the impact of the pre-conjugated fluorophore on compound internalization relative to ^{67}Ga-DFO. To this end, we investigated the uptake of ^{67}Ga-DFO-azir-05 in a cell fractionation experiment. The overall uptake of ^{67}Ga-DFO and ^{67}Ga-DFO-azir-05 displayed comparable levels between wild-type and mutant strains, in spite of the presence of a DFO-binding outer membrane transporter in the *E. coli* Lemo21 strain (Figure 4.4) Collectively, these experiments suggest that the majority of bound probe activity arises from a transmembrane transport via an *E. coli* endogenous transporter; this highlights the potential to identify the DFO-translocating protein in this strain using the previously developed diazirine probes.

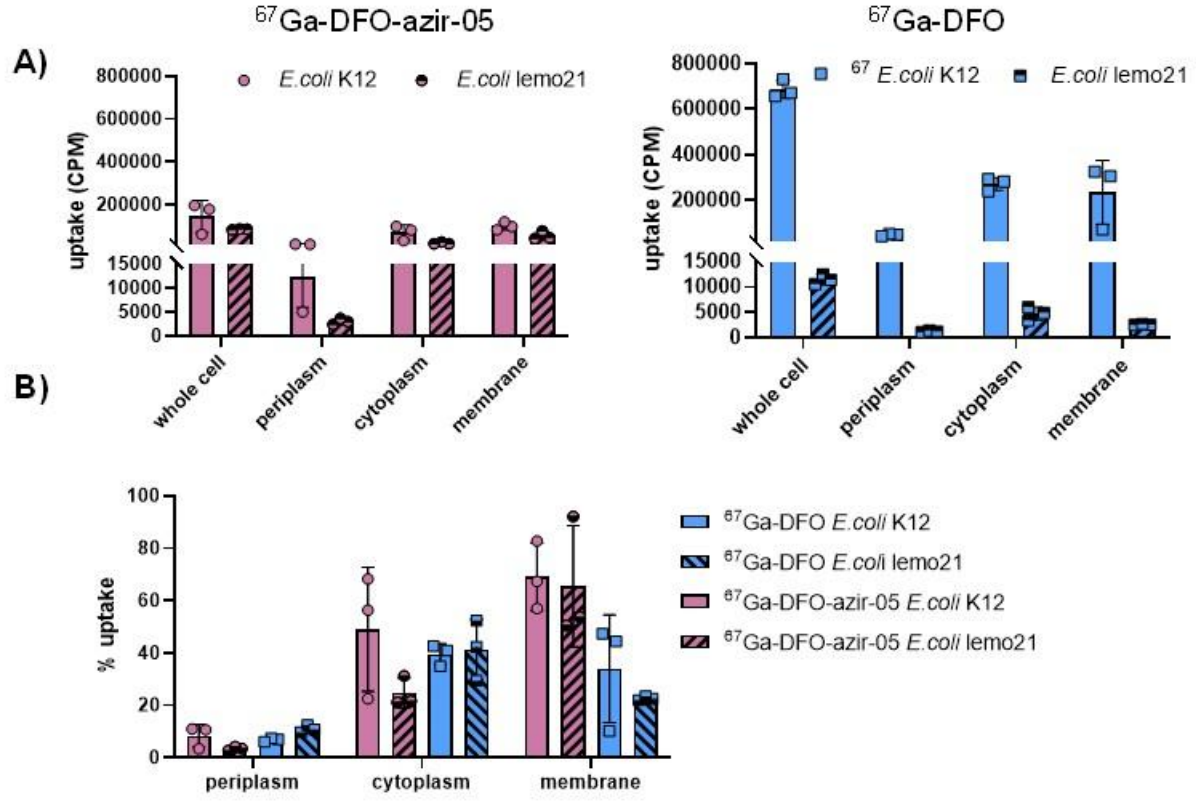

Figure 4. 4: Cell fractionation assay with radioactive labeled ^{67}Ga-DFO-azir-05 and ^{67}Ga-DFO in *E.coli* lemo 21 and *E.coli* K12 strains. A) Compound distribution shown in CPM. B) Compound distribution shown in percentage uptake comparing ^{67}Ga-DFO-azir-05 and ^{67}Ga-DFO across *E.coli* strains.

4.3.2 Live cell labeling

To demonstrate the functional application of our DFO-diazirine probes, we performed live-cell tagging of FoxA in mutant *E. coli* Lemo21 strains. Cells were incubated with M-DFO-azir-01 or M-DFO-azir-02 (5 µM) at 37°C for 30 minutes, followed by 15 minutes of photo-irradiation. Subsequently, bacterial cells were lysed, and labeling was visualized by conjugation with azide-fluor 545 via copper-catalyzed azide-alkyne cycloaddition (CuAAC) and in-gel fluorescence. For M-DFO-azir-01, we observed probe-dependent fluorescence, though the bands were weak and provided limited evidence of significant FoxA protein tagging (Figure 4.30*)*. Furthermore, CuAAC compatibility with DFO-diazirine alkyne probes appeared suboptimal, consistent with

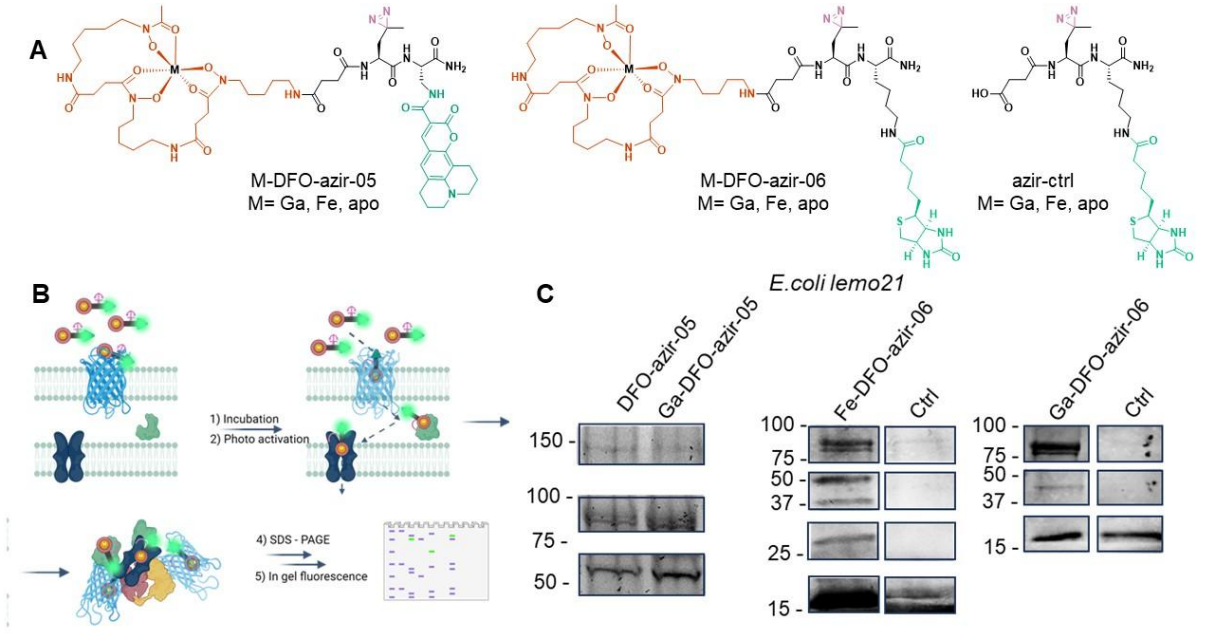

Figure 4. 5: A) M-DFO-azir-05,M-DFO-azir-06, and azir-ctrl structure. B) Live bacteria cell labeling with siderophore photoaffinity probe scheme. C) Live E.coli Lemo21 strain labeling with Ga/DFO-azir-06, showed in in gel fluorescence, and Fe/Ga-DFO-azir-06, showed as western blot anti-biotin. Ctrl= no probe added. (Full gel Figure 4.36A, 4.37).

observations from FoxA isolates. Additionally, we were unable to detect M-DFO-azir-02 probe-dependent fluorescence in live cells. These results highlighted challenges associated with the post-conjugation CuAAC approach in complex biological media, prompting us to utilize pre-linked DFO-diazirine probes DFO-azir-5 and DFO-azir-06 to simplify the protein tagging process and circumvent the need for post-conjugation click chemistry.

The results revealed that both Ga and apo-DFO-azir-05 were effective in labeling FoxA in live cells, with fluorescence bands observed at approximately 100 kDa and 150 kDa (Figure 4.4 B). This finding was corroborated by western blot analysis for the His-tag on FoxA (Figure 4.6, 4.31-33). Notably, both Ga and apo-DFO-azir-05 exhibited comparable reactivity, suggesting that they label similar proteins, as indicated by the presence of identical fluorescence bands. Additional fluorescence band (above 50 kDa), which did not correspond to FoxA, suggest that the probes were successfully internalized by the bacterial cells and likely targeted different cellular receptors or proteins involved in downstream transport.

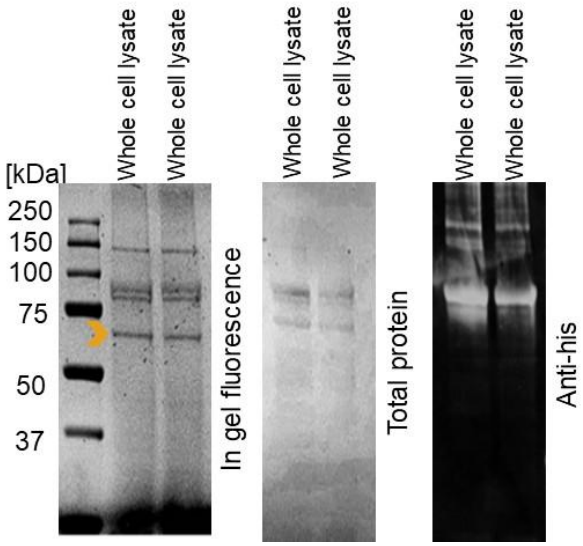

Figure 4. 6: live cell labeling with Ga-DFO-azir-05 gel, visualized by in-gel fluorescence, total protein staining, and Western blot. The orange arrow highlights a labeled protein band below 70kDa on in-gel fluorescence, which is identified as not being FoxA. Full gel: figures 4.31-4.34.

Having established the efficacy of pre-linked DFO-diazirines in mutant strains, we sought to extend the scope of our investigation to encompass wild-type bacterial species. We observed

labeling in *E. coli* K-12 with both M-DFO-azir-05 and M-DFO-azir-06. This labeling appeared to be siderophore-dependent, as it differed from the control azir-06, which lacks DFO (Figure 4.7A). Similarly, we observed labeling in *P. aeruginosa* with Ga-DFO-azir-05 and Fe-DFO-azir-05 (Figure 4.7B). However, due to the high levels of endogenous, biotinylated proteins in these strains, [156] we were unable to detect specific M-DFO-azir-06 labeling (Figure 4.40). Conversely, we successfully observed M-DFO-azir-06-specific labeling in *S. aureus* (Figure 4.7C). Specifically, we observed a band at 35 kDa for both Fe-DFO-azir-06 and Ga-DFO-azir-06, which was notably absent in control lanes.

These experiments collectively indicate that pre-linked DFO-diazirines can be applied to identify siderophore-binding proteins in various wild-type strains, including both Gram-negative and Gram-positive bacteria, but results must be carefully evaluated with control experiments that

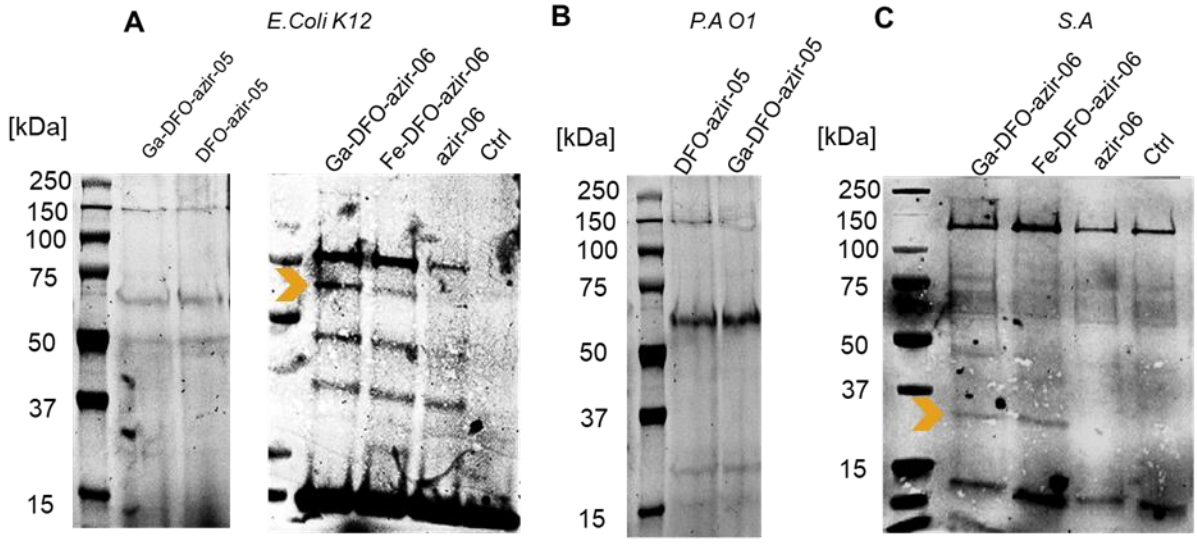

Figure 4. 7: Live bacterial cell labeling in wild type strains *E.coli* K12, *P. aeruginosa* P.AO1, and *S. aureus* with M-DFO-azir-05 and M-DFO-azir-06 probes. The protein band indicated by the orange arrow represents a labeled protein that seems specific to samples treated with Ga and Fe-DFO-azir-06. (Full gel figure 4.36, 4.37,4.38,4.40)

determine if the pre-crosslinking binding even has occurred with the target substrate or the fluorophore/biotin pulldown tag.

4.3.3 Challenge uptake assay

To determine if the tagged proteins represent correct "hits" containing a siderophore-binding moiety, it is important to determine the extent to which the observed fluorescence bands are dependent on siderophore binding. The pre-tagged optical and pull-down probes used in this study may interact with proteins through both specific interactions, mediated by siderophore binding (head-on), and non-target specific interactions, which arise from interactions with the fluorophore or biotin tag (tail-on). To distinguish between head-on and tail-on binding, the second-generation probes were subjected to a challenge using the parent siderophore, Fe-DFO. The results from *E. coli* Lemo 21 strains indicated that, with increasing concentrations of Fe-DFO several bands exhibited a reduction in fluorescence intensity: including a band at approximately 100 kDa, 50 kDa and 25 kDa, with the bands fully suppressed by 100 equivalents of Fe-DFO. For Ga-DFO-azir-06, we observed the gradual suppression of tagging the 50 kDa band, (at 50 equivalents of Fe-DFO). However, some bands, including a band around 25 kDa band for Ga-DFO-azir-05, remained unaffected by the presence of Fe-DFO, suggesting the occurrence of off target/tail-on interactions (Figure 4.8).

This finding suggests both M-DFO-azir-05 and M-DFO-azir-06 are capable of effectively labeling proteins, including FoxA, in live *E. coli* Lemo 21 cells. Additionally, the presence of

additional bands sensitive to Fe-DFO displacement suggests the probe's ability to target other siderophore proteins, potentially related to receptor uptake or downstream transport processes.

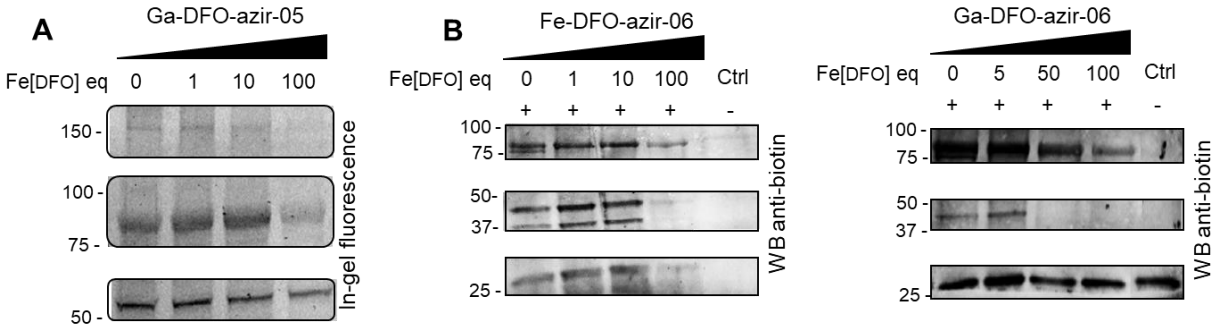

Figure 4. 8: Challenge live bacterial cell labeling in E.coli Lemo21 strains with Ga-DFO-azir-05 and Ga-DFO-azir-06 in increased amount of Fe-DFO. (Full gel figure 4.34B,4.35)

4.3.4 Enrichment experiments

To identify the proteins targeted by our DFO-diazirine probes, we conducted an enrichment assay for protein identification. *E. coli* Lemo21 cells were incubated with Fe-DFO-azir-06 and Ga-DFO-azir-06 (125 μM), photoirradiated, and labeled proteins were enriched using streptavidin magnetic beads, followed by elution and SDS-PAGE separation.[126] Mass spectrometry (MS/MS) was utilized to generate a protein enrichment profile, with FoxA (89 kDa), OmpF (39 kDa), OmpA (35 kDa), and TuFa (41 kDa) emerging as the most abundant labeled proteins (Figure 6B). TuFa, an elongation factor (EF), facilitates GTP-dependent aminoacyl-tRNA binding to the ribosomal A-site during protein biosynthesis. Its expression level is correlated with cellular fitness and growth rate regulation. TuFa, an elongation factor (EF), facilitates GTP-dependent aminoacyl-tRNA binding to the ribosomal A-site during protein biosynthesis. Its expression level is correlated with cellular fitness and growth rate regulation.[157] OmpF and OmpA, both considered outer membrane porins,[158] dominated the enrichment results for both Ga- and Fe-DFO-azir-06,

suggesting interaction with our probes. Further mass spectrometric analysis of the OmpF fragments revealed the selective covalent tagging through tyrosine residue Y220 as a specific labeling site for Fe-DFO-azir-06 (Figure 4.9 C).

The enrichment of two porins, OmpF and OmpA, alongside FoxA is particularly intriguing. OmpF, is generally considered to facilitate small molecule transport across the membrane non-specifically. However, several reports detail Fe^{2+} translocation in conjunction with OmpC under anaerobic conditions.[159] Its expression, tightly regulated by the EnvZ/OmpR two-component signal transduction systems (TCS), is implicated in iron homeostasis.[160] Other studies have demonstrated that deletion of both OmpC and OmpF in a tonB mutant strain renders the cells non-viable due to the loss of functional ferric transport systems.[161] While OmpF is classically understood to transport hydrophilic molecules weighing approximately 600 Da,[162] its capacity to

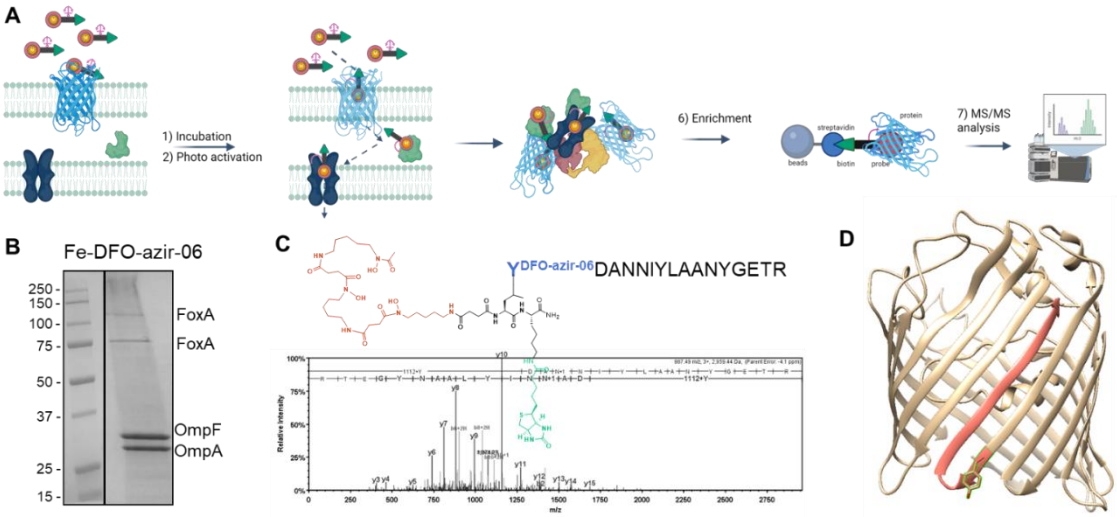

Figure 4. 9: A) Schematic representation of the enrichment assay. B) Elution profile of affinity chromatography using biotin-streptavidin with cell extracts from *E. coli* Lemo21 cells following in vivo labeling with Fe-DFO-azir-06 (Full gel figure 4.48). C) Mass spectrometry chromatogram from the enrichment analysis, demonstrating labeling of OmpF by DFO-azir-06. D) Protein fragment of OmpF identified with probe conjugation.

translocate larger molecules, such as the 2.9 kDa HPA3P peptide [163] and small proteins like YebF [158] as well as translocate many small molecule antibiotics is well documented.[164,165]

Taken together, these results suggest that OmpF may serve as an alternative entry point for deferoxamine-based probes, facilitating their uptake into bacterial cells via porin-mediated transduction. This observation challenges the conventional understanding of OmpF's substrate specificity and suggests a broader role in the cellular import of larger molecules and iron homeostasis. Further experiments to corroborate these findings are ongoing.

4.4 Summary and conclusion

In this study, we successfully demonstrated the use of photocrosslinker-siderophore affinity probes for the identification of known and unknown siderophore-binding proteins in bacterial live cell assays. As a proof-of-concept, we effectively tagged FoxA using pre-linked DFO-diazirine-fluorophore and biotin-pulldown probes effectively in live *E. coli* Lemo21 cells. While the cell fractionation results indicated that the ^{67}Ga-DFO-azir-05 probe had lower uptake compared to ^{67}Ga-DFO in *E. coli* K12, this discrepancy suggests that excessive modification of the pre-linked probe away from the parent siderophore can reduce probe affinity for *E. coli* transporters. Pre-linked pulldown probes produce hits considered off-target/tail-on binding interactions through the fluorophore/biotin moiety, which must be carefully identified by substrate challenge assays. Collectively, our results indicate that further refinement of the pre-linked DFO-diazirine probes provides powerful tools to identify proteins implicated in siderophore-mediated internalization in live bacteria.

Our preliminary enrichment results have provided valuable insights into the uptake mechanisms of deferoxamine (DFO)-based probes in *E. coli*. While the identity of a deferoxamine receptor in *E. coli* remains unknown, this and previous radioactive uptake studies with ^{67}Ga-D1 support the existence of a deferoxamine-specific transporter. Specifically, we found that siderophore-mediated uptake of Ga-D1 remains selective in *E. coli* K-12, with its minimum inhibitory concentration (MIC) remaining unchanged in FhuA- (ferrichrome transporter) mutants.[87] Additionally, Grinter et al. demonstrated that *E. coli* Δ*TDBT* mutants, which rely on FhuE for iron import, show limited growth with deferoxamine, suggesting that neither FhuA nor FhuE alone is responsible for DFO-conjugate uptake.[166] This points to the existence of an alternative pathway for uptake. Our enrichment assays using Fe- and Ga-DFO-azir-06 in *E. coli* Lemo21 point to the potential involvement of OmpF. Although the precise role of OmpF in siderophore conjugate uptake remains speculative, previous reports indicate that resistance mechanisms in Cefiderocol-resistant strains involve downregulation of OmpF porins.[50] This could suggest that further deviations of the siderophore conjugate from the parent siderophore could result in a combination of passive diffusion and siderophore-mediated uptake by low-affinity binders such as the OmpX class of porins. Given the complexities of these systems, further studies are needed to confirm whether OmpF contributes to iron homeostasis under aerobic conditions, beyond its established role in Fe^{2+} uptake under anaerobic conditions.[167]

Moreover, due to the inherent complexity of protein-ligand interactions, we posit that a singular linker length is unlikely to comprehensively represent the full spectrum of relevant interactions. Consequently, we propose that future investigations should explore the development of a diverse library of probes with varied linker lengths, drawing inspiration from the established

methodology employing heme-diazirine probes by Sieber et al. Furthermore, to minimize off-target interactions and ensure minimal structural perturbations, further optimization of the DFO-diazirine alkyne probes and the improvement of post-crosslinking CuAAC methodologies is warranted. This combined approach may further facilitate a more thorough understanding of siderophore-mediated iron uptake in bacteria.

4.5 Experimental and supporting information.

4.5.1 Quantum yield

Quantum yield for each complex and corresponding ligands were determined using the following equation:

$$\Phi_x = \Phi_S \frac{\text{Gradient}_x}{\text{Gradient}_S} \quad \text{Eq.1}$$

Where "S" refers to the organic coumarin fluorophore standard (7-(diethylamino)coumarin-3-carboxylic acid, Φ = 0.50 for M-DFO-azir-04; coumarin 343, Φ = 0.62 for M-DFO-azir-05) and "x" is the unknown. The gradient is the slope of the graph plotting integrated emission intensity against peak absorption value for a range of concentrations. The excitation wavelength for each complex and corresponding ligand was their corresponding λmax (7-(diethylamino)coumarin-3-carboxylic acid: Ex = 415 nm, Em = 465 nm; coumarin 343: Ex = 444 nm, Em = 480 nm). All samples were measured in ethanol.

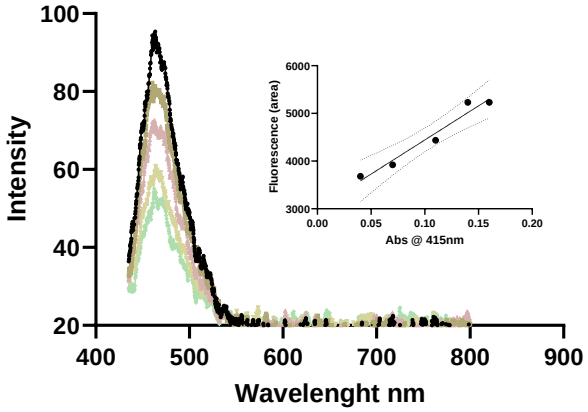

Figure 4. 10: 7-(Diethylamino)coumarin-3-carboxylic Φ = 0.5

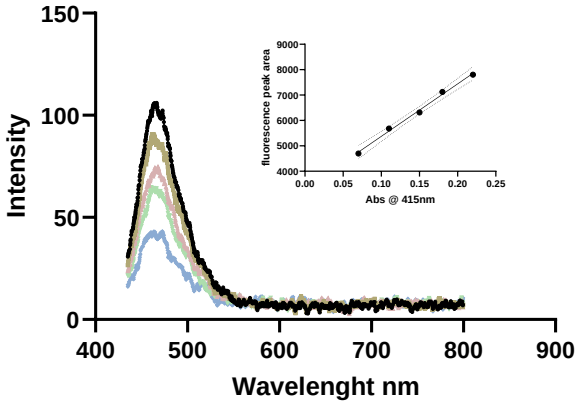

Figure 4. 11: DFO-azir-04 Φ = 0.8

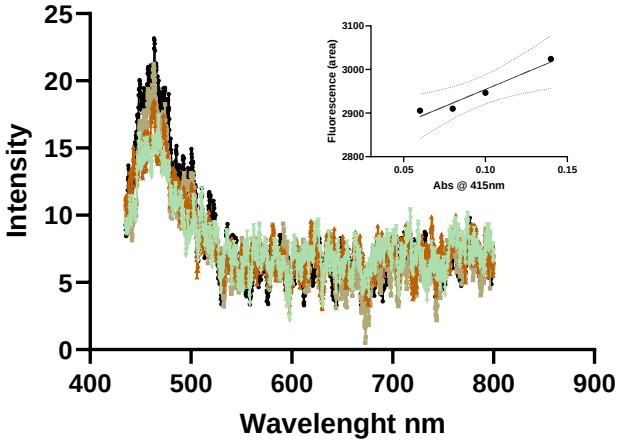

Figure 4. 12: Fe-DFO-azir-04 Φ =0.0

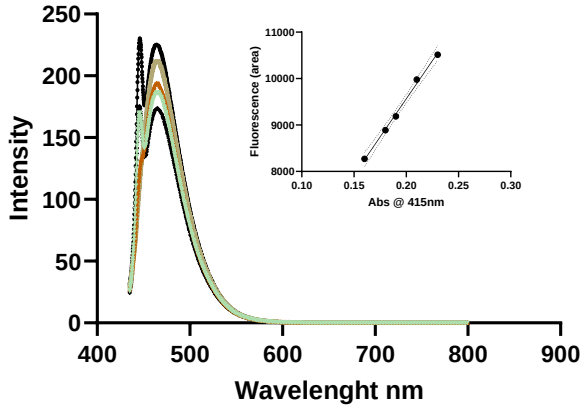

Figure 4. 13: Ga-DFO-azir-04 Φ = 1

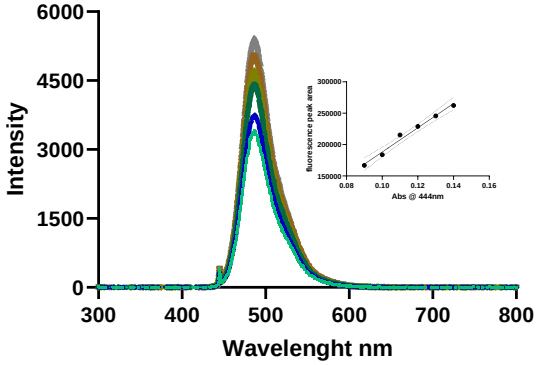

Figure 4. 14: Coumarin 343 Φ = 0.63

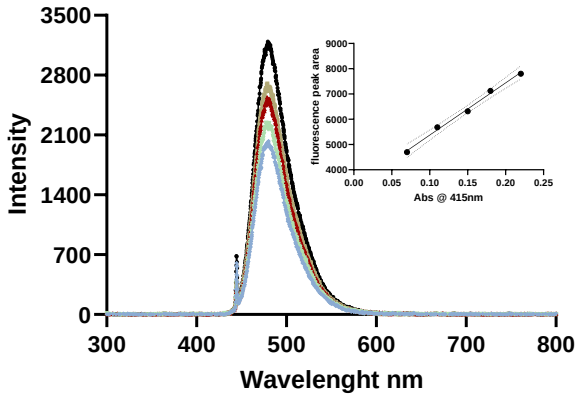

Figure 4. 15:Ga-DFO-azir-05 Φ =0.48

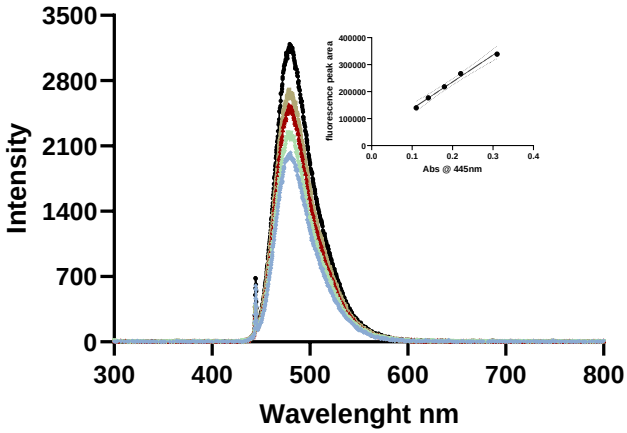

Figure 4. 16: DFO-azir-05 Φ =0.31

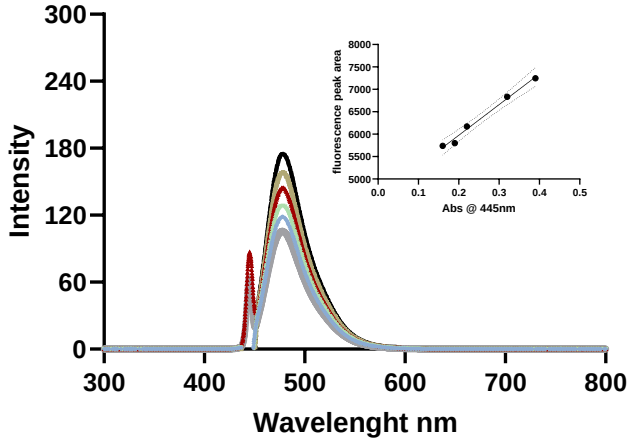

Figure 4. 17:Fe-DFO-azir-05 Φ = 0.06

4.5.2 Bacteria culture

E. coli (K-12), *S. aureus* (RA RN4220) *and P. aeruginosa* (PAO1)*:* An overnight culture grown at 37 °C in iron-deficient LB medium (containing 1 mg/mL DP) was inoculated (1:50) into 10 mL of fresh iron-deficient LB medium and grown until the OD_{600} reached 0.6.

E. coli Lemo 21 C43(DE3)*:* A stock culture was streaked onto an LB agar plate containing 25 µg/mL kanamycin and 35 µg/mL chloramphenicol and incubated overnight at 37 °C. A single

colony was inoculated into 50 mL of fresh LB medium containing antibiotics and grown until the OD_{600} reached approximately 0.6. The bacterial culture was cooled, induced with 0.1 mM IPTG for protein expression, and incubated for 16 hours at 20 °C.[168]

4.5.3 FoxA purification

Bacterial culture and lysis: A 100 mL bacterial culture with an OD_{600} of 0.6 was pelleted by centrifugation at 4 °C, 4000 rpm for 15 minutes and resuspended in 5 mL of lysis buffer 1 (50 mM Tris, pH 7.6, 250 mM NaCl, 1% w/v Triton X-100, 1% w/v OG, 10% w/v glycerol) an final concentration of 2mM of PMSF. [126] Cells were lysed by sonication on ice using a Fisher Scientific Model 505 Sonic Dismembrator CL-18 with 1s bursts and a 4s off interval at 70-80% intensity for a total of 8 minutes of sonication. The lysate was incubated overnight at 4 °C on a rotary shaker. Insoluble material was removed by centrifugation at 4 °C, 21,000 rpm for 30 minutes. The first supernatant is set aside and the pellet was resuspended in lysis buffer 2 (50 mM Tris, pH 7.6, 250 mM NaCl, 5% w/v Triton X-100, 5% w/v OG, 10% w/v glycerol) and sonicated as described above for total of 1min. Insoluble material was once more removed by centrifugation at 4 °C, 21,000 rpm for 30 minutes. The two supernatants then combined for affinity chromatography.

Affinity column chromatography: A Ni-Sepharose 6 Fast Flow histidine-tagged protein purification resin was used for the purification of FoxA. 1 ml of resin was equilibrated with 20 column volumes (CV) of 25 mM imidazole in lysis buffer 1. The equilibrated resin was added to the lysate and incubated for 1 hour at 4 °C on a rotary shaker. The flow-through was reloaded onto the column twice, and the column was washed with 20 CV of lysis buffer containing 25 mM imidazole. The protein was eluted with 250 mM imidazole in lysis buffer 1 in five 300 µL fractions. The fractions were analyzed by SDS-PAGE to identify the protein-containing fractions followed

by western plot. The protein was solvent exchange to lysis buffer 1 and protein concentration was quantified by BCA assay.

4.5.4 Radiochemical assay

4.5.4.1 Radiolabeling with ^{67}Ga.

Converting ^{67}Ga citrate to ^{67}Ga chloride standard procedure: Preparation of ^{67}Ga chloride from ^{67}Ga citrate: ^{67}Ga citrate was received from Jubilant Radiopharma at an average specific activity of 4 mCi/mL. The ^{67}Ga citrate solution was mixed with two-thirds of its volume of DI water. The solution was then filtered manually over a 100 mg Sep-Pak® Vac 1 cc (100 mg) silica cartridge (Waters) with a plastic syringe. The column was washed with 15mL of DI water to remove citrate ions. The retained radioactivity was eluted from the cartridge with 500 µl of 0.1M HCl to yield ^{67}Ga chloride. The elution was collected in 100 µL fractions in eppendorf tubes and the fractions with maximum activity were used for radiolabeling. The average specific activity of the $^{67}GaCl_3$ solution used for radiolabeling was 5.95 µCi/ µl.

^{67}Ga-DFO-azir-01 radiolabeling: An aliquot of $^{67}GaCl_3$ (110 µCi, 25µl) was mixed with a solution of the apo-probe (20 µl, 0.4mM). The pH of the solution was adjusted with HEPES (0.1M, pH 7.5) to 7. Complexation was monitored with radio-HPLC method C, ^{67}Ga-DFO-azir-01, Rt= 7.49min, RYC $\geq$ 95%. Radiolabeling was found to proceed after 10 min at room temperature .

^{67}Ga-DFO-NCS labeling: $^{67}GaCl_3$ (110 µCi, 25 µl) was added to a solution DFO-NCS (0.17mM, 25uL, DMSO). The pH of the solution was adjusted with HEPES (100mM, pH 7.5) to 7 and incubated for 10 min at room temperature. Complexation was monitored with radio-HPLC method C, ^{67}Ga-DFO-NCS, Rt= 9.41min, RYC $\geq$ 95%.

^{67}Ga-DFO-NCS conjugation to BSA: A solution of BSA (0.4 mg/mL, 50 equivalents, 16 μL) in DPBS (10 mM, pH 7.3, 0.4% SDS, 1% Triton X-100) was mixed with 60 μL of 0.1 M NaHCO3 (pH 9), resulting in a final pH~ 9. ^{67}Ga-DFO-NCS was then added to the mixture. The reaction proceeded at 60 °C for 2 hours on a heating block with shaking. Excess ^{67}Ga-DFO-NCS was removed by precipitating the protein three times with 1 mL of cold acetone, followed by three washes with 1 mL of cold methanol. The protein was then resuspended in DPBS. Labeling was confirmed using size-exclusion radio-HPLC method E.

^{67}Ga-DFO-azir-01 and 02 conjugation to BSA: BSA (0.4 mg/mL, 50 equivalents, 16 μL) in DPBS (0.4% C8E4, 1% Triton X-100) was added to a 96-well plate. ^{67}Ga-DFO-azir-01 or -02 was then added to the BSA solution, and the mixture was photoirradiated at 365 nm for 15 minutes over an ice pack. To remove excess unreacted probe, the BSA samples were precipitated with acetone at -80 °C for 30 minutes and then centrifuged at 21,000 g for 10 minutes. The resulting protein pellet was resuspended in DPBS. Protein labeling was confirmed using size-exclusion radio-HPLC method E.

^{67}Ga-DFO-azir-01 and 02 conjugation to FoxA: FoxA (0.4 mg/mL, 50 equivalents, 16 μL) in DPBS (0.4% C8E4, 1% Triton X-100) was added to a 96-well plate. ^{67}Ga-DFO-azir-01 or -02 was then added to the FoxA solution, and the mixture was photoirradiated at 365 nm for 15 minutes over an ice pack. To remove excess unreacted probe, pre-packed disposable size exclusion desalting column (Zeba™ Spin Desalting Columns, 7K MWCO, 0.5–100 mL) was used. Protein labeling was confirmed with size exclusion radio-HPLC method E.

4.5.4.2 Gel electrophoresis

Method II: Live bacterial cell labeling was performed as described in 4.5.4 with ^{67}Ga-DFO-azir-0x labeled samples (50uCi/sample). PAGE was performed using a 40% acrylamide gel in a large plate system (Glass Plates for the omniPAGE Maxi Plus Cleaver scientific # VS30NGS1) at 120 volts for 7 hours at 4 °C in running buffer (25 mM Tris pH 7.5, 192 mM glycerol). PageRuler™ Prestained Protein Ladder was used as a molecular weight marker. Prior to electrophoresis, protein samples were mixed with a premixed solution of running dye (5% β-mercaptoethanol in 2x Laemmli buffer) at a 1:1 ratio and heated to 95 °C for 2 minutes. To create a fiducial marker that aligned with the protein ladder on the phosphor imaging plate, free $_{67}GaCl_3$ was quenched with TCL.Following electrophoresis, the gel was incubated overnight on a phosphor imaging plate. The phosphor imaging plate was then imaged using a Typhoon 9400 Variable Mode Imager.

4.5.4.3 Radiotracers and phosphor imaging

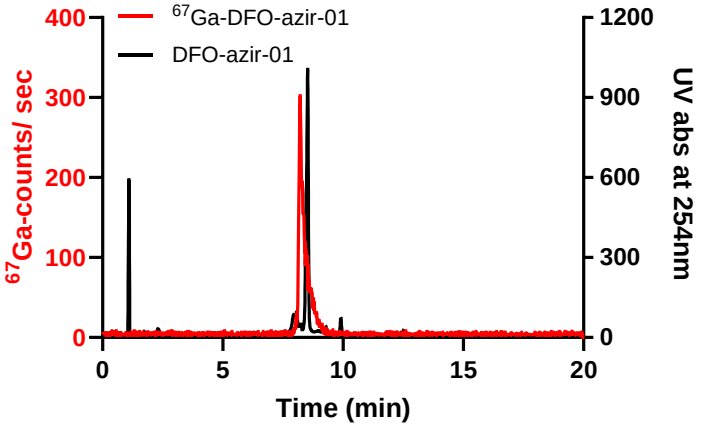

Figure 4. 18: Radiotracer for ^{67}Ga-DFO-azir-01 (r_t = 8.2min) overlay with DFO-azir-01 UV tracer (r_t =8.5min). HPLC method C.

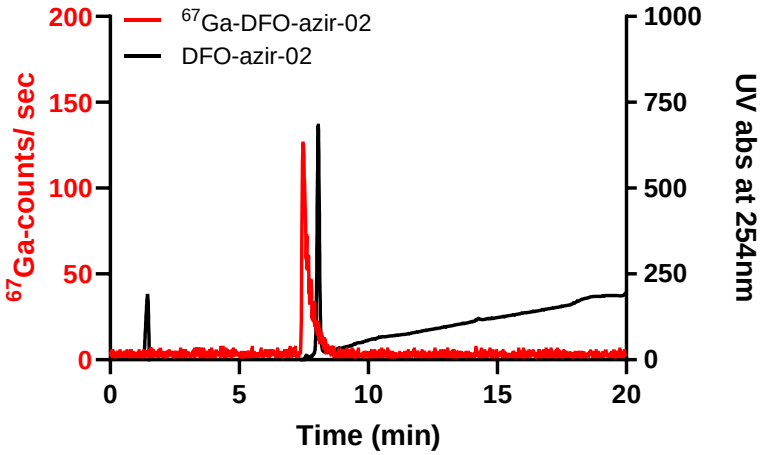

Figure 4. 19: Radiotracer for ^{67}Ga-DFO-azir-02 (r_t = 7.5min) overlay with DFO-azir-02 UV tracer (r_t =8min) . HPLC method C.

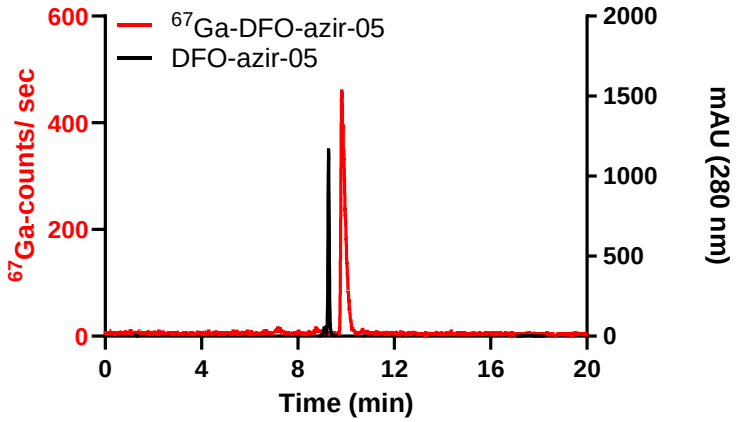

Figure 4. 20: Radiotracer for ^{67}Ga-DFO-azir-05 (r_t = 9.8min) overlay with DFO-azir-05 UV tracer (r_t =9.2min) . HPLC method C.

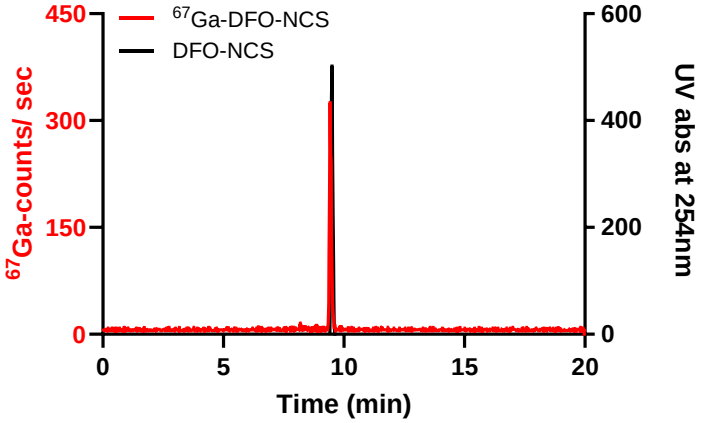

Figure 4. 21: Radiotracer for ^{67}Ga-DFO-NCS (r_t =9.4min) overlay with DFO-NCS (r_t =9.53min) UV tracer. HPLC method C

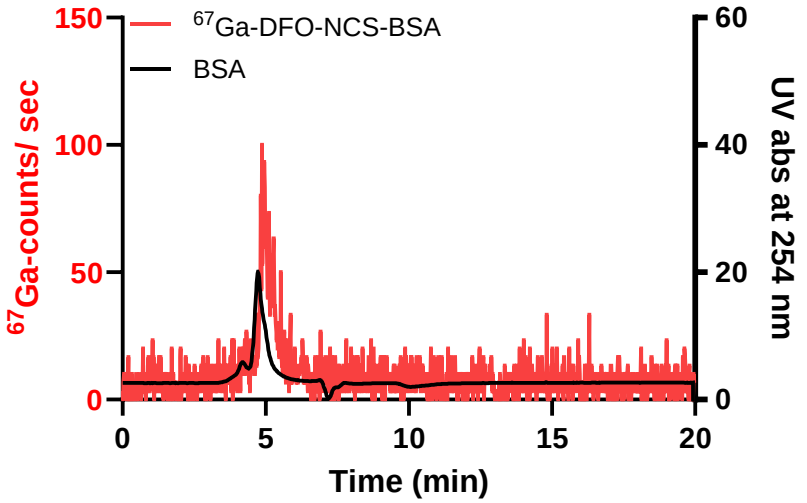

Figure 4. 22: Radiotracer for ^{67}Ga-DFO-NCS conjugated to BSA (r_t = 4.9min) overlay with BSA UV tracer (r_t = 4.7min). HPLC method E.

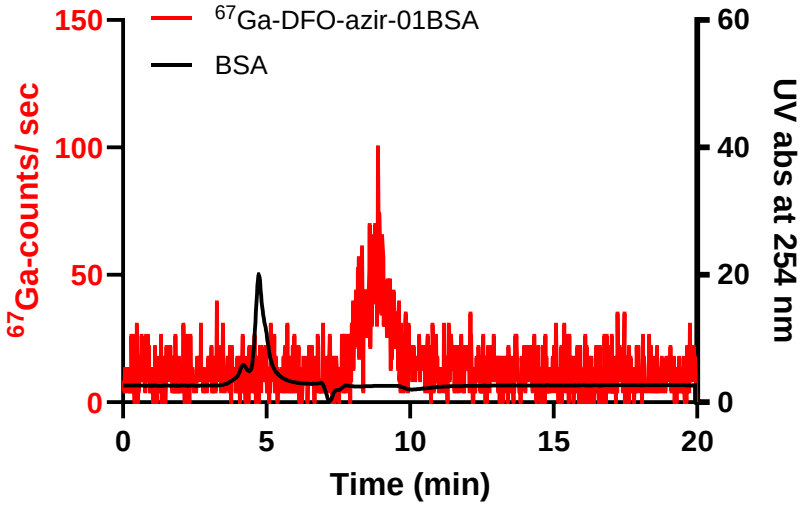

Figure 4. 23: Radiotracer for ^{67}Ga-DFO-azir-01 conjugated to BSA (r_t = 8.8 min) overlay with BSA UV tracer (r_t = 4.7min) . HPLC method E.

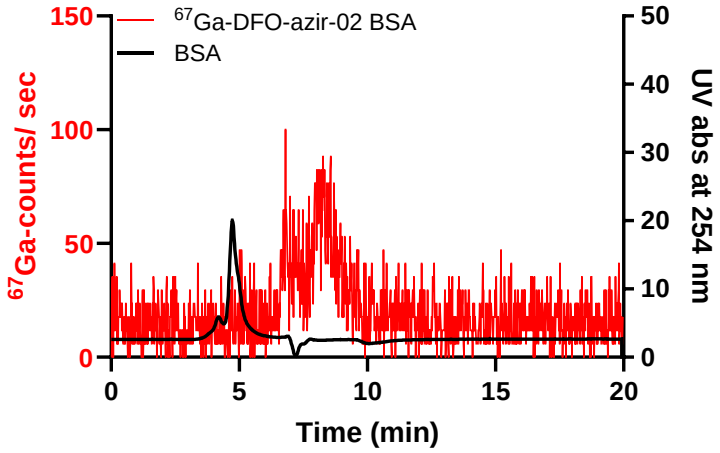

Figure 4. 24: Radiotracer for ^{67}Ga-DFO-azir-02 conjugated to BSA (r_t = 8 min) overlay with BSA UV tracer (r_t = 4.7min). HPLC method E.

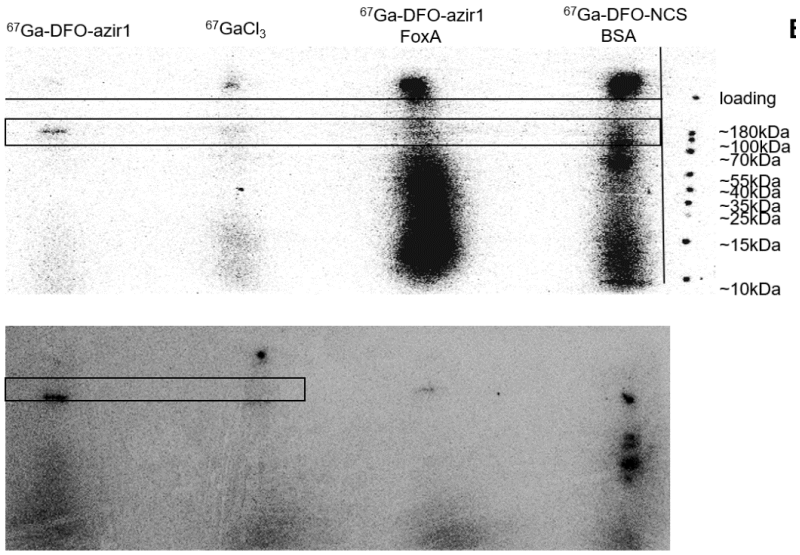

Figure 4. 25: Labeling of live *E. coli* Lemo21 cells with ^{67}Ga-DFO-azir, using $^{67}GaCl_3$ as a control. ^{67}Ga-DFO-azir-01 labeled FoxA and ^{67}Ga-DFO-DFO-labeled BSA were included as molecular weight references. The top and bottom portions of the image represent two separate gel runs. Gel electrophoresis method II.

4.5.5 Fluorescence microscopy

After growing the bacterial culture and adding probes according to the live cell labeling protocol, a small portion of the culture was diluted to an OD_{600} ~ 0.1 **in LB media**. This diluted culture was then lightly sonicated to obtain single cells. Separately, a 1.5% w/v low melting agarose solution was prepared by dissolving agarose in DI water. This solution was allowed to solidify between two coverslips and subsequently cut into small square pads. 1µL of the sonicated bacterial culture (OD600 ~0.1) was then placed onto each agarose pad. Finally, another coverslip was placed over the pad with the bacteria, and the edges were sealed with clear nail polish.

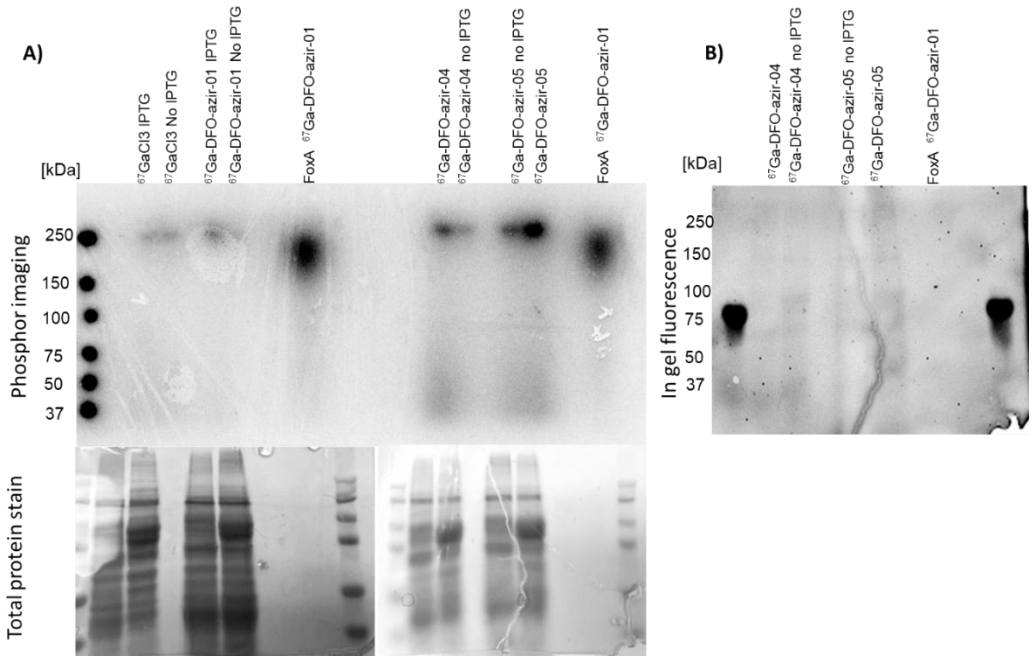

Figure 4. 26: A) Labeling of live *E. coli* Lemo21 cells, induced or not induced with 1mM ITPG, with ^{67}Ga-DFO-azir-01,04 and 05. ^{67}Ga-DFO-azir-01 labeled FoxA and ^{67}Ga-DFO-01 labeled FoxA were included as molecular weight references. B) The in-gel fluorescence imaging belongs the same gel as in the phosphors imaging.

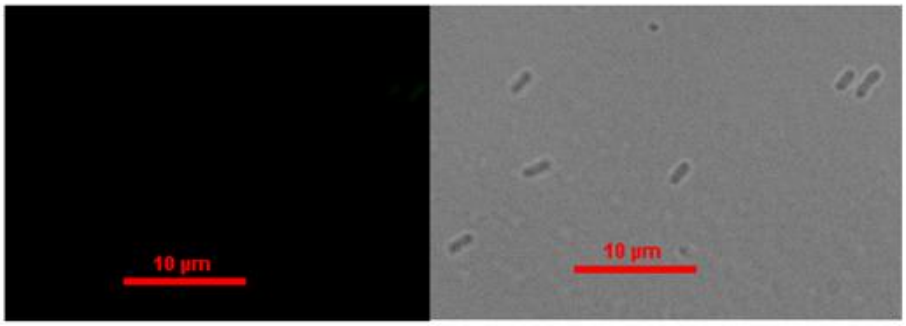

Figure 4. 27: Fluorescence microscopy of untreated *E. coli* Lemo21 cell. Lef fluorescence image and right bright field overlay with fluorescence image.

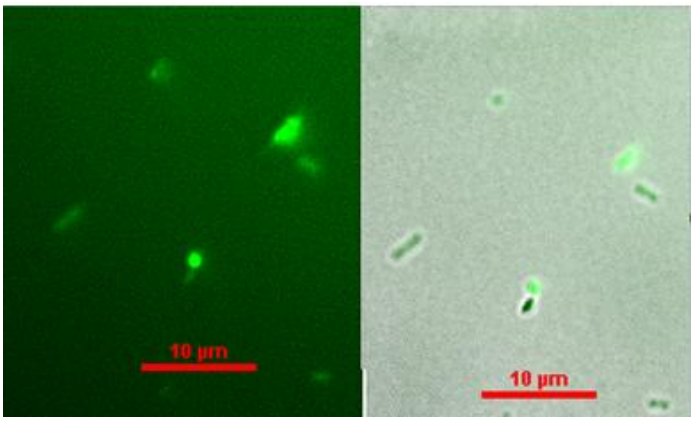

Figure 4. 28: Fluorescence microscopy of *E. coli* Lemo21 cells incubated with coumarin 343 control. Lef fluorescence image and right bright field overlay with fluorescence image.

4.5.6 Bacterial lysate and protein labeling

Bacterial lysate labeling: The lysate was obtained as previously described. Sample concentration was determined using a nanodrop. The control probe MP01 (final concentration 5 µM) was added to 100 µL of bacterial cell lysate and exposed to 365 nm UV light for 15 minutes on ice. For CuAAC, the following cocktail was added to the reaction mixture: Azide Fluor 545 (10 mM, 2 µL), a premixed solution of CuSO4 (50 mM, 2 µL) and TBTA (1.67 mM, 6 µL), and tris(2-carboxyethyl) phosphine (TCEP, 52 mM, 2 µL). The reaction mixture was incubated at 45°C in the dark while stirring overnight. The reaction was quenched by adding an equal volume of loading

buffer (5% β-mercaptoethanol in 2x Laemmli). 15 uL of the sample were loaded per lane on the gel (gel conditions as previously described).

Live cell labeling: The bacterial pellet was obtained by centrifugation (50 mL, 4000 rpm, 15 min) and washed with 50 mL DPBS (4 °C, 4000 rpm, 15 min). The cell pellet was resuspended in 5 mL DPBS, and 1 mL was transferred to a 6-well plate. The M-DFO-azir-0x probe (final concentration 25 µM) was added to the resuspended bacterial sample and incubated at 37 °C for 30 min (M-DFO-azir-01 and 02) or 2-4 h (M-DFO-azir-04, 05, and 06) in the dark. The samples were UV-irradiated (365 nm) on ice for 15 min with stirring. Bacteria were transferred to 2 mL Eppendorf tubes, pelleted, and washed three times with 500 µL DPBS buffer. Cell lysate was prepared as described above. For M-DFO-azir-01 and 02 the CuAAC reaction was performed as mentioned previously. To further solubilize the insoluble pellet, it was suspended in lysis buffer containing 5% Triton X-100 and 5% SDS and sonicated for 1 min at 4 °C on ice. A similar procedure was performed for cell lysis in urea, where 7 M urea was added to the lysis buffer. For heat-induced cell lysis, the washed bacterial cells were suspended in a 1:1 mixture of lysis buffer and loading buffer (SDS adjusted to 6%) and heated at 95 °C for 6 min.

Competition labeling with Fe-DFO: The bacterial culture was grown and prepared as previously described. To each well, increasing concentrations of Fe-DFO were added (0 eq., 1 eq. 25 µM, 10 eq. 250 µM, and 100 eq. 2.5 mM), followed by the addition of probes M-DFO-azir-05 and M-DFO-azir-06 (final concentration 25 µM) to the resuspended bacterial samples. These samples were then incubated at 37 °C for 4 h in the dark. Following incubation, the samples were transferred to 2 mL Eppendorf tubes, pelleted, and washed three times with 500 µL DPBS buffer. The cells were lysed with 5% SDS lysis buffer (50 mM Tris, pH 7.6, 250 mM NaCl, 5% w/v SDS,

10% w/v glycerol) and a final concentration of 2mM of PMSF by heating at 95 °C for 6 min. Protein concentration was quantified by BCA assay and normalized. SDS-PAGE, as described above, was used to separate the proteins, which were then visualized using a Typhoon 9400 Variable Mode Imager for fluorescence or stained with Coomassie R-250.

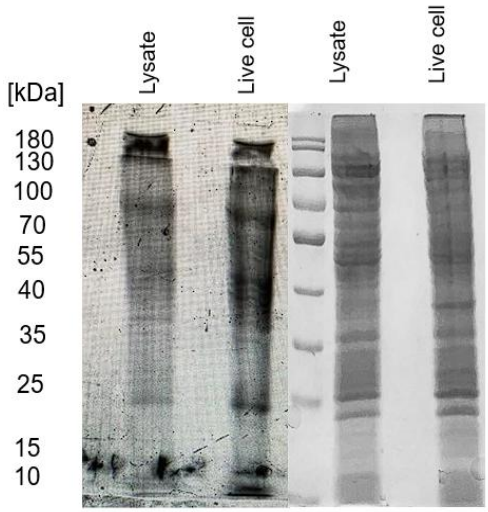

Figure 4. 29: *E.coli* K12 lysate labeling with MP01 (5uM) was visualized by gel-based fluorescent imaging (left panel) and total protein staining (right panel).

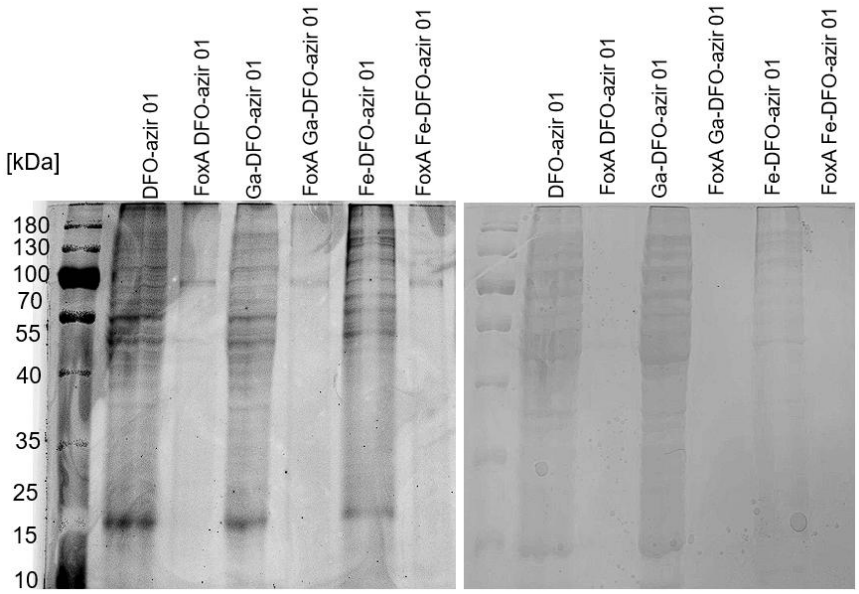

Figure 4. 30: Live labeling of *E. coli* Lemo21 with M-DFO-azir-01 (25 µM) at the 30 min time point. Fluorescent imaging is shown on the left panel, and total protein stain on the right. FoxA M-DFO-azir-01 is the purified protein reference labeled with the M-DFO-azir-01.

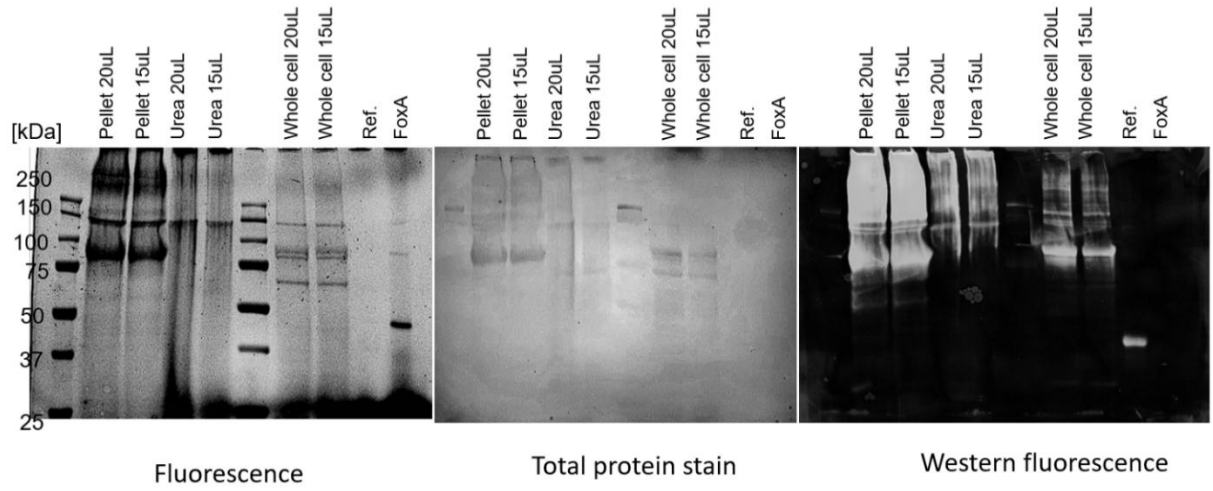

Figure 4. 31: Live labeling of *E. coli* Lemo 21 with Ga-DFO-azir-05 (25 µM) was performed at 2- and 4-hours post-exposure. Cells were subjected to different lysis methods: Pellet: pellet solubilization in 5% SDS and Triton X-100, urea: lysis buffer containing 7 M urea, or whole cell: heat lysis at 95 °C for 6 minutes. FoxA was used as a reference protein labeled with Ga-DFO-azir-05 and ref, a positive his-tag protein control. Fluorescent gel imaging (left panel), total protein stain (middle panel), and western blot (right panel) analyses were conducted.

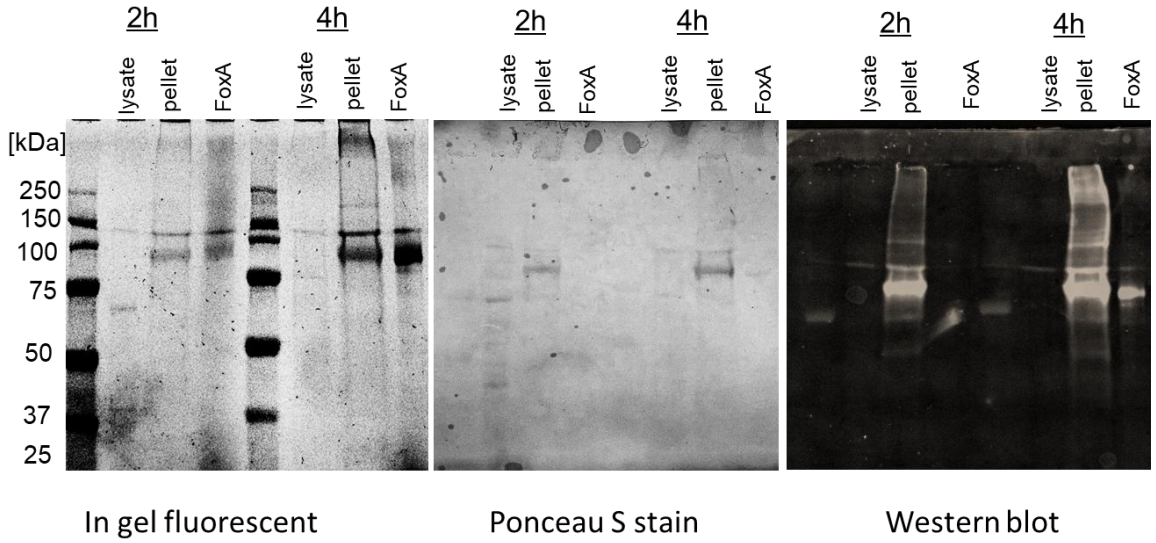

Figure 4. 32: Live labeling of *E. coli* Lemo 21 with Ga-DFO-azir-05 and coumarin 343 (25 µM) was performed at 2 and 4 hours. Cells were subjected to different lysis methods: Pellet: pellet solubilization in 5% SDS and Triton X-100 and. FoxA was used as a reference protein labeled with Ga-DFO-azir-05. Fluorescent gel imaging (left panel), total protein stain (middle panel), and western blot (right panel).

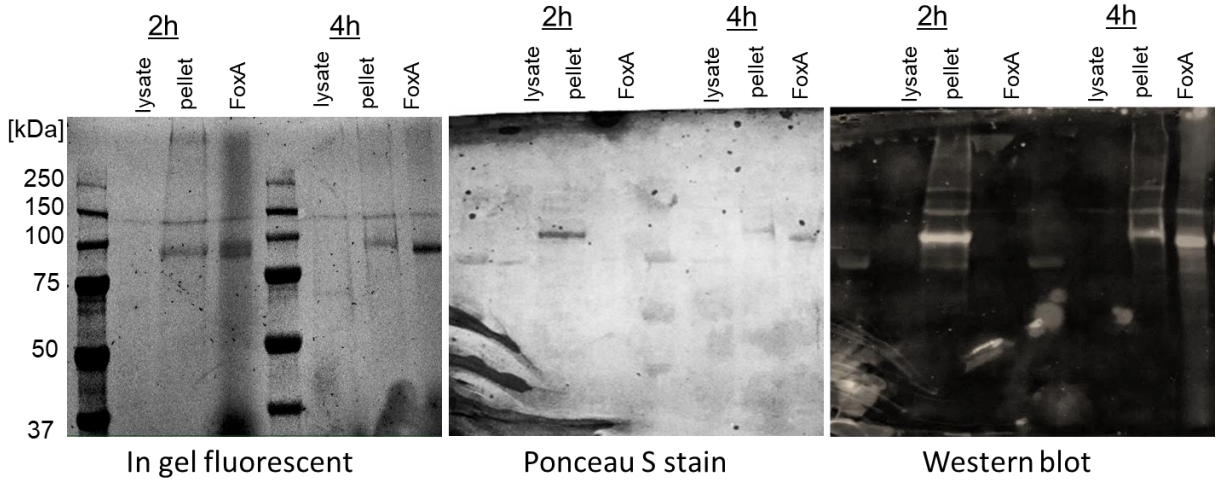

Figure 4. 33: Live labeling of *E. coli* Lemo 21 with DFO-azir-05 and coumarin 343 (25 µM) was performed at 2 and 4 hours. Cells were subjected to different lysis methods: Pellet: pellet solubilization in 5% SDS and Triton X-100 and. FoxA was used as a reference protein labeled with DFO-azir-05. Fluorescent gel imaging (left panel), total protein stain (middle panel), and western blot (right panel).

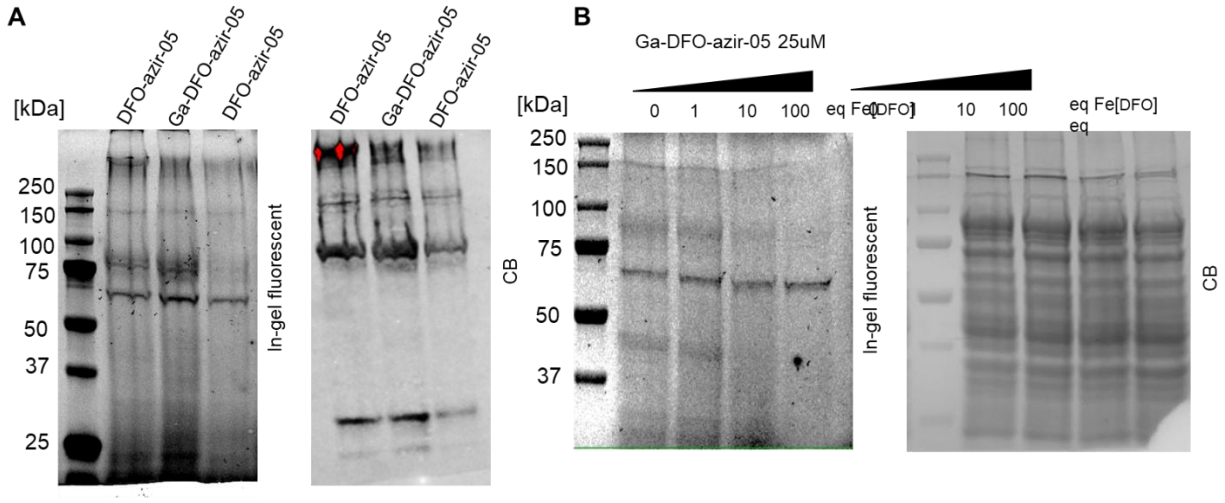

Figure 4. 34: In-gel fluorescent of Ga and DFO-azir-05(25uM) in E.coli lemo 21 cell lysate prior 4h incubation (A). Challenge displacement experiment where Ga-DFO-azir-05 (25uM) co-incubated with increasing amount of Fe-DFO for 4h in *E.coli* lemo21 cells (B). CB= coomassie blue stain.

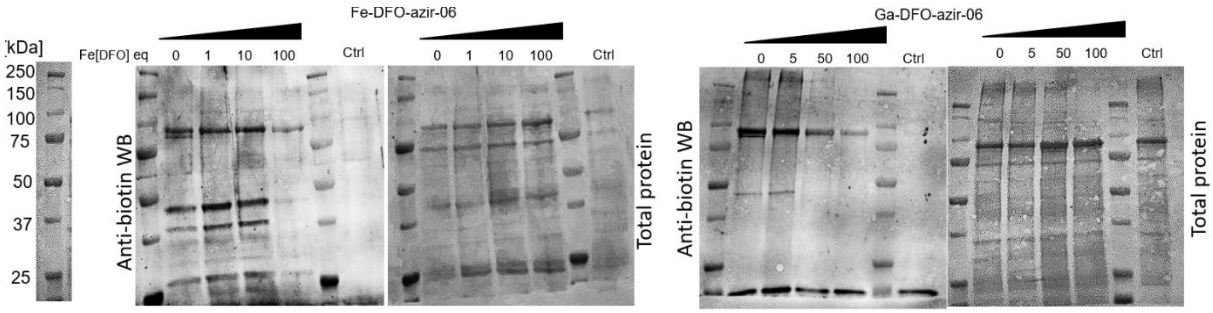

Figure 4. 35: A challenge displacement experiment was conducted to investigate the interaction between Fe and Ga-DFO-azir-06 (25 µM) in the presence of increasing concentrations of Fe-DFO (0, 5, 50, and 100 equivalents). A negative control (ctrl) lacking the probe was also included. All samples were incubated for 4 hours in *E. coli* lemo21 cells under iron-sufficient media conditions.

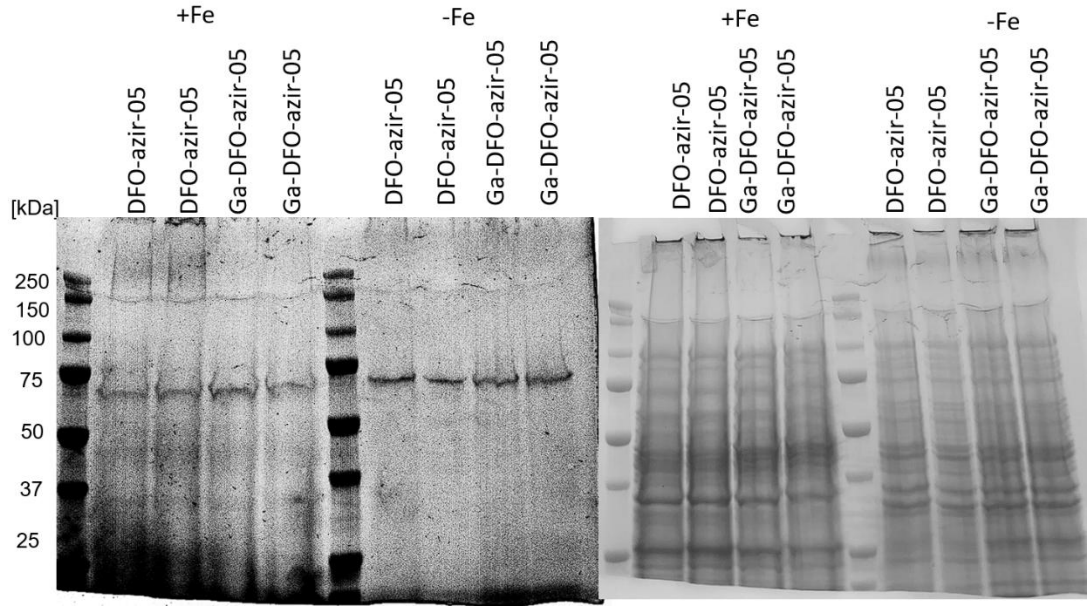

Figure 4. 36: Whole lysate fluorescence imaging of *E. coli* K12 cells labeled with Ga and DFO-azir-05 (25 µM) for 4 hours under iron-sufficient and iron-deficient conditions. Fluorescent gel imaging is shown on the left, and total protein stain on the right.

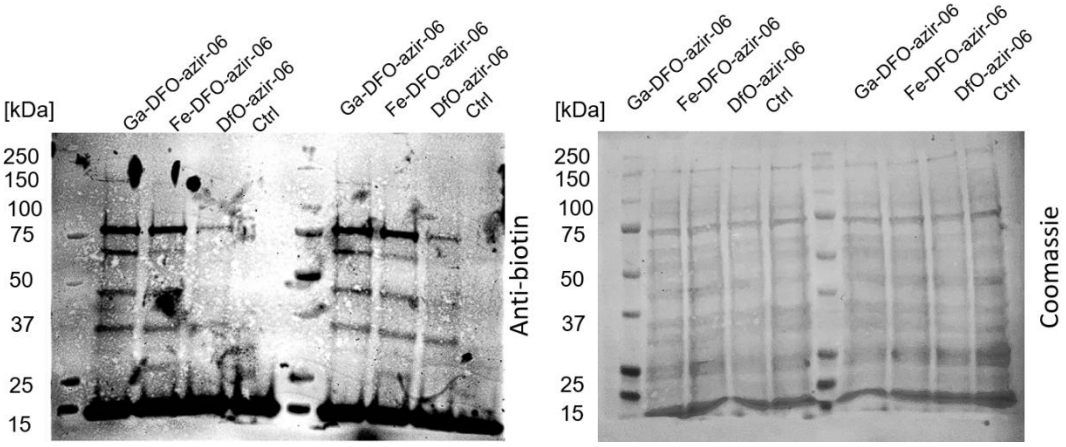

Figure 4. 37: Whole lysate fluorescence imaging of *E. coli* K12 cells labeled with Ga and M-DFO-azir-06 (25 µM) for 4 hours . Western blot is shown on the left, and total protein stain on the right.

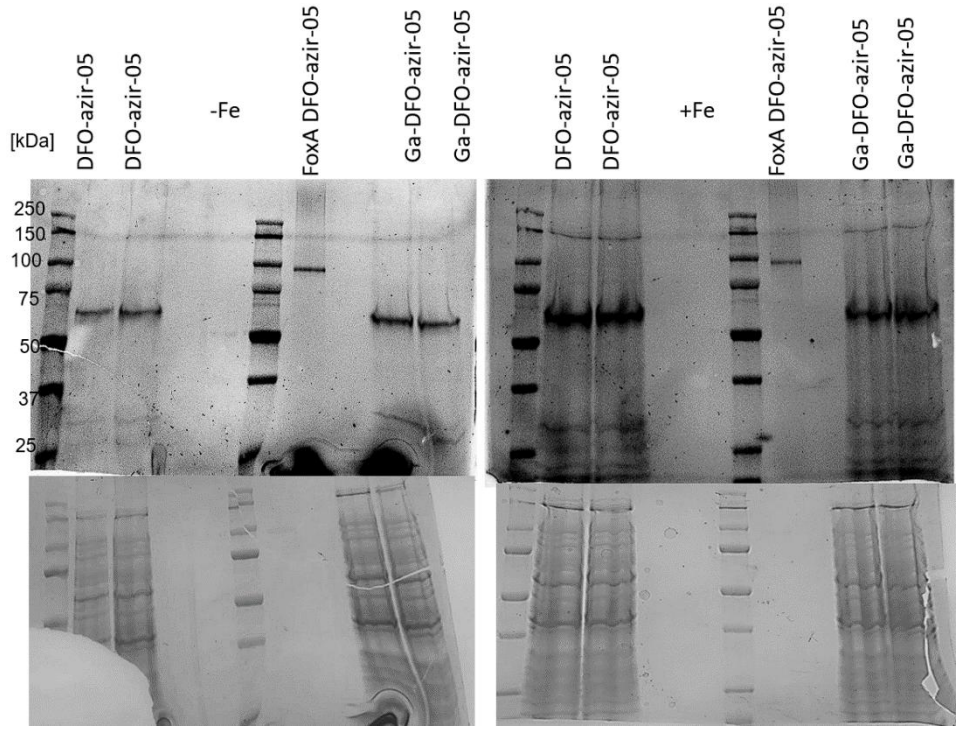

Figure 4. 38: Whole lysate fluorescence imaging of *P. aeruginosa* PA01 cells labeled with Ga and DFO-azir-05 (25 µM) for 4 hours under iron-sufficient (right) and iron-deficient conditions (left). Fluorescent gel imaging is shown on the top, and total protein stain on the bottom.

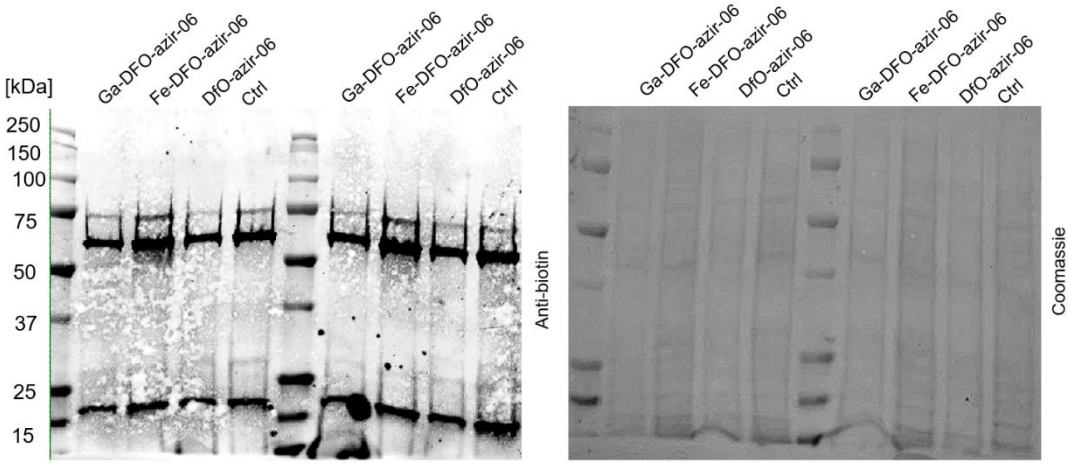

Figure 4. 39: Whole lysate fluorescence imaging of *P. aeruginosa* PA01 cells labeled with M-DFO-azir-06 (25 µM) for 4 hours. Western blot is shown on the left, and total protein stain on the right.

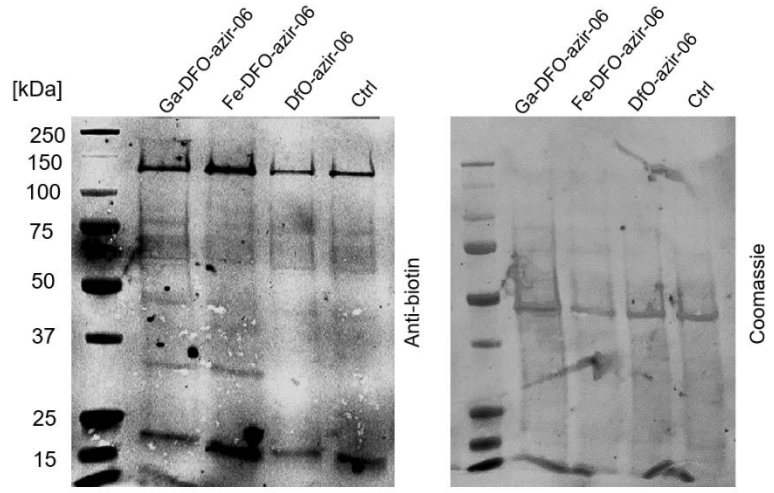

Figure 4. 40: Whole lysate fluorescence imaging of *S. aureus* labeled with M-DFO-azir-06 (25 µM) for 4 hours. Western blot is shown on the left, and total protein stain on the right.

4.5.7 Mass spectrometry

4.5.7.1 Enzymatic "In Gel" Digestion

Coomassie stained gel pieces were de-stained completely in MeOH/H_20/NH_4HCO_3 [50%/50%/100mM], dehydrated for 5min in ACN/H_20/NH_4HCO_3 [50%/50%/25mM] then once more for 30sec in 100% ACN. Dried in a Speed-Vac for 1min, reduced in 25mM DTT [Dithiotreitol in 25mM NH_4HCO_3] for 15min at 56°C, alkylated with 55mM CAA [Chloroacetamide in 25mM NH_4HCO_3] in darkness at room temperature for 15min, washed once in H20, dehydrated for 2min in ACN/H_20/NH_4HCO_3 [50%:50%:25mM] then once more for 30sec in 100% ACN. Dried again and rehydrated with 20µl of trypsin solution with 0.01% ProteaseMAX™ surfactant [10ng/µl Trypsin from Promega Corp. in 25mM NH_4HCO_3/0.01% w/v of ProteaseMAX™ from Promega Corp.]. Let stand for 2min at room temperature then additional 30µl of overlay solution [25mM NH_4HCO_3/0.01% w/v of ProteaseMAX™] was added to keep gel pieces immersed throughout the digestion. The digestion was conducted for 3hrs at 42°C. Peptides

generated from digestion were transferred to a new tube and acidified with 2.5% TFA [trifluoroacetic Acid] to 0.3% final. Gel pieces were additionally extracted with ACN:H_2O:TFA [70%:29.25%:0.75%] for 10min while vortexing and solutions combined and dried completely in a Speed-Vac (~20min). Extracted peptides were solubilized in 30µl of 0.05% TFA. Degraded ProteaseMAX™ was removed via centrifugation [max speed, 10minutes] and the peptides solid phase extracted (Pierce® C18 tips, 10µl volume from Thermo Scientific) according to manufacturer protocol. Peptides were eluted off the C18 SPE column with 5µl of acetonitrile/H_2O/TFA (70%:30%:0.1%) dried to completion then resolubilized in 20µl total volume for with 0.1% formic acid and 5% Acetonitrile.

4.5.7.2 Data analysis

Raw MS/MS data were converted to mgf file format using MSConvert (ProteoWizard: Open Source Software for Rapid Proteomics Tools Development) for downstream analysis. Resulting mgf files were used to search against Escherichia coli (UP000000625; 4,521 entries) or Pseudomonas aeruginosa (UP000002438; 5,681 entries) Uniprot reference proteome database along with a list of common lab contaminants (172 total entries) using in-house Mascot search engine 2.7.0 [Matrix Science] with variable Methionine oxidation, Asparagine and Glutamine deamidation plus fixed cysteine Carbamidomethylation. A user defined metal-coordinated or no metal containing versions of DFO-azir-0x conjugated probe on aspartic acid, glutamic acid and tyrosine were also considered as variable modification. Peptide mass tolerance was set at 10 ppm and fragment mass at 0.6 Da. Protein annotations, significance of identification and spectral based quantification were done with help of Scaffold software (version 5.0.1, Proteome Software Inc., Portland, OR). Peptide identifications were accepted if they could be established at greater than

80.0% probability by the Peptide Prophet algorithm (Keller, A et al Anal. Chem. 2002;74(20):5383-92) with Scaffold delta-mass correction. Protein identifications were accepted if they could be established at greater than 95.0% probability and contained at least 2 identified peptides. Protein probabilities were assigned by the Protein Prophet algorithm (Nesvizhskii, Al et al Anal. Chem. 2003;75(17):4646-58). Proteins that contained similar peptides and could not be differentiated based on MS/MS analysis alone were grouped to satisfy the principles of parsimony. Proteins sharing significant peptide evidence were grouped into clusters.

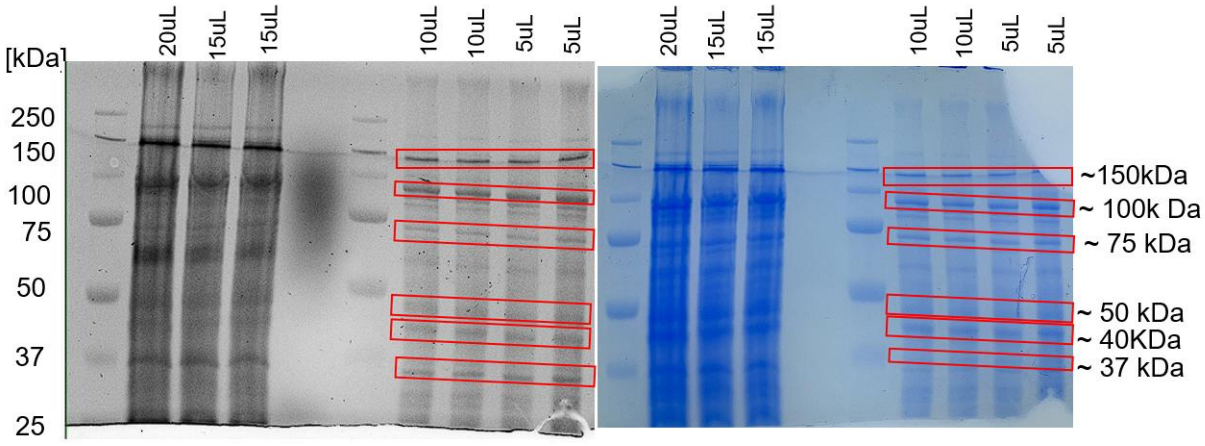

Figure 4. 41: DFO-azir-05 gel used for MS/MS analysis of the fluorescent bands. Highlighted in red box were the band extracted for analysis. Right in-gel fluorescence and left Coomassie stain.

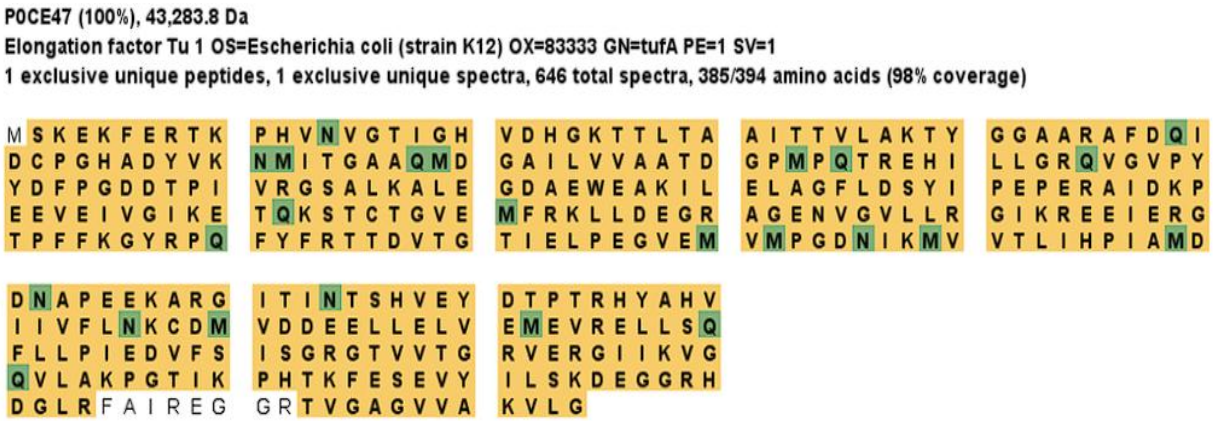

Figure 4. 43: ~ 40kDa fluorescent gel band sequence coverage identification indicated the most abundant protein is Elongation factor Tu 1.

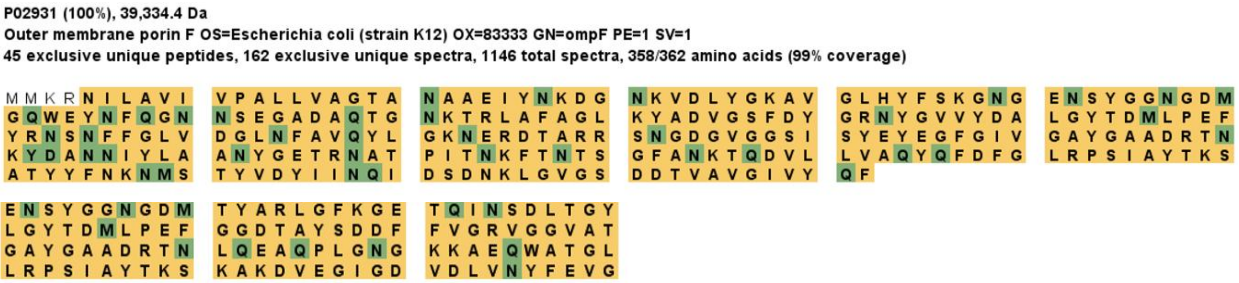

Figure 4. 42: ~ 37kDa fluorescent gel band sequence coverage identification indicated the most abundant protein is outer membrane porin F .

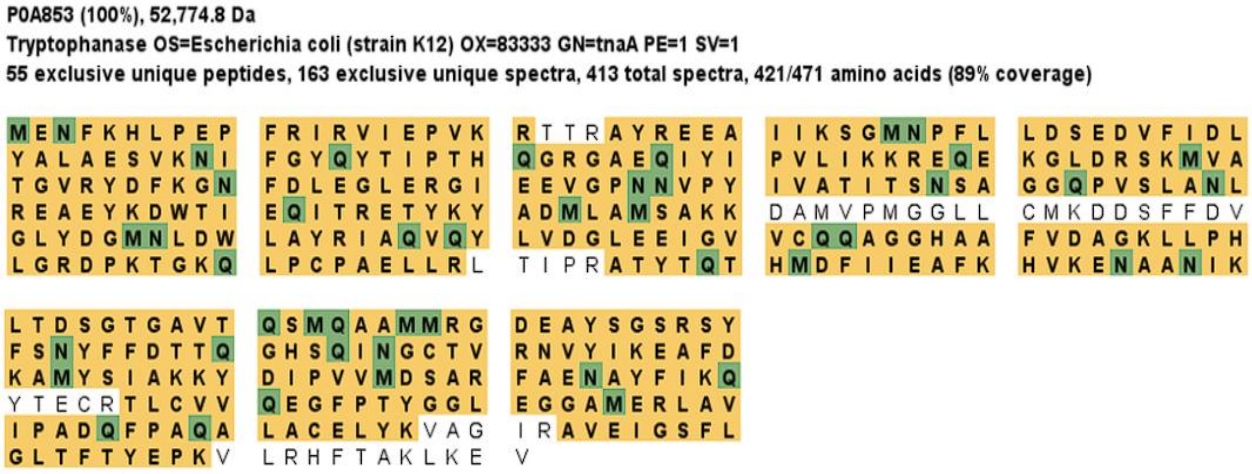

Figure 4. 44: ~ 37kDa fluorescent gel band sequence coverage identification indicated the most abundant protein is tryptophanase (TnaA).

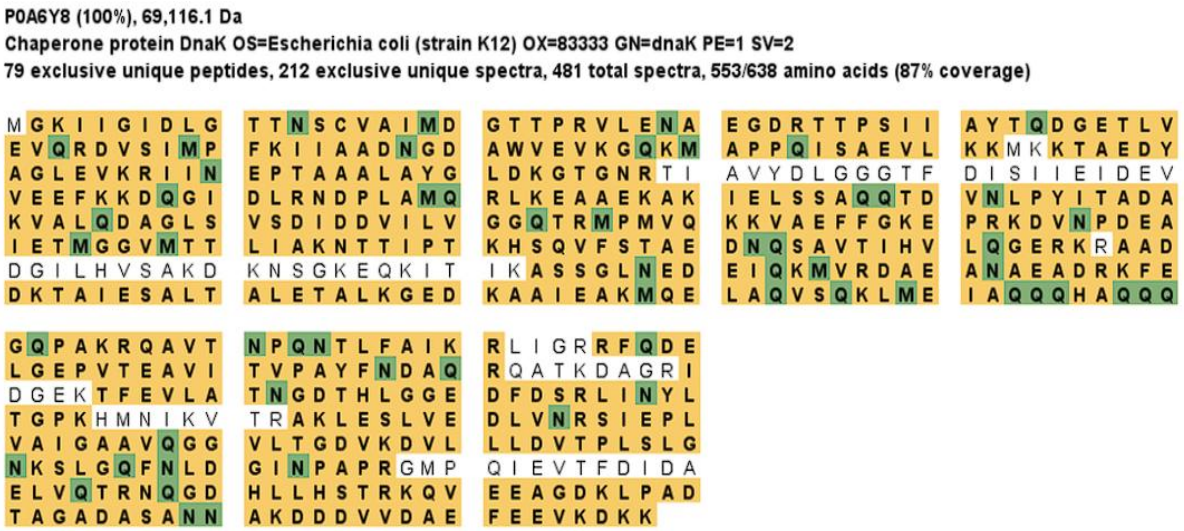

Figure 4. 45: ~ 75kDa fluorescent gel band sequence coverage identification indicated the most abundant protein Chaperone protein DnaK.

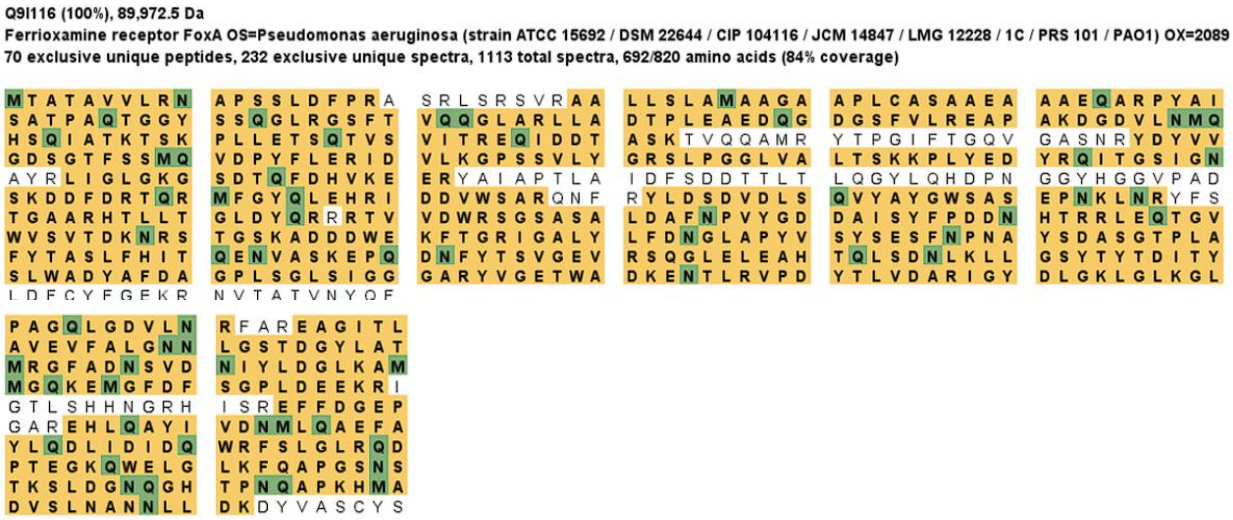

Figure 4. 46: ~ 100kDa fluorescent gel band sequence coverage identification indicated the most abundant protein is outer membrane receptor FoxA.

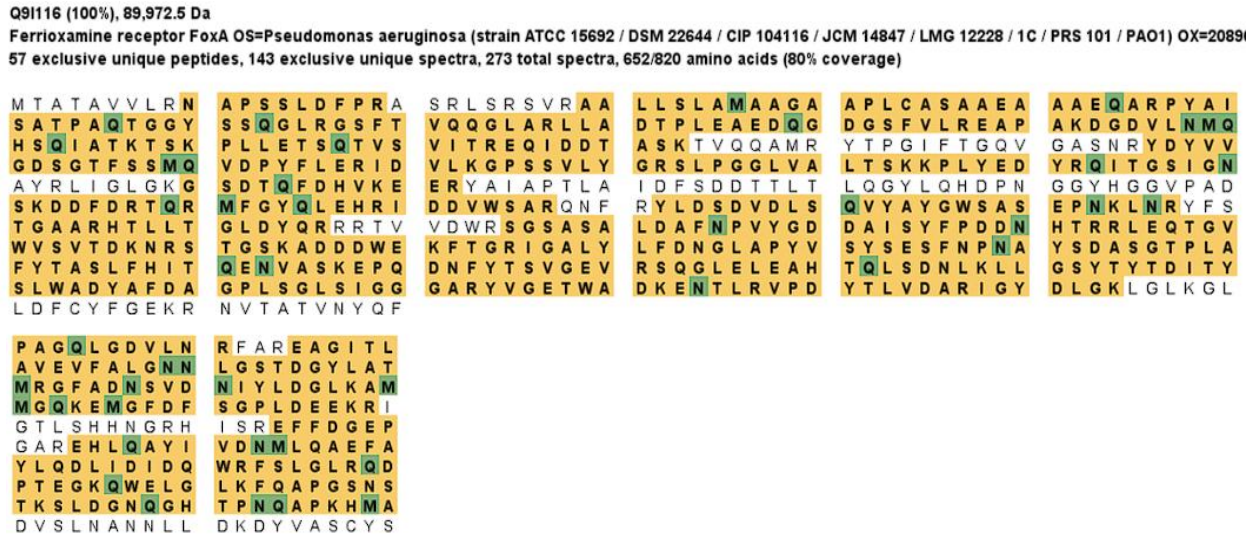

Figure 4. 47: 150kDa fluorescent gel band sequence coverage identification indicated the most abundant protein is outer membrane receptor FoxA.

4.5.8 Biotin enrichment

Bacterial cultures were grown as previously described. 50 ml of bacterial culture at an OD_{600} of 0.6 was washed twice with 50 mL PBS and resuspended in 1 mL PBS. The suspension was distributed into a 12-well plate. The probe was added to the bacterial solution to a final concentration of 125 µM. Bacteria were incubated with the probe for 4 hours followed by photoirradiation at 365 nm for 15 minutes on ice. Samples were pelleted, washed three times with 1 mL PBS, and resuspended in lysis buffer containing 2 mM PMSF. Cells were lysed using a fine-tip sonicator with six cycles of alternating 1-second pulses on and 1-second pulses off for a total of 3 minutes on and 3 minutes off. The lysate was incubated on a rotary shaker for 16 hours at 4 °C. Subsequently, the sample was centrifuged at 19,000 rpm for 30 minutes to separate the supernatant from the pellet. The pellet was resuspended in 500 µL of lysis buffer containing 5% Triton X-100 and 5% OG, sonicated for 1 minute, and incubated on a rotary shaker for 16 hours at 2 °C. 100 uL of streptavidin magnetic beads (S1420S, New England Biolabs) were equilibrated

with lysis buffer (4 × 500 µL) and incubated with the combined supernatant and solubilized pellet for 2 hours at room temperature on a rotary shaker. Beads were washed three times with 1 mL lysis buffer, with a 10-minute incubation on a rotary shaker between washes. For elution, 50 µL of elution buffer (4% SDS, 50 mM Tris, 5 mM EDTA, 25% glycerol, 5% β-mercaptoethanol, pH 6.8) was added. To ensure complete protein elution, an additional 50 µL of elution buffer was added, and the mixture was heated at 95 °C for 3 minutes.

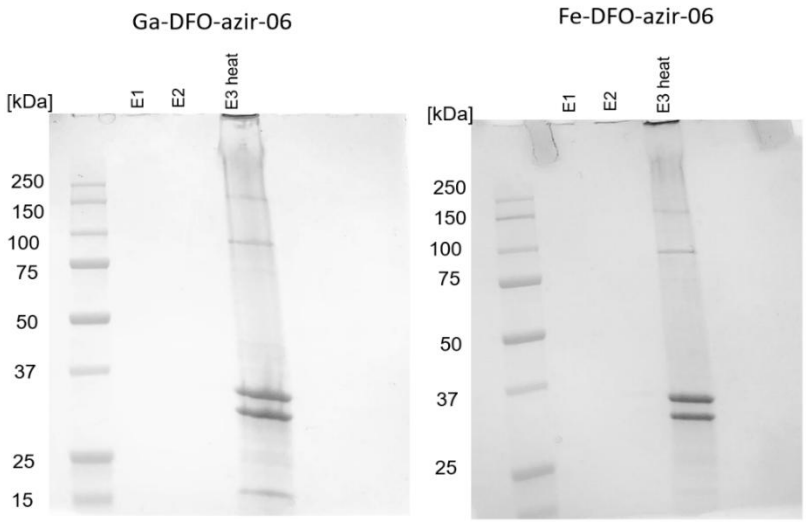

Figure 4. 49: Enrichment of biotinylated proteins from E. coli lemo21 lysate using streptavidin affinity purification in SDS-PAGE .

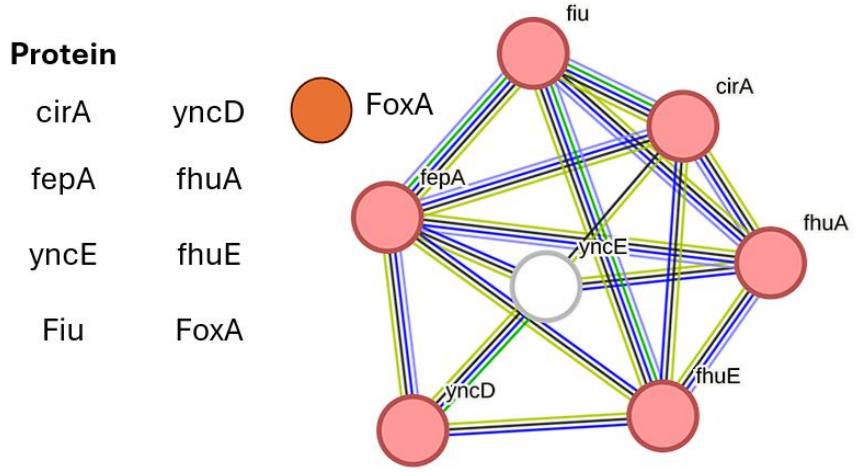

Figure 4. 48: The most abundant protein identified by MS/MS of the enrichment gel for both Fe and Ga-DFO-azir-06.

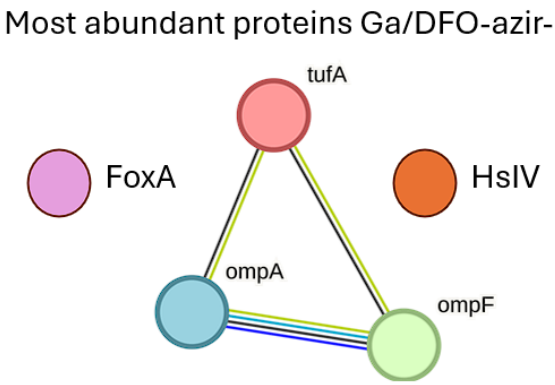

	Ga-DFO-azir 06		Fe-DFO-azir-06	
15Kda	HsIV	439	-	
25Kda	ompA	957	ompA	949
35kDa	ompF	1774	ompF	1564
60kDa	-		tufA	705
100kDa	FoxA	1024	FoxA	1405
150kDa	FoxA	340	FoxA	1205

Figure 4. 50: The most abundant protein identified by MS/MS of the enrichment gel (figure 3.84) for both Fe and Ga-DFO-azir-06.

Chapter 5: Conclusions and Future directions

5.1 Conclusion

This dissertation presents the development and application of small molecular tools, specifically radiolabeled and photoaffinity labeled compounds, to elucidate the in vitro and in vivo stability and uptake mechanisms of xenometal siderophores. First, a dual radiolabeling strategy employing ^{67}Ga and ^{124}I was developed to facilitate the investigation of in vitro uptake and in vivo stability. Next, photoaffinity probes were rationally designed to target siderophore-binding membrane proteins, allowing for the screening of reactivity profiles and the isolation of target proteins. Third, these siderophore photoaffinity probes were successfully implemented in live bacterial cell assays to isolate and identify siderophore-binding proteins. Collectively, these findings provide valuable insights into the stability and uptake of xenometal siderophore conjugates.

Chapter 2 demonstrated the development of dual-labeled siderophore probe platforms, designed to track both in vitro and in vivo behavior. These platforms enable radiolabeling of the metal cargo with ^{67}Ga and the ligand with ^{124}I to track in vitro and in vivo behavior of these probes. We demonstrated that these xenometal siderophore-conjugates are internalized as metal complex into the bacterial via a siderophore mediated uptake, with comparable ^{67}Ga and ^{124}I uptake. The introduction of iodo-tyrosine can alter the affinity of these siderophore probes, leading to decreased uptake in certain strains, such as *E. coli* for Ga-D7-I (~2%), and increased uptake in others, such as *P. aeruginosa* (~20%). In vivo evaluation in a murine infection model revealed that these probes undergo degradation, primarily through loss/dechelation of the metal cargo, rather than ligand degradation. These findings provide crucial insights into xenometal-siderophore

conjugates, highlighting potential avenues for the adaptation of structural designs that result in more inert and in vivo compatible siderophore-conjugate probes for infection imaging and therapy.

Chapter 3 detailed the rational design and synthesis of deferoxamine (DFO)-based photoaffinity probes, specifically targeting siderophore transmembrane transporters. The design of our compound library was informed by the co-crystal structure of Fe-D1, a deferoxamine-based siderophore antibiotic, complexed with FoxA, an outer membrane transporter in *Pseudomonas aeruginosa*. This structural insight guided the selection of the diazirine photoaffinity moiety and optimization of its linker length to facilitate efficient crosslinking within the FoxA binding pocket. We synthesized six DFO-diazirine probes, employing two distinct reporter element conjugation strategies: post-labeling via CuAAC and pre-linked conjugation of the fluorophore/biotin moiety for in-gel visualization. The pre-linked strategy was implemented when MS/MS analysis failed to confirm successful fluorophore click conjugation following photocrosslinking, likely due to limitations in efficiency of the CuAAC reaction in lysed live cell media. We then evaluated the reactivity profile of these probes with amino acid side chains known to be present in the FoxA siderophore-binding pocket and demonstrated the probes' ability to label isolated FoxA protein. These results identified our DFO-diazirine probes as promising candidates for siderophore target identification and validation, offering a valuable tool for studying siderophore-mediated transmembrane transport in bacteria.

Chapter 4 investigated the application of DFO-diazirine probes for live bacterial cell labeling, utilizing mutant *E. coli* Lemo21 overexpressing FoxA, as well as wild-type *E. coli* and *S. aureus* strains. Initial experiments with DFO-diazirine alkyne probes (M-DFO-azir-01, 02, and 03), employing a post-labeling click-conjugation strategy, presented significant challenges for live

cell applications. Consequently, pre-linked DFO-diazirine probes (M-DFO-azir-05 and 06) were synthesized to circumvent these issues. We demonstrated intracellular accumulation of the pre-linked probes using fluorescence microscopy and radiolabeling techniques. Live cell labeling of siderophore-binding proteins was confirmed through fluorescence imaging and Western blot analysis. We further validated selective siderophore binding by conducting a competitive binding assay. By increasing concentrations of the parent siderophore, Fe-DFO, we identified proteins that exhibited a dose-dependent reduction in probe uptake, indicative of specific siderophore transporter interactions. However, off-target interactions were also observed, as several labeled protein bands were insensitive to Fe-DFO displacement. Enrichment assay with M-DFO-azir-06 probes identified OmpF as one of the most significantly enriched proteins, suggesting a possible role for this porin in the uptake of xenometal-siderophore conjugates. This observation highlights the potential complexity of siderophore uptake pathways and the importance of considering low-affinity membrane proteins such as porins as candidates enabling siderophore piracy in future studies.

5.2 Future directions

5.2.1 Investigating role of OmpF in siderophore-conjugate uptake.

Outer membrane porin F (OmpF), a highly abundant porin traditionally known for facilitating the diffusion of small hydrophilic molecules across the bacterial membrane, exhibits a broader functional repertoire.[161] Furthermore, modifications of OmpF, alongside OmpC,[169] and mutations in envZ[50] have been implicated in Cefiderocol resistance in Enterobacter isolates. Our preliminary data indicates a potential role for OmpF in the uptake of DFO-diazirine.

To rigorously investigate this hypothesis and elucidate OmpF's contribution to siderophore uptake, we propose a multi-faceted approach. First, we will employ radiolabeling studies using ^{67}Ga and ^{55}Fe with DFO-diazirine and other DFO-conjugates (D1 and D7) in *E. coli ΔOmpF* strains. Comparing uptake rates to non-deletion strains will reveal if OmpF deletion significantly impacts compound uptake. A statistical decrease in uptake within the ΔOmpF mutant would strongly suggest OmpF's involvement in DFO-conjugate transport. Additionally, blocking studies using parent siderophores with radiolabeled compounds in *E. coli ΔOmpF* will determine if these compounds utilize established siderophore import pathways. To further explore alternative uptake routes, we will conduct radiolabeled uptake assays in *E. coli ΔFhuE ΔFhuA* strains, lacking the primary hydroxamate siderophore outer membrane transporters. Successful uptake in these mutants would reinforce the existence of alternative pathways and highlight OmpF's potential role.

Beyond uptake assays, we will investigate the regulatory mechanisms governing OmpF expression. Transcriptomic analysis will track OmpF expression levels in response to DFO-based siderophores, such as Ga-D1 (MIC 1.9μM), in *E. coli* K12.[87] Analyzing a Ga-D1 resistant strain will provide insights into resistance mechanisms and their potential impact on OmpF gene expression. This integrated approach, combining genetic mutants, radiolabeling, and transcriptomic analysis, will provide a comprehensive understanding of OmpF's role in siderophore conjugate uptake, shedding light on potential resistance mechanisms and alternative transport pathways.

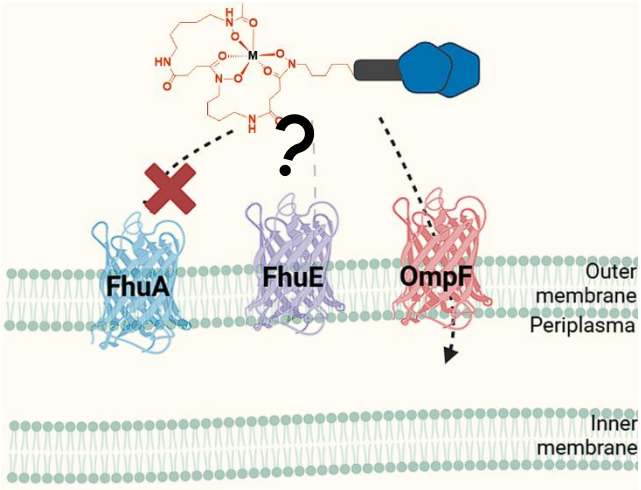

Figure 5. 1: Proposed mechanism of uptake for DFO-conjugate in *E.coli*.

5.2.2 Tris-catechol based siderophore photoaffinity probes.

Invasive infections, particularly those deep-seated and difficult to access, pose a significant clinical challenge. Current diagnostic methodologies, reliant on sample collection and microbial identification via RNA or DNA analysis, are often slow, cumbersome, and fail to provide real-time insights into infection progression.[170] Xenometal siderophores offer a compelling solution. Their inherent ability to selectively target bacterial receptors makes them ideal candidates for therapy and imaging applications.[87,171]

Tris-catecholate chelators, exemplified by TREN-CAM, a synthetic mimic of enterobactin, have demonstrated good in vivo stability with ^{68}Ga and ^{45}Ti,[172,173] PET isotopes, and potent antimicrobial activity.[174,175] By elucidating the structure-activity relationship between siderophore uptake and potency, we can rationally design optimized conjugates with enhanced therapeutic indices. This approach opens the door to incorporating diverse tris-catecholate siderophores, expanding the scope of treatable infections.

Understanding the structural activity relationships between uptake and potency can inform the design of siderophore conjugates that could potentially incorporate different types of tris-catecholate siderophores. As we have already demonstrated the applicability of siderophore photoaffinity probes with deferoxamine siderophore, an extension to catecholate siderophores would provide insight into uptake mechanisms in bacteria strains beyond *E.coli* and *P. aeruginosa.*

By mapping the interaction landscape between siderophores and their transporters, we can determine the structural flexibility tolerated by these receptors and identify key residues crucial for binding. This knowledge will be instrumental in designing the next generation of highly specific and potent siderophore conjugates.

Preliminary data demonstrates the synthetic accessibility and modularity of tris-catecholate photoaffinity probes. This versatility, achievable through both solution and solid-phase synthesis, allows for seamless integration of diverse catecholate siderophore mimics. This synthetic flexibility enables rapid iteration and optimization of our probes and exploration of siderophores beyond hydroxamate and catechol classes.

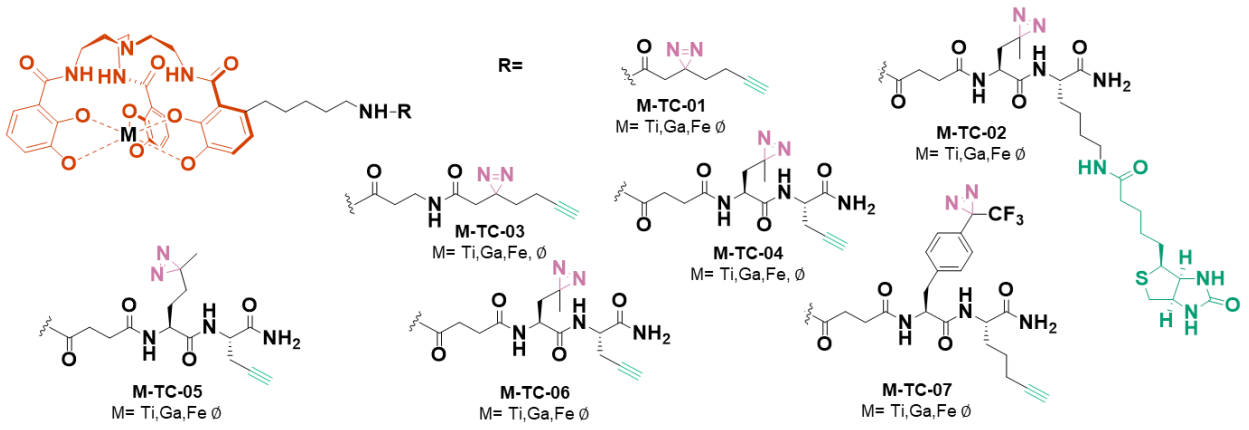

Figure 5. 2: Proposed library design of tris-catechol based siderophore mimic TREN-CAM photoaffinity probes.

References

(1) Page, M. G. P. The Role of Iron and Siderophores in Infection, and the Development of Siderophore Antibiotics. *Clin Infect Dis* **2019**, *69* (Suppl 7), S529-S537. DOI: 10.1093/cid/ciz825 PubMed.

(2) Centers for Disease Control, U. S. Antibiotic Resistance Threats in the United States, 2019. **2019**, 150. DOI: 10.15620/cdc:82532.

(3) Reygaert, W. C. An overview of the antimicrobial resistance mechanisms of bacteria. *AIMS Microbiol* **2018**, *4* (3), 482-501. DOI: 10.3934/microbiol.2018.3.482.

(4) Krewulak, K. D.; Vogel, H. J. Structural biology of bacterial iron uptake. *Biochim. Biophys. Acta, Biomembr.* **2008**, *1778* (9), 1781-1804.

(5) Alain Stintzi, C. B., Jide Xu, and Kenneth N. Raymond*. Microbial iron transport via a siderophore shuttle: A membrane ion transport paradigm. *PNAS* **2000**, *97* (20). DOI: 10.1073/pnas.200318797.

(6) Yep, A.; McQuade, T.; Kirchhoff, P.; Larsen, M.; Mobley, H. L. T.; Kolter, R. Inhibitors of TonB Function Identified by a High-Throughput Screen for Inhibitors of Iron Acquisition in Uropathogenic Escherichia coli CFT073. *mBio* **2014**, *5* (2), e01089-01013. DOI: doi:10.1128/mBio.01089-13.

(7) Darby, E. M.; Trampari, E.; Siasat, P.; Gaya, M. S.; Alav, I.; Webber, M. A.; Blair, J. M. A. Molecular mechanisms of antibiotic resistance revisited. *Nat. Rev. Microbiol.* **2023**, *21* (5), 280-295. DOI: 10.1038/s41579-022-00820-y.

(8) Archibald L. Hoyne, M. D. A. A. W., M.D.; Leona Prim, R.N. Fatality rates in the treatment of 998 erysipelas patients: the influence of sulfanilamide. *JAMA* **1939**, *113* (26), 2279-2281. DOI: 10.1001/jama.1939.02800510001001.

(9) Shlaes, D. M.; Bradford, P. A. Antibiotics-From There to Where?: How the antibiotic miracle is threatened by resistance and a broken market and what we can do about it. *Pathog Immun* **2018**, *3* (1), 19-43. DOI: 10.20411/pai.v3i1.231 From NLM.

(10) Ishak, A.; Mazonakis, N.; Spernovasilis, N.; Akinosoglou, K.; Tsioutis, C. Bactericidal versus bacteriostatic antibacterials: clinical significance, differences and synergistic potential in clinical practice. *J. Antimicrob. Chemother.* **2024**, *80* (1), 1-17. DOI: 10.1093/jac/dkae380.

(11) Uddin, T. M.; Chakraborty, A. J.; Khusro, A.; Zidan, B. M. R. M.; Mitra, S.; Emran, T. B.; Dhama, K.; Ripon, M. K. H.; Gajdács, M.; Sahibzada, M. U. K.; et al. Antibiotic resistance in microbes: History, mechanisms, therapeutic strategies and future prospects. *J. Infect. Public Health* **2021**, *14* (12), 1750-1766.

(12) Cox, G.; Wright, G. D. Intrinsic antibiotic resistance: Mechanisms, origins, challenges and solutions. *IJMM* **2013**, *303* (6), 287-292.

(13) Coculescu, B.-I. Antimicrobial resistance induced by genetic changes. *J Med Life* **2009**, *2* (2), 114-123. PubMed.

(14) Murray, C. J. L.; Ikuta, K. S.; Sharara, F.; Swetschinski, L.; Robles Aguilar, G.; Gray, A.; Han, C.; Bisignano, C.; Rao, P.; Wool, E.; et al. Global burden of bacterial antimicrobial resistance in 2019: a systematic analysis. *Lancet* **2022**, *399* (10325), 629-655. DOI: 10.1016/S0140-6736(21)02724-0.

(15) Kadri, S. S. Key Takeaways From the U.S. CDC's 2019 Antibiotic Resistance Threats Report for Frontline Providers. *Crit Care Med* **2020**, *48* (7), 939-945. DOI: 10.1097/CCM.0000000000004371 PubMed.

(16) Santajit, S.; Indrawattana, N. Mechanisms of Antimicrobial Resistance in ESKAPE Pathogens. *Biomed Res Int* **2016**, *2016*, 2475067-2475067. DOI: 10.1155/2016/2475067 PubMed.

(17) Holden, V. I.; Bachman, M. A. Diverging roles of bacterial siderophores during infection. *Metallomics* **2015**, *7* (6), 986-995. DOI: 10.1039/c4mt00333k From NLM.

(18) Ouyang, Z.; Isaacson, R. Identification and characterization of a novel ABC iron transport system, fit, in Escherichia coli. *Infect Immun* **2006**, *74* (12), 6949-6956. DOI: 10.1128/iai.00866-06 From NLM.

(19) Raymond, K. N.; Dertz, E. A.; Kim, S. S. Enterobactin: an archetype for microbial iron transport. *PNAS* **2003**, *100* (7), 3584-3588. DOI: 10.1073/pnas.0630018100 From NLM.

(20) Pinochet-Barros, A.; Helmann, J. D. Redox Sensing by Fe(2+) in Bacterial Fur Family Metalloregulators. *Antioxid Redox Signal* **2018**, *29* (18), 1858-1871. DOI: 10.1089/ars.2017.7359 From NLM.

(21) Daskaleros, P. A.; Stoebner, J. A.; Payne, S. M. Iron uptake in Plesiomonas shigelloides: cloning of the genes for the heme-iron uptake system. *Infect. Immun.* **1991**, *59* (8), 2706-2711. DOI: 10.1128/iai.59.8.2706-2711.1991.

(22) Miethke, M.; Marahiel, M. A. Siderophore-based iron acquisition and pathogen control. *Microbiol Mol Biol Rev* **2007**, *71* (3), 413-451. DOI: 10.1128/mmbr.00012-07 From NLM.

(23) Loomis, L. D.; Raymond, K. N. Solution equilibria of enterobactin and metal-enterobactin complexes. *Inorg. Chem.* **1991**, *30* (5), 906-911.

(24) Wencewicz, T. A.; Miller, M. J. Sideromycins as Pathogen-Targeted Antibiotics. In *Antibacterials: Volume II*, Fisher, J. F., Mobashery, S., Miller, M. J. Eds.; Springer International Publishing, 2018; pp 151-183.

(25) Kramer, J.; Özkaya, Ö.; Kümmerli, R. Bacterial siderophores in community and host interactions. *Nat Rev Microbiol* **2020**, *18* (3), 152-163. DOI: 10.1038/s41579-019-0284-4 From NLM.

(26) Lin, Y.-M.; Ghosh, M.; Miller, P. A.; Möllmann, U.; Miller, M. J. Synthetic sideromycins (skepticism and optimism): selective generation of either broad or narrow spectrum Gram-negative antibiotics. *BioMetals* **2019**, *32* (3), 425-451. DOI: 10.1007/s10534-019-00192-6.

(27) Cavas, L.; Kirkiz, I. Characterization of siderophores from Escherichia coli strains through genome mining tools: an antiSMASH study. *AMB Express* **2022**, *12* (1), 74. DOI: 10.1186/s13568-022-01421-x From NLM.

(28) Tsylents, U.; Burmistrz, M.; Wojciechowska, M.; Stępień, J.; Maj, P.; Trylska, J. Iron uptake pathway of Escherichia coli as an entry route for peptide nucleic acids conjugated with a siderophore mimic. *Front. microbiol.* **2024**, *15*, Original Research. DOI: 10.3389/fmicb.2024.1331021.

(29) Zhang, Y.; Sen, S.; Giedroc, D. P. Iron Acquisition by Bacterial Pathogens: Beyond Tris-Catecholate Complexes. *Chembiochem* **2020**, *21* (14), 1955-1967. DOI: 10.1002/cbic.201900778.

(30) Pandey, A.; Boros, E. Coordination Complexes to Combat Bacterial Infections: Recent Developments, Current Directions and Future Opportunities. *Chemistry* **2021**, *27* (26), 7340-7350. DOI: 10.1002/chem.202004822.

(31) Bonneau, A.; Roche, B.; Schalk, I. J. Iron acquisition in Pseudomonas aeruginosa by the siderophore pyoverdine: an intricate interacting network including periplasmic and membrane proteins. *Sci. Rep.* **2020**, *10* (1), 120. DOI: 10.1038/s41598-019-56913-x.

(32) Wilson, B. R.; Bogdan, A. R.; Miyazawa, M.; Hashimoto, K.; Tsuji, Y. Siderophores in Iron Metabolism: From Mechanism to Therapy Potential. *Trends Mol Med* **2016**, *22* (12), 1077-1090. DOI: 10.1016/j.molmed.2016.10.005.

(33) Khasheii, B.; Mahmoodi, P.; Mohammadzadeh, A. Siderophores: Importance in bacterial pathogenesis and applications in medicine and industry. *Microbiol. Res.* **2021**, *250*, 126790.

(34) Page, M. G. P. The Role of Iron and Siderophores in Infection, and the Development of Siderophore Antibiotics. *Clin Infect Dis* **2019**, *69*, S529-s537. DOI: 10.1093/cid/ciz825 From NLM.

(35) Stintzi, A.; Barnes, C.; Xu, J.; Raymond, K. N. Microbial iron transport via a siderophore shuttle: A membrane ion transport paradigm. *PNAS* **2000**, *97* (20), 10691-10696. DOI: doi:10.1073/pnas.200318797.

(36) Cassat, J. E.; Skaar, E. P. Iron in infection and immunity. *Cell Host Microbe* **2013**, *13* (5), 509-519. DOI: 10.1016/j.chom.2013.04.010.

(37) Chakraborty, S.; Kaur, S.; Guha, S.; Batra, S. K. The multifaceted roles of neutrophil gelatinase associated lipocalin (NGAL) in inflammation and cancer. *Biochim. Biophys. Acta* **2012**, *1826* (1), 129-169. DOI: 10.1016/j.bbcan.2012.03.008 From NLM.

(38) Müller, S. I.; Valdebenito, M.; Hantke, K. Salmochelin, the long-overlooked catecholate siderophore of Salmonella. *BioMetals* **2009**, *22* (4), 691-695. DOI: 10.1007/s10534-009-9217-4.

(39) Ferguson, A. D.; Braun, V.; Fiedler, H. P.; Coulton, J. W.; Diederichs, K.; Welte, W. Crystal structure of the antibiotic albomycin in complex with the outer membrane transporter FhuA. *Protein Sci.* **2000**, *9* (5), 956-963. DOI: 10.1110/ps.9.5.956 From NLM.

(40) Pramanik, A.; Braun, V. Albomycin Uptake via a Ferric Hydroxamate Transport System of Streptococcus pneumoniae R6. *J. Bacteriol.* **2006**, *188* (11), 3878-3886. DOI: doi:10.1128/JB.00205-06.

(41) Pramanik, A.; Stroeher, U. H.; Krejci, J.; Standish, A. J.; Bohn, E.; Paton, J. C.; Autenrieth, I. B.; Braun, V. Albomycin is an effective antibiotic, as exemplified with Yersinia enterocolitica and Streptococcus pneumoniae. *Int J Med Microbiol* **2007**, *297* (6), 459-469. DOI: 10.1016/j.ijmm.2007.03.002 From NLM.

(42) Braun, V.; Pramanik, A.; Gwinner, T.; Köberle, M.; Bohn, E. Sideromycins: tools and antibiotics. *Biometals* **2009**, *22* (1), 3-13. DOI: 10.1007/s10534-008-9199-7 PubMed.

(43) Tsunoda, T.; Tanoeyadi, S.; Proteau, P. J.; Mahmud, T. The chemistry and biology of natural ribomimetics and related compounds. *RSC chem. biol.* **2022**, *3* (5), 519-538, 10.1039/D2CB00019A. DOI: 10.1039/D2CB00019A.

(44) Travin, D. Y.; Severinov, K.; Dubiley, S. Natural Trojan horse inhibitors of aminoacyl-tRNA synthetases. *RSC Chemical Biology* **2021**, *2* (2), 468-485, 10.1039/D0CB00208A. DOI: 10.1039/D0CB00208A.

(45) Zeng, Y.; Roy, H.; Patil Preeti, B.; Ibba, M.; Chen, S. Characterization of Two Seryl-tRNA Synthetases in Albomycin-Producing Streptomyces sp. Strain ATCC 700974. *AAC* **2009**, *53* (11), 4619-4627. DOI: 10.1128/aac.00782-09.

(46) Wencewicz, T. A.; Möllmann, U.; Long, T. E.; Miller, M. J. Is drug release necessary for antimicrobial activity of siderophore-drug conjugates? Syntheses and biological studies of the naturally occurring salmycin “Trojan Horse” antibiotics and synthetic desferridanoxamine-antibiotic conjugates. *BioMetals* **2009**, *22* (4), 633-648. DOI: 10.1007/s10534-009-9218-3.

(47) Johnstone, T. C.; Nolan, E. M. Beyond iron: non-classical biological functions of bacterial siderophores. *Dalton Trans* **2015**, *44* (14), 6320-6339. DOI: 10.1039/c4dt03559c.

(48) Miller, M. J.; Liu, R. Design and Syntheses of New Antibiotics Inspired by Nature's Quest for Iron in an Oxidative Climate. *Acc Chem Res* **2021**, *54* (7), 1646-1661. DOI: 10.1021/acs.accounts.1c00004.

(49) Guo, C.; Nolan, E. M. Heavy-Metal Trojan Horse: Enterobactin-Directed Delivery of Platinum(IV) Prodrugs to Escherichia coli. *JACS* **2022**, *144* (28), 12756-12768. DOI: 10.1021/jacs.2c03324 From NLM.

(50) Kriz, R.; Spettel, K.; Pichler, A.; Schefberger, K.; Sanz-Codina, M.; Lötsch, F.; Harrison, N.; Willinger, B.; Zeitlinger, M.; Burgmann, H.; et al. In vitro resistance development gives insights into molecular resistance mechanisms against cefiderocol. *J Antibiot.* **2024**, *77* (11), 757-767. DOI: 10.1038/s41429-024-00762-y.

(51) Zhanel, G. G.; Golden, A. R.; Zelenitsky, S.; Wiebe, K.; Lawrence, C. K.; Adam, H. J.; Idowu, T.; Domalaon, R.; Schweizer, F.; Zhanel, M. A.; et al. Cefiderocol: A Siderophore Cephalosporin with Activity Against Carbapenem-Resistant and Multidrug-

Resistant Gram-Negative Bacilli. *Drugs* **2019**, *79* (3), 271-289. DOI: 10.1007/s40265-019-1055-2.

(52) Peukert, C.; Vetter, A. C.; Fuchs, H. L. S.; Harmrolfs, K.; Karge, B.; Stadler, M.; Brönstrup, M. Siderophore conjugation with cleavable linkers boosts the potency of RNA polymerase inhibitors against multidrug-resistant E. coli. *Chem Sci* **2023**, *14* (20), 5490-5502, 10.1039/D2SC06850H. DOI: 10.1039/D2SC06850H.

(53) Chiu, C.-H.; Huang, D.-Y.; Ma, W.-H.; Chen, Y.-X.; Yang, S.-Y.; Chen, Y.-C.; Tony Mong, K.-K. Chemical Approach for Investigation of the Structure-Activity Relationship of Salmycin and Identification of a Glycan-based Analogue for Drug Resistant Staphylococcus aureus. *Adv. Synth. Catal.* **2024**, *366* (1), 101-113.

(54) Guo, C.; Wang, K.-K. A.; Nolan, E. M. Investigation of Siderophore–Platinum(IV) Conjugates Reveals Differing Antibacterial Activity and DNA Damage Depending on the Platinum Cargo. *ACS Infect. Dis.* **2024**, *10* (4), 1250-1266. DOI: 10.1021/acsinfecdis.3c00686.

(55) Pals, M. J.; Wijnberg, L.; Yildiz, Ç.; Velema, W. A. Catechol-Siderophore Mimics Convey Nucleic Acid Therapeutics into Bacteria. *Angew. Chem. Int. Ed.* **2024**, *63* (19), e202402405.

(56) Wang, Y.-Y.; Luo, B.-Z.; Li, C.-M.; Liang, J.-L.; Liu, Z.; Chen, W.-M.; Guo, J.-L. Discovery of 3-hydroxypyridin-4(1H)-ones ester of ciprofloxacin as prodrug to combat biofilm-associated Pseudomonas aeruginosa. *Eur. J. Med. Chem.* **2025**, 117396. DOI: doi.org/10.1016/j.ejmech.2025.117396.

(57) Weber, B. S.; Ritchie, N. E.; Hilker, S.; Chan, D. C. K.; Peukert, C.; Deisinger, J. P.; Ives, R.; Årdal, C.; Burrows, L. L.; Brönstrup, M.; et al. High-Throughput Discovery of Synthetic Siderophores for Trojan Horse Antibiotics. *ACS Infect. Dis.* **2024**, *10* (11), 3821-3841. DOI: 10.1021/acsinfecdis.4c00359.

(58) Rogers, H. J. S., C.; Woods, V. E. Antibacterial Effect of Scandium and Indium Complexes of Enterochelin on *Klebsiella pneumoniae*. *AAC* **1980**, *18* (1), 63-68.

(59) Polosak, M.; Piotrowska, A.; Krajewski, S.; Bilewicz, A. Stability of (47)Sc-complexes with acyclic polyamino-polycarboxylate ligands. *J. Radioanal. Nucl. Chem.* **2013**, *295* (3), 1867-1872. DOI: 10.1007/s10967-012-2188-x.

(60) Clarke, T., Ku, SY., Dougan, D. et al. . The structure of the ferric siderophore binding protein FhuD complexed with gallichrome. *Nat. Struct. Mol. Biol.* **2000**, *7* (4), 287-291.

(61) Plaha, D. S.; Rogers, H. J. Antibacterial effect of the scandium complex of enterochelin studies of the mechanism of action. *Biochim. Biophys. Acta* **1983**, *760* (2), 246-255.

(62) Chitambar, C. R. Gallium-containing anticancer compounds. *Future Med Chem* **2012**, *4* (10), 1257-1272. DOI: 10.4155/fmc.12.69 From NLM.

(63) Rzhepishevska, O.; Ekstrand-Hammarstrom, B.; Popp, M.; Bjorn, E.; Bucht, A.; Sjostedt, A.; Antti, H.; Ramstedt, M. The antibacterial activity of Ga3+ is influenced by

ligand complexation as well as the bacterial carbon source. *Antimicrob. Agents Chemother.* **2011**, *55* (12), 5568-5580. DOI: 10.1128/AAC.00386-11.

(64) Pfister, J.; Summer, D.; Petrik, M.; Khoylou, M.; Lichius, A.; Kaeopookum, P.; Kochinke, L.; Orasch, T.; Haas, H.; Decristoforo, C. Hybrid Imaging of Aspergillus fumigatus Pulmonary Infection with Fluorescent, (68)Ga-Labelled Siderophores. *Biomolecules* **2020**, *10* (2). DOI: 10.3390/biom10020168.

(65) Antunes, L. C.; Imperi, F.; Minandri, F.; Visca, P. In vitro and in vivo antimicrobial activities of gallium nitrate against multidrug-resistant Acinetobacter baumannii. *Antimicrob. Agents Chemother.* **2012**, *56* (11), 5961-5970. DOI: 10.1128/aac.01519-12.

(66) Cohen, A.; Lechtzin, N.; Boas, S.; Pena, T.; McBennett, K.; Gross, J.; Dorgan, D.; Couch, L.; Hoffman, L.; Saavedra, M.; et al. WS05.06 Phase 1/2a randomized, double-blind, placebo-controlled study: safety, Pk, and Efficacy outcome measures of inhaled Gallium Citrate (AR-501) in P Aeruginosa infected Cystic Fibrosis patients. *J Cyst Fibros.* **2023**, *22*, S11. DOI: 10.1016/S1569-1993(23)00216-3.

(67) Juárez-Hernández, R. E.; Miller, P. A.; Miller, M. J. Syntheses of Siderophore–Drug Conjugates Using a Convergent Thiol–Maleimide System. *ACS Med. Chem. Lett.* **2012**, *3* (10), 799-803. DOI: 10.1021/ml300150y.

(68) Rogers, H. J.; Woods, V. E.; Synge, C. Antibacterial effect of the scandium and indium complexes of enterochelin on Escherichia coli. *Microbiol.* **1982**, *128* (10), 2389-2394.

(69) Rogers, H. J. S., C.; Woods, V. E. Antibacterial effect of scandium and indium complexes of enterochelin on Klebsiella pneumoniae. *AAC* **1980**, *18* (1), 63-68. DOI: 10.1128/aac.18.1.63 From NLM.

(70) Kawai, K.; Wang, G.; Okamoto, S.; Ochi, K. The rare earth, scandium, causes antibiotic overproduction in Streptomyces spp. *EMS Microbiol. Lett.* **2007**, *274* (2), 311-315. DOI: 10.1111/j.1574-6968.2007.00846.x.

(71) Raviranga, N. G. H.; Ayinla, M.; Perera, H. A.; Qi, Y.; Yan, M.; Ramström, O. Antimicrobial Potency of Nor-Pyochelin Analogues and Their Cation Complexes against Multidrug-Resistant Pathogens. *ACS Infect. Dis.* **2024**, *10* (11), 3842-3852. DOI: 10.1021/acsinfecdis.4c00421.

(72) Wang, C.; Xia, Y.; Wang, R.; Li, J.; Chan, C.-L.; Kao, R. Y.-T.; Toy, P. H.; Ho, P.-L.; Li, H.; Sun, H. Metallo-sideromycin as a dual functional complex for combating antimicrobial resistance. *Nat. Commun.* **2023**, *14* (1), 5311. DOI: 10.1038/s41467-023-40828-3.

(73) Banin, E.; Lozinski, A.; Brady, K. M.; Berenshtein, E.; Butterfield, P. W.; Moshe, M.; Chevion, M.; Greenberg, E. P.; Banin, E. The potential of desferrioxamine-gallium as an anti-Pseudomonas therapeutic agent. *Proc Natl Acad Sci U S A* **2008**, *105* (43), 16761-16766. DOI: 10.1073/pnas.0808608105 From NLM.

(74) Pandey, A.; Savino, C.; Ahn, S. H.; Yang, Z.; Van Lanen, S. G.; Boros, E. Theranostic Gallium Siderophore Ciprofloxacin Conjugate with Broad Spectrum Antibiotic Potency. *J. Med. Chem.* **2019**, *62* (21), 9947-9960. DOI: 10.1021/acs.jmedchem.9b01388.

(75) Rayner, B.; Verderosa, A. D.; Ferro, V.; Blaskovich, M. A. T. Siderophore conjugates to combat antibiotic-resistant bacteria. *RSC med. chem.* **2023**, *14* (5), 800-822, 10.1039/D2MD00465H. DOI: 10.1039/D2MD00465H.

(76) Marlin, A.; Cao, M.; Glaser, O. M.; El Hamouche, J.; Boros, E. Decoding Growth Inhibitory Associated Pathways of Xenometal-Siderophore antibiotic conjugates in S. aureus. *Chem Sci* **2025**, 10.1039/D4SC08509D. DOI: 10.1039/D4SC08509D.

(77) Southwell, J. W.; Black, C. M.; Duhme-Klair, A.-K. Experimental Methods for Evaluating the Bacterial Uptake of Trojan Horse Antibacterials. *ChemMedChem* **2021**, *16* (7), 1063-1076.

(78) Wencewicz, T. A.; Long, T. E.; Möllmann, U.; Miller, M. J. Trihydroxamate Siderophore–Fluoroquinolone Conjugates Are Selective Sideromycin Antibiotics that Target Staphylococcus aureus. *Bioconjug Chem* **2013**, *24* (3), 473-486. DOI: 10.1021/bc300610f.

(79) Zheng, T.; Bullock, J. L.; Nolan, E. M. Siderophore-Mediated Cargo Delivery to the Cytoplasm of Escherichia coli and Pseudomonas aeruginosa: Syntheses of Monofunctionalized Enterobactin Scaffolds and Evaluation of Enterobactin–Cargo Conjugate Uptake. *JACS* **2012**, *134* (44), 18388-18400. DOI: 10.1021/ja3077268.

(80) Lee, A. A.; Chen, Y.-C. S.; Ekalestari, E.; Ho, S.-Y.; Hsu, N.-S.; Kuo, T.-F.; Wang, T.-S. A. Facile and Versatile Chemoenzymatic Synthesis of Enterobactin Analogues and Applications in Bacterial Detection. *Angew. Chem. Int. Ed.* **2016**, *55* (40), 12338-12342.

(81) Hoegy, F.; Gwynn, M. N.; Schalk, I. J. Susceptibility of Pseudomonas aeruginosa to catechol-substituted cephalosporin is unrelated to the pyochelin–Fe transporter FptA. *Amino Acids* **2010**, *38* (5), 1627-1629. DOI: 10.1007/s00726-009-0353-5.

(82) Lankford, C. E.; Byers, B. R. Bacterial Assimilation of iron. *Crit. Rev. Microbiol.* **1973**, *2* (3), 273-331. DOI: 10.3109/10408417309108388.

(83) Petrik, M.; Zhai, C.; Haas, H.; Decristoforo, C. Siderophores for molecular imaging applications. *Clin Transl Imaging* **2017**, *5* (1), 15-27. DOI: 10.1007/s40336-016-0211-x.

(84) Pandey, A.; Cao, M.; Boros, E. Tracking Uptake and Metabolism of Xenometallomycins Using a Multi-Isotope Tagging Strategy. *ACS Infect. Dis.* **2022**, *8* (4), 878-888. DOI: 10.1021/acsinfecdis.2c00005.

(85) Krauser, J. A. A perspective on tritium versus carbon-14: ensuring optimal label selection in pharmaceutical research and development. *J. Labelled Compd. Radiopharm.* **2013**, *56* (9-10), 441-446. (acccessed 2025/03/02).

(86) Pandey, A.; Śmiłowicz, D.; Boros, E. Galbofloxacin: a xenometal-antibiotic with potent in vitro and in vivo efficacy against S. aureus. *Chem Sci* **2021**, *12* (43), 14546-14556, 10.1039/D1SC04283A. DOI: 10.1039/D1SC04283A.

(87) Pandey, A.; Savino, C.; Ahn, S. H.; Yang, Z.; Van Lanen, S. G.; Boros, E. Theranostic Gallium Siderophore Ciprofloxacin Conjugate with Broad Spectrum Antibiotic Potency. *J. Med. Chem.* **2019**, *62* (21), 9947-9960. DOI: 10.1021/acs.jmedchem.9b01388.

(88) Lin, Z.; Xu, X.; Zhao, S.; Yang, X.; Guo, J.; Zhang, Q.; Jing, C.; Chen, S.; He, Y. Total synthesis and antimicrobial evaluation of natural albomycins against clinical pathogens. *Nat. Commun.* **2018**, *9* (1), 3445. DOI: 10.1038/s41467-018-05821-1.

(89) Braun, V.; Pramanik, A.; Gwinner, T.; Köberle, M.; Bohn, E. Sideromycins: tools and antibiotics. *Biometals* **2009**, *22* (1), 3-13. DOI: 10.1007/s10534-008-9199-7 From NLM.

(90) Dong, L.; Roosenberg, J. M.; Miller, M. J. Total Synthesis of Desferrisalmycin B. *JACS* **2002**, *124* (50), 15001-15005. DOI: 10.1021/ja028386w.

(91) Caudy, A. A.; Hanchard, J. A.; Hsieh, A.; Shaan, S.; Rosebrock, A. P. Functional genetic discovery of enzymes using full-scan mass spectrometry metabolomics (1). *Biochem. Cell Biol.* **2019**, *97* (1), 73-84. DOI: 10.1139/bcb-2018-0058 From NLM.

(92) Zampieri, M.; Zimmermann, M.; Claassen, M.; Sauer, U. Nontargeted Metabolomics Reveals the Multilevel Response to Antibiotic Perturbations. *Cell Rep* **2017**, *19* (6), 1214-1228. DOI: 10.1016/j.celrep.2017.04.002 From NLM.

(93) Zampieri, M.; Szappanos, B.; Buchieri, M. V.; Trauner, A.; Piazza, I.; Picotti, P.; Gagneux, S.; Borrell, S.; Gicquel, B.; Lelievre, J.; et al. High-throughput metabolomic analysis predicts mode of action of uncharacterized antimicrobial compounds. *Sci Transl Med* **2018**, *10* (429). DOI: 10.1126/scitranslmed.aal3973 From NLM.

(94) Hoerr, V.; Duggan, G. E.; Zbytnuik, L.; Poon, K. K.; Große, C.; Neugebauer, U.; Methling, K.; Löffler, B.; Vogel, H. J. Characterization and prediction of the mechanism of action of antibiotics through NMR metabolomics. *BMC Microbiol* **2016**, *16*, 82. DOI: 10.1186/s12866-016-0696-5 From NLM.

(95) Petrik, M.; Umlaufova, E.; Raclavsky, V.; Palyzova, A.; Havlicek, V.; Haas, H.; Novy, Z.; Dolezal, D.; Hajduch, M.; Decristoforo, C. Imaging of Pseudomonas aeruginosa infection with Ga-68 labelled pyoverdine for positron emission tomography. *Sci. Rep.* **2018**, *8* (1), 15698. DOI: 10.1038/s41598-018-33895-w.

(96) Petrik, M.; Zhai, C.; Novy, Z.; Urbanek, L.; Haas, H.; Decristoforo, C. In Vitro and In Vivo Comparison of Selected Ga-68 and Zr-89 Labelled Siderophores. *Mol Imaging Biol* **2016**, *18* (3), 344-352. DOI: 10.1007/s11307-015-0897-6 From NLM.

(97) Petrik, M.; Haas, H.; Schrettl, M.; Helbok, A.; Blatzer, M.; Decristoforo, C. In vitro and in vivo evaluation of selected 68Ga-siderophores for infection imaging. *Nucl Med Biol* **2012**, *39* (3), 361-369. DOI: 10.1016/j.nucmedbio.2011.09.012 From NLM.

(98) Kuker, R.; Sztejnberg, M.; Gulec, S. I-124 Imaging and Dosimetry. *Mol Imaging Radionucl Ther* **2017**, *26* (Suppl 1), 66-73. DOI: 10.4274/2017.26.suppl.07 From NLM.

(99) Moroz, M. A.; Serganova, I.; Zanzonico, P.; Ageyeva, L.; Beresten, T.; Dyomina, E.; Burnazi, E.; Finn, R. D.; Doubrovin, M.; Blasberg, R. G. Imaging hNET reporter gene expression with 124I-MIBG. *J Nucl Med* **2007**, *48* (5), 827-836. DOI: 10.2967/jnumed.106.037812 From NLM.

(100) Cistaro, A.; Quartuccio, N.; Caobelli, F.; Piccardo, A.; Paratore, R.; Coppolino, P.; Sperandeo, A.; Arnone, G.; Ficola, U. 124I-MIBG: a new promising positron-emitting radiopharmaceutical for the evaluation of neuroblastoma. *Nucl Med Rev Cent East Eur* **2015**, *18* (2), 102-106. DOI: 10.5603/nmr.2015.0024 From NLM.

(101) Schneider, R. F.; Engelhardt, E. L.; Stobbe, C. C.; Fenning, M. C.; Chapman, J. D. The synthesis and radiolabelling of novel markers of tissue hypoxia of the iodinated azomycin nucleoside class. *J. Labelled Compd. Radiopharm.* **1997**, *39* (7), 541-557. DOI: doi.org/10.1002/(SICI)1099-1344(199707)39:7<541::AID-JLCR5>3.0.CO;2-B.

(102) Riedl, C. C.; Brader, P.; Zanzonico, P.; Reid, V.; Woo, Y.; Wen, B.; Ling, C. C.; Hricak, H.; Fong, Y.; Humm, J. L. Tumor hypoxia imaging in orthotopic liver tumors and peritoneal metastasis: a comparative study featuring dynamic 18F-MISO and 124I-IAZG PET in the same study cohort. *Eur J Nucl Med Mol Imaging* **2008**, *35* (1), 39-46. DOI: 10.1007/s00259-007-0522-2 From NLM.

(103) Riedl, C. C.; Brader, P.; Zanzonico, P. B.; Chun, Y. S.; Woo, Y.; Singh, P.; Carlin, S.; Wen, B.; Ling, C. C.; Hricak, H.; et al. Imaging hypoxia in orthotopic rat liver tumors with iodine 124-labeled iodoazomycin galactopyranoside PET. *Radiology* **2008**, *248* (2), 561-570. DOI: 10.1148/radiol.2482071421 From NLM.

(104) Stahlschmidt, A.; Machulla, H.-J.; Reischl, G.; Knaus, E. E.; Wiebe, L. I. Radioiodination of 1-(2-deoxy-β-d-ribofuranosyl)-2,4-difluoro-5-iodobenzene (dRFIB), a putative thymidine mimic nucleoside for cell proliferation studies. *Appl. Radiat. Isot.* **2008**, *66* (9), 1221-1228. DOI: doi.org/10.1016/j.apradiso.2008.01.014.

(105) Bettegowda, C.; Foss, C. A.; Cheong, I.; Wang, Y.; Diaz, L.; Agrawal, N.; Fox, J.; Dick, J.; Dang, L. H.; Zhou, S.; et al. Imaging bacterial infections with radiolabeled 1-(2′-deoxy-2′-fluoro-β-D-arabinofuranosyl)-5-iodouracil. *PNAS* **2005**, *102* (4), 1145-1150. DOI: doi:10.1073/pnas.0408861102.

(106) Koziorowski, J.; Henssen, C.; Weinreich, R. A new convenient route to radioiodinated N-succinimidyl 3- and 4-iodobenzoate, two reagents for radioiodination of proteins. *Appl. Radiat. Isot.* **1998**, *49* (8), 955-959. DOI: doi.org/10.1016/S0969-8043(97)10112-9.

(107) Robinson, M. K.; Doss, M.; Shaller, C.; Narayanan, D.; Marks, J. D.; Adler, L. P.; González Trotter, D. E.; Adams, G. P. Quantitative immuno-positron emission tomography imaging of HER2-positive tumor xenografts with an iodine-124 labeled anti-HER2 diabody. *Cancer Res* **2005**, *65* (4), 1471-1478. DOI: 10.1158/0008-5472.Can-04-2008 From NLM.

(108) Dolence, E. K.; Minnick, A. A.; Lin, C. E.; Miller, M. J.; Payne, S. M. Synthesis and siderophore and antibacterial activity of N5-acetyl-N5-hydroxy-L-ornithine-derived siderophore-beta-lactam conjugates: iron-transport-mediated drug delivery. *J. Med. Chem.* **1991**, *34* (3), 968-978. DOI: 10.1021/jm00107a014 From NLM.

(109) Adams, C. J.; Wilson, J. J.; Boros, E. Multifunctional Desferrichrome Analogues as Versatile 89Zr(IV) Chelators for ImmunoPET Probe Development. *Mol. Pharm.* **2017**, *14* (8), 2831-2842. DOI: 10.1021/acs.molpharmaceut.7b00343.

(110) Hunsaker, E. W.; Franz, K. J. Emerging Opportunities To Manipulate Metal Trafficking for Therapeutic Benefit. *Inorg. Chem.* **2019**, *58* (20), 13528-13545.

(111) Pandey, A.; Śmiłowicz, D.; Boros, E. Galbofloxacin: a xenometal-antibiotic with potent in vitro and in vivo efficacy against S. aureus. *Chem Sci* **2021**, *12* (43), 14546-14556. DOI: 10.1039/d1sc04283a.

(112) Rix, U.; Superti-Furga, G. Target profiling of small molecules by chemical proteomics. *Nat. Chem. Biol* **2009**, *5* (9), 616-624. DOI: 10.1038/nchembio.216.

(113) Smith, E.; Collins, I. Photoaffinity labeling in target- and binding-site identification. *Future Med Chem* **2015**, *7* (2), 159-183. DOI: 10.4155/fmc.14.152 From NLM.

(114) Westheimer, F. H. Photoaffinity Labeling-Retrospect and Prospect. *Ann. N. Y. Acad. Sci.* **1980**, *346* (1), 134.

(115) Jiang, Y.; Zhang, X.; Nie, H.; Fan, J.; Di, S.; Fu, H.; Zhang, X.; Wang, L.; Tang, C. Dissecting diazirine photo-reaction mechanism for protein residue-specific cross-linking and distance mapping. *Nat. Commun.* **2024**, *15* (1), 6060. DOI: 10.1038/s41467-024-50315-y.

(116) Burton, N. R.; Kim, P.; Backus, K. M. Photoaffinity labelling strategies for mapping the small molecule-protein interactome. *Org Biomol Chem* **2021**, *19* (36), 7792-7809. DOI: 10.1039/d1ob01353j From NLM.

(117) Das, J. Aliphatic Diazirines as Photoaffinity Probes for Proteins: Recent Developments. *Chem. Rev.* **2011**, *111* (8), 4405-4417. DOI: 10.1021/cr1002722.

(118) Platz, M. S. A Perspective on Physical Organic Chemistry. *J. Org. Chem.* **2014**, *79* (6), 2341-2353. DOI: 10.1021/jo500044d.

(119) West, A. V.; Muncipinto, G.; Wu, H.-Y.; Huang, A. C.; Labenski, M. T.; Jones, L. H.; Woo, C. M. Labeling Preferences of Diazirines with Protein Biomolecules. *JACS* **2021**, *143* (17), 6691-6700. DOI: 10.1021/jacs.1c02509.

(120) West, A. V.; Amako, Y.; Woo, C. M. Design and Evaluation of a Cyclobutane Diazirine Alkyne Tag for Photoaffinity Labeling in Cells. *Journal of the American Chemical Society* **2022**, *144* (46), 21174-21183. DOI: 10.1021/jacs.2c08257.

(121) Li, Z.; Hao, P.; Li, L.; Tan, C. Y. J.; Cheng, X.; Chen, G. Y. J.; Sze, S. K.; Shen, H. M.; Yao, S. Q. Design and Synthesis of Minimalist Terminal Alkyne-Containing Diazirine Photo-Crosslinkers and Their Incorporation into Kinase Inhibitors for Cell- and Tissue-Based Proteome Profiling. *Angew. Chem., Int. Ed.* **2013**, *52* (33), 8551.

(122) Prokofeva, P.; Höfer, S.; Hornisch, M.; Abele, M.; Kuster, B.; Médard, G. Merits of Diazirine Photo-Immobilization for Target Profiling of Natural Products and Cofactors. *ACS Chem. Biol* **2022**, *17* (11), 3100-3109. DOI: 10.1021/acschembio.2c00500.

(123) Yu, S. H.; Boyce, M.; Wands, A. M.; Bond, M. R.; Bertozzi, C. R.; Kohler, J. J. Metabolic labeling enables selective photocrosslinking of O-GlcNAc-modified proteins to their binding partners. *Proc. Natl. Acad. Sci. U. S. A.* **2012**, *109* (13), 4834.

(124) Homan, R. A.; Jadhav, A. M.; Conway, L. P.; Parker, C. G. A Chemical Proteomic Map of Heme-Protein Interactions. *JACS* **2022**, *144* (33), 15013-15019. DOI: 10.1021/jacs.2c06104 PubMed.

(125) Gao, J.; Mfuh, A.; Amako, Y.; Woo, C. M. Small Molecule Interactome Mapping by Photoaffinity Labeling Reveals Binding Site Hotspots for the NSAIDs. *J. Am. Chem. Soc.* **2018**, *140* (12), 4259.

(126) Wilkinson, I. V. L.; Bottlinger, M.; El Harraoui, Y.; Sieber, S. A. Profiling the Heme-Binding Proteomes of Bacteria Using Chemical Proteomics. *Angew. Chem. Int. Ed.* **2023**, *62* (9), e202212111.

(127) Takamura, A.; Thuy-Boun, P. S.; Kitamura, S.; Han, Z.; Wolan, D. W. A photoaffinity probe that targets folate-binding proteins. *Bioorg Med Chem Lett* **2021**, *40*, 127903. DOI: 10.1016/j.bmcl.2021.127903 From NLM.

(128) Bugdahn, N.; Peuckert, F.; Albrecht, A. G.; Miethke, M.; Marahiel, M. A.; Oberthür, M. Direct Identification of a Siderophore Import Protein Using Synthetic Petrobactin Ligands. *Angew. Chem. Int. Ed.* **2010**, *49* (52), 10210-10213.

(129) Homan, R. A.; Jadhav, A. M.; Conway, L. P.; Parker, C. G. A Chemical Proteomic Map of Heme–Protein Interactions. *Journal of the American Chemical Society* **2022**, *144* (33), 15013-15019. DOI: 10.1021/jacs.2c06104.

(130) Pandey, A.; Boros, E. Coordination Complexes to Combat Bacterial Infections: Recent Developments, Current Directions and Future Opportunities. *Chem. Eur. J.* **2021**, *27* (26), 7340-7350.

(131) Pinkert, L.; Lai, Y.-H.; Peukert, C.; Hotop, S.-K.; Karge, B.; Schulze, L. M.; Grunenberg, J.; Brönstrup, M. Antibiotic Conjugates with an Artificial MECAM-Based Siderophore Are Potent Agents against Gram-Positive and Gram-Negative Bacterial Pathogens. *J. Med. Chem.* **2021**, *64* (20), 15440-15460. DOI: 10.1021/acs.jmedchem.1c01482.

(132) Miller, M. J.; Liu, R. Design and Syntheses of New Antibiotics Inspired by Nature's Quest for Iron in an Oxidative Climate. *Acc. Chem. Res.* **2021**, *54* (7), 1646-1661. DOI: 10.1021/acs.accounts.1c00004.

(133) Josts, I.; Veith, K.; Tidow, H. Ternary structure of the outer membrane transporter FoxA with resolved signalling domain provides insights into TonB-mediated siderophore uptake. *eLife* **2019**, *8*, e48528. DOI: 10.7554/eLife.48528.

(134) Ferguson, A. D.; Coulton, J. W.; Diederichs, K.; Welte, W.; Braun, V.; Fiedler, H.-P. Crystal structure of the antibiotic albomycin in complex with the outer membrane transporter FhuA. *Protein Sci.* **2000**, *9* (5), 956-963.

(135) Ferguson, A. D.; Ködding, J.; Walker, G.; Bös, C.; Coulton, J. W.; Diederichs, K.; Braun, V.; Welte, W. Active Transport of an Antibiotic Rifamycin Derivative by the Outer-Membrane Protein FhuA. *Structure* **2001**, *9* (8), 707-716. DOI: 10.1016/S0969-2126(01)00631-1 (acccessed 2024/09/05).

(136) Clarke, T. E.; Braun, V.; Winkelmann, G.; Tari, L. W.; Vogel, H. J. X-ray Crystallographic Structures of the Escherichia coli Periplasmic Protein FhuD Bound to Hydroxamate-type Siderophores and the Antibiotic Albomycin*. *JBC* **2002**, *277* (16), 13966-13972.

(137) Sarih, N. M.; Ciupa, A.; Moss, S.; Myers, P.; Slater, A. G.; Abdullah, Z.; Tajuddin, H. A.; Maher, S. Furo[3,2-c]coumarin-derived Fe3+ Selective Fluorescence Sensor: Synthesis, Fluorescence Study and Application to Water Analysis. *Sci. Rep.* **2020**, *10* (1), 7421. DOI: 10.1038/s41598-020-63262-7.

(138) Chen, J.; Browne, W. R. Photochemistry of iron complexes. *Coord. Chem. Rev.* **2018**, *374*, 15-35.

(139) Gertsik, N.; Am Ende, C. W.; Geoghegan, K. F.; Nguyen, C.; Mukherjee, P.; Mente, S.; Seneviratne, U.; Johnson, D. S.; Li, Y. M. Mapping the Binding Site of BMS-708163 on gamma-Secretase with Cleavable Photoprobes. *Cell Chem. Biol.* **2017**, *24* (1), 3.

(140) Qi, B.; Han, M. Microbial Siderophore Enterobactin Promotes Mitochondrial Iron Uptake and Development of the Host via Interaction with ATP Synthase. *Cell* **2018**, *175* (2), 571-582.e511. DOI: doi.org/10.1016/j.cell.2018.07.032.

(141) Domínguez-Vera, J. M. Iron(III) complexation of Desferrioxamine B encapsulated in apoferritin. *J. Inorg. Biochem.* **2004**, *98* (3), 469-472. DOI: 10.1016/j.jinorgbio.2003.12.015 From NLM.

(142) Danilovtseva, E. N.; Pal'shin, V. A.; Krishnan, U. M.; Annenkov, V. V.; Zelinskiy, S. N. Tagging synthetic polymers with coumarin group for study nucleic acid interaction with gene delivery agents. *MethodsX* **2019**, *6*, 212-218. DOI: 10.1016/j.mex.2019.01.008 From NLM.

(143) Reynolds, G. A.; Drexhage, K. H. New coumarin dyes with rigidized structure for flashlamp-pumped dye lasers. *Opt. Commun.* **1975**, *13* (3), 222-225. DOI: doi.org/10.1016/0030-4018(75)90085-1.

(144) Kleiner, P.; Heydenreuter, W.; Stahl, M.; Korotkov, V. S.; Sieber, S. A. A Whole Proteome Inventory of Background Photocrosslinker Binding. *Angew. Chem. Int. Ed.* **2017**, *56* (5), 1396-1401. DOI: doi.org/10.1002/anie.201605993.

(145) Hantke, K. Dihydroxybenzoylserine--a siderophore for E. coli. *FEMS Microbiol. Lett.* **1990**, *55* (1-2), 5-8. DOI: 10.1016/0378-1097(90)90158-m From NLM.

(146) Grinter, R.; Lithgow, T. The structure of the bacterial iron-catecholate transporter Fiu suggests that it imports substrates via a two-step mechanism. *J. Biol. Chem.* **2019**, *294* (51), 19523-19534. DOI: 10.1074/jbc.RA119.011018 From NLM.

(147) Moynié, L.; Milenkovic, S.; Mislin, G. L. A.; Gasser, V.; Malloci, G.; Baco, E.; McCaughan, R. P.; Page, M. G. P.; Schalk, I. J.; Ceccarelli, M.; et al. The complex of ferric-enterobactin with its transporter from Pseudomonas aeruginosa suggests a two-site model. *Nat. Commun.* **2019**, *10* (1), 3673. DOI: 10.1038/s41467-019-11508-y.

(148) Najimi, M.; Lemos, M. L.; Osorio, C. R. Identification of siderophore biosynthesis genes essential for growth of Aeromonas salmonicida under iron limitation conditions.

Appl. Environ. Microbiol. **2008**, *74* (8), 2341-2348. DOI: 10.1128/aem.02728-07 From NLM.

(149) Stojiljkovic, I.; Bäumler, A. J.; Hantke, K. Fur Regulon in Gram-negative Bacteria: Identification and Characterization of New Iron-regulated Escherichia coli Genes by a Fur Titration Assay. *J. Mol. Biol.* **1994**, *236* (2), 531-545. DOI: doi.org/10.1006/jmbi.1994.1163.

(150) Josts, I.; Veith, K.; Normant, V.; Schalk, I. J.; Tidow, H. Structural insights into a novel family of integral membrane siderophore reductases. *PNAS* **2021**, *118* (34), e2101952118. DOI: 10.1073/pnas.2101952118.

(151) Sargun, A.; Johnstone, T. C.; Zhi, H.; Raffatellu, M.; Nolan, E. M. Enterobactin- and salmochelin-beta-lactam conjugates induce cell morphologies consistent with inhibition of penicillin-binding proteins in uropathogenic Escherichia coli CFT073. *Chem Sci* **2021**, *12* (11), 4041-4056. DOI: 10.1039/d0sc04337k.

(152) Sargun, A.; Sassone-Corsi, M.; Zheng, T.; Raffatellu, M.; Nolan, E. M. Conjugation to Enterobactin and Salmochelin S4 Enhances the Antimicrobial Activity and Selectivity of beta-Lactam Antibiotics against Nontyphoidal Salmonella. *ACS Infect Dis* **2021**, *7* (5), 1248-1259. DOI: 10.1021/acsinfecdis.1c00005.

(153) Kumar, A.; Yang, T.; Chakravorty, S.; Majumdar, A.; Nairn, B. L.; Six, D. A.; Marcondes dos Santos, N.; Price, S. L.; Lawrenz, M. B.; Actis, L. A.; et al. Fluorescent sensors of siderophores produced by bacterial pathogens. *J. Biol. Chem.* **2022**, *298* (3), 101651. DOI: doi.org/10.1016/j.jbc.2022.101651.

(154) Ni, J.; Wood, J. L.; White, M. Y.; Lihi, N.; Markham, T. E.; Wang, J.; Chivers, P. T.; Codd, R. Reduction-cleavable desferrioxamine B pulldown system enriches Ni(ii)-superoxide dismutase from a Streptomyces proteome. *RSC Chemical Biology* **2023**, *4* (12), 1064-1072, 10.1039/D3CB00097D. DOI: 10.1039/D3CB00097D.

(155) Guo, C.; Nolan, E. M. Exploring the Antibacterial Activity and Cellular Fates of Enterobactin–Drug Conjugates That Target Gram-Negative Bacterial Pathogens. *Acc. Chem. Res.* **2024**, *57* (7), 1046-1056. DOI: 10.1021/acs.accounts.3c00814.

(156) Shi, Y.; Cao, Q.; Sun, J.; Hu, X.; Su, Z.; Xu, Y.; Zhang, H.; Lan, L.; Feng, Y. The opportunistic pathogen Pseudomonas aeruginosa exploits bacterial biotin synthesis pathway to benefit its infectivity. *PLOS Pathogens* **2023**, *19* (1), e1011110. DOI: 10.1371/journal.ppat.1011110.

(157) Kacar, B.; Garmendia, E.; Tuncbag, N.; Andersson Dan, I.; Hughes, D. Functional Constraints on Replacing an Essential Gene with Its Ancient and Modern Homologs. *mBio* **2017**, *8* (4), 10.1128/mbio.01276-01217. DOI: 10.1128/mbio.01276-17 (acccessed 2025/03/27).

(158) Prehna, G.; Zhang, G.; Gong, X.; Duszyk, M.; Okon, M.; McIntosh, Lawrence P.; Weiner, Joel H.; Strynadka, Natalie C. J. A Protein Export Pathway Involving Escherichia coli Porins. *Structure* **2012**, *20* (7), 1154-1166.

(159) Gerken, H.; Vuong, P.; Soparkar, K.; Misra, R. Roles of the EnvZ/OmpR Two-Component System and Porins in Iron Acquisition in Escherichia coli. *mBio* **2020**, *11* (3). DOI: 10.1128/mBio.01192-20 From NLM.

(160) Sauer, M.; Hantke, K.; Braun, V. Ferric-coprogen receptor FhuE of Escherichia coli: processing and sequence common to all TonB-dependent outer membrane receptor proteins. *J. Bacteriol.* **1987**, *169* (5), 2044-2049. DOI: 10.1128/jb.169.5.2044-2049.1987 From NLM.

(161) Gerken, H.; Vuong, P.; Soparkar, K.; Misra, R. Roles of the EnvZ/OmpR Two-Component System and Porins in Iron Acquisition in Escherichia coli. *mBio* **2020**, *11* (3), 10.1128/mbio.01192-01120. DOI: 10.1128/mbio.01192-20 (acccessed 2024/08/08).

(162) Yamashita, E.; Zhalnina, M. V.; Zakharov, S. D.; Sharma, O.; Cramer, W. A. Crystal structures of the OmpF porin: function in a colicin translocon. *EMBO J.* **2008**, *27* (15), 2171-2180. DOI: 10.1038/emboj.2008.137 From NLM.

(163) Apetrei, A.; Asandei, A.; Park, Y.; Hahm, K.-S.; Winterhalter, M.; Luchian, T. Unimolecular study of the interaction between the outer membrane protein OmpF from E. coli and an analogue of the HP(2–20) antimicrobial peptide. *J Bioenerg Biomembr.* **2010**, *42* (2), 173-180. DOI: 10.1007/s10863-010-9273-z.

(164) Masi, M.; Vergalli, J.; Ghai, I.; Barba-Bon, A.; Schembri, T.; Nau, W. M.; Lafitte, D.; Winterhalter, M.; Pagès, J.-M. Cephalosporin translocation across enterobacterial OmpF and OmpC channels, a filter across the outer membrane. *Commun. Biol* **2022**, *5* (1), 1059. DOI: 10.1038/s42003-022-04035-y.

(165) Ziervogel, B. K.; Roux, B. The binding of antibiotics in OmpF porin. *Structure* **2013**, *21* (1), 76-87. DOI: 10.1016/j.str.2012.10.014 From NLM.

(166) Grinter, R.; Lithgow, T. Determination of the molecular basis for coprogen import by Gram-negative bacteria. *IUCrJ* **2019**, *6* (Pt 3), 401-411. DOI: 10.1107/s2052252519002926 From NLM.

(167) Mey Alexandra, R.; Gómez-Garzón, C.; Payne Shelley, M. Iron Transport and Metabolism in Escherichia, Shigella, and Salmonella. *EcoSal Plus* **2021**, *9* (2), eESP-0034-2020. DOI: 10.1128/ecosalplus.ESP-0034-2020 (acccessed 2025/04/16).

(168) Josts, I.; Veith, K.; Tidow, H. Ternary structure of the outer membrane transporter FoxA with resolved signalling domain provides insights into TonB-mediated siderophore uptake. *eLife* **2019**, *8*. DOI: 10.7554/elife.48528.

(169) Rolston Kenneth, V. I.; Gerges, B.; Shelburne, S.; Aitken Samuel, L.; Raad, I.; Prince Randall, A. Activity of Cefiderocol and Comparators against Isolates from Cancer Patients. *Antimicrob. Agents Chemother.* **2020**, *64* (5), 10.1128/aac.01955-01919. DOI: 10.1128/aac.01955-19 (acccessed 2025/03/25).

(170) Lambregts, M. M. C.; Bernards, A. T.; van der Beek, M. T.; Visser, L. G.; de Boer, M. G. Time to positivity of blood cultures supports early re-evaluation of empiric broad-spectrum antimicrobial therapy. *PLOS ONE* **2019**, *14* (1), e0208819. DOI: 10.1371/journal.pone.0208819.

(171) Petrik, M.; Umlaufova, E.; Raclavsky, V.; Palyzova, A.; Havlicek, V.; Pfister, J.; Mair, C.; Novy, Z.; Popper, M.; Hajduch, M.; et al. (68)Ga-labelled desferrioxamine-B for bacterial infection imaging. *Eur J Nucl Med Mol Imaging* **2021**, *48* (2), 372-382. DOI: 10.1007/s00259-020-04948-y From NLM.

(172) Marlin, A.; Tran, P. N.; Dierolf, M.; DeLuca, M.; Joaqui Joaqui, M. A.; Glaser, O. M.; Koller, A. J.; Alucio-Sarduy, E.; Gork, M.; Śmiłowicz, D.; et al. Evaluation of PSMA-Targeted TREN-CAM Conjugates for Targeted Imaging of Cancer with 68Ga(III) and 45Ti(IV). *Bioconjugate Chem.* **2025**. DOI: 10.1021/acs.bioconjchem.5c00099.

(173) Koller, A. J.; Glaser, O.; DeLuca, M. C.; Motz, R. N.; Amason, E. K.; Carbo-Bague, I.; Mixdorf, J. C.; Guzei, I. A.; Aluicio-Sarduy, E.; Śmiłowicz, D.; et al. “Off-Label Use” of the Siderophore Enterobactin Enables Targeted Imaging of Cancer with Radioactive Ti(IV). *Angew. Chem. Int. Ed.* **2024**, *63* (18), e202319578. DOI: doi.org/10.1002/anie.202319578 (acccessed 2025/03/26).

(174) Motz, R. N.; Guo, C.; Sargun, A.; Walker, G. T.; Sassone-Corsi, M.; Raffatellu, M.; Nolan, E. M. Conjugation to Native and Nonnative Triscatecholate Siderophores Enhances Delivery and Antibacterial Activity of a β-Lactam to Gram-Negative Bacterial Pathogens. *JACS* **2024**, *146* (11), 7708-7722. DOI: 10.1021/jacs.3c14490.

(175) Peukert, C.; Gasser, V.; Orth, T.; Fritsch, S.; Normant, V.; Cunrath, O.; Schalk, I. J.; Brönstrup, M. Trojan Horse Siderophore Conjugates Induce Pseudomonas aeruginosa Suicide and Qualify the TonB Protein as a Novel Antibiotic Target. *J. Med. Chem.* **2023**, *66* (1), 553-576. DOI: 10.1021/acs.jmedchem.2c01489.